


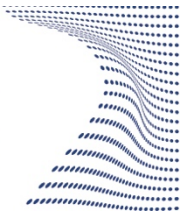

Doctoral Dissertation
Doctoral Program in Civil and Environmental Engineering (33rd Cycle)

Elastic Lattice Models: From Proteins to Diagrid Tall Buildings

Domenico Scaramozzino
* * * * * *

Supervisors

Prof. Alberto Carpinteri
Prof. Giuseppe Lacidogna

Doctoral Examination Committee:

Prof. Luciano Lamberti, Referee, Politecnico di Bari, Italy
Prof. Sanichiro Yoshida, Referee, Southeastern Louisiana University, USA
Prof. Horacio D. Espinosa, Northwestern University, USA
Prof. Fernando Fraternali, Univerità di Salerno, Italy

Politecnico di Torino
October, 2020

I hereby declare that, the contents and organisation of this dissertation constitute my own original work and does not compromise in any way the rights of third parties, including those relating to the security of personal data.

…….

Domenico Scaramozzino

Turin, October 31, 2020

Summary

What do proteins and diagrid tall buildings have in common? Apparently nothing. The former are nanoscopic biological systems, functioning in a complex chemo-physical environment, whose activity is pivotal to carry out a variety of physiological processes. The latter are macroscopic structural systems that are employed nowadays for the design and construction of tall buildings. Nevertheless, in this Thesis, it will be shown that both proteins and diagrid tall buildings can be investigated and modeled by means of the same structural system, the Elastic Lattice Model (ELM). ELMs are spatial structures usually made of springs or bars connected in correspondence of nodes, that can be treated as spherical hinges. In this Thesis, we will use the ELMs to explore a variety of behaviors and features of proteins and diagrids.

In particular, it will be shown that proteins can be efficiently modeled as a network of springs and point masses. Within the framework of modal analysis, these ELMs will be very useful to obtain accurate information regarding protein dynamics and vibrations. Specifically, the low-frequency vibrations extracted from the protein ELMs will be shown to correlate truthfully with the protein biological mechanisms and conformational changes, as well as to provide correct insights on the protein experimental flexibility, as obtained from the experimental B-factors. For this purpose, various modeling approaches will be presented and analyzed. Furthermore, we will see that applying point forces on the protein ELM also provides remarkable insights on protein flexibility. Two novel force application patterns will be reported for this purpose and the results will show that the protein ELMs coupled with the traditional linear static analysis can lead to correct predictions of the protein deformability. Finally, the possible role of geometrical non-linearities will also be investigated within the large-scale conformational changes, which are usually known to exhibit fairly large displacements. From the analyses, it will be shown that these conformational changes often imply curvilinear pathways and possible mechanical non-linearities in the structural response.

Switching to the subject of diagrid tall buildings, the ELMs will then be used to develop a matrix-based method (MBM) for the structural analysis of generic three-dimensional diagrid systems. Based on matrix calculus and the displacements method, the MBM will be applied to perform the structural analysis of diagrids, both alone and coupled with internal cores. The force distribution and the interaction of the external diagrid with the internal resisting element will be studied by inserting the MBM within the General Algorithm (GA), a semi-analytical framework developed few decades ago for the investigation of complex three-dimensional buildings. Furthermore, the MBM will be deeply exploited to investigate the influence of the diagrid geometry on the structural response. Namely, geometrical parameters such as the diagonal inclination, floor shape and building aspect ratio, will be changed in order to obtain information on the lateral and torsional flexibility of the diagrid. From these analysis, it will be shown that different diagrid geometries have a marked effect on the structural response and often a unique solution that allows to optimize all the responses does not exist. For this reason, a novel multi-response optimization will be presented, which makes use, for the first time in this field, of the desirability function approach. Based on the results of the MBM structural analyses, the desirability function will be applied to evaluate the optimal diagrid geometry that simultaneously optimizes the lateral and torsional rigidity, the amount of used material as well as the construction complexity. The outcomes will show that the desirability approach, coupled with the ELM-based MBM, is a simple yet valuable and robust tool for the selection of the optimal diagrid geometry.

Acknowledgments

As I have come to the end of this three-year journey, that has been for me a great opportunity for my professional development and mostly for my personal growth, it is amazing to think of how many people have taken part to this chapter of my life. Some for few moments and some others without breaks, some who I met during the journey and some others who were here from the very beginning and will keep on being here.

The first acknowledgment goes obviously to my family. To my dad, who has always been for me a life example since when I can remember of. Thank you for being and to be my Polar Star. To my mum, from whom I have taken perhaps most of my defects, but surely also all my merits and my strengths. Thank you for always being there and for your daily efforts in making our family better. To my sister. What should I say? She is the most important person of my life, from whom I have learnt and keep learning much more than she could ever imagine. Thank you simply for the gift I had having you as my sister.

The second acknowledgment goes to my supervisors. To Prof. Carpinteri, for believing in me from the very beginning, urging me to apply for the PhD before my intended plans and giving me the trust that has allowed me to become the independent person that I am today. Thank you for giving me this amazing opportunity. To Prof. Lacidogna, with whom, despite our different roles in the workplace, a good friendship was immediately born. Thank you for always giving me extreme trust and supporting me continuously since the time of my MSc Thesis.

An additional acknowledgment needs to be addressed to all my friends and colleagues, without whom these past years would certainly have been more difficult to face. Thanks to all my friends that I met at the very beginning of my university journey and never left, with whom I really feel part of a group. Thank you Pietro, Nino, Michele and Beppe. Thanks also to the friends I met few years later, but now part of my most sincere friendships. Thank you Maurizio, Alessio and Peyman. Thanks also to all the colleagues of the DISEG third floor, with whom the days in the office were joyfully spent between laughs and semi-serious

speeches. Thank you Gianfranco, Federico, Francesco, Oscar, Gianni, Giuseppe and Fabio.

Now it is time to move to the international acknowledgments. A special thanks goes to Prof. Jernigan, thanks to whom I had the opportunity to spend six months in the United States at Iowa State University. Six months, not without difficulties, but which were nevertheless very useful both for my scientific and personal growth. I also thank him for the several researches that we have conducted together, some of which are reported in Chapters 2 and 3 of this Thesis and some others still under development. A big thanks also goes to all those who welcomed me into the Jernigan Computational Lab and made me feel a little less alone on the other side of the world. So thank you Kejue, Dan and Sayane. A special thanks goes to Pranav and Ambuj, with whom I have formed a sincere friendship and a strong scientific collaboration. I feel that our works about force applications on proteins and hdANM are just the starting point of an amazing collaboration, and I feel grateful for that.

Ringraziamenti

Arrivato alla fine di questo percorso durato tre anni, che ha rappresentato per me una grande occasione di crescita professionale ma soprattutto personale, è incredibile pensare a quante persone hanno preso parte a questo capitolo della mia vita. Chi per pochi istanti e chi in maniera continuativa, chi ci è entrato a treno in corsa e chi c'era fin dall'inizio e continuerà ad esserci.

Il primo ringraziamento va sicuramente alla mia famiglia. A mio papà, che è sempre stato per me un esempio da emulare fin da quando ne ho memoria. Grazie per essere stato ed essere tutt'ora la mia stella polare. A mia mamma, dalla quale ho preso forse gran parte dei miei difetti, ma sicuramente tutti i miei pregi e punti di forza. Grazie per esserci stata ed esserci sempre, e per lo sforzo che fai ogni giorno per rendere la nostra famiglia migliore. A mia sorella. Che dire, la persona più importante della mia vita, da cui ho imparato e continuo ad imparare più di quanto lei possa immaginare. Grazie semplicemente per la fortuna che ho avuto ad averti come sorella.

Il secondo ringraziamento va ovviamente ai miei tutori. Al prof. Carpinteri, per aver creduto in me sin dall'inizio, avermi spronato ad entrare nel dottorato in anticipo rispetto ai miei piani e ad avermi dato quella fiducia che mi ha concesso di diventare la persona indipendente che sono oggi. Grazie per avermi dato questa opportunità. Al prof. Lacidogna, con cui, nonostante i diversi ruoli in ambito lavorativo, è da subito nata quella che spero di poter definire una buona amicizia. Grazie per avermi sempre dato estrema fiducia e per avermi sostenuto ininterrottamente fin dai tempi della tesi di laurea magistrale.

Un ulteriore ringraziamento va a tutti i miei amici e colleghi, senza i quali questi anni sarebbero stati sicuramente più difficili da affrontare. Grazie agli amici incontrati fin dai primi anni dell'università e mai più lasciati, con il quale mi sento davvero parte di un gruppo. Grazie Pietro, Nino, Michele e Beppe. Grazie anche agli amici incontrati qualche anno più in là, ma ormai parte delle mie amicizie più sincere. Grazie Maurizio, Alessio e Peyman. Grazie anche a tutti i colleghi del terzo piano del DISEG, con i quali le giornate in ufficio sono trascorse tra risate e

discorsi semi-seri. Grazie Gianfranco, Federico, Francesco, Oscar, Gianni, Giuseppe e Fabio.

Ora si passa ai ringraziamenti internazionali. Un grazie particolare va al Prof. Jernigan, grazie al quale ho avuto la possibilità di passare sei mesi negli Stati Uniti presso la Iowa State University. Sei mesi non senza difficoltà, ma che sono stati comunque molto utili sia per la mia crescita scientifica che personale. A lui va anche un ringraziamento per le tante ricerche che abbiamo condotto insieme, alcune delle quali sono riportate nei Capitoli 2 e 3 di questa Tesi, alcune ancora in fase di sviluppo. Un forte ringraziamento va anche a tutti coloro che mi hanno accolto nel Jernigan Computational Lab e mi hanno fatto sentire un po' meno solo dall'altra parte del mondo. Grazie quindi Kejue, Dan e Sayane. Un ringraziamento speciale va a Pranav e Ambuj, con i quali sento di aver stretto una forte amicizia ed una ancor più forte collaborazione scientifica. Sento che i nostri lavori sulle proteine sono solo il punto di partenza di una straordinaria collaborazione, e per questo ve ne sono grato.

To my parents Giuseppe and Agnese
To my sister (and bedrock) Maria Sara

Contents

List of Tables

List of Figures

Figure 4.15. Relative stiffness of diagrid and shear wall: (a) lateral stiffness, (b) torsional stiffness. Used with permission from Lacidogna et al. [129].
Figure 5.1. Different diagonal angle patterns: (a) varying-angle with steeper diagonals at the base; (b) uniform-angle; (c) varying-angle with steeper angle at the top, used with permission from Moon [110]; (d) varying-angle with straight diagonals; (e) varying-angle with curved diagonals, used with permission from Zhao and Zhang [130].
Figure 5.2. (a) Different geometrical patterns from Montuori et al. [133]: uniform-angle patterns (60°, 70°, 80°), varying-angle patterns according to Moon approach (VA1, VA2) [110,131], varying-angle pattern according to Zhang approach (VA3) [132], variable-density patterns (VD1, VD2). (b) Efficiency parameters for the investigated solutions. Used with permission from Montuori et al. [133].
Figure 5.3. Variable-density (VD) patterns proposed by Angelucci and Mollaioli [108]: (a-b) concentrated outrigger-like VD pattern; (c-d) distributed VD pattern. Used with permission from Angelucci and Mollaioli [108].
Figure 5.4. (a) Geometrical patterns for the 90-story tall diagrid building considered by Tomei et al. [134]: uniform-angle patterns (60°, 70°, 80°), varying-angle pattern according to Zhang approach (VA) [132], double-density pattern (DD), variable-density pattern (VD), stress lines pattern (ISO). (b) Unit structural weight (blue bars) and complexity index (red curve) for the investigated diagrid patterns. VA_IDR, VD_1, VD_15, ISO_15, ISO_9, ISO_5, ISO_5* refer to additional subsets of the corresponding patterns, as reported in [134]. Used with permission from Tomei et al. [134].
Figure 5.5. Geometry of the generated diagrid buildings: (a) four different total heights; (b) four different floor plan shapes; (c) six different diagonal inclinations. Used with permission from Lacidogna et al. [137].
Figure 5.6. Displacements and rotations for the 36-story building: (a–b) lateral displacements; (c–d) torsional rotations. Used with permission from Lacidogna et al. [137].
Figure 5.7. Displacements and rotations for the 48-story building: (a–b) lateral displacements; (c–d) torsional rotations. Used with permission from Lacidogna et al. [137].
Figure 5.8. Displacements and rotations for the 60-story building: (a–b) lateral displacements; (c–d) torsional rotations. Used with permission from Lacidogna et al. [137].
Figure 5.9. Displacements and rotations for the 72-story building: (a–b) lateral displacements; (c–d) torsional rotations. Used with permission from Lacidogna et al. [137].
Figure 5.10. Graphical representation of the individual desirability functions $d_i(y_i)$ for different optimization criteria. The response y_i is most desirable if it reaches (a) the upper value U_i, (b) the lower value L_i, (c) a specified target value T_i. Continuous lines are obtained with r_i equal to 1, dashed lines with r_i less than 1 and dotted lines with r_i higher than 1.
Figure 5.11. (a) Individual desirability values for the four response variables (r_i = 1) and (b) OD values. Used with permission from [142].
Figure 5.12. Surface representation of the OD with respect to the diagrid geometrical parameters (diagonal angle and floor shape). OD values are reported in the vertical axis and represented by means of color shades. Used with permission from [142].
Figure 5.13. Optimal diagrid geometry based on 4096 simulations with different exponents of the individual desirability values. Used with permission from [142].
Figure 5.14. Results for the 126-meter tall building: (a) surface representation of the OD obtained with $r_\delta = r_\varphi = r_M = r_{CI} = 1$; (b) optimal diagrid geometry based on 4096 simulations with different exponents r_i. Used with permission from [142].
Figure 5.15. Results for the 210-meter tall building: (a) surface representation of the OD obtained with $r_\delta = r_\varphi = r_M = r_{CI} = 1$; (b) optimal diagrid geometry based on 4096 simulations with different exponents r_i. Used with permission from [142].

Chapter 1

Introduction

The ground foundation of every Structural Mechanics course is based on the Hooke's law. It is the simplest constitutive relation that describes the mechanical behavior of an elastic material. In 1679, Robert Hooke published a book titled *Lectures Cutlerianae, or a Collection of Lectures* [1], where various systems and topics were addressed in details, ranging from the observation of the earth motion to the description of helioscopes and microscopes, from the observation of comets to the description of wind-fountains and force pumps. The wide variety of investigated subjects reveals the different sensibility of past scientists, at a time when science was not broken into smaller and smaller pieces but it was deemed to provide answers for multiple questions.

One of the lectures contained within the Hooke's collection, titled *De Potentia Restitutiva or of Spring* [1], has become particularly of interest for civil and mechanical engineers of the centuries to come. At the beginning of that lecture, Hooke writes:

> The Theory of Springs, though attempted by drivers eminent Mathematicians of this Age has hitherto not been Published by any. It is now about eighteen years since I first found it out, but designing to apply it to some particular use, I omitted the publishing thereof.
>
> About three years since His Majesty was pleased to see the Experiment that made out this Theory tried at *White-Hall*, as also my Spring Watch.
>
> About two years since I printed this Theory in an Anagram at the end of my Book of the Description of Helioscopes, *viz. c e i i i n o s s s t t u v*, id est, *Ut tensio sic vis*; That is, the Power of any Spring is in the same proportion with the Tension thereof: That is, if one power stretch or bend it one space, two will bend it two, and three will bend it three, and so forward. Now as the Theory is very short, so the way of trying is very easie [1].

Ut tension sic vis. This is the basic idea of Hooke's law, firstly printed as an encrypted anagram, that can also be formulated with the expression *As the extension, so the force*. Therefore, there exists a linear proportion between the applied force and the corresponding extension. If the force doubles or is halved, so does the extension. In mathematical terms, this law can be expressed as the famous:

$$F = k\delta, \tag{1.1}$$

F being the force, δ the extension and k the so-called spring constant, that plays the role of the stiffness of the system. Hooke carried out several experiments when suggesting this law. Figure 1.1 shows the picture of one of these experiments, as reported in *De Potentia Restitutiva* [1].

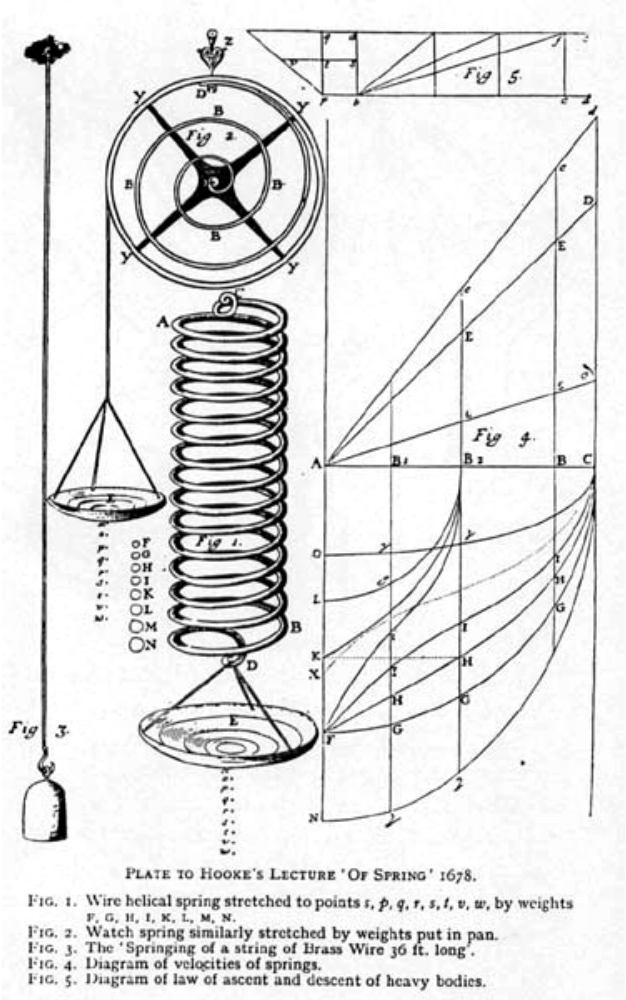

PLATE TO HOOKE'S LECTURE 'OF SPRING' 1678.

FIG. 1. Wire helical spring stretched to points *s*, *p*, *q*, *r*, *s*, *t*, *v*, *w*, by weights F, G, H, I, K, L, M, N.
FIG. 2. Watch spring similarly stretched by weights put in pan.
FIG. 3. The 'Springing of a string of Brass Wire 36 ft. long'.
FIG. 4. Diagram of velocities of springs.
FIG. 5. Diagram of law of ascent and descent of heavy bodies.

Figure 1.1. Experimental set-up regarding the Hooke's law, as reported in *De Potentia Restitutiva* [1].

More than three centuries after the publication of Hooke's collection of lectures, today we know that the Hooke's law is valid in certain cases, but it does not hold true in a variety of other cases. Most likely, Hooke already observed this during his experiments. Materials are known to exhibit a linear elastic behavior for low stress levels and subsequently they can show non-linear responses in the load-deflection curve because of several phenomena, such as internal damaging process, cracking, yielding, etc. Also at the level of the structural elements, such as beams, plates, trusses, frames, etc., we know that the linearity between the applied forces and the corresponding deformations holds true for low values of the external perturbation. After a certain point and depending on the characteristics of the structural elements and employed materials, non-linear paths can show up in the load-deflection curve due to various effects, such as geometrical non-linearities, fracturing of some members, etc.

However, the Hooke's law is still the building block of most of the first-order approaches to analyze the response of the most common structural elements. In its

original formulation, it has been referred to the most simple structural element, i.e. the linear spring. Given the spring constant k, we can immediately know the spring elongation δ for a given external perturbation F based on Eq. (1.1). Also, we can estimate the amount of force F which is required to obtain a certain spring elongation δ. This simple equation can be generalized in matrix form to obtain what is usually referred to as the generalized Hooke's law:

$$\boldsymbol{F} = \boldsymbol{K}\boldsymbol{\delta}, \tag{1.2}$$

being $\boldsymbol{F}$ the generalized force vector, $\boldsymbol{\delta}$ the generalized displacement vector and $\boldsymbol{K}$ the stiffness matrix. By means of Eq. (1.2), much more complex systems than the simple linear spring can be analyzed. In this case, given the stiffness matrix of the structure $\boldsymbol{K}$, we can immediately obtain the structure displacements $\boldsymbol{\delta}$ for a given set of external perturbations $\boldsymbol{F}$, or we can estimate the amount of external forces $\boldsymbol{F}$ which is required to obtain certain structure displacements $\boldsymbol{\delta}$.

It is then clear that, despite the simplicity of Eq. (1.1), the generalization of such a law to more complex structural systems allows their solution to become quite simple and automatic. Equation (1.2) is the foundation of one of the most used approaches to solve structures, which is taught to every student in Structural Mechanics classes: the displacements method. It relies on the calculation of the stiffness matrix of the structural members that form the structure, which is nothing more than the application of the Hooke's law for systems with a higher number of degrees of freedom (DOFs). One of the advantages of the displacements method to solve structures is that it can be easily made automatic and coded within modern computers. This is what is usually done within the framework of the Finite Element Method (FEM). These methodologies can be applied to a wide variety of structural systems with different types and numbers of DOFs, e.g. springs, beams, shells, plates, solids, frames, trusses, etc.

In the next Section, one kind of structural system will be described, which can be thought of as the generalization of the Hookean linear elastic spring and will be deeply analyzed in this Thesis with respect to two diverse fields of investigation: the Elastic Lattice Model (ELM).

1.1. Elastic Lattice Models (ELMs)

The Elastic Lattice Model (ELM) is an elastic truss system where various elements are connected together, generally in a complex three-dimensional fashion. Depending on the specific application, the ELMs can be thought of as made of springs or bars, connected together at nodal points which usually embody spherical hinges. The difference between thinking of the ELM as made of springs or rods is that the flexural stiffness of the former (the spring) is usually negligible, whereas the latter (the bar) can exhibit a significant resistance against bending actions. However, in most cases, the external perturbations are often applied to the nodal points of the ELM, thus the bending stiffness of the elementary members is not involved into the deformation mechanism and therefore it becomes not relevant. The axial rigidity of the members, either springs or rods, is the fundamental characteristic of the structure and drives the deformation mode. For this reason, in the ELM each member is supposed to obey to Eq. (1.1), where k can be seen as the spring constant for the ELM springs or the axial stiffness for the ELM bar members.

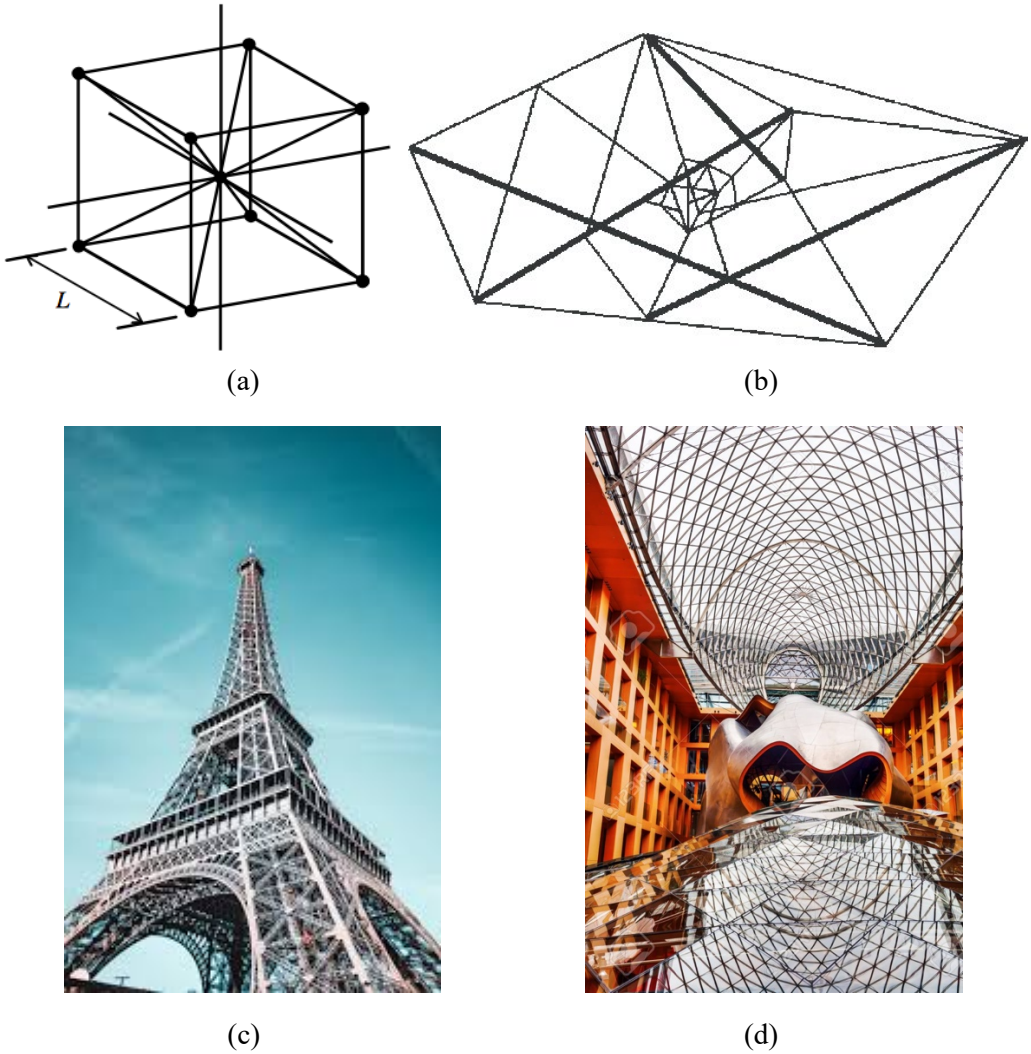

Figure 1.2. ELMs and their different field of (methodological or physical) application: (a) ELM as the basic unit of the truss-like Discrete Element Method for the investigation of fracture and damage mechanics (used with permission from Kosteski et al. [2]); (b) ELM-based tensegrity structure for the analysis of the bio-mechanical response of cells (used with permission from Verdier [3]); (c) ELM for the realization of the high-rise Eiffel Tower in Paris; (d) ELM for the construction of the DZ Bank roof in Berlin.

ELMs are employed in a wide variety of cases and research fields to describe properties of materials and structures. A typical example is the lattice modeling of inter-atomic interactions in crystalline materials. The recurring pattern of connections among the atomic networks is often modeled through the lattice representation. ELMs are also used to simulate the micro-mechanical characteristics of materials, the continuum solid being discretized into tiny elementary components. In this case, modeling the micro-mechanical features of the lattice allows to investigate the mechanical behavior of the continuum. One of the examples is represented by the truss-like Discrete Element Method (Figure 1.1a), useful for the investigation of fracture and damaging processes [2,4]. Also, special types of ELMs have been developed, called tensegrity structures, where members under compression are not in contact with each other and are kept in equilibrium by means of a network of pretensioned cables. These ELMs have been shown to be impressively successful in describing the bio-mechanical features of cells, such as their shape, movements and response to mechanical stimuli (Figure 1.1b) [5]. Obviously, ELMs do not represent only methodological

frameworks useful to investigate some ethereal feature of the microscopic world. They are also exploited in the world of constructions and architecture, typically as steel or timber truss structures. Well-known examples of lattice (truss) structures range from the high-rise Eiffel Tower in Paris (Figure 1.1c) to the DZ Bank roof in Berlin (Figure 1.1d), up to the giant electric poles which are found in every sub-urban environment. As can be deduced, ELMs have a variety of (physical or methodological) applications in a wide variety of fields, ranging from atomic and crystal matter up to continuum solid mechanics, through biology and structural engineering.

The ELMs will be the major focus of this Thesis. As will be introduced in the next Section and will be seen in the next Chapters, these structural systems will be applied to two diverse research fields. Notwithstanding, it is to be remarked how the theoretical and methodological framework is essentially the same, as we refer to the same structural system.

During the research work behind the results that will be presented in this Thesis, the ELMs have been exploited by making use of essentially three kinds of structural analyses: the linear static analysis, modal analysis and geometrically non-linear analysis. All of these start from the basic relationship reported in Hooke's lecture from 1679, that relates the elongation of the ELM basic member (spring or bar) to the corresponding internal stress state. In the next sub-sections these three structural analyses will be described referring to the ELMs.

1.1.1. ELMs and linear static analysis

Linear static analysis is the basic structural analysis that allows to evaluate the displacements and deformations of any structural system given the external perturbation (forces, moments, thermal distortions, imposed displacements, etc.). The ELM is a structural system made up of elastic connections that link various nodes in the three-dimensional space. Therefore, there exists a double way of thinking about the ELM in terms of free objects and internal constraints. The first one identifies the bars as the free objects, whose displacements and deformations are to be computed, and the point nodes as the internal constraints in the form of internal hinges. The second one recognizes the nodes as the moving points in the space, characterized by three unknown DOFs each, and the bars as the compliant constraints that restrict the free motion of the nodes based on the bars axial rigidity. Although the first point of view can be useful to evaluate the degree of statically (in)determination of the structure via the computation of the number of DOFs of the members and constraints due to the internal hinges, the second perspective is more useful to carry out the structural analysis in a quick and efficient way.

Each node is thus seen as a point with known coordinates with respect to the global reference system XYZ and whose displacements δ_x, δ_y and δ_z are the three DOFs to be calculated. Correspondingly, in the realm of linear static analysis, the ELM is subjected to force vectors acting at the level of each node, whose components in the global reference system are F_x, F_y and F_z. Therefore, for an ELM counting N nodes, we deal with a $3N \times 1$ displacement vector $\boldsymbol{\delta}$, which contains all the three unknown displacements for each of the N nodes, and a $3N \times 1$ force vector $\boldsymbol{F}$, which contains all the three force components for each node.

At this point, the linear structural analysis yields the simple application of Eq. (1.2), i.e. the generalized Hooke's law, to solve the structural problem. For a given set of applied forces, we then obtain the corresponding displacements of the

nodes, thus obtaining information about the overall motion and deformation of the ELM.

The problem that needs to be addressed at this point to solve the problem is how to compute the stiffness matrix $\boldsymbol{K}$ reported in Eq. (1.2). Several methodologies can be applied for this purpose. Since we are posing the linear problem in matrix form, the most proper one seems to be the displacements method, which is based on the direct calculation of the stiffness coefficients. As a matter of fact, by expanding Eq. (1.2) we can observe that each *i-j* entry of the stiffness matrix, i.e. the element at row *i* and column *j*, exactly corresponds to the force component on the i^{th} row of the force vector when the displacement component on the j^{th} row of the displacement vector is equal to 1, the others being identically equal to 0. This observation tells us that in order to calculate each entry of the $3N \times 3N$ stiffness matrix it is sufficient to apply unitary displacements in a certain direction and computing the resulting force components for each direction at each node.

To do so from an operative perspective, once the directional displacement is applied at the generic node, the deformations of all the bars joining to that node are computed based on kinematic (compatibility) equations, taking also into account the external constraint conditions. Then, once the deformation of the bars is known, the corresponding stress state and internal axial force can be computed through the constitutive equations, i.e. the Hooke's law from Eq. (1.1). Finally, once all the internal forces in the deformed bars are known, the component of the force in the generic direction at each node can be computed, based on equilibrium equations. This is the core of the displacements method: starting from the displacement we come up with the force [6]. In this way, the stiffness matrix reported in Eq. (1.2) can be completely computed and the linear static analysis can be carried out to evaluate the displacements of the ELM nodes. Once the motion of the nodes is known, we can apply once again the kinematic (compatibility) and constitutive equations, to find out the stress state, i.e. the axial force, within each ELM elementary member. As can be seen, this is not an energetic approach, but a displacement-based method. Due to the fact that ELMs are easily implementable in matrix form into computer-based codes, this is likely to be the most rational way to tackle the problem.

In the following Chapters, this approach will be used various times to directly compute the stiffness matrices of the ELMs and perform the linear static analysis. As will also be seen in the following Chapters, the procedure for the calculation of the global stiffness matrix will be applied with slight differences depending on the underlying assumptions for the different cases under investigation, e.g. taking into account internal constraint conditions that restrict certain nodes to move together, etc.

1.1.2. ELMs and modal analysis

In the framework of linear static analysis, external perturbations are usually applied to the structure and the goal is to evaluate the motion of the structural elements as well as their internal stress state. All we need in order to solve the problem is the information about the geometry of the ELM and the stiffness characteristics of its members. We then acknowledge that the mass of the structure does not play any role.

Vice versa, the goal of modal analysis, i.e. linear dynamic analysis, is to evaluate the dynamic characteristics of a certain structure in the linear regime. In

this contest, the mass of the structure does play a role, since it affects the dynamical properties of the system. The main objective of modal analysis is to evaluate the intrinsic vibrational modes of the structure, from which we can obtain important information about its dynamic features. The problem is usually tackled by posing the global equilibrium of the system, which is subjected to the elastic forces due to the internal deformations of the ELM members and the inertia forces due to the mass-based accelerations of the nodes. The elastic forces arise from the stiffness characteristics of the ELM and can be obtained from the nodal displacements via the generalized Hookean's law reported in Eq. (1.2). Instead, the inertia forces depend on the mass of the ELM and can be calculated through:

$$\boldsymbol{F_{in}} = \boldsymbol{M}\ddot{\boldsymbol{\delta}}, \tag{1.3}$$

being $\boldsymbol{F_{in}}$ the $3N \times 1$ vector of the inertia forces, $\boldsymbol{M}$ the $3N \times 3N$ mass matrix of the ELM and $\ddot{\boldsymbol{\delta}}$ the $3N \times 1$ vector of the nodal accelerations. The modal analysis yields the equilibrium between the stiffness-based elastic forces from Eq. (1.2) and the mass-based inertia forces from Eq. (1.3), leading to:

$$\boldsymbol{K\delta} + \boldsymbol{M}\ddot{\boldsymbol{\delta}} = \boldsymbol{0}. \tag{1.4}$$

In order to find the free vibrations of the system, we usually look for a stationary harmonic solution in the following form:

$$\boldsymbol{\delta} = \boldsymbol{A}\sin\omega t, \tag{1.5}$$

being $\boldsymbol{A}$ the amplitude of motion, t the time variable, and ω the angular frequency (rad/s) which is related to the frequency of vibration (Hz) through the relationship $\omega = 2\pi f$. By substituting Eq. (1.5) into Eq. (1.4), one obtains:

$$(\boldsymbol{K} - \omega^{\boldsymbol{2}}\boldsymbol{M})\boldsymbol{A} = \boldsymbol{0}. \tag{1.6}$$

Equation 1.6 represents the fundamental equation of modal analysis for the investigation of a multi degree-of-freedom (MDOF) system [6]. Besides the trivial solution $\boldsymbol{A} = \boldsymbol{0}$, which represents the case of the system being motionless, the $3N$ vibrational modes of the ELM can be found in the following way. Pose the determinant of the matrix $\boldsymbol{K} - \omega^{\boldsymbol{2}}\boldsymbol{M}$ equal to zero, so that one finds the set of $3N$ angular frequencies ω_n associated to each vibrational mode n. Consequently, by applying again Eq. (1.6), one obtains the complete set of the $3N$ mode shapes $\boldsymbol{A_n}$.

Therefore, from Eq. (1.6), modal analysis yields the evaluation of the complete ensemble of eigenvalues (vibrational frequencies) and eigenvectors (mode shapes) of the modal problem. The former is informative of the number of cycles performed during the unit time and it is the inverse of the period of vibration T. The latter provides information about the directions and spatial characteristics of each vibrational motion. In Chapter 2, this theoretical framework will be thoroughly exploited for the investigation of the dynamics of particular ELMs.

1.1.3. ELMs and geometrically non-linear analysis

The ELMs which will be used in this Thesis exploit the Hooke's equation regarding the constitutive law of the members. This means that the deformation state of the members is always linearly proportional to the underlying stress state. However, ELMs can sometimes exhibit non-linear responses due to the geometrical effects, which are usually referred to as geometrically non-linearities.

To show this phenomenon, we can refer to one of the simplest ELMs, the Von Mises truss [6,7] (Figure 1.3a). In its basic two-dimensional representation, it is a plane truss made of two axially deformable bars, with axial stiffness *k*, joint together by means of an internal hinge and fixed to the ground by means of two external hinges. If the arch is subjected to a vertical downward force applied on the apex node, it is easy to understand that the loaded node will move downward, causing an axial shortening of the inclined bars. At the very beginning of the loading process, i.e. for low values of the force and displacement, the global force-displacement relationship will be linear. However, it is easy to show that for higher loads the force-displacement curve will exhibit strong non-linearities, potentially leading to instability phenomena.

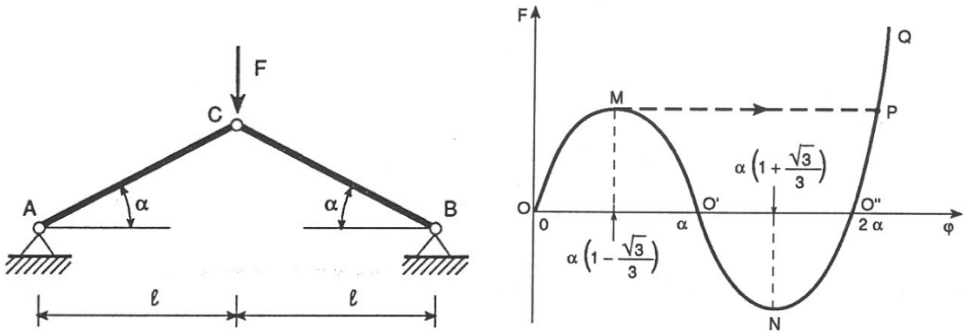

(a) (b)

Figure 1.3. Geometrical non-linearity in one of the simplest ELMs, the Von Mises truss: (a) geometry of the truss; (b) non-linearity in the loading curve. Adapted from [6].

Assuming the rotation of the bars to be the Lagrangian parameter of the system, the force-rotation curve shown in Figure 1.3b is representative of the loading process. This curve shows us that the response is linear for low values of the force, and then it exhibits significant non-linearities leading to lower tangential stiffness values as long as the force increases. Eventually, when reaching point M in Figure 1.3b, the tangential stiffness gets to zero and then the curve exhibits a softening behavior, i.e. the force needs to decrease if the rotation (or the vertical displacement of the node) has to keep increasing.

If we control the loading process just by monotonically increasing the force, the point M represents a point of instability. Reached that point, the system will undergo an instability phenomenon, which is called *snap-through*, that makes the structure jump directly into point P, following the dashed arrow shown in Figure 1.3b. The snap-through usually takes place in a dynamic fashion and can also lead to the final collapse of the structure if the released energy is strong enough to break some of the members. Conversely, if the system does not collapse due to the dynamic effect, the force-deflection curve then follows a stiffening pathway beyond point P, where the structure is completely overturned but it is still able to carry some additional load and the inclined bars start experiencing tensile stresses.

Vice versa, if the loading process is controlled by monotonically increasing the Lagrangian parameter, i.e. the vertical displacement of the apex node or the rotation of the bars, the entire MO'NO''P branch is followed and the structure avoids the dynamic snap-through between point M and point P. In this case, the force has to decrease in order for the load-deflection pathway to be followed up to point O'. After that, the force also needs to change its arithmetic sign, meaning that the apex node starts experiencing an upward force, even though it is still moving downwards.

The case of the Von Mises truss shown above is quite simple as it represents a one-DOF system. Tracing these non-linear curves gets more difficult for MDOF systems, where multiple Lagrangian parameters are necessary to describe the motion and deformation of the system, while multiple forces act simultaneously in various directions. Nevertheless, there exist various ways to trace these curves: by writing the total potential of the system and analyzing its derivatives [6], by applying the global equilibrium in the deformed configuration [7], etc. In this Thesis, especially in Chapter 3, the procedure relying on the application of the equilibrium equations in the deformed configuration will be applied to investigate the geometrical non-linearities of ELMs. Still, it has to be kept in mind that these non-linearities do not arise from a non-linear constitutive behavior of the single bar members, which still obey the Hooke's law from Eq. (1.1), but rather they occur due to geometrical effects related to the difference that exists between the initial (undeformed) and final (deformed) structural configuration upon which the forces need to find the equilibrium.

1.2. Fields of Application of ELMs: Proteins and Diagrid Tall Buildings

In the previous Sections of this Introduction, a general overview of the ELMs has been carried out, together with three of the most common structural analyses that are usually performed, namely linear static analysis, modal analysis and geometrically non-linear analysis. The ELMs have been introduced in a completely general way, without any specification on their detailed nature or purpose of investigation, although a short overview of some of their methodological and physical applications has been briefly presented, as shown in Figure 1.2. Here, more details will be provided on the specific fields of application which will be addressed in this Thesis, namely proteins and diagrid tall buildings.

One might wonder what proteins and diagrid tall buildings have in common. Apparently, nothing. Proteins are tiny biological systems, few nanometers large, that carry out most of the important tasks in every human and animal body and act in an environment with complex chemo-physical features. Conversely, diagrids are special systems that have been exploited worldwide in the last decade for the realization of tall buildings, which are made of inclined mega-diagonals placed all over the exterior of the structure. So, why are proteins and diagrids part of the same PhD Thesis? The answer to this question relies on the Elastic Lattice Model. As a matter of fact, this Thesis will show that various aspects of the behavior of both proteins and diagrid systems can be investigated by means of the ELMs, basically relying on the same methodological framework (Figure 1.4).

As can be seen in Figure 1.4a and as will be thoroughly described in the following Chapters, proteins are complex biological systems that are made of a

specific collection of small groups of atoms, called the amino acids. They usually have a well-defined three dimensional shape, which will be shown to be strongly related to the biological functionality. Conversely, Figure 1.4b shows the 180-meter tall Swiss Re Tower in London, which is also known as The Gherkin and is one of the first realized diagrid systems for tall buildings. As will be extensively described in the upcoming Chapters, diagrids are structural systems made of inclined mega-diagonals placed on the building surface, which are able to carry both vertical and horizontal loadings. For this reasons, the tall buildings adopting the diagrid framework usually do not need the traditional space-consuming vertical columns. Diagrids have been shown to achieve extreme structural efficiency and also allow to reach remarkable architectural effect. The interesting thing is that both proteins and diagrids can be analyzed – and their behavior can be deeply investigated – by means of the same theoretical, numerical and methodological framework relying on the ELM.

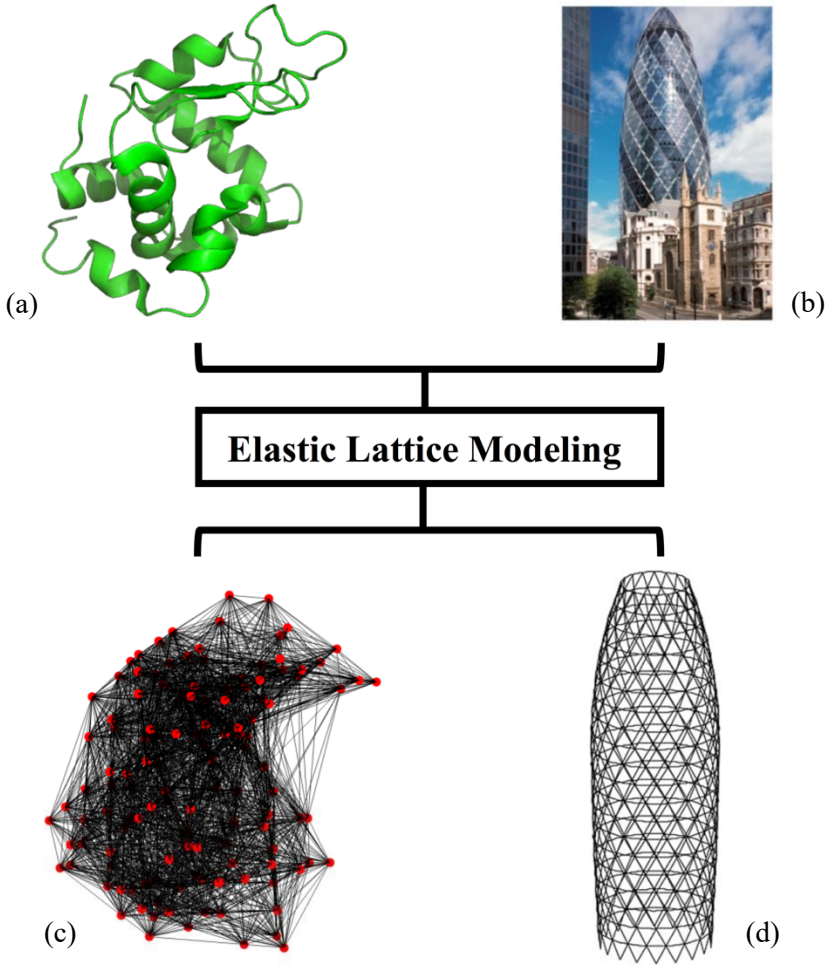

Figure 1.4. ELMs used for the investigation of two different systems: (a) protein, (b) diagrid tall building, (c) protein ELM, (d) diagrid ELM.

Figure 1.4c shows the protein from Figure 1.4a modeled through an ELM, where certain atoms are selected as the nodes of the ELM (in red) and their chemo-physical interactions are modeled through elastic bars (in black). As will be shown in Chapters 2 and 3, the ELMs applied to proteins allow to obtain useful information about their dynamics, their flexibility and their biological mechanisms. Similarly, Figure 1.4d shows the Swiss Re Tower from Figure 1.4b modeled through the ELM. In this case, the external mega-diagonals are

obviously the bar members of the ELM and the nodes are the physical nodes which are present in the building. As will be extensively reported in Chapters 4 and 5, the ELMs applied to diagrids allow to quickly perform their structural analysis and obtain information about their flexibility and their structural response under external loads. Ultimately, these information also allow to carry out optimization processes, leading to the selection of the optimal diagrid structure under certain loading and constraint conditions.

Therefore, the structure of this Thesis is as follows: Chapters 2 and 3 describe the application of the ELMs to the field of proteins, whereas Chapters 4 and 5 deal with the structural analysis and optimization of diagrid systems. Both are investigated by means of the theoretical framework relying on the ELMs.

1.3. Outline of the Thesis

Specifically, Chapter 2 contains three Sections. The first Section provides a brief yet fairly exhaustive description of the proteins as biological systems (Figure 1.4a). Starting from the description of the basic chemical building block of the protein, i.e. the amino acid, the four hierarchical levels of the protein structure are reported. Then, the process of protein folding, which allows the protein to reach the functional three-dimensional structure starting from the linear sequence of amino acids, is described and the fundamental sequence-structure-dynamics-function paradigm is discussed. The second Section puts the attention on the protein dynamics and the numerical methodologies that are nowadays used for its investigation. Particularly, the more recent approaches relying on Normal Mode Analysis (NMA), i.e. modal analysis, are addressed. After a brief overview of the methods that have been developed in the literature in the last decades, such as the Gaussian Network Model (GNM) and the Anisotropic Network Model (ANM), attention is paid to the coarse-grained Elastic Lattice Models (ELMs) that describe the protein as a network of point masses bonded by elastic connections (Figure 1.4c). In particular, a recently developed Finite Element (FE)-based ELM is presented, which is useful to describe the low-frequency global protein vibrations, occurring in the THz frequency range, and is shown to be methodologically consistent with the traditional ANM. Finally, the last Section of this Chapter shows the close correspondence between the low-frequency modes of the protein ELM and the functional motions, i.e. the conformational changes, observed during the biological activity. The ELM-based low-frequency modes are found to correlate fairly accurately with the conformational changes, which represent the fingerprints of the biological mechanism, as well as with the Principal Components (PCs) arising from the ensemble of the protein crystal structures. The latter derive from the protein dynamic communities and are representative of the functional flexibility of the protein. Finally, the Chapter is concluded with the presentation of a new and computationally efficient ELM for the prediction of the protein functional global motions. This method relies on the discretization of the protein structure as made of (flexible) hinges and (rigid) domain regions, which has been called the hinge-domain ANM (hdANM). By means of this highly coarse-grained model, we are able to obtain useful predictions of the protein functional motions (conformational changes) and information about the generation of the dynamic community (PCs).

Chapter 3 also focuses on the ELMs applied to the protein structure, but from a static perspective rather than a dynamic one. As in Chapter 2 modal analysis was the main tool applied to the protein ELMs, in this Chapter linear static

analysis and geometrically non-linear analysis are the main players, the former being exploited in the first Section, while the latter in the second Section. In the first Section of this Chapter, two force-based methodologies are proposed and developed for the measurement of the protein internal flexibility, based on linear static analysis. The flexibility of a protein is often experimentally obtained by means of the B-factors, also known as the temperature factors, which are extracted by X-ray crystallographic experiments on protein samples. The first proposed force-based approach relies on a pairwise force application framework, where point forces are applied to each couplets of nodes in the protein ELM. Typical Structural Mechanics metrics are suggested in order to assess the protein flexibility, i.e. compliance and stiffness, which are found to show a good correlation with the experimental B-factors. The second force-based approach relies on a random application of point forces on the protein surface. Based on the evaluation of the displacements of the protein ELM, it is shown that this external random force bombardment can also provide a good correlation with the experimental B-factors, i.e. the experimental protein flexibility. These force-based approaches suggest that the intrinsic protein flexibility can be seen as the result of both the internal residue-residue (pairwise) interactions as well as the effect of the bombardment due to the external environment. Conversely, the second (and last) Section of this Chapter, investigates the possible role of geometrical non-linearities on the protein ELM when it goes through a conformational change. To this purpose, the geometrically non-linear analysis is applied. First, for a given conformational transition, the forces that guarantee the equilibrium of the final configuration are evaluated both via the linear and non-linear approach, i.e. by posing the equilibrium on the undeformed or deformed structure. The comparison between the two quantifies the influence of the geometrical non-linearities in the conformational transition. Secondly, a step-by-step evaluation of the equilibrium forces is carried out through the conformational pathway and synthetic indexes are computed in order to assess the magnitude of these geometrical non-linearities.

In Chapter 4 the field of application of the ELMs is switched from proteins to diagrid tall buildings. This Chapter is divided into two main Sections. The first one is devoted to a brief description of the diagrid as a modern and efficient structural system for tall buildings (Figure 1.4b). In particularly, after presenting the specific structural features that characterize the diagrid, such as the inclined mega-diagonals, the tubular arrangement, etc., the methodologies that have been developed in the literature for the diagrid preliminary design and structural analysis are thoroughly addressed. The second Section of this Chapter is devoted to the presentation of a recently developed ELM-based methodology for the structural analysis of diagrid systems. In particular, the diagrid is modeled as an ELM, with additional constraints at the level of the rigid floor slabs (Figure 1.4d). This novel method, which is grounded on matrix calculus and has been called the matrix-based method (MBM), is useful for the prediction of the building deformation and stress state, due to horizontal, torque and vertical loads acting at the floor level. Moreover, the MBM is also shown to be suitable for the investigation of the force distribution among different resisting elements. For the purpose, the MBM is inserted within the framework of the so-called General Algorithm, a semi-analytical approach that allows to evaluate the structural response of tall buildings, made up of various resisting elements, such as frames, tubes, shear walls, etc. Based on the coupling of the MBM with the General

Algorithm, the force distribution between an external diagrid tube and an internal shear wall is investigated.

Chapter 5 also focuses on the diagrid tall buildings, with attention to the optimization of the geometrical characteristics for the enhancement of the structural response. Particularly, three Sections are present in this Chapter. The first one provides a brief yet fairly complete overview of the literature work that has been carried out in the last decade about the optimization of the diagrid performance. As will be seen, most of the researches are based on FE calculations, often coupled with Genetic Algorithms, which look for the diagrid structure that minimizes the amount of structural weight, while complying with the maximum allowed lateral deflection. In the second Section, the influence of the diagrid geometry (floor shape and diagonal inclination) is thoroughly investigated on the diagrid flexibility, both in terms of lateral deflections and torsional rotations, as obtained from the ELM-based MBM. From the results obtained in this Section, it is shown that minimizing the lateral flexibility of the building can be in contrast with the minimization of the torsional flexibility and vice versa. For this reason, there is the need of a multi-response optimization technique, that allows to find the geometry that minimizes several responses simultaneously. Based on this consideration, the third (and last) Section of this Chapter, introduces the application of the desirability function approach for the optimization of the diagrid geometry. Specifically, four responses are taken into account for the optimization of both uniform- and varying-angle diagrid structures, i.e. the top lateral displacement, top torsional rotation, structural mass and complexity index. The first two are related to the structural response under external loads, and their minimization is important for safety and serviceability issue. The third one is related to the diagrid weight and needs to be minimized for sustainability and economic purposes. Finally, the fourth one is an index which takes into account the easiness of construction of the diagrid geometry and depends on the number of nodes, number of different cross-sections, etc. Based on the application of this multi-response desirability approach, the designer is quickly able to select the diagrid geometry that can better reach a good tradeoff to achieve a stiff, light and easily constructible tall building.

Finally, Chapter 6 summarizes the work contained in this Thesis and discusses possible further developments. Note that, since the analyses and results reported in this Thesis expand in a fairly wide range of topics, each individual Chapter has already been incorporated of a specific Conclusions Section, in order to better discuss the potential developments of each topic.

Chapter 2

ELMs and Proteins: Introduction, Vibrations and Biological Mechanisms

Proteins represent one of the main building blocks of the biological reactions that occur every day in our body and that allow a variety of crucial processes to take place properly. Proteins are in charge of pivotal transportation activities, such as carrying nutrients and molecules within the cell (e.g. molecular motors), across the cellular membrane (e.g. transmembrane proteins) and throughout the body (e.g. hemoglobin). Some proteins are necessary to provide the required strength and stiffness to tissues (e.g. collagen), while others act as antibodies to recognize and get rid of external pathogens. Certain proteins are associated with enzymatic activities and catalyze important biochemical reactions (e.g. lysozyme), while others are involved in signaling pathways (e.g. MAPK) and other much more diverse tasks.

Astonishingly, such a variety of functions only depends on the different arrangement of the same few tiny components, the amino acids. Tens, hundreds or thousands of amino acids can assemble with each other to give birth to a specific protein structure, through the complex chemo-physical phenomenon which is known as the protein folding. Nowadays, it is fairly well-established that the specific protein structure is evolutionary related to the required biological task, and protein dynamics represents the bridge between the structure and functionality. Despite the extreme complexity of protein formation and activity, simplified models based on Structural Mechanics concepts have proven amazingly effective to unravel certain aspects of protein features and mechanisms. In particular, despite their minimalism, the ELMs coupled with Structural Mechanics concepts such as modal analysis are discovered to provide extremely useful insight into protein flexibility and biological mechanisms.

In this Chapter, the use of ELMs for the investigation of protein activity is addressed. In Section 2.1 a brief overview of the fundamental protein features is provided, which focuses on the different levels of protein structure, the complex phenomenon of protein folding and the main paradigm that relates the protein

structure to biological functionality through protein dynamics. In Section 2.2, the use of the ELMs is addressed for the investigation of protein dynamics and vibrations, starting from the first models that have been developed in the literature up to the most recent ones, which mostly exploit Structural Mechanics concepts. In Section 2.3, the relationship between protein vibrations and biological function is presented through the analysis of protein conformational changes. From the analyses and results presented in this Chapter, it will be seen that, despite their minimalism, simplified models purely based on Structural Mechanics concepts, such as the ELMs, are still able to provide remarkable insights regarding protein features, flexibility and biological functionality.

2.1 Proteins: The Building Blocks of Biological Activity

As briefly mentioned in the beginning of this Chapter, the function of proteins in our body can be extremely diverse. In the human body, we have hundreds of thousands of different proteins, that work relentlessly to accomplish the variety of tasks to be carried out for the proper functioning of our cells, tissues and organs. Nevertheless, such a variety of activities is based on the same basic characteristics shared by the protein structure, as will be described in this Section.

2.1.1 From the amino acid to the three-dimensional structure

The elementary building block of the protein structure is the amino acid [8,9]. The amino acid is a chemical group made up of a central carbon atom, typically called the alpha-carbon (C^{α}), which is covalently bonded to a hydrogen atom H, an amine group ($-NH_2$), a carboxyl group (-COOH) and a side chain R_i (Figure 2.1). What really distinguishes one amino acid from each other is the side chain R_i.

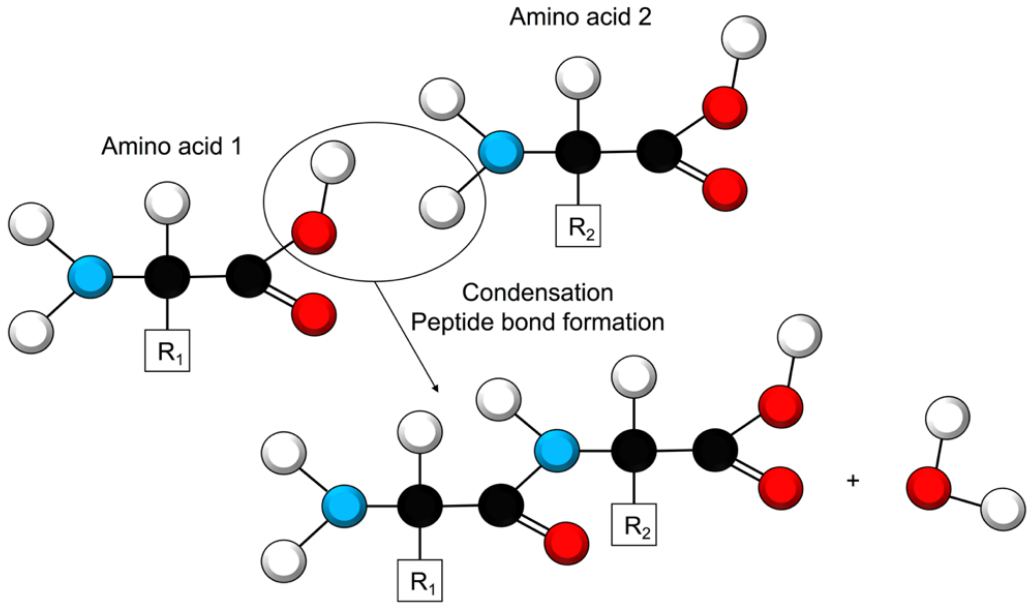

Figure 2.1. Condensation reaction between two amino acids to form a dipeptide. Colors for the atoms: white for hydrogen, black for carbon, red for oxygen and cyan for nitrogen.

Under physiological conditions, the amino acid is usually found in the ionized form, meaning that the amine group is in the form $-NH_3^+$ and the carboxyl group

in the form -COO^-. Two amino acids can interact with each other in order to create a dipeptide, as shown in Figure 2.1. The carboxyl group of one amino acid interacts with the amine group of the other, leading to the generation of a strong C-N covalent bond, which is called the peptide bond. This reaction is usually known as condensation reaction, since a water molecule is expelled as a secondary result. The condensation reaction can take place repeatedly among several amino acids, leading to the formation of a polypeptide chain, which in turn is the linear arrangement of the protein structure. Note that, when the amino acids combine themselves to form a polypeptide chain, they are often called residues, as this is what remains after the expulsion of the water molecule. This term, i.e. residue, will be used in the remaining of this Thesis to refer to the specific amino acid in the protein chain.

The amino acids differ from each other depending on the specific side chain R_i. In eukaryotes, twenty different types of amino acids are often found in proteins (Figure 2.2). They can be classified into groups depending on the characteristics of the side chain R_i.

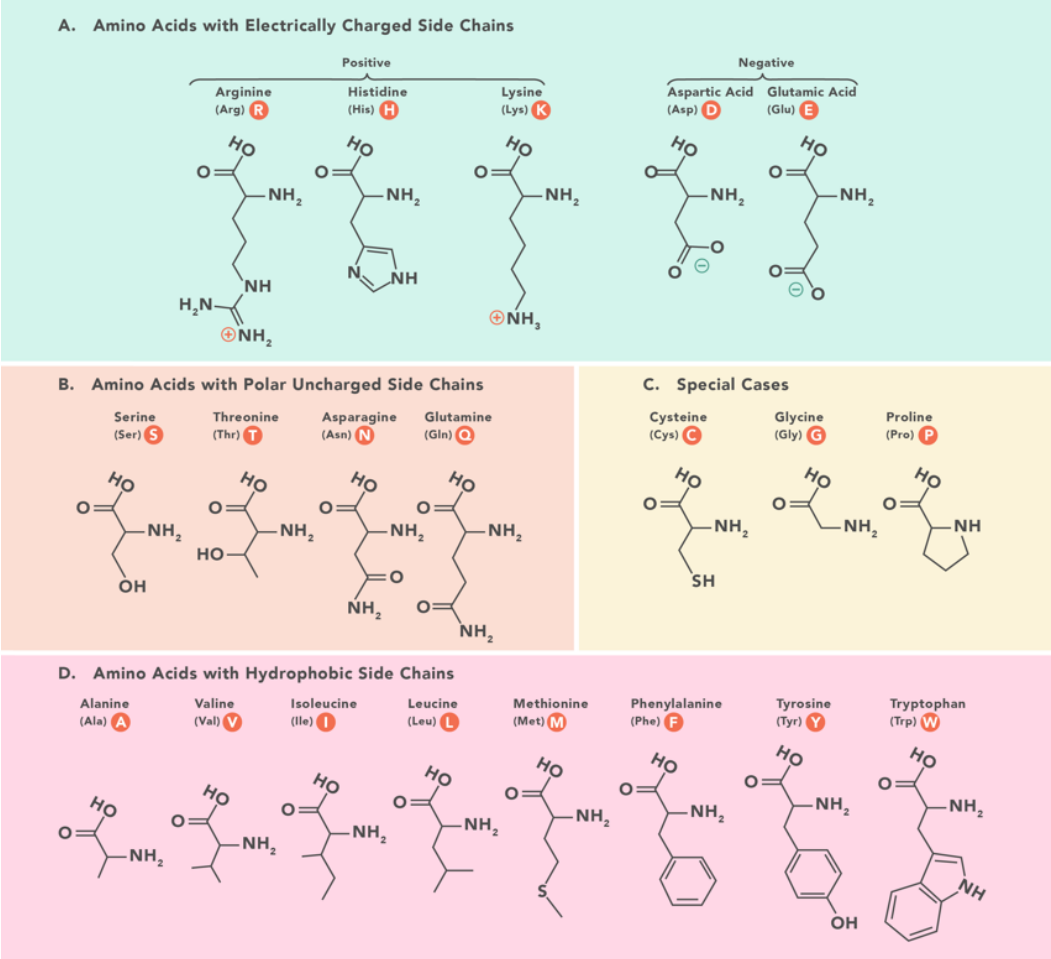

Figure 2.2. The most common twenty amino acids found in eukaryotes. The amino acids are grouped depending on the characteristics of the side chain. The one- and three-letter code used to identify each amino acid is also shown. Used with permission from [10].

A typical classification is based on the definition of hydrophobic or polar amino acid. The former has a side chain that tends to avoid the contact with the surrounding water molecules, whereas the latter mostly generates interactions with water molecules based on hydrogen bonds. Among polar amino acids,

residues can have uncharged or charged (both positively and negatively) side chains. Based on the hydrophobicity or hydrophilicity of the side chains, hydrophobic amino acids tend to aggregate within the core of the protein, while polar amino acids often distribute on the protein surface. As will be shown below, the hydrophobicity is one of the main driving force of the folding phenomenon and for the formation of the protein three-dimensional structure. Other classifications based on the amino acid side chains can also take into account the presence of aromatic or aliphatic groups, as well as the presence of sulphur or nitrogen atoms, the tendency to act as acids or bases, etc.

The amino acids combine themselves according to a specific sequence in order to generate the protein polypeptide chain. The linear sequence of amino acids is known as the primary structure of the protein (Figure 2.3a). By convention, the primary structure extends from the amino group of the first amino acid (N-terminus) to the carboxyl group of the last one (C-terminus) and it is usually expressed as a string of letters that are associated to each amino acid. Each sequence depends on the genetic information related to the codification of the protein to be expressed. This process is known as protein biosynthesis.

Protein biosynthesis starts into the cell nucleus. The genes encoded within the DNA contain all the necessary information for making proteins. The genetical information of the gene is firstly transcripted by an enzyme, the RNA polymerase, into a strand of messenger RNA (mRNA). When the mRNA is mature enough to be processed, it gets translated outside the cell nucleus by a complex molecular machine, the ribosome, into the specific amino acid sequence. In this final step, the job of the ribosome is made possible through the support of another key player, the transfer RNA (tRNA), which is able to deliver a certain amino acid for each specific triplet of mRNA bases.

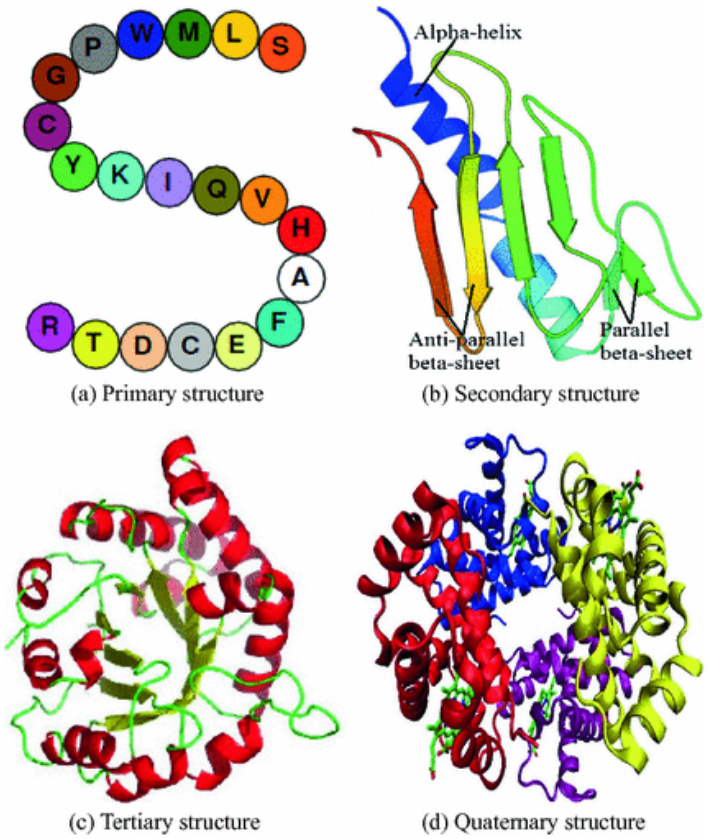

Figure 2.3. The four hierarchical levels of the protein structure. Used with permission from [11].

Once the formation of the primary structure gets done, as the polypeptide chain starts to get out from the ribosome into the cytoplasm, the amino acids start interacting with each other and with the environment, and give birth to new spatial arrangements. As a result, local segments which share the same geometrical patterns are often found in proteins. This is the case of the secondary structures (Figure 2.3b).

The most common secondary structures found in proteins are the α-helix [12] and β-sheet [13]. Both are stabilized by specific patterns of hydrogen bonds. The former is a spiral-like geometrical configuration, where each helical turn consists of 3.6 amino acids and the side chains usually point outwards the helix. The latter is a pleated sheet, where two or more amino acids strands are connected side-by-side by hydrogen bonds, in a parallel or anti-parallel fashion, the amino acid side chains pointing out of the sheet plane. Despite the α-helix and the β-sheet are the most common secondary structures, other local patterns can be observed in some cases, such as the π-helix, the 3_{10}-helix, loops and β-turns, each of them exhibiting distinctive geometrical features. Sometimes, assemblies of multiple secondary structures, which are known as structural motifs, can also be found in proteins.

The third hierarchical level of the protein structure is referred to as the tertiary structure and basically represents the three-dimensional shape of the protein (Figure 2.3c). This is generated due to the chemo-physical interaction between the amino acids and the surrounding environment, through the complex phenomenon of protein folding. In this process, the native protein structure is generated due to specific driving forces which often lead to densely-packed structures, with hydrophobic residues embedded within the core and polar residues exposed on the surface. Nowadays, thanks to crystallographic experiments with X-ray or Nuclear Magnetic Resonance (NMR) techniques, plenty of detailed protein structures are available on public databases, such as the Protein Data Bank (PDB) [14].

Finally, certain proteins are also found to exhibit a fourth hierarchical level, which corresponds to the so-called quaternary structure (Figure 2.3d). This is the case of proteins that are made up of more than one amino acid chain, which interact and stabilize with each other via non-covalent bonds. These amino acid chains form distinct subunits, which act cooperatively to carry out the protein biological task. The most famous example is hemoglobin, which is made up of four subunits, each of them coupled with one heme group which is in charge of carrying one oxygen molecule.

2.1.2 Protein folding

As mentioned above, the linear sequence of amino acids evolves into the protein tertiary structure due to the folding process. This phenomenon is a complex chemo-physical process involving the balancing of different forces to achieve a final stable configuration. Covalent interactions, hydrogen bonds, electro-static forces and Van der Waals interactions balance themselves simultaneously and lead the random coil configuration of the primary structure (Figure 2.3a) to the folded three-dimensional protein structure (Figure 2.3c).

The folding process does not take place in vacuum, conversely it occurs within a specific environment, made up of water molecules, ions, other proteins, etc. This has led to the belief that hydrophobic interactions should play a relevant role in driving the folding process. Hydrophobic residues tend to avoid water molecules, therefore they often form a bulk core embedded within the interior of

the final fold. Conversely, polar residues easily form hydrogen bonds with water molecules, thus they are mostly positioned on the protein surface (Figure 2.4).

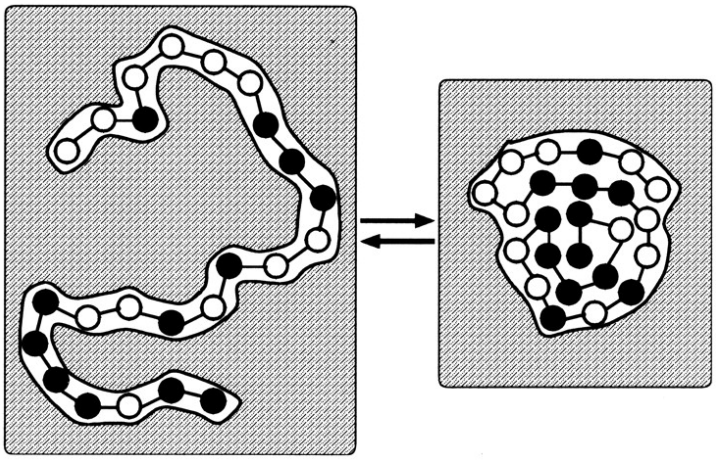

Figure 2.4. Influence of amino acid hydrophobicity in the folding process. Black dots stand for hydrophobic residues, whereas white dots represent polar amino acids. Used with permission from [15]. Copyright 2000 National Academy of Sciences.

The interactions between the amino acids that form the protein chain and with the water molecules are not the only parameters affecting the folding process. Environmental conditions, such as temperature, pH, ion concentration, presence of denaturants, etc., play a significant role as well. As a matter of fact, despite under physiological conditions a certain amino acid sequence has the potential to lead to the correctly folded protein, increasing the temperature or the pH of the surrounding environment may cause the unfolding of the protein structure, with formation of the random coil configuration. Similar results occur when certain concentrations of denaturants or specific molecules are added to the environment. However, it is true that, under specified external conditions, there exists a one-to-one correspondence between the amino acid sequence and the folded protein structure. Based on this observation, the Anfisen's dogma, known also as the thermodynamic hypothesis, was formulated. It states that, in the conditions where the folding can occur properly, the folded state is unique, stable and kinetically accessible [16,17].

Many scientists have wondered how is possible that the linear amino acid sequence, initially in the random coil configuration, is able to sample the entire conformational space to finally achieve the unique functional folded structure. Based on this, the Levinthal's paradox has derived [18,19]. It states that, given the incredibly high number of available conformations, if the final folded structure had to be reached by randomly sampling the whole conformational ensemble, the process would require more than the life of the universe even for a small polypeptide chain. This paradox basically refuses the idea of random sampling.

If not a random search process, how can the protein folding be explained? The answer relies on the concept of energy minimization. Based on the Anfinsen's dogma and taking into account the Levinthal's paradox, it implies that the final folded shape is reached through a series of energetically-favorable intermediate states. Thus, the protein folding can be described as a thermodynamic phenomenon that drives the random coil configuration to the unique and stable folded shape which minimizes the energy of the system. This process is straightforwardly represented by the so-called folding energy funnel (Figure 2.5) [20]. This plot is a useful graphical representation of the folding

pathway. Initially the protein lies in the random coil configuration (upper part of the funnel), which is characterized by high energy (height of the funnel) and high conformational entropy (width of the funnel). The folding process drives the protein through a series of energetically-favorable conformations towards the bottom of the funnel. Meanwhile, the width of the funnel decreases, since the conformational entropy of the new configurations is much smaller than the random coil's one. After sampling a few intermediate conformations, the final folded shape is usually reached (bottom part of the funnel).

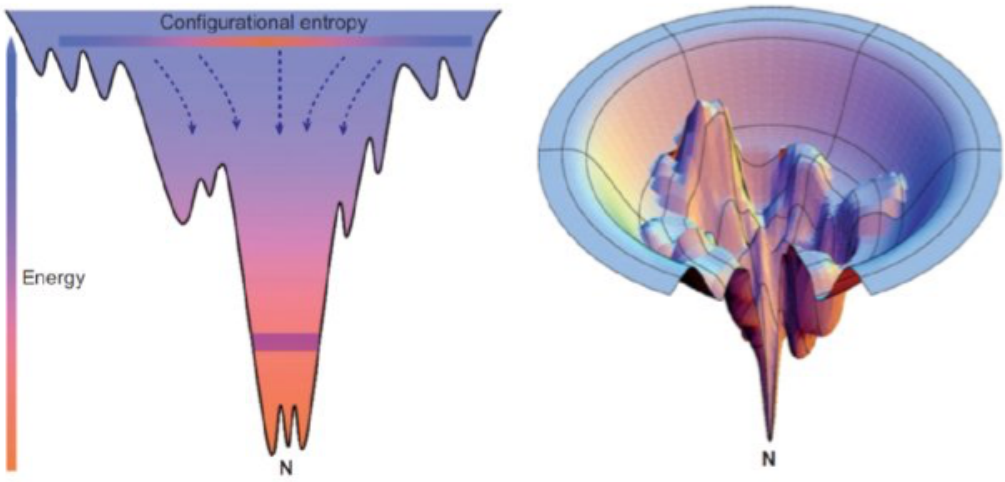

Figure 2.5. Energy funnel of the protein folding (two- and three-dimensional representations), from [21].

As can be seen from the simplified representation of the funnel shown in Figure 2.5, the pathway is not necessarily unique, as it depends on the starting point. Moreover, sometimes proteins might also remain trapped in local minima of the energy funnel, thus adopting intermediate states. Also, the energy funnel is not a static feature which only depends on the specific protein. It also depends on the conditions of the environment, meaning that if something changes in the surrounding environment (temperature, pH, ion concentration, electric charge, presence of denaturants, etc.), the energy funnel gets modified as well. As a consequence, this means that the most stable, i.e. energetically-favorable, folded conformation in physiological conditions might not coincide with that in the modified environment.

From the energy funnel represented in Figure 2.5, it is also worthy to observe that in the bottom part of the funnel, multiple minima can exist. This means that, for certain proteins, multiple folded conformations are possible which are similar from an energetical point of view. This brings to two additional observations.

First, proteins are not static in nature, but they keep jiggling and vibrating around the folded equilibrium state. If their vibrational state is strong enough, they can "jump" from one local minimum to another which is close to the initial one. This leads to the occurrence of multiple similar conformations and to the definition of the so-called conformational ensemble. It means that the correct and functional folded shape is not a fixed structure, but rather a distribution of similar conformations generated by the continuous protein motions. More details about the conformational ensemble and protein vibrations will be provided in the remaining of this Chapter, when introducing the concept of Principal Component Analysis (PCA) and multiple protein conformations.

The second observation is associated with the concept of conformational changes. Despite the concept of conformational change is in a way related to the conformational ensemble described above, there exists a fundamental difference. As described above, the conformational ensemble represents the union of the multiple similar conformations of the folded state, which is generated by the intrinsic protein vibrations. Conversely, the conformational change is usually defined as that particular conformational transition involved into the biological mechanism. This is, for example, the case of proteins associated with ligand-binding activities. These proteins often exhibit two different conformations, generally called the "open" and "closed" form. The former is found when the protein is free, while the latter often occurs when the protein is bounded to the ligand. In this case, the "jump" from one conformation to the other in the energy funnel is due to the interaction with the ligand, which can modify the shape of the funnel and bias the preference of the protein towards the closed conformation. As will be thoroughly described in Section 2.3, the dynamics of the protein structure plays an important role on driving these conformational changes.

To conclude this brief section about protein folding, it is worthy to observe that, understood the main principles governing this process, many researchers and scientists have been struggling to simulate the three-dimensional protein structure given the amino acid sequence. Simplified theoretical models have been proven quite effective to the purpose [22,23]. However, nowadays, the most exploited approaches rely on numerical simulations, mostly based on Molecular Dynamics (MD). Despite the supposed accuracy of MD simulations, its computational complexity is often a limit for the investigation of long polypeptide chains. Recent approaches tend to exploit shared computational resources from volunteers all over the world to achieve enough computational power to successfully simulate the protein folding [24].

2.1.3 The sequence-structure-dynamics-function paradigm

The Anfinsen's dogma and the studies developed in the twentieth century established that, under proper conditions, there exists a one-to-one correspondence between the protein sequence and structure. As described in the previous Section, protein folding is the complex phenomenon linking these two. It has also been established that the protein biological function is strictly related to the three-dimensional structure, as this one is found to be related to the biological mechanism. Note that, with the word "mechanism", we refer here to the specific functional motion or set of motions required for the protein to perform its biological task. The structure of collagen, in the form of a triple helix, seems to be the most rational shape to perform the task of maintaining the required mechanical strength and stiffness of tissues. The shape of globular proteins usually involves specific binding pockets, whose geometry is precisely suitable for the ligand-binding task to be carried out. These are just few example of the general sequence-structure-function relationship which holds true for the majority of proteins. The biological function is thus connected to the specific amino acid sequence through the protein structure.

However, although the sequence-structure-function paradigm explains the reason why proteins are evolutionary conserved and have kept adjusting themselves in order to improve the biological functionality during the evolution, it does not explain completely how they are able to carry out their task. The fundamental answer to this question was given in the last decades and it relies on

protein dynamics. The sequence generates the three-dimensional structure, which is not a static element but rather it keeps vibrating around the equilibrium fold. These vibrations are in turn driven by the structure and can generate mechanisms and functional motions. The biological functionality is thus adjusted from the structure through the dynamics. In this way, the fundamental paradigm for protein activity becomes sequence-structure-dynamics-function [9].

This paradigm has been used to explain protein mechanisms, it has been deeply exploited in recent years to investigate several aspects of their biological activity, such as the effect of amino acid mutations, and it has involved different disciplines and methodologies. As already mentioned above, the sequence-structure relationship is mainly addressed by the investigation and simulation of protein folding. The structure-dynamics relationship is often analyzed through MD simulations, even though simplified models based on Structural Mechanics concepts have proven their efficacy in recent years. This subject will be addressed in Section 2.2. Finally, the dynamics-function relationship is strongly related to the concept of the conformational changes, since protein vibrations have been found to drive the protein transitions. This will be the subject of Section 2.3.

2.2 Protein Vibrations and ELMs

Protein dynamics has been found to explain fairly successfully protein mechanisms and functionality. For this reason, plenty of research has been conducted in the last decades to investigate protein dynamics by means of numerical approaches. Molecular Dynamics (MD) is nowadays one of the most used methodologies to simulate protein dynamics and vibrations [25]. The main feature of MD relies on the formulation of the interaction potentials between each couple of atoms, that should be as accurate as possible to properly model the system (Van der Waals interactions, electro-static potential, hydrogen bonding, etc.). Numerical integration strategies are then applied to solve the Newton's laws of motion, which allow to obtain the trajectories of the atoms, thus providing information about the dynamics. Despite its capability to simulate the most complex details of the system, its computational complexity often prevents its application to large macromolecules and might make lose confidence in the results.

Still relying on the definition of complex interaction potentials among all the atoms of the system, another approach was developed to focus on the intrinsic dynamics of the protein. This is the case of Normal Mode Analysis (NMA) [26,27]. NMA assumes that the vibrations of the atoms are sufficiently small to be approximated as a sum of terms that are quadratic in the degrees of freedom (DOFs). Therefore, NMA gives up calculating the complete atom trajectory, as in MD simulations, but it focuses on the evaluation of the small-amplitude harmonic dynamics. Note that, in this approach, the harmonicity assumption is only on the motion, and not on the interaction potential which is generally as complex as in MD simulations. The first studies showed that NMA was indeed a powerful tool to evaluate the internal dynamics of the protein, allowing to obtain good agreements with the experimental fluctuations of the atoms found in crystallographic experiments [26,28]. In particular, low-frequency modes were found to contribute for the most part to the fluctuations and seemed to represent collective functional motions [28].

As it is still based on the formulation of detailed potentials, NMA usually requires the energy minimization of the initial crystal structure, which can be

costly and inaccurate. Moreover, the detailed potentials usually require taking into account multiple DOFs of the system. A typical example of semi-empirical potential used in MD and NMA analysis takes the following form:

$$E_p = \frac{1}{2}\sum_{bonds} K_b(b-b_0)^2 + \frac{1}{2}\sum_{angles} K_\theta(\theta-\theta_0)^2 + \frac{1}{2}\sum_{dihedrals} K_\phi[1+\cos(n\phi-\delta)] + \sum_{non-bonded\ pairs}\left[\frac{A}{r^{12}} - \frac{B}{r^6} + \frac{q_1 q_2}{Dr}\right], \quad (2.1)$$

where the first two terms refer to the quadratic potentials related to the bond lengths and bond angles, the third term refers to dihedral angles, and the last one contains the Van der Waals attractions, steric repulsions and electro-static interactions between non-bonded pairs [29]. In her ground-breaking work, for the first time, Tirion [29] showed that a simplified single-parameter potential, such as the Hookean pairwise potential (between atoms *a* and *b*)

$$E(\boldsymbol{r}_a, \boldsymbol{r}_b) = \frac{C}{2}(|\boldsymbol{r}_{a,b}| - |\boldsymbol{r}_{a,b}{}^0|)^2, \quad (2.2)$$

is sufficient to represent the slow dynamics of the protein with sufficient details. In Eq. (2.2), $\boldsymbol{r}_{a,b} = \boldsymbol{r}_b - \boldsymbol{r}_a$ denotes the vector connecting atoms *a* and *b*, and the zero subscript indicates the given initial configuration. Thus, it is shown that the harmonicity hypothesis can be used both assuming the smallness of the atom displacements and as regards the energy potential. Despite its simplification, this model provides accurate results for the prediction of the low-frequency protein dynamics, while drastically reducing the computational cost with respect to both MD and NMA calculations.

2.2.1 The coarse-grained Elastic Network Models

The Tirion's model is the first example of ELM developed in the literature for the investigation of protein dynamics, as it relies on a network of elastic Hookean springs that connect all the protein atoms. Further developments of this model were developed in the following years, which take the Tirion's simplification even further, considering a coarse-grained model for the protein structure. This is the case of the so-called Elastic Network Models (ENMs): the Gaussian Network Model (GNM) [30] and Anisotropic Network Model (ANM) [31].

2.2.1.1 Gaussian Network Model

The fundamental postulate in the Gaussian Network Model (GNM) is that the protein in the folded state is equivalent to the reference three-dimensional elastic network to be used for the calculations [30]. Only the C^α atoms are considered in the original GNM as the nodes of the network. Close C^α atoms are connected by linear Hookean springs, based on the geometrical cutoff limit r_c. This means that nodes whose distance is lower than r_c are connected, while nodes whose distance

is greater are not. Usual values of the geometrical cutoff limit in the GNM are around 7 Å.

Based on the three-dimensional coordinates of the C^{α} atoms of the crystal structure and the value of r_c, a $N \times N$ connectivity matrix is derived, N being the number of protein residues, i.e. the number of C^{α} atoms. Figure 2.6a shows the connectivity map of the hen egg white (HEW) lysozyme GNM (PDB: 4ym8), obtained with a geometrical cutoff equal to 7.3 Å. Black dots in the *i-j* position of the matrix denote a contact between nodes i and j, while white dots denote no interaction. Once the connectivity matrix is derived, the GNM yields the definition of the $N \times N$ Kirchhoff matrix $\boldsymbol{\Gamma}$, as follows:

$$\Gamma_{i,j} = \begin{cases} -1, & i \neq j, \ R_{i,j} < r_c \\ 0, & i \neq j, \ R_{i,j} > r_c \\ -\sum_{j=1, j \neq i}^{N} \Gamma_{i,j}, & i = j \end{cases}, \tag{2.3}$$

$\Gamma_{i,j}$ being the *i-j* entry of the Kirchhoff matrix, $R_{i,j}$ the geometrical distance between nodes i and j in the three-dimensional structure and r_c the cutoff limit. Note that in the original formulation of the GNM, equal spring constants are used to connect nodes within the cutoff limit, without any dependence on their actual distance $R_{i,j}$.

Computed the Kirchhoff matrix, the eigenvalue-eigenvector decomposition is carried out to obtain the dynamical features of the protein ELM, namely the N-1 non-rigid mode shapes $\boldsymbol{\delta}_n{}^{GNM}$ and the N-1 non-zero eigenvalues $\lambda_n{}^{GNM}$. Note that, being the protein structure not externally constrained, the first mode has zero frequency as it corresponds to the uniform translation of the network. The calculated eigenvectors and eigenvalues are used to compute the pseudo-inverse of the Kirchhoff matrix $\widetilde{\boldsymbol{\Gamma}}^{-1}$, as follows:

$$\widetilde{\boldsymbol{\Gamma}}^{-1} = \sum_{n=2}^{N} \frac{\boldsymbol{\delta}_n \boldsymbol{\delta}_n{}^{T}}{\lambda_n}. \tag{2.4}$$

Assuming that the fluctuations of the atoms obey a Gaussian distribution, it is proven that the elements of the pseudo-inverse matrix are proportional to the cross-correlations between the residues fluctuations:

$$< \Delta R_i \cdot \Delta R_j >= \frac{3 k_B T}{\gamma} \, \tilde{\Gamma}^{-1}{}_{i,j}, \tag{2.5}$$

being ΔR_i and ΔR_j the fluctuations of atoms i and j, respectively, k_B the Boltzmann constant, T the absolute temperature in Kelvin, and γ the force constant of the springs. From Eq. (2.5) the mean-square fluctuation of the i^{th} C^{α} atom $< \Delta R_i{}^2 >$ are readily evaluated from the diagonal elements of the pseudo-inverse matrix, i.e. with $j = i$ [30]. Figure 2.6b shows the map, in color scale, of the normalized cross-correlations for the HEW lysozyme GNM, defined as:

$$< \Delta R_i \cdot \Delta R_j >_{norm} = \frac{< \Delta R_i \cdot \Delta R_j >}{\sqrt{< \Delta R_i{}^2 >} \sqrt{< \Delta R_j{}^2 >}}. \tag{2.6}$$

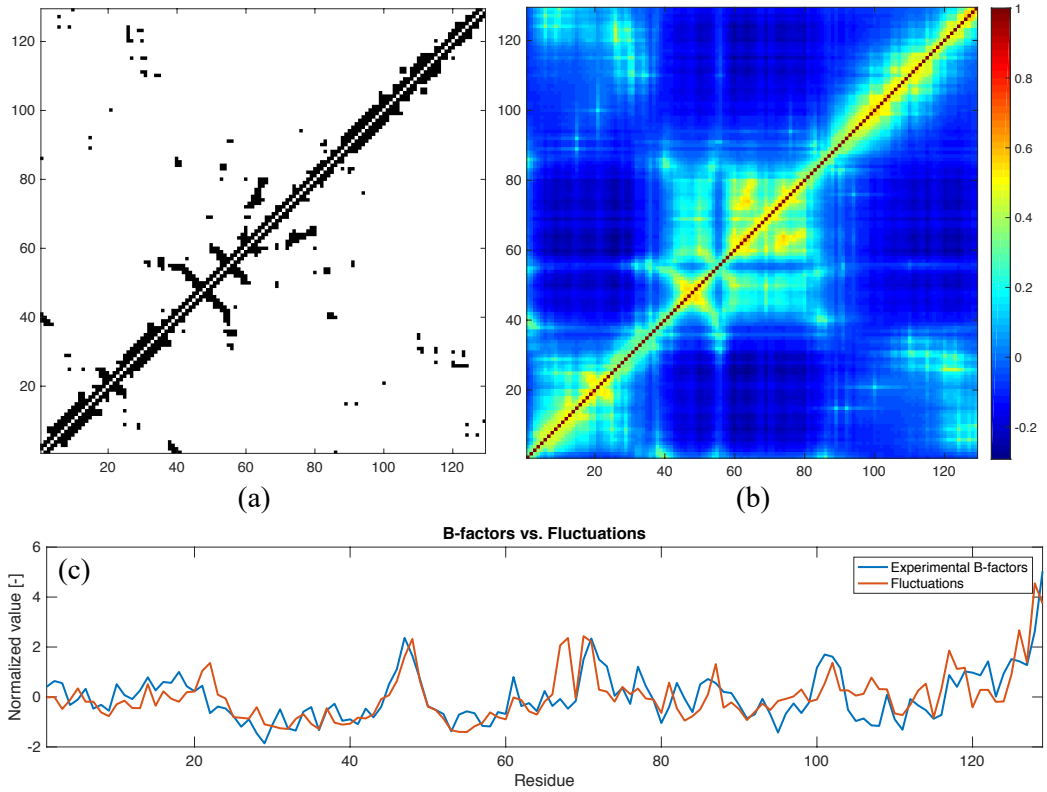

Figure 2.6. GNM for HEW lysozyme (PDB: 4ym8), r_c = 7.3 Å: (a) connectivity map; (b) cross-correlation map; (c) experimental B-factors vs. computed fluctuations (ρ = 0.71).

Despite the extreme simplification of the GNM, it has proven to be effective in the prediction of the mean-square fluctuations of the protein residues. These are usually compared to the experimental B-factors, also called temperature factors, that are obtained from crystallographic experiments. Experimental B-factors result from the local uncertainty about the atom position and, although they can result from a combination of different elements, for very high-resolution protein structures they can provide information about the inherent flexibility of the protein. B-factors are related to the computed GNM fluctuations as:

$$B_i = \frac{8\pi^2}{3} < \Delta R_i{}^2 >= \frac{8\pi^2 k_B T}{\gamma} \tilde{\Gamma}^{-1}{}_{i,i} . \tag{2.7}$$

Figure 2.6c shows the comparison of the computed fluctuations from Eq. (2.7) and the experimental B-factors for HEW lysozyme. As can be seen, the computed fluctuations are in good accordance with the experimental B-factors, with a Pearson correlation coefficient ρ of 0.71.

The fact that the GNM provides accurate predictions of the protein fluctuations is fascinating, considering the extreme simplification of this model. The mean-square fluctuations are due to the protein thermal vibrations, which in turn depend on several factors, such as the intramolecular interactions among all the atoms and the interactions with the environment. These are not deterministic factors, being stochastic in nature. Nevertheless, a simple and deterministic model

that is only dependent on the folded crystal structure and on a network of linear elastic springs, such as the GNM, is amazingly able to provide an accurate description of the mean-square fluctuations (Figure 2.6c). This suggests that the folded protein structure potentially contains in itself all the information we need to extract the dynamical features.

The agreement of the GNM outcomes with experimental data is even improved when distance-dependent spring constants are considered in the model. Yang et al. [32] suggested a parameter-free GNM (pfGNM), where the need of the arbitrary cutoff limit r_c is avoided. Each node is connected to each other and the spring constants are inversely proportional to the square distance between the nodes. Applying both the GNM and pfGNM on a set of 1220 protein structures, the pfGNM is shown to outperform the GNM, with an improvement of the mean correlation values around 5%. This shows that considering higher ranges of cooperativity, coupled with the distance-dependent information, improves the accuracy of the ENM in the fluctuation prediction [32].

The GNM has still some limitations. The most important one relies on the fact that, given the nature of the $N \times N$ Kirchhoff matrix, the GNM does not take into account the directionality of the protein motions and dynamics. As a matter of fact, the GNM dynamics is only informative of the different amplitudes of motion among different residues, but does not provide any information about the directions of these motions in the three-dimensional space. This limitation has been overcome with the introduction of another ENM, the so-called Anisotropic Network Model (ANM). Moreover, as will be pointed out after the description of the ANM, both these ENMs do not include the explicit information about the mass of the system, at least in their original definition. For this reason, the eigenvalues obtained from the matrix decomposition are only representative of the vibrational frequencies, but they do not allow to quantitatively estimate the absolute frequency values in Hz.

2.2.1.2 Anisotropic Network Model

To include the directionality feature in the protein ENM, the Anisotropic Network Model (ANM) was developed by Atilgan et al. in 2001 [31]. Similarly to the GNM, the ANM considers the protein elastic network as made up of a set of nodes connected by linear springs. For a system counting N nodes, i.e. the C^{α} atoms of the protein, the ANM yields the definition of the $3N \times 3N$ Hessian matrix $\boldsymbol{H}$, which is defined as follows:

$$\boldsymbol{H} = \begin{bmatrix} \boldsymbol{H_{1,1}} & \dots & \boldsymbol{H_{1,i}} & \dots & \boldsymbol{H_{1,j}} & \dots & \boldsymbol{H_{1,N}} \\ \dots & \dots & \dots & \dots & \dots & \dots & \dots \\ \boldsymbol{H_{i,1}} & \dots & \boldsymbol{H_{i,i}} & \dots & \boldsymbol{H_{i,j}} & \dots & \boldsymbol{H_{i,N}} \\ \dots & \dots & \dots & \dots & \dots & \dots & \dots \\ \boldsymbol{H_{j,1}} & \dots & \boldsymbol{H_{j,i}} & \dots & \boldsymbol{H_{j,j}} & \dots & \boldsymbol{H_{j,N}} \\ \dots & \dots & \dots & \dots & \dots & \dots & \dots \\ \boldsymbol{H_{N,1}} & \dots & \boldsymbol{H_{N,i}} & \dots & \boldsymbol{H_{N,j}} & \dots & \boldsymbol{H_{N,N}} \end{bmatrix}, \tag{2.8}$$

where $\boldsymbol{H_{i,j}}$ is a 3×3 matrix related to the nodes i and j. This can be calculated by taking the second derivatives of the potential $V_{i,j}$, with respect to the three directions of the global reference system XYZ:

$$\boldsymbol{H_{i,j}} = \begin{bmatrix} \frac{\partial^2 V_{i,j}}{\partial x^2} & \frac{\partial^2 V_{i,j}}{\partial x \partial y} & \frac{\partial^2 V_{i,j}}{\partial x \partial z} \\ \frac{\partial^2 V_{i,j}}{\partial x \partial y} & \frac{\partial^2 V_{i,j}}{\partial y^2} & \frac{\partial^2 V_{i,j}}{\partial y \partial z} \\ \frac{\partial^2 V_{i,j}}{\partial x \partial z} & \frac{\partial^2 V_{i,j}}{\partial y \partial z} & \frac{\partial^2 V_{i,j}}{\partial z^2} \end{bmatrix}. \tag{2.9}$$

The potential $V_{i,j}$ is assumed as the elastic potential of the Hookean spring connecting residues *i* and *j*, which takes the following quadratic form:

$$V_{i,j} = \frac{1}{2}\gamma\left(R_{i,j} - {R_{i,j}}^0\right)^2, \tag{2.10}$$

being $R_{i,j}$ and ${R_{i,j}}^0$ the current and initial distance between nodes *i* and *j*, and γ the force constant of the spring. In the original ANM, γ is the same for all the couple of nodes which are closer than the imposed cutoff limit r_c. Typical values of r_c in the ANM are in the range 12-18 Å. In Figure 2.7a, the ANM of HEW lysozyme (PDB: 4ym8) is shown, with cutoff limit of 15 Å.

Inserting the equation of the elastic potential in Eq. (2.9) and calculating the partial derivatives in the equilibrium position, i.e. $R_{i,j} = {R_{i,j}}^0$, one obtains:

$$\boldsymbol{H_{i,j}} = -\gamma \begin{bmatrix} \frac{(x_j - x_i)^2}{\left({R_{i,j}}^0\right)^2} & \frac{(x_j - x_i)(y_j - y_i)}{\left({R_{i,j}}^0\right)^2} & \frac{(x_j - x_i)(z_j - z_i)}{\left({R_{i,j}}^0\right)^2} \\ \frac{(x_j - x_i)(y_j - y_i)}{\left({R_{i,j}}^0\right)^2} & \frac{(y_j - y_i)^2}{\left({R_{i,j}}^0\right)^2} & \frac{(y_j - y_i)(z_j - z_i)}{\left({R_{i,j}}^0\right)^2} \\ \frac{(x_j - x_i)(z_j - z_i)}{\left({R_{i,j}}^0\right)^2} & \frac{(y_j - y_i)(z_j - z_i)}{\left({R_{i,j}}^0\right)^2} & \frac{(z_j - z_i)^2}{\left({R_{i,j}}^0\right)^2} \end{bmatrix}, \tag{2.11}$$

where x_i, y_i and z_i are the crystal coordinates of residue *i*, and x_j, y_j and z_j are the crystal coordinates of residue *j*. Known $\boldsymbol{H_{i,j}}$ for each $i \neq j$, the diagonal matrices $\boldsymbol{H_{i,i}}$ can be computed as:

$$\boldsymbol{H_{i,i}} = -\sum_{j=1, j\neq i}^{N} \boldsymbol{H_{i,j}}. \tag{2.12}$$

Once the complete Hessian matrix from Eq. (2.8) is calculated, it undergoes the eigenvalue-eigenvector decomposition to extract the dynamical features, namely the 3*N*-6 non-rigid mode shapes ${\boldsymbol{\delta}_n}^{ANM}$ and the 3*N*-6 non-zero eigenvalues ${\lambda_n}^{ANM}$. Note that, in the ANM, since the protein is not externally constrained, one obtains six zero eigenvalues that are related to the six rigid-body motions, composition of three global translations and three rigid rotations.

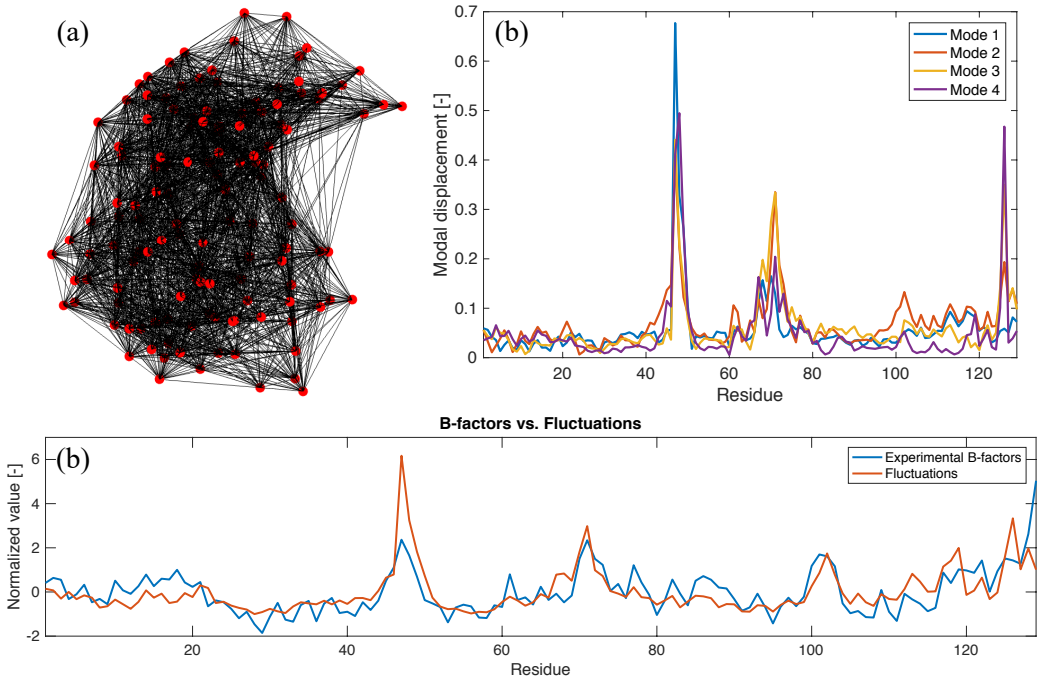

Figure 2.7. ANM for HEW lysozyme (PDB: 4ym8), r_c = 15 Å: (a) graphical representation of the ENM (red dots: C^{α} atoms, black lines: springs); (b) the first four non-rigid motions; (c) experimental B-factors vs. computed fluctuations (ρ = 0.68).

The $3N \times 1$ eigenvectors $\boldsymbol{\delta}_n$ provide the normal modes of the elastic network, whereas the eigenvalues λ_n are proportional to the corresponding frequencies of vibrations. Figure 2.7b shows the first four non-rigid motions of lysozyme, with the profiles of absolute displacements, that provide information about the most flexible parts of the protein structure. Differently from the GNM, the ANM eigenvectors contain three-components for each residue modal displacement. Therefore, one can also visualize the directionality of motion, and not only its amplitude distribution along the protein chain [33]. As will be shown below, this is of great help in order to understand the biological mechanisms of the protein. However, it should be noted that, since no explicit mass is included in the original ANM, the information about the vibrational frequency is still only qualitative, and not quantitative.
Similarly to Eq. (2.4) for the GNM, the ANM eigenvectors and eigenvalues are used to calculate the pseudo-inverse Hessian matrix:

$$\widetilde{\boldsymbol{H}}^{-1} = \sum_{n=7}^{3N} \frac{\boldsymbol{\delta}_n \boldsymbol{\delta}_n{}^T}{\lambda_n}. \tag{2.13}$$

The cross-correlations of the residue fluctuations and the mean-square fluctuations can be finally obtained from the entries of the pseudo-inverse matrix as follows:

$$< \Delta R_i \cdot \Delta R_j >= \frac{3k_B T}{\gamma} \left[\widetilde{H}^{-1}{}_{3i-2,3j-2} + \widetilde{H}^{-1}{}_{3i-1,3j-1} + \widetilde{H}^{-1}{}_{3i,3j} \right], \tag{2.14}$$

which are then used to compare the ANM results to the experimental data, such as the experimental B-factors. Figure 2.7c reports this comparison for the HEW lysozyme, where a Pearson correlation coefficient of 0.68 is reached. Despite the

fact that often the GNM slightly outperforms the ANM in the prediction of experimental B-factor (see Figures 2.6c and 2.7c, and corresponding correlation coefficients), the ANM has the advantage to provide the additional information about the motion directionality, which is pivotal for understanding the protein mechanism.

As seen from Eqs. (2.10) and (2.11), the original ANM takes into account equal spring constants for each couple of connected nodes, despite their distance. Distance-dependent springs were then considered in subsequent works from Eyal et al. [34] and Yang et al. [32], where each spring constant $\gamma_{i,j}$ depends on the actual inter-residue distance $R_{i,j}$ with an inverse power decay:

$$\gamma_{i,j} \propto \frac{1}{{R_{i,j}}^{p}}, \tag{2.15}$$

p being the decay parameter. Extensive analyses based on large sets of protein structures showed that p values greater than one lead to higher correlations with the experimental B-factors [32,34].

2.2.1.3 Further developments and assessments of the ENMs

Beside the GNM and ANM, other models based on the elastic description have been developed in the last decades for the investigation of protein vibrations and dynamics. Hinsen [35] made use of simplified mechanical models for the investigation of low-frequency protein vibrations, that were found to be independent of the force field details, and he showed that these simplified models are effective in predicting the protein flexibility as well as the existence of quasi-rigid domains. Durand et al. [36] and Tama et al. [37] developed a new kind of ENM, where low-frequency normal modes of proteins can be described as pure rigid-body motions of blocks of consecutive protein residues. This approach has been called RTB (rotations-translations of blocks) and it has been proven useful to predict the low-frequency protein dynamics as well as to reduce the computational cost. Recently, the RTB was further enriched by Hoffmann and Grudinin [38] to describe the non-linear normal modes, obtained by extrapolating the contribution of the translations and rotations of the blocks. Mixed coarse-grained strategies, where both high- and low-resolution modeling representations are applied in the ENMs, were also employed by Kurkcuoglu et al. [39,40], showing high efficiency in the prediction of the low-frequency dynamics. An enhanced ENM, based on rigid domains and flexible hinges, was also proposed by Song and Jernigan [41] to represent the motions of domain-swapping proteins.

Despite their very simplified nature, the Elastic Network Models coupled with normal mode calculations are extremely useful in order to obtain insights about protein flexibility and low-frequency dynamics [9,42,43]. In this regards, other than reducing the computational costs, coarse-graining strategies seem to be beneficial in terms of low-frequency dynamics evaluation [44,45]. Beside the B-factors prediction, ENMs have been used to discover the similarities and differences in the large-scale dynamics of proteins with similar architectures [46]. Normal modes from coarse-grained ENMs were also found to closely align to the dynamic communities extracted from MD simulations [47] and those extracted from the experimental ensembles of crystal structures [48,49]. Yang et al. [50] also made use of the ANM to predict the anisotropic counterpart of the thermal fluctuations, i.e. the anisotropic B-factors, which are available in highly-refined

protein structures. As will be shown in Section 2.3, plenty of work has also been carried out to investigate the conformational transitions of proteins, that are associated to the biological mechanism, through the evaluation of the ENM normal modes.

2.2.2 Finite-element-based ELMs and experimental tests for the investigation of protein vibrations

Given the clear relevance of Structural Mechanics concepts in the ENM formulation described above, some models were also developed within the framework of the Finite Element Method (FEM) for the calculation of protein vibrations. Bathe [51] treated proteins as continuum elastic solids with molecular volumes defined by their solvent-excluded surface. The FE-based protein surface was used to calculate normal modes, that were found in agreement with experimental data and previous approaches, such as RTB. More recently, the method was also enriched by adding Brownian dynamics accounting for the presence of solvent, simulated by taking into account viscous forces and diffusion phenomena [52]. Following FE-based approached were also based on frame-like structures and ELMs, as described below, in order to focus on the low-frequency protein vibrations, that are found to occur in the THz range.

2.2.2.1 Protein vibrations in the THz range: Experimental tests

Experimental investigations, by means of spectroscopy techniques such as Raman and THz Time Domain Spectroscopy (THz-TDS), have shown that low-frequency protein vibrations are mostly found in the THz frequency range.

Raman spectroscopy is a vibrational spectroscopy technique, based on the detection of the light scattered by the sample under investigation and further processed by a spectrometer. Eventually, from the experimental test, one obtains the Raman spectrum of the material, that provides useful information about the vibrational levels of the molecular bonds and allows to recognize the fingerprints of specific chemical groups. Raman spectroscopy has been deeply used for the analysis of peptides and proteins [53,54]. Although it poses challenges for the analysis of biological materials such as proteins [55], Raman technique can be very helpful for the detection of low-frequency protein modes.

In 1972, Brown et al. [56] found a pronounced peak at 29 cm^{-1} (~ 0.87 THz) in the Raman spectra of α-chymotrypsin samples prepared in several ways. Remarkably, this peak is absent only when the protein is denatured by means of sodium dodecyl sulfate (SDS). This led the authors to conclude that this THz vibration must involve all, or very large portions, of the protein molecule [56]. Chou suggested that low-frequency vibrations involve collective motions of the protein and can be relevant for its biological functionality [57,58]. Peaks below 50 cm^{-1} were also found in several protein structures by Painter et al. [59]. More recently, Carpinteri et al. [60] and Lacidogna et al. [61] made use of special ultra-low-frequency (ULF) filters and detected some pronounced Raman peaks around 30 cm^{-1} in HEW lysozyme and Na/K-ATPase powder samples (Figure 2.8).

Another spectroscopy technique which has been recently exploited for the investigation of protein vibrations is THz-TDS [62], that enables to measure photons in the range of THz frequencies. The range 0.1–1.5 THz was previously known as the “Terahertz Gap”, as it was difficult to investigate due to the lack of a suitable light source. This technique allowed the discovery of the infrared (IR)

activity of a large number of low-frequency protein collective motions in the THz range [63]. THz-TDS absorbance spectra were found to well represent the density of the protein normal modes [64]. The first optical observation of long-range THz vibrational modes was achieved with THz-TDS by Acbas et al. [65]. By thorough analyses via THz-TDS, it was found that these motions are related to the protein biological mechanisms through the protein conformational changes and to the allosteric activity [66,67].

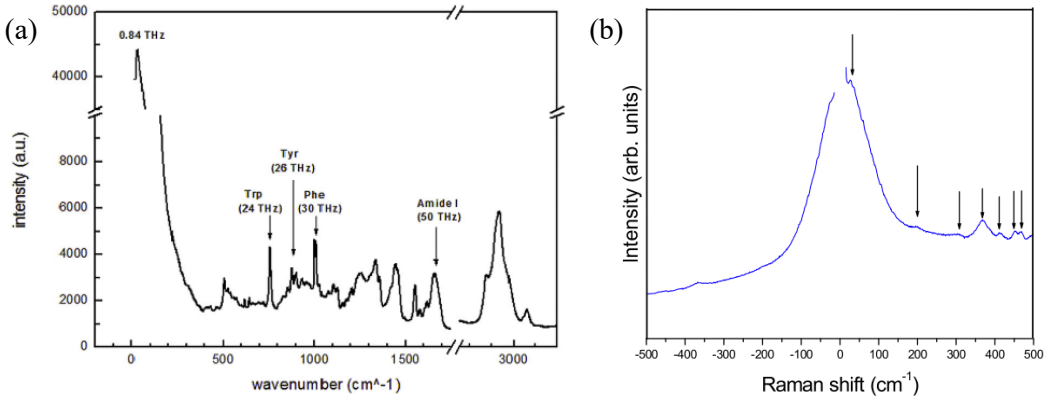

Figure 2.8. Low-frequency Raman spectra obtained with ULF filters on: (a) HEW lysozyme [60]; (b) Na/K-ATPase [61]. Used with permission from [60,61].

2.2.2.2 Protein vibrations in the THz range: Numerical FE models

In order to focus mostly on the THz frequency range of the vibrational space, Carpinteri et al. [60,68] developed a FE model where the expansion-contraction modes of the protein backbone were investigated. These models included all the heavy atoms of the protein and were based on a frame-like elastic representation of the protein structure. Based on the atomic mass values and the stiffness values of the covalent bonds, the FE models were applied to the case studies of HEW lysozyme [60] and Na/K-ATPase [68]. The outcomes from modal analysis calculations provided some explanations on the possible low-frequency expansion-contraction modes found in the THz range, with comparison to the vibrations obtained from Raman experiments [60,61]. Further analyses by Lacidogna et al. [69,70] showed that coarse-grained FE models, using the same frame-like representations but based only on the C^{α} atoms, allowed to obtain the same results in terms of low-frequency expansion-contraction modes, while reducing the computational cost.

The FE frame-like models presented above allowed to obtain information regarding the expansion-contraction protein modes occurring in the THz range. However, to properly describe also the low-frequency distortional motions, a FE-based ELM was recently developed by Scaramozzino et al. [71], which is the counterpart of the ANM by following a purely Structural Mechanics approach.

The FE-based ELM was developed within the FE commercial code LUSAS [72]. The model is made up of point masses, corresponding to the C^{α} atoms of the protein, and an assembly of elastic bars that simulate the interactions between the amino acids. The connections are generated by using a geometrical cutoff limit r_c, hence only the nodes whose distance is lower than this value are connected by an elastic bar. The model is applied to the case study of HEW lysozyme (PDB: 4ym8) by considering five different cutoff values, i.e. 8, 10, 12, 15 and 20 Å.

Based on these different geometrical constraints, five different FE models were generated, as shown in Figure 2.9.

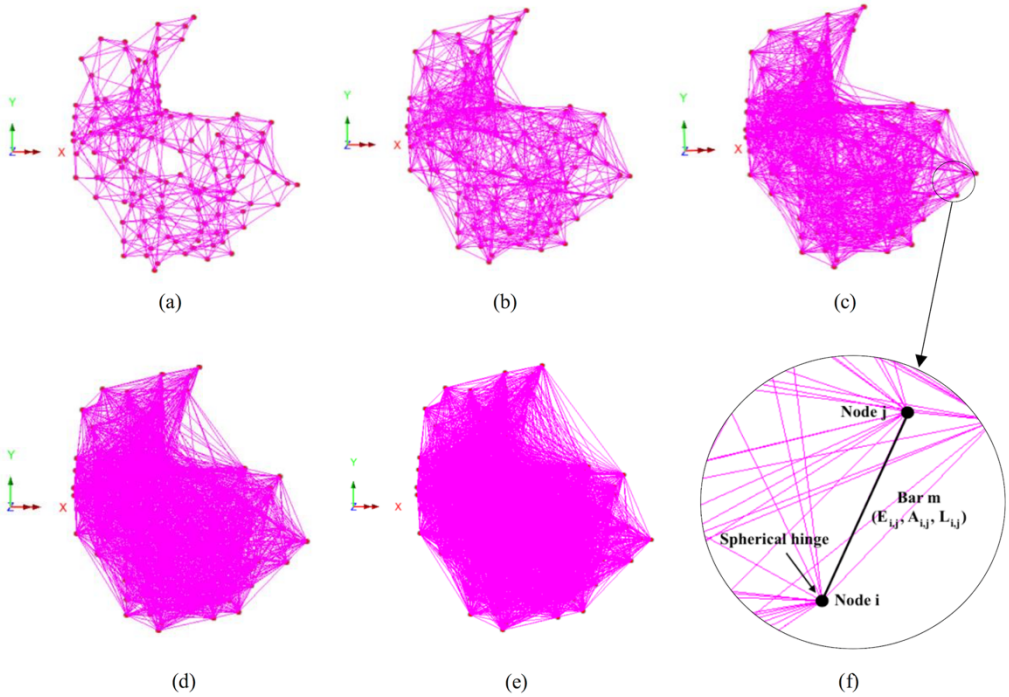

Figure 2.9. HEW lysozyme models with varying cutoff values: (a) 8 Å; (b) 10 Å; (c) 12 Å; (d) 15 Å; (e) 20 Å. (f) zoomed picture of the FE-based ELM highlighting the single bar element. Used with permission from [71].

According to the FE theory [6], for an ELM made up of N nodes and M connections, one can compute the global $3N \times 3N$ stiffness matrix $\boldsymbol{K}$, in this case N being the number of C^{α} atoms and M the total number of elastic bars. The calculation starts from the definition of the 2×2 local stiffness matrix $\boldsymbol{k}_{\boldsymbol{m}}^{*}$, associated to the m^{th} elastic bar (Figure 2.9f), which is defined as:

$$\boldsymbol{k}_{\boldsymbol{m}}^{*} = \frac{E_{i,j}A_{i,j}}{R_{i,j}}\begin{bmatrix} 1 & -1 \\ -1 & 1 \end{bmatrix}, \tag{2.16}$$

being $E_{i,j}$, $A_{i,j}$ and $R_{i,j}$ the Young's modulus, the cross-sectional area and the length of the m^{th} bar connecting nodes i and j, respectively. In the proposed FE-based ELM, the elastic and geometrical properties of the bars were kept constant for all the connections, i.e. $E_{i,j}A_{i,j} = EA$. This implies that the stiffness of each bar k_m turns out to be inversely proportional to its length ($k_m \propto {R_{i,j}}^{-1}$). However, assigning different patterns of $E_{i,j}$ and $A_{i,j}$ throughout the ELM, one can also obtain different distance-dependence stiffness patterns.

Taking into account the local orientation of the m^{th} bar with respect to the global reference system XYZ, the 2×2 local stiffness matrix $\boldsymbol{k}_{\boldsymbol{m}}^{*}$ can be converted into the 6×6 stiffness matrix $\boldsymbol{k}_{\boldsymbol{m}}$ expressed in the global system. This is achieved by means of the 2×6 rotation matrix $\boldsymbol{N}_{\boldsymbol{m}}$, which is related to the m^{th} bar element and contains the three directional cosines between the local and global reference systems:

$$\boldsymbol{N_m} = \begin{bmatrix} \frac{x_j - x_i}{R_{i,j}} & \frac{y_j - y_i}{R_{i,j}} & \frac{z_j - z_i}{R_{i,j}} & 0 & 0 & 0 \\ 0 & 0 & 0 & \frac{x_j - x_i}{R_{i,j}} & \frac{y_j - y_i}{R_{i,j}} & \frac{z_j - z_i}{R_{i,j}} \end{bmatrix}, \tag{2.17}$$

being x_i (x_j), y_i (y_j) and z_i (z_j) the three-dimensional coordinates of node i (j) in the global reference system XYZ, and $R_{i,j}$ their spatial distance. Based on Eqs. (2.16) and (2.17), the 6 × 6 stiffness matrix of the element $\boldsymbol{k_m}$ in the global reference system takes the following form:

$$\boldsymbol{k_m} = \boldsymbol{N_m}^T \boldsymbol{k_m^*} \boldsymbol{N_m} = \begin{bmatrix} \boldsymbol{\alpha_m} & -\boldsymbol{\alpha_m} \\ -\boldsymbol{\alpha_m} & \boldsymbol{\alpha_m} \end{bmatrix}, \tag{2.18}$$

being $\boldsymbol{\alpha_m}$ the 3 × 3 matrix containing the stiffness values and the directional cosines:

$$\boldsymbol{\alpha_m} = \frac{E_{i,j} A_{i,j}}{R_{i,j}} \begin{bmatrix} \frac{(x_j - x_i)^2}{{R_{i,j}}^2} & \frac{(x_j - x_i)(y_j - y_i)}{{R_{i,j}}^2} & \frac{(x_j - x_i)(z_j - z_i)}{{R_{i,j}}^2} \\ \frac{(x_j - x_i)(y_j - y_i)}{{R_{i,j}}^2} & \frac{(y_j - y_i)^2}{{R_{i,j}}^2} & \frac{(y_j - y_i)(z_j - z_i)}{{R_{i,j}}^2} \\ \frac{(x_j - x_i)(z_j - z_i)}{{R_{i,j}}^2} & \frac{(y_j - y_i)(z_j - z_i)}{{R_{i,j}}^2} & \frac{(z_j - z_i)^2}{{R_{i,j}}^2} \end{bmatrix}. \tag{2.19}$$

Note that Eq. (2.19) is analogous to Eq. (2.11) arising from the ANM framework, showing that there exists complete consistency between the ANM and the FE-based ELM. Once the stiffness matrix of the single bar $\boldsymbol{k_m}$ is computed in the global system from Eqs. (2.18) and (2.19), the FE-based theoretical framework relies on the expansion of the element matrix to the global structural dimension $3N$ ($\boldsymbol{K_m}$), by means of the $6 \times 3N$ expansion matrix $\boldsymbol{C_m}$ [6]. Finally, the $3N \times 3N$ global stiffness matrix $\boldsymbol{K}$ of the whole ELM is computed by assembling all the elements' stiffness matrices as follows:

$$\boldsymbol{K} = \sum_{m=1}^{M} \boldsymbol{K_m} = \sum_{m=1}^{M} \boldsymbol{C_m}^T \boldsymbol{k_m} \boldsymbol{C_m} = \sum_{m=1}^{M} \boldsymbol{C_m}^T \boldsymbol{N_m}^T \boldsymbol{k_m^*} \boldsymbol{N_m} \boldsymbol{C_m}. \tag{2.20}$$

The stiffness matrix $\boldsymbol{K}$ is consistent with the $3N \times 3N$ Hessian matrix $\boldsymbol{H}$ of the ANM reported in Eq. (2.8).

Beside the calculation of the stiffness matrix, the FE model yields the definition of the $3N \times 3N$ global mass matrix $\boldsymbol{M}$, associated with the mass of the ELM. This is a diagonal matrix, made up of 3 × 3 diagonal sub-matrices $\boldsymbol{M_i}$, containing the mass values of the i^{th} node. Since in globular proteins the distribution of the mass throughout the system does not deviate so much from the uniform distribution, the total mass of the protein has been equally divided among the N nodes of the Lattice Model. This simplifies the input procedure, while capturing the global behavior of the system.

It has also to be noted that, since we are dealing with very small quantities, with masses in the order of magnitude of 10^{-26} kg and distances in the order of 10^{-10} m, this might cause issues when working within a FE environment meant for

larger systems. For this reason, a numerical scaling procedure is applied to masses and distances, as thoroughly reported in [60,68].

Once the stiffness and mass matrix are computed within the FE code, a free vibration analysis, i.e. modal analysis, is carried out. It consists of solving the equations of motion for a multi degree-of-freedom (MDOF) undamped oscillator [6], which leads to the generalized eigenvalue-eigenvector problem:

$$(\boldsymbol{K} - {\omega_n}^2 \boldsymbol{M}) \cdot \boldsymbol{\delta_n} = \boldsymbol{0}, \tag{2.21}$$

where ${\omega_n}^2$ and $\boldsymbol{\delta_n}$ represent the n^{th} eigenvalue and eigenvector, respectively. The latter has dimension of $3N \times 1$ and is associated to the vibrational shape of the n^{th} mode, while the former is related to the vibrational frequency of the mode f_n, through the following relationship:

$$f_n = \frac{\omega_n}{2\pi}. \tag{2.22}$$

Equation (2.21) is solved by setting the determinant of the matrix within the brackets equal to zero and finding the $3N$ set of eigenvalues and corresponding eigenvectors. Note that, in accordance to what reported in Section 2.2.1.2 regarding the ANM, since the protein is not externally constrained, the first six eigenvectors are rigid-body motions at zero frequency. From the seventh mode onwards, we obtain the information about the internal deformation modes of the protein ELM.

Based on the evaluated set of frequencies and mode shapes, the numerical B-factor for the i^{th} node of the FE model can be computed as follows [43]:

$$B_i = \frac{8}{3}\pi^2 k_B T \sum_{n=7}^{3N} \frac{{\delta_{i,n}}^2}{{\omega_n}^2}, \tag{2.23}$$

being $\delta_{i,n}$ the absolute mass-weighted modal displacement of node i corresponding to the mode n, and the other terms having same meaning explained above. The B-factors computed by the FE ELM are finally compared to the experimental thermal fluctuations available in the PDB file. The comparison is also used to set the rigidity value of the elastic bars ($E_{i,j}A_{i,j}$), which initially is set as a tentative value. By posing that the mean value of the experimental and computed B-factors along the protein chain are equal, one is able to define the material (E) and geometrical (A) properties of the elastic bars. For more details, refer to Scaramozzino et al. [71]. Ultimately, based on these rigidity values and the mass values contained in the mass matrix, it is finally possible to obtain quantitative information about the values of the vibrational frequencies.

In Figure 2.10, the normalized B-factors obtained from Eqs. (2.23) are compared to the experimental values from the PDB file. The correlation coefficients between numerical and experimental distributions vary from 0.57 to 0.72, depending on the adopted cutoff value. A complete consistency between the FE-based ELM is found with the ANM, when a distance-dependent decay is considered with p equal to one. Whereas, slightly better results are found when comparing the FE ELM to the original ANM with p equal to zero [71].

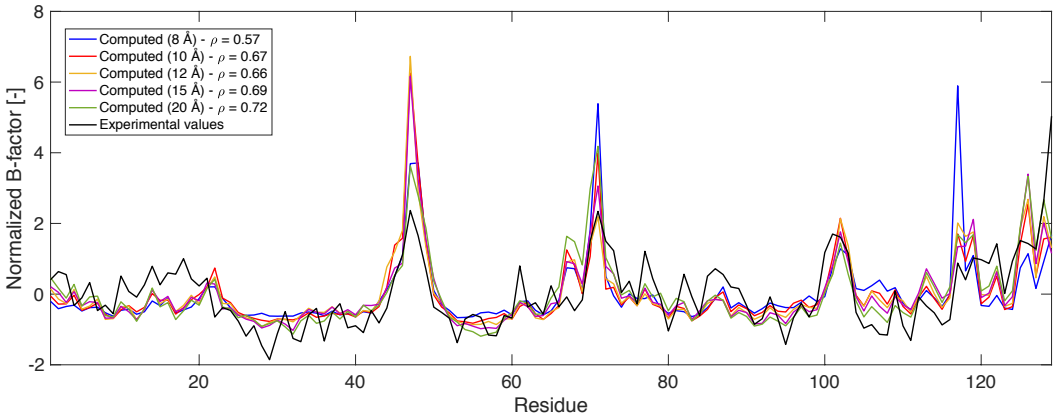

Figure 2.10. FE-based ELM of HEW lysozyme. Comparison between experimental and computed B-factors (normalized values). Adapted with permission from [71].

The utility of models like the ANM and the FE-based ELM presented here relies on their capability to show the directionality of the protein motions. Since low-frequency modes have been found to involve collective motions and to be generally related to the biological mechanisms (see Section 2.3), their investigation and visualization is of great interest [33,73].

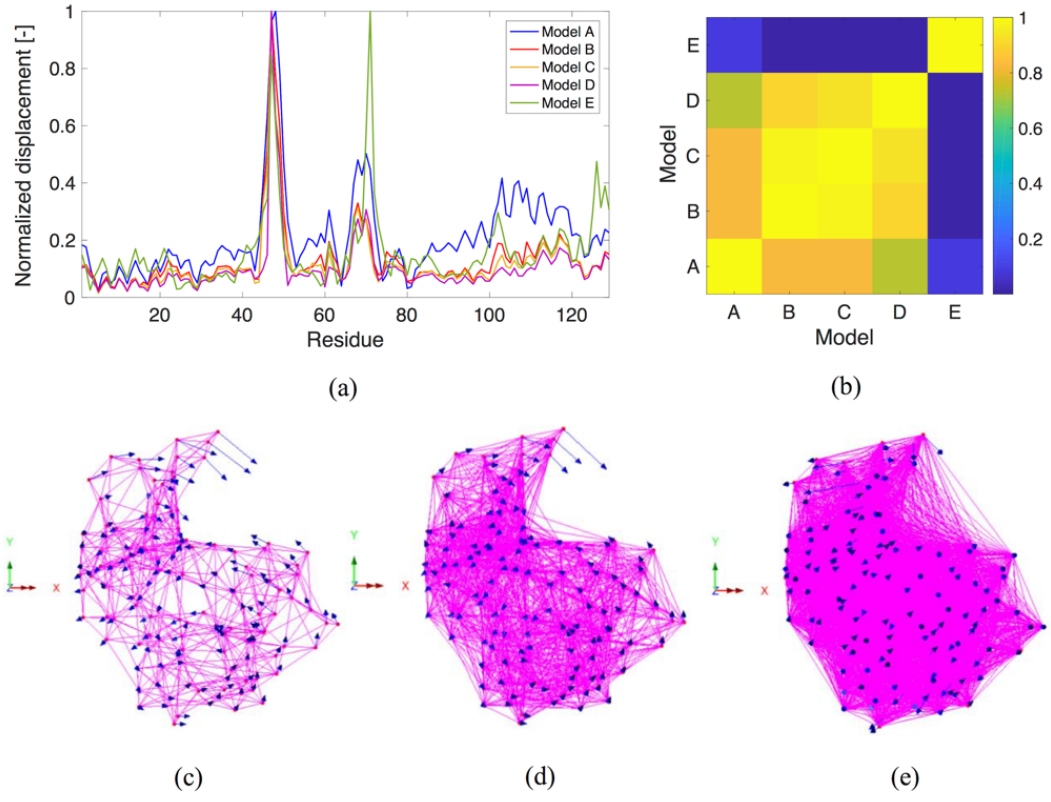

Figure 2.11. First non-rigid mode of HEW lysozyme: (a) normalized absolute displacements; (b) MAC matrix; (c,d,e) 3D mode shapes from Model A, C, E. Used with permission from [71].

The first two non-rigid modes extracted from modal analysis on the ELM of HEW lysozyme are shown in Figure 2.11 and 2.12, respectively. Specifically, Figures 2.11a and 2.12a show the normalized modal displacements associated to the first and second non-rigid mode, respectively, depending on the cutoff limit.

Models A, B, C, D and E stand for the models with cutoff limits equal to 8, 10, 12, 15 and 20 Å, respectively. As can be seen, changing the cutoff limit can affect the vibrational shape. In order to quantitively assess this influence, Figures 2.11b and 2.12b show the MAC (Modal Assurance Criterion) matrix between the vibrational modes arising from the different models. MAC values are calculated as follows [74,75]:

$$MAC_{i,j} = \frac{\left(\boldsymbol{\delta_i}^T \cdot \boldsymbol{\delta_j}\right)^2}{\left(\boldsymbol{\delta_i}^T \cdot \boldsymbol{\delta_i}\right)\left(\boldsymbol{\delta_j}^T \cdot \boldsymbol{\delta_j}\right)}, \tag{2.24}$$

$\boldsymbol{\delta_i}$ and $\boldsymbol{\delta_j}$ corresponding to the two eigenvectors of the vibrational modes to be compared. MAC values are always between 0 and 1, the former meaning complete orthogonality and the latter meaning complete similarity between the modes. Finally, Figures 2.11c-e and 2.12c-e show the 3D mode shapes for models A, C and E. As can be seen from the profiles of the normalized absolute displacements, both the first and second non-rigid mode associate great amount of flexibility to the protein regions close to residues 46–49 and 70–72. This is in accordance with the hinge-bending motion already found by Levitt et al. [28], who made use of NMA using internal coordinates. Moreover, from Eq. (2.23), it is clear that the B-factors are dominated by the low-frequency motions, as they are weighted by the inverse of the squared vibrational frequency. As can be seen by comparing Figure 2.10 to Figures 2.11a and 2.12a, the first low-frequency motions have an important role in defining the peaks of flexibility in the final B-factors distribution.

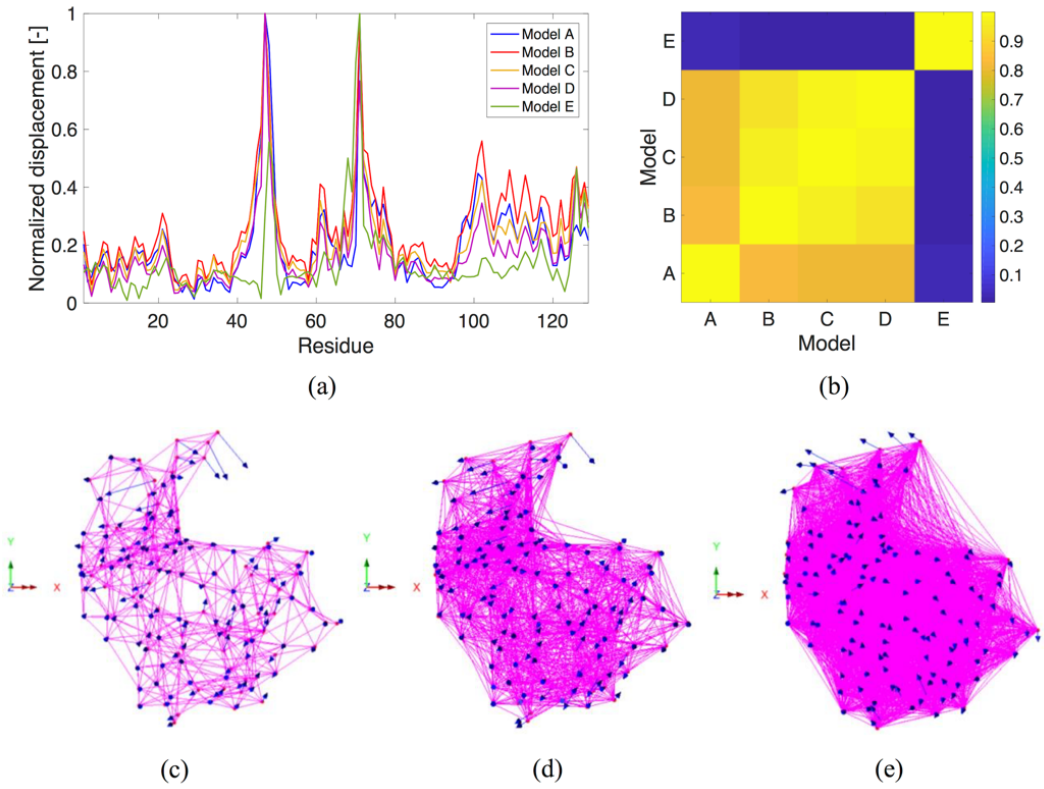

Figure 2.12. Second non-rigid mode of HEW lysozyme: (a) normalized absolute displacements; (b) MAC matrix; (c,d,e) 3D mode shapes from Model A, C, E. Used with permission from [71].

The three-dimensional visualization of the protein motions is shown in the lower panels of Figures 2.11 and 2.12, as obtained from the commercial code LUSAS [72]. These modes are clearly associated with a hinge-bending motion, the lysozyme vibrating in a way that it opens and closes its binding cleft. However, it is evident that changing the model parameter, e.g. the cutoff limit, affects the modal results. The MAC matrices in Figures 2.11b and 2.12b show that model B, C and D provide relatively similar results, being their cutoff values fairly close (10, 12 and 15 Å). Conversely, models A and E provide modal displacements which correlate less with the other models. This is especially true for the latter, where MAC values lower than 0.2 are found when comparing the modes from model E to the ones arising from the other models. This is found to occur because of a switch between the first and second mode in model E [71]. This aspect, e.g. the role of the model parameters on the outcomes, needs therefore to be properly taken into account when investigating the low-frequency protein modes via ANM-like approaches, such as the ELM presented here.

By setting the values of the bar stiffness based on the experimental B-factor distribution, it was also possible to obtain quantitative information about the absolute values of the vibrational frequencies. In Figure 2.13 the first five non-zero frequencies are reported depending on the geometrical cutoff limit. The lowest motions are found to vibrate in the low-THz frequency range, but the exact value exhibits a significant dependence on the model parameter. The fundamental frequency, i.e. the frequency associated to the lowest mode, is found to vary from 0.046 THz (~ 1.5 cm^{-1}) for model A to 0.117 THz (~ 3.9 cm^{-1}) for model E. Despite the not negligible variation, these values are still in line with the frequency values obtained by Levitt et al. [28] and Markelz et al. [64]. The former used NMA with internal coordinates and found that the lowest mode in lysozyme occurs at 2.98 cm^{-1} and involves high motility near residues 47, 70 and 103 (which is in accordance with Figure 2.11). The latter made use of Chemistry at HARvard Molecular Mechanics (CHARMm) simulations, and found similar frequency values for the lowest vibrational modes.

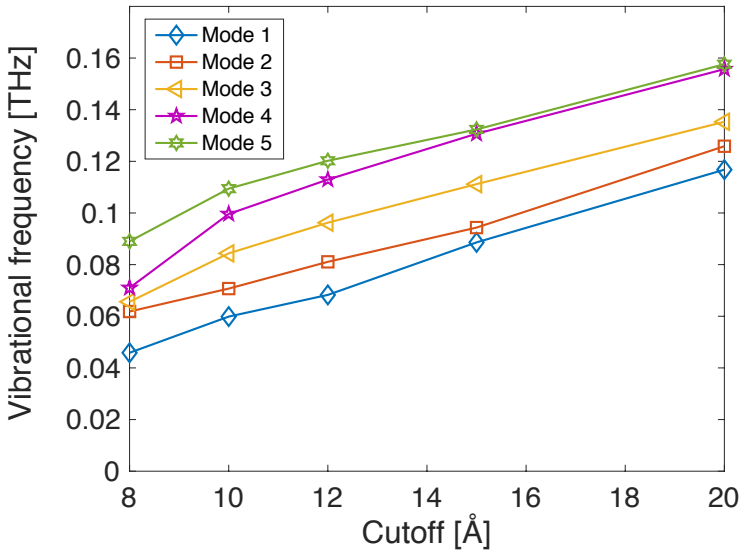

Figure 2.13. Lowest five non-zero vibrational frequencies of HEW lysozyme. Used with permission from [71].

The proposed FE-based ELM represents then a valid engineering-based approach for analyzing the small-amplitude low-frequency collective protein

vibrations. As already mentioned above, this model can be seen as the counterpart of the ANM, obtained by following a purely Structural Mechanics approach according to the FE framework [71]. This makes this model more easily accessible to the engineering community, for the investigation of the low-frequency protein dynamics as well as other structural aspects, such as the effect of force application on the ELM, instability phenomena, etc.

All the models presented in this Section have an important feature: they tackle the complexity of the protein behavior and dynamics by means of simplified mechanical models. First, the complex interaction potentials have been simplified into the Hookean pairwise potential related to the elastic spring [29]. Then, it has been shown that even considering a coarse-grained model for the protein structure works fairly accurately if one wants to obtain the information on the low-frequency dynamics [30,31,35]. These results are remarkable as they tell us that even simplified models purely based on Structural Mechanics concepts can provide important information about the protein low-frequency vibrations. As will be reported in the next Section, these vibrations are found to be strictly related to the protein conformational changes, which in turn are the fingerprints of protein biological behavior and mechanisms. This makes the outcomes of the ELMs even more astonishing, as they are ultimately able to provide information about protein biological functionality.

2.3 Protein Vibrations and Biological Mechanisms

Understanding the way in which proteins perform their biological function is crucial for theoretical purposes, disease control and prevention, and drug design. It is known that proteins often perform their biological tasks through a modification of their structural conformation. The structural modification can be small or significant and defines the so-called conformational change. The most common case occurs when the protein binds to an external ligand and it switches its conformation from an “open” form to a “closed” one that is more energetically favorable for the protein-ligand system. This conformational change is often reversible, so that when the ligand is not present anymore the protein usually returns to its “open” configuration. Therefore, it can be said that the conformational change occurs in a continuous timeframe and affects the biological activity of the protein. Various proteins can also show more than two conformations. Furthermore, since proteins are dynamic entities in nature, they generate the so-called conformational ensemble where multiple similar, but not identical, structures are clustered together. The comprehension of the mechanisms and motions that govern the protein conformational changes and define the conformational ensembles is a central issue addressed by computational biologists.

As already mentioned in the previous Section, one of the leading approaches for these purposes relies on MD simulations [25]. Although MD simulations have been successful in predicting several aspects of protein functionality, their computational complexity usually prevent a thorough application to complex macromolecular systems that act on longer time scales. For this reason, the use of simplified ELMs, with all the different alternatives (GNM, ANM, FE-based models, etc.), has proven high efficacy in recent times for the prediction and analysis of protein mechanisms. In the remaining of this Section, the strict relationship between protein vibrations extracted from the ELMs and the conformational changes will be described. Eventually, a novel ELM, which has

been called the hinge-domain ANM (hdANM) and developed for the purpose of describing and predicting protein mechanisms, will be presented at the end of this Section.

2.3.1 Protein normal modes and conformational changes

A conformational change occurs when the protein undergoes a modification of its structural shape due to the biological activity to be carried out. Consider two different conformations *A* and *B* of the same protein structure. If $\boldsymbol{A}$ and $\boldsymbol{B}$ denote the $3N \times 1$ vectors containing the X, Y and Z coordinates of the *N* atoms (or residues) of the protein, the conformational change $\boldsymbol{CC}$ that leads from structure $\boldsymbol{A}$ to structure $\boldsymbol{B}$ can be expressed through the following equation:

$$\boldsymbol{B} = \boldsymbol{RA} + \boldsymbol{T} + \boldsymbol{CC}, \tag{2.25}$$

being $\boldsymbol{R}$ and $\boldsymbol{T}$ the $3N \times 3N$ rotation matrix and $3N \times 1$ translation vector, respectively. The former takes into account the rigid-body rotation of the protein, whereas the latter accounts for the uniform translation. By posing the Ordinary Least Squares Method condition on the components of vector $\boldsymbol{CC}$, one can numerically obtain the estimate of the rotation matrix $\overline{\boldsymbol{R}}$ and translation vector $\overline{\boldsymbol{T}}$ that best superimpose the two conformations. For this reason, this procedure is traditionally called superimposition. Figure 2.14 shows the superimposition of the closed form of LAO-binding protein (PDB: 1lst) to the open form (PDB: 2lao).

Known the estimated parameters that account for the rigid-body rotation and translation, the final structure $\boldsymbol{B}$ is superimposed onto the reference system of the initial structure (Figure 2.14), obtaining:

$$\boldsymbol{B_{RT}} = \overline{\boldsymbol{R}}^{-1}\,(\boldsymbol{B} - \overline{\boldsymbol{T}}), \tag{2.26}$$

$\boldsymbol{B_{RT}}$ containing the coordinates of the conformation $\boldsymbol{B}$ after the rigid superimposition onto structure $\boldsymbol{A}$. Finally, the $3N \times 1$ vector of the conformational change $\boldsymbol{CC}$, containing the displacements along the X, Y and Z direction, is computed as:

$$\boldsymbol{CC} = \boldsymbol{B_{RT}} - \boldsymbol{A} = \overline{\boldsymbol{R}}^{-1}\,(\boldsymbol{B} - \overline{\boldsymbol{T}}) - \boldsymbol{A}. \tag{2.27}$$

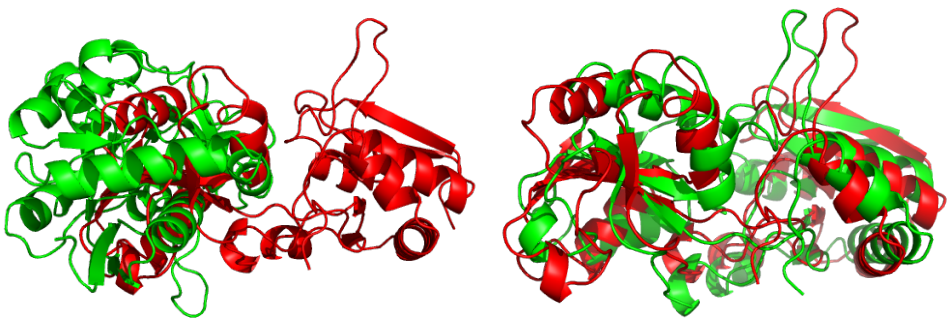

(a) (b)

Figure 2.14. Superimposition of the open and closed forms of LAO-binding proteins. Open form (PDB: 2lao) is represented in red. Closed form (PDB: 1lst) in green. (a) Not superimposed structures; (b) superimposed structures.

In the ground-breaking work from Tama and Sanejouand [76], it was firstly shown that the low-frequency normal modes arising from the simplified ELMs exhibit an astonishing correlation with the motion observed in the conformational change vector $\boldsymbol{CC}$. In their seminal work, Tama and Sanejounad [76] made use of the ANM, with a relatively short cutoff limit (8 Å), to investigate the conformational changes of twenty selected proteins, which are known to show two different conformations upon ligand-binding. The normal modes extracted from the ANM were compared to the conformational change by means of the overlap I_j:

$$I_j = \frac{\left|\boldsymbol{\delta}_j \cdot \boldsymbol{CC}\right|}{\sqrt{\boldsymbol{\delta}_j \cdot \boldsymbol{\delta}_j}\sqrt{\boldsymbol{CC} \cdot \boldsymbol{CC}}}, \tag{2.28}$$

being $\boldsymbol{\delta}_j$ the $3N \times 1$ eigenvector related to the j^{th} normal mode and $\boldsymbol{CC}$ the conformational change vector from Eq. (2.27). Note that the overlap value in Eq. (2.28) basically corresponds to the square root of the MAC reported in Eq. (2.24), evaluated between each normal mode and the conformational change. Similarly to the MAC value, the overlap I_j varies between 0 and 1, 0 meaning complete inconsistency and 1 complete similarity.

From the results, it is shown that high overlap values (up to 0.86) are found between the conformational change and one of the first low-frequency modes extracted from the ANM [76]. In Figure 2.15, the comparison between the displacements of the second low-frequency mode and the conformational change is shown for the 238-residue LAO-binding protein. In this case, the maximum overlap is found for the second normal mode and is equal 0.84. This confirms that the low-frequency dynamics plays a pivotal role in governing the protein biological mechanism, as it is involved in the conformational change. Moreover, as seen in Section 2.2, these vibrations are usually found to occur in the THz range and, although the exact estimate of these frequencies is strongly dependent on the model parameters, these results suggest the possible occurrence of resonance phenomena at THz frequencies that might drive the protein biological activity. Moreover, once again it is found that, despite their simplified nature, ELMs yet provide impressive results for the prediction of the protein behavior and mechanism.

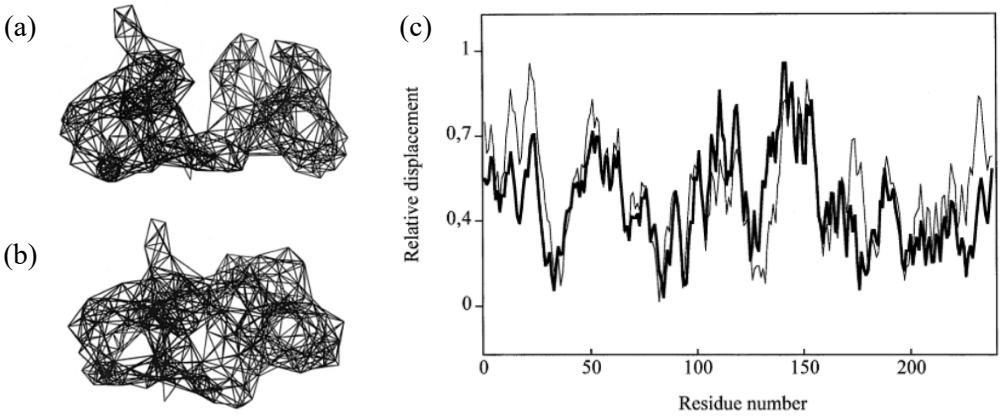

Figure 2.15. ANM normal modes and open-to-close conformational change in LAO-binding protein: (a) ANM of open conformation; (b) ANM of closed conformation; (c) absolute displacements of conformational change (thick line) and second low-frequency mode (thin line). Used with permission from [76].

The results found in [76] inform us also that ELMs are likely to predict fairly accurately the protein conformational change when the latter is more collective, thus it involves large portions of the protein, rather than a localized region. Moreover, it is found that the open-to-closed conformational change is more correlated to the normal modes extracted from the open form (Figure 2.15a). Conversely, it is more difficult to obtain high correlations when calculating the modes in the closed form (Figure 2.15b) and comparing them to the closed-to-open transition. This is mostly due to the fact that the ELM of the closed conformation usually has more connections in the spring network, that ultimately might prevent to obtain the observed opening mechanism.

After the seminal work of Tama and Sanejouand [76], several studies have investigated the relationship between low-frequency modes and the biologically-relevant conformational changes [77]. Tobi and Bahar [78] made use of the GNM and ANM to analyze such relationship for protein complexes. Zheng and Brooks [79] used a linear combination of low-frequency modes to predict the conformational transition incorporating distance constraints. Petrone and Pande [80] suggested a methodology to identify the number of low-frequency normal modes needed to map the conformational change accurately. Yang et al. [81] thoroughly investigated the efficacy of the ELMs in predicting the transitions through the normal modes, finding that the collectivity of the motion is the fundamental parameter. More recently, Scaramozzino et al. [82] showed that also the low-frequency expansion-contraction modes evaluated by coarse-grained frame-like FE models are found to provide an important contribution to the conformational change. Finally, by taking into account that the large-scale transitions might also contain an important contribution given by the rotation of rigid portions of the protein structure, a new definition of the overlap metric was proposed by Song and Jernigan [41].

The amount of studies shown above confirm that there exists a close correspondence between the low-frequency protein dynamics and its mechanism, as observed by the conformational change. However, although this advocates that the protein flexibility and its dynamical features do play a role in influencing the conformational transition, it is still not clear whether the conformational change is only accommodated through that specific motion as it is energetically favorable (note in fact that low-frequency motions are also usually the low-energy ones), or if the low-frequency dynamics actually is able to trigger the conformational change. This is still an open question for computational biologists. However, it is evident that there exists a high correlation between the experimentally observed protein conformational change and the low-frequency protein motions. Therefore, a thorough investigation of the latter is surely beneficial to try and predict the protein functional modes.

In order to predict the biologically-relevant motions and simulate the protein conformational changes, a novel ELM based on the partition of the protein into rigid domains and flexible regions was recently developed, which has been called the hinge-domain ANM (hdANM) [83]. This model has been used not only for the prediction of the conformational change between two known conformations, but also in order to study the entire conformational ensemble deriving from a set of known experimental structures. For this reason, before describing the framework of the hdANM, few remarks are given on the characteristics of the experimental ensemble and the typical analysis which is carried out to extract the dynamic features from it, which is called Principal Component Analysis (PCA).

2.3.2 Protein normal modes and Principal Component Analysis

As mentioned in Section 2.1, the intrinsic dynamic nature of the protein structure generates a conformational ensemble made up of multiple conformations. PCA can be performed on a set of X-ray experimental structures, as well as on MD communities. It aims at extracting the motions from a set of known structures superimposed onto the reference one. The input is a $n \times 3N$ coordinate matrix $\boldsymbol{X}$, where n is the number of available structures and N is the total number of nodes (atoms or residues). When dealing with coarse-grained models, the rows of $\boldsymbol{X}$ essentially contain the XYZ coordinates of the C^{α} atoms [84]. Based on the coordinate matrix $\boldsymbol{X}$, PCA relies on the calculation of the $3N \times 3N$ covariance matrix $\boldsymbol{\sigma}$, whose elements can be calculated as:

$$\sigma_{i,j} = \langle \big(X_{i,j} - \langle X_i \rangle\big)\big(X_{i,j} - \langle X_j \rangle\big) \rangle, \tag{2.29}$$

where the average $\langle - \rangle$ extends over all the n conformations. Based on the eigenvalue-eigenvector decomposition, the covariance matrix is further decomposed as:

$$\boldsymbol{\sigma} = \boldsymbol{P} \Delta \boldsymbol{P^T}, \tag{2.30}$$

$\boldsymbol{P}$ and Δ being the eigenvector and eigenvalue matrix, respectively. $\boldsymbol{P}$ contains the so-called principal components (PCs), which in this case reflect the virtual motions extracted from the set of experimental structures. Conversely, Δ is the diagonal matrix containing the eigenvalues associated to each PCs, usually sorted in descending order. Each eigenvalue provides an estimate of the total variance captured in the corresponding PC. The PCs, namely the motions extracted from the set of experimental structures, provide the information about the mechanisms of the protein during its biological activity.

Based on sets of experimental structures from both X-ray and NMR experiments, Yang et al. [48] showed that the low-frequency modes calculated from ANM exhibit significant similarities with the first PCs of the experimental ensemble of HIV-1 protease. Therefore, it is concluded that the global vibrations extracted from the ELMs are able to describe the biologically-relevant mechanisms observed in the experimental ensemble. More recently, Sankar et al. [49] showed similar results for a set of 50 proteins, comparing the ANM-based normal modes to the PCs extracted from the experimental ensemble. In the following sub-section, the newly developed hdANM is presented and the corresponding normal modes will be compared to the motions extracted from the experimental structure ensemble with PCA.

2.3.3 A new ELM for the investigation of the protein mechanisms: The hdANM

The idea behind the generation of the hinge-domain ANM (hdANM) is that protein mechanisms often involve the rigid translation and rotation of entire domains and the deformation of local flexible parts that constitute the hinges of the motion. The ANM and the FE-based ELM presented in Section 2.2 model the protein as a network of nodes connected by linear springs. This implies that the

higher rigidity of certain portions of the protein is only the result of the clustering of stronger springs in that area. Conversely, the RTB methodology [37] considers the protein as made up of a sequence of rigid blocks, that translate and rotate around their center of mass (COM). The hdANM is the generalization of both, as it represents the protein as a union of both rigid and flexible parts (Figure 2.16). The former is called a domain, the latter a hinge.

Various methodologies have been developed in the literature to predict domain and hinge regions in experimental protein structures. One of the most recent ones was suggested by Khade et al. [85], that identifies protein hinges based on Delaunay tessellation of the protein surface and generation of alpha shapes. Based on these results, one can have the information about the hinge-domain distribution within the protein structure.

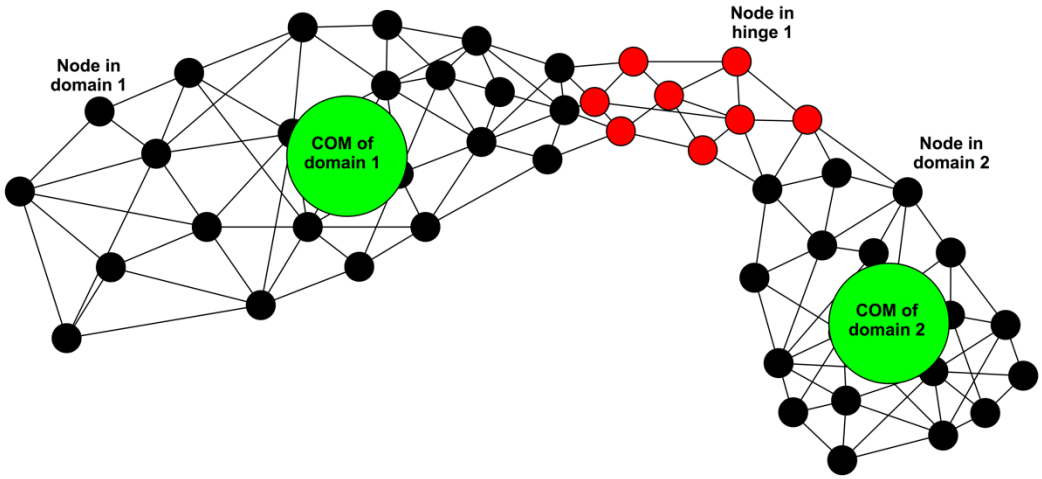

Figure 2.16. Scheme of protein structure according to the hdANM. Black dots represent nodes in rigid domains, red dots represent nodes in flexible hinge regions, green dots represent the COMs of the domains.

The fundamental equations of the hdANM are the ones involving the dynamic equilibrium of an MDOF system. These can be obtained starting from the ANM equations with the addition of the mass of the system and the rigid-body equations applied to the rigid domains. Consider a protein ELM made up of N nodes. The mass-enriched ANM dynamic problem can be formulated in matrix form as follows:

$$(\boldsymbol{H} - \omega_n{}^2 \boldsymbol{M}) \cdot \boldsymbol{\delta_n} = \boldsymbol{0}, \tag{2.31}$$

being $\boldsymbol{H}$ the $3N \times 3N$ Hessian matrix, $\boldsymbol{M}$ the $3N$ x $3N$ mass matrix, ω_n the angular frequency related to the n^{th} eigenmode and $\boldsymbol{\delta_n}$ the $3N \times 1$ vector containing the displacements of the n^{th} mode shape. $\boldsymbol{H}$ is computed according to the ANM methodology once the geometrical cutoff limit is chosen, and $\boldsymbol{M}$ is simply the diagonal matrix containing the masses of the protein atoms/residues.

The equations for the rigid-body motions are then taken into account for the rigid portions of the protein structure, i.e. the rigid domains, that are considered to move as rigid bodies. These equations relate the XYZ displacements of each node to the three translations of the domain's COM and the three rotations of the domain with respect to its COM. Under the assumption of small displacements and rotations, these equations can be written as follows:

$$\delta_{x,i} = \delta_x{}^d - \varphi_z{}^d(y_i - y_d) + \varphi_y{}^d(z_i - z_d), \tag{2.32a}$$

$$\delta_{y,i} = \delta_y{}^d + \varphi_z{}^d(x_i - x_d) - \varphi_x{}^d(z_i - z_d), \tag{2.32b}$$

$$\delta_{z,i} = \delta_z{}^d - \varphi_y{}^d(x_i - x_d) + \varphi_x{}^d(y_i - y_d), \tag{2.32c}$$

being $\delta_{x,i}, \delta_{y,i}, \delta_{z,i}$ the displacements of the i^{th} node within the domain d, x_i, y_i, z_i its coordinates, $\delta_x{}^d, \delta_y{}^d, \delta_z{}^d$ the translations of the domain's COM, $\varphi_x{}^d, \varphi_y{}^d, \varphi_z{}^d$ the rotations of the domain with respect to the COM, and x_d, y_d, z_d the coordinates of the COM.

The $3N \times 3N$ Hessian matrix $\boldsymbol{H}$ corresponds to the stiffness matrix of the protein ELM, therefore it relates the $3N \times 1$ vector of elastic forces $\boldsymbol{F_{el}}$ acting on the structure to the vector of the corresponding nodal displacements $\boldsymbol{\delta_{el}}$. Similarly, the mass matrix $\boldsymbol{M}$ relates the $3N \times 1$ vector of inertia forces $\boldsymbol{F_{in}}$ to the vector of the corresponding nodal accelerations $\ddot{\boldsymbol{\delta}}_{\boldsymbol{in}}$.

By applying the equations of rigid-body motion to the displacements and accelerations of the nodes that belong to the domains, the hdANM Hessian matrix $\widetilde{\boldsymbol{H}}$ and mass matrix $\widetilde{\boldsymbol{M}}$ can be obtained. These matrices are smaller than the ANM ones, as their dimension correspond to $(3n_H + 6D) \times (3n_H + 6D)$, being n_H the total number of nodes in the hinge regions and D the total number of rigid domains. These dimensions arise from the fact that, in the hdANM, the DOFs of the system correspond to three translations for each node of the hinge regions and six DOFs (three translations and three rotations) for each rigid domain. The hdANM Hessian matrix $\widetilde{\boldsymbol{H}}$ relates the $(3n_H + 6D) \times 1$ vector of elastic forces $\widetilde{\boldsymbol{F}}_{\boldsymbol{el}}$ to the vector of the corresponding displacements $\widetilde{\boldsymbol{\delta}}_{\boldsymbol{el}}$. Similarly, the mass matrix $\widetilde{\boldsymbol{M}}$ relates the $(3n_H + 6D) \times 1$ vector of inertia forces $\widetilde{\boldsymbol{F}}_{\boldsymbol{in}}$ to the vector of the corresponding accelerations $\widetilde{\ddot{\boldsymbol{\delta}}_{\boldsymbol{in}}}$.

The dynamic problem of the hdANM can then be reformulated as follows:

$$\left(\widetilde{\boldsymbol{H}} - \widetilde{\omega}_n{}^2 \widetilde{\boldsymbol{M}}\right) \cdot \widetilde{\boldsymbol{\delta}}_{\boldsymbol{n}} = \boldsymbol{0}, \tag{2.33}$$

being $\widetilde{\omega}_n$ and $\widetilde{\boldsymbol{\delta}}_{\boldsymbol{n}}$ the hdANM angular frequency and mode shape, respectively, and $\widetilde{\boldsymbol{H}}$ and $\widetilde{\boldsymbol{M}}$ the hdANM Hessian and mass matrix.

Based on the domain-hinge partition of the hdANM vectors of displacements and accelerations, the hdANM Hessian and mass matrices can be expanded as follows:

$$\widetilde{\boldsymbol{H}} = \begin{bmatrix} \widetilde{\boldsymbol{H}}_{\boldsymbol{DD}} & \widetilde{\boldsymbol{H}}_{\boldsymbol{DH}} \\ \widetilde{\boldsymbol{H}}_{\boldsymbol{HD}} & \widetilde{\boldsymbol{H}}_{\boldsymbol{HH}} \end{bmatrix}, \tag{2.34a}$$

$$\widetilde{\boldsymbol{M}} = \begin{bmatrix} \widetilde{\boldsymbol{M}}_{\boldsymbol{DD}} & \widetilde{\boldsymbol{M}}_{\boldsymbol{DH}} \\ \widetilde{\boldsymbol{M}}_{\boldsymbol{HD}} & \widetilde{\boldsymbol{M}}_{\boldsymbol{HH}} \end{bmatrix}, \tag{2.34b}$$

being $\widetilde{\boldsymbol{H}}_{\boldsymbol{DD}}$ the $6D \times 6D$ matrix relating the forces and torques acting on the domains' COMs to the corresponding translations and rotations, $\widetilde{\boldsymbol{H}}_{\boldsymbol{DH}}$ the $6D \times 3n_H$ matrix relating the forces and torques acting on the domains' COMs to the displacements of the hinge nodes, $\widetilde{\boldsymbol{H}}_{\boldsymbol{HD}}$ the $3n_H \times 6D$ matrix relating the forces

acting on the hinge nodes to the translations and rotations of the domains' COMs, $\widetilde{\boldsymbol{H}}_{\boldsymbol{HH}}$ the $3n_H \times 3n_H$ matrix relating the forces acting on the hinge nodes to the corresponding displacements. The same definitions apply for the component of the mass matrix in Eq. (2.34b), by taking into account inertia forces and torques and the corresponding translational and rotational accelerations.

The $3n_H \times 3n_H$ submatrices $\widetilde{\boldsymbol{H}}_{\boldsymbol{HH}}$ and $\widetilde{\boldsymbol{M}}_{\boldsymbol{HH}}$ are the easiest to compute as they simply constitute a rearrangement of the submatrices contained in the ANM-based $\boldsymbol{H}$ and $\boldsymbol{M}$ matrices. Specifically:

$$\widetilde{\boldsymbol{H}}_{\boldsymbol{HH}} = \begin{bmatrix} \boldsymbol{H}_{\mathbf{1}_H,\mathbf{1}_H} & \dots & \boldsymbol{H}_{\mathbf{1}_H,i_H} & \dots & \boldsymbol{H}_{\mathbf{1}_H,j_H} & \dots & \boldsymbol{H}_{\mathbf{1}_H,n_H} \\ \dots & \dots & \dots & \dots & \dots & \dots & \dots \\ \boldsymbol{H}_{i_H,\mathbf{1}_H} & \dots & \boldsymbol{H}_{i_H,i_H} & \dots & \boldsymbol{H}_{i_H,j_H} & \dots & \boldsymbol{H}_{i_H,n_H} \\ \dots & \dots & \dots & \dots & \dots & \dots & \dots \\ \boldsymbol{H}_{j_H,\mathbf{1}_H} & \dots & \boldsymbol{H}_{j_H,i_H} & \dots & \boldsymbol{H}_{j_H,j_H} & \dots & \boldsymbol{H}_{j_H,n_H} \\ \dots & \dots & \dots & \dots & \dots & \dots & \dots \\ \boldsymbol{H}_{n_H,\mathbf{1}_H} & \dots & \boldsymbol{H}_{n_H,i_H} & \dots & \boldsymbol{H}_{n_H,j_H} & \dots & \boldsymbol{H}_{n_H,n_H} \end{bmatrix}, \tag{2.35a}$$

$$\widetilde{\boldsymbol{M}}_{\boldsymbol{HH}} = \begin{bmatrix} \boldsymbol{M}_{\mathbf{1}_H,\mathbf{1}_H} & \dots & \mathbf{0} & \dots & \mathbf{0} & \dots & \mathbf{0} \\ \dots & \dots & \dots & \dots & \dots & \dots & \dots \\ \mathbf{0} & \dots & \boldsymbol{M}_{i_H,i_H} & \dots & \mathbf{0} & \dots & \mathbf{0} \\ \dots & \dots & \dots & \dots & \dots & \dots & \dots \\ \mathbf{0} & \dots & \mathbf{0} & \dots & \boldsymbol{M}_{j_H,j_H} & \dots & \mathbf{0} \\ \dots & \dots & \dots & \dots & \dots & \dots & \dots \\ \mathbf{0} & \dots & \mathbf{0} & \dots & \mathbf{0} & \dots & \boldsymbol{M}_{n_H,n_H} \end{bmatrix}, \tag{2.35b}$$

being $\boldsymbol{H}_{i_H,j_H}$ the 3×3 submatrix from the ANM Hessian $\boldsymbol{H}$ corresponding to the i^{th} and j^{th} nodes in the hinge region, and $\boldsymbol{M}_{i_H,i_H}$ the 3×3 diagonal submatrix from the mass matrix $\boldsymbol{M}$ corresponding to the i^{th} node in the hinge region. Note that, as a general property of the mass matrices of ELMs, $\widetilde{\boldsymbol{M}}_{\boldsymbol{HH}}$ is diagonal.

The $3n_H \times 6D$ submatrices $\widetilde{\boldsymbol{H}}_{\boldsymbol{HD}}$ and $\widetilde{\boldsymbol{M}}_{\boldsymbol{HD}}$ relate the elastic and inertia forces on the hinge nodes to the DOFs of the rigid domains. Based on the application of Eqs. (2.32) and rearrangement of the Hessian and mass matrix, it can be shown that $\widetilde{\boldsymbol{M}}_{\boldsymbol{HD}}$ is a null matrix, while $\widetilde{\boldsymbol{H}}_{\boldsymbol{HD}}$ can be expanded as follows:

$$\widetilde{\boldsymbol{H}}_{\boldsymbol{HD}} = \begin{bmatrix} \widetilde{\boldsymbol{H}}_{\mathbf{1}_H,\boldsymbol{D}_1} & \dots & \widetilde{\boldsymbol{H}}_{\mathbf{1}_H,\boldsymbol{D}_d} & \dots & \widetilde{\boldsymbol{H}}_{\mathbf{1}_H,\boldsymbol{D}_D} \\ \dots & \dots & \dots & \dots & \dots \\ \widetilde{\boldsymbol{H}}_{i_H,\boldsymbol{D}_1} & \dots & \widetilde{\boldsymbol{H}}_{i_H,\boldsymbol{D}_d} & \dots & \widetilde{\boldsymbol{H}}_{i_H,\boldsymbol{D}_D} \\ \dots & \dots & \dots & \dots & \dots \\ \widetilde{\boldsymbol{H}}_{n_H,\boldsymbol{D}_1} & \dots & \widetilde{\boldsymbol{H}}_{n_H,\boldsymbol{D}_d} & \dots & \widetilde{\boldsymbol{H}}_{n_H,\boldsymbol{D}_D} \end{bmatrix}, \tag{2.36}$$

being $\widetilde{\boldsymbol{H}}_{i_H,\boldsymbol{D}_d}$ the 3×6 submatrix relating the three elastic forces acting on the i^{th} node of the hinge region to the three translations and three rotations of the d^{th} rigid domain. This submatrix depends on the elastic connections involving the hinge node i and all the nodes j belonging to the d^{th} domain [83]. Once the $\widetilde{\boldsymbol{H}}_{\boldsymbol{HD}}$ matrix is computed, $\widetilde{\boldsymbol{H}}_{\boldsymbol{DH}}$ can be simply evaluated as the transpose of $\widetilde{\boldsymbol{H}}_{\boldsymbol{HD}}$ due to the symmetry of the global stiffness matrix. Similarly, $\widetilde{\boldsymbol{M}}_{\boldsymbol{DH}}$ being the transpose of $\widetilde{\boldsymbol{M}}_{\boldsymbol{HD}}$, it is a null matrix as well.

Finally, the $6D \times 6D$ submatrices $\widetilde{\boldsymbol{H}}_{\boldsymbol{DD}}$ and $\widetilde{\boldsymbol{M}}_{\boldsymbol{DD}}$ relate the elastic and inertia forces and torques on the domains' COMs to the corresponding DOFs. Based on the partitioning used above, these matrices can be expanded as follows:

$$\widetilde{\boldsymbol{H}}_{\boldsymbol{DD}} = \begin{bmatrix} \widetilde{\boldsymbol{H}}_{\boldsymbol{D_1,D_1}} & \dots & \widetilde{\boldsymbol{H}}_{\boldsymbol{D_1,D_d}} & \dots & \widetilde{\boldsymbol{H}}_{\boldsymbol{D_1,D_e}} & \dots & \widetilde{\boldsymbol{H}}_{\boldsymbol{D_1,D_D}} \\ \dots & \dots & \dots & \dots & \dots & \dots & \dots \\ \widetilde{\boldsymbol{H}}_{\boldsymbol{D_d,D_1}} & \dots & \widetilde{\boldsymbol{H}}_{\boldsymbol{D_d,D_d}} & \dots & \widetilde{\boldsymbol{H}}_{\boldsymbol{D_d,D_e}} & \dots & \widetilde{\boldsymbol{H}}_{\boldsymbol{D_d,D_D}} \\ \dots & \dots & \dots & \dots & \dots & \dots & \dots \\ \widetilde{\boldsymbol{H}}_{\boldsymbol{D_e,D_1}} & \dots & \widetilde{\boldsymbol{H}}_{\boldsymbol{D_e,D_d}} & \dots & \widetilde{\boldsymbol{H}}_{\boldsymbol{D_e,D_e}} & \dots & \widetilde{\boldsymbol{H}}_{\boldsymbol{D_e,D_D}} \\ \dots & \dots & \dots & \dots & \dots & \dots & \dots \\ \widetilde{\boldsymbol{H}}_{\boldsymbol{D_D,D_1}} & \dots & \widetilde{\boldsymbol{H}}_{\boldsymbol{D_D,D_d}} & \dots & \widetilde{\boldsymbol{H}}_{\boldsymbol{D_D,D_e}} & \dots & \widetilde{\boldsymbol{H}}_{\boldsymbol{D_D,D_D}} \end{bmatrix}, \tag{2.37a}$$

$$\widetilde{\boldsymbol{M}}_{\boldsymbol{DD}} = \begin{bmatrix} \widetilde{\boldsymbol{M}}_{\boldsymbol{D_1,D_1}} & \dots & \boldsymbol{0} & \dots & \boldsymbol{0} & \dots & \boldsymbol{0} \\ \dots & \dots & \dots & \dots & \dots & \dots & \dots \\ \boldsymbol{0} & \dots & \widetilde{\boldsymbol{M}}_{\boldsymbol{D_d,D_d}} & \dots & \boldsymbol{0} & \dots & \boldsymbol{0} \\ \dots & \dots & \dots & \dots & \dots & \dots & \dots \\ \boldsymbol{0} & \dots & \boldsymbol{0} & \dots & \widetilde{\boldsymbol{M}}_{\boldsymbol{D_e,D_e}} & \dots & \boldsymbol{0} \\ \dots & \dots & \dots & \dots & \dots & \dots & \dots \\ \boldsymbol{0} & \dots & \boldsymbol{0} & \dots & \boldsymbol{0} & \dots & \widetilde{\boldsymbol{M}}_{\boldsymbol{D_D,D_D}} \end{bmatrix}, \tag{2.37b}$$

where $\widetilde{\boldsymbol{H}}_{\boldsymbol{D_d,D_e}}$ represents the 6×6 Hessian matrix that relates the elastic forces and torques acting on the COM of domain d to the translations and rotations of the COM of domain e, while $\widetilde{\boldsymbol{M}}_{\boldsymbol{D_d,D_d}}$ represents the 6×6 mass matrix that relates the inertia forces and torques acting on the COM of domain d to the corresponding translational and rotational accelerations. Note that $\widetilde{\boldsymbol{M}}_{\boldsymbol{DD}}$ is a diagonal matrix. The generic blocks $\widetilde{\boldsymbol{H}}_{\boldsymbol{D_d,D_e}}$ and $\widetilde{\boldsymbol{M}}_{\boldsymbol{D_d,D_d}}$ can be further expanded by separating the contributions of the translational and rotational DOFs as follows:

$$\widetilde{\boldsymbol{H}}_{\boldsymbol{D_d,D_e}} = \begin{bmatrix} \widetilde{\boldsymbol{H}}^{\boldsymbol{F\delta}}_{\boldsymbol{D_d,D_e}} & \widetilde{\boldsymbol{H}}^{\boldsymbol{F\varphi}}_{\boldsymbol{D_d,D_e}} \\ \widetilde{\boldsymbol{H}}^{\boldsymbol{T\delta}}_{\boldsymbol{D_d,D_e}} & \widetilde{\boldsymbol{H}}^{\boldsymbol{T\varphi}}_{\boldsymbol{D_d,D_e}} \end{bmatrix}, \tag{2.38a}$$

$$\widetilde{\boldsymbol{M}}_{\boldsymbol{D_d,D_d}} = \begin{bmatrix} \widetilde{\boldsymbol{M}}^{\boldsymbol{F\ddot{\delta}}}_{\boldsymbol{D_d,D_d}} & \boldsymbol{0} \\ \boldsymbol{0} & \widetilde{\boldsymbol{M}}^{\boldsymbol{T\ddot{\varphi}}}_{\boldsymbol{D_d,D_d}} \end{bmatrix}, \tag{2.38b}$$

being $\widetilde{\boldsymbol{H}}^{\boldsymbol{F\delta}}_{\boldsymbol{D_d,D_e}}$ the 3×3 stiffness matrix relating the forces acting on the COM of domain d to the translations of domain e, $\widetilde{\boldsymbol{H}}^{\boldsymbol{F\varphi}}_{\boldsymbol{D_d,D_e}}$ the 3×3 stiffness matrix relating the forces acting on the COM of domain d to the rotations of domain e, $\widetilde{\boldsymbol{H}}^{\boldsymbol{T\delta}}_{\boldsymbol{D_d,D_e}}$ the 3×3 stiffness matrix relating the torques acting on the COM of domain d to the translations of domain e, $\widetilde{\boldsymbol{H}}^{\boldsymbol{T\varphi}}_{\boldsymbol{D_d,D_e}}$ the 3×3 stiffness matrix relating the torques acting on the COM of domain d to the rotations of domain e, $\widetilde{\boldsymbol{M}}^{\boldsymbol{F\ddot{\delta}}}_{\boldsymbol{D_d,D_d}}$ the 3×3 mass matrix relating the inertia forces acting on the COM of domain d to the corresponding translations, and $\widetilde{\boldsymbol{M}}^{\boldsymbol{T\ddot{\varphi}}}_{\boldsymbol{D_d,D_d}}$ the 3×3 mass matrix relating the inertia torques acting on the COM of domain d to the corresponding rotations. Note that, again, the matrix $\widetilde{\boldsymbol{M}}_{\boldsymbol{D_d,D_d}}$ is diagonal. These six matrices are derived by starting from the ANM Hessian and mass matrix, by applying the equations of rigid-body

motion and by calculating the total elastic and inertia forces and torques in the COM of domain d [83].

Once the complete hdANM Hessian and mass matrix are obtained as reported above, the eigenvalue-eigenvector problem in Eq. (2.33) can be solved to obtain the hdANM vibrational frequencies and mode shapes. Note that the hdANM eigenvectors reported in Eq. (2.33) have dimension $(3n_H + 6D) \times 1$, as they contain the three modal displacements of the hinge nodes and the six DOFs per domain. By applying once again the equations of rigid-body motion from Eqs. (2.32) for each domain, one easily obtains the modal displacements of all the protein residues. Finally, the modal displacements obtained from the hdANM can be directly compared to the protein conformational changes and PCs from the ensemble of known crystal structures, to verify whether this new method can indeed capture the protein biological mechanism.

The first example that has been investigated refers to the LAO-binding protein, whose conformational change and its relationship with ANM normal modes have already been discussed in Section 2.3.1. In Table 2.1, the sixteen crystal structures that have been used to calculate the PCs of LAO-binding protein are shown. Based on the application of Eqs. (2.29) and (2.30), the results of PCA are shown in Figure 2.17, where PC1 is plotted against PC2. Note that PC1 captures 98.1% of the variance, and PC2 the 1.2%. From Figure 2.17, it can also be noted that the PC1 direction generates two main clusters of the protein structures: the tight cluster on the left of the PC map is mainly associated with closed forms of the protein, whereas the loose cluster on the right is associated with the open forms. For this reason, PC1 mainly corresponds to the LAO-binding protein conformational change between the open and closed conformations.

Table 2.1. Crystal structures of LAO-binding protein from the PDB.

2LAO (reference)	1LST	6MLA	6MLI
1LAF	6MKU	6MLD	6MLO
1LAG	6MKX	6MLE	6MLP
1LAH	6ML0	6MLG	6MLV

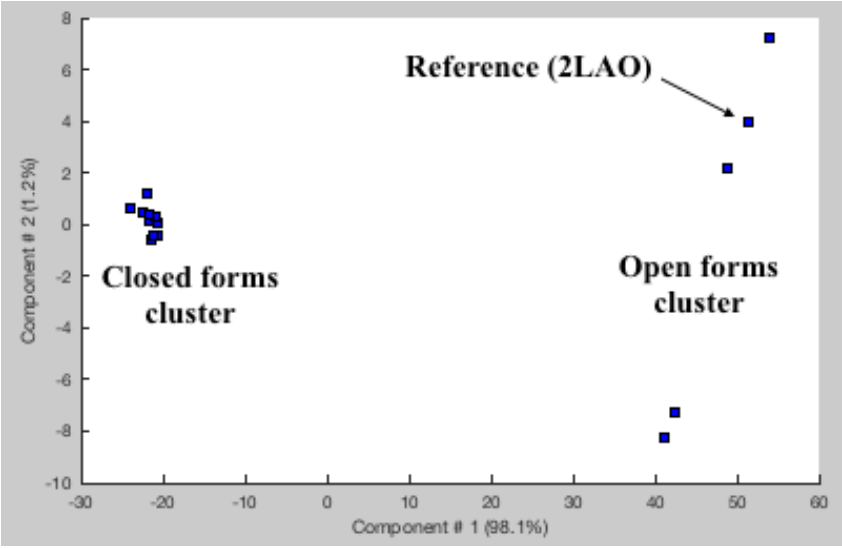

Figure 2.17. PC plot of the sixteen crystal structures of LAO-binding protein (PC1 vs. PC2).

By comparing the hdANM modes of the reference structure (PDB: 2lao), obtained by using the hinge prediction method from Khade et al. [85] and a geometrical cutoff of 8 Å, to the obtained PCs from the structure ensemble by means of the overlap metric from Eq. (2.28), one obtains an overlap of 0.65 between the first mode and PC1. Figure 2.18 reports the normalized displacements of PC1 against the first hdANM mode, showing a fairly good agreement. Note that the correlation found with the hdANM is lower than the one found with the standard ANM (Figure 2.15). However, with ANM the high correlation is found with the second lowest mode, whereas with the hdANM the fundamental vibrational mode is the one most associated with the biological mechanism.

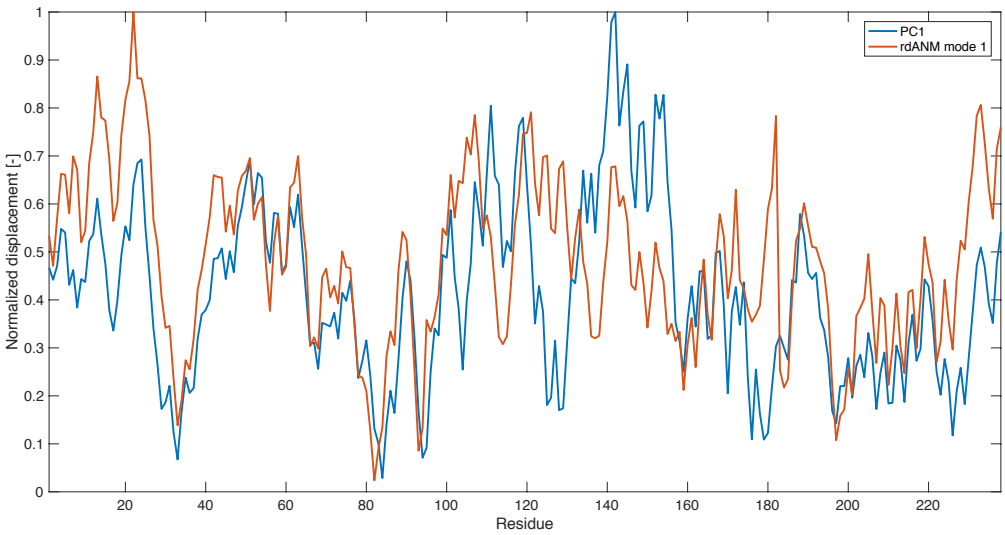

Figure 2.18. PC1 vs. the first hdANM mode of LAO-binding protein.

The second example refers to the subunit of the GroEL large macromolecular complex [86]. The subunit is made up of 524 residues, and the fourteen crystal structures used for the PCA are shown in Table 2.2. The results of PCA are reported in Figure 2.19, where PC1 is plotted against PC2. In this case, PC1 captures 99.3% of the variance, and PC2 0.2%. Similarly to the previous case related to LAO-binding protein, from Figure 2.19 it can be noted that the PC1 direction generates two main clusters of the protein structures: the tight cluster on the left is associated with the open forms of the subunit, whereas the loose cluster on the right is associated with the closed forms. For this reason, PC1 mainly corresponds to the GroEL subunit conformational change between the open and closed conformations.

Table 2.2. Crystal structures of GroEL subunit from the PDB (chains A).

1AON (reference)	1PCQ	1SVT	2NWC
1OEL	1PF9	1SX4	3E76
1KP8	1J4Z	1XCK	
1MNF	1SS8	2EU1	

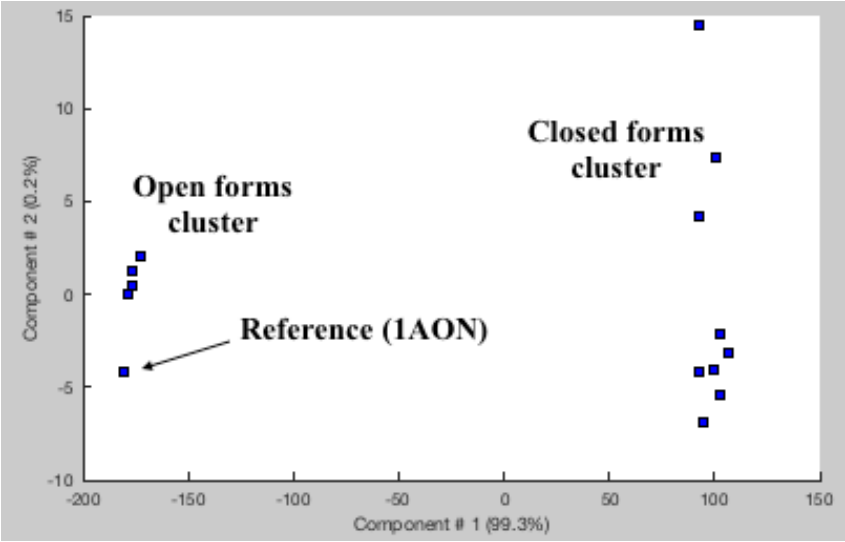

Figure 2.19. PC plot of the fourteen crystal structures of GroEL subunit (PC1 vs. PC2).

By comparing the hdANM modes of the refence structure (PDB: 1aon), obtained by using a geometrical cutoff of 15 Å, to the obtained PCs from the structure ensemble, one obtains an overlap of 0.73 between the first mode and PC1. Figure 2.20 reports the normalized displacements of PC1 against the first hdANM mode, showing again a clear agreement.

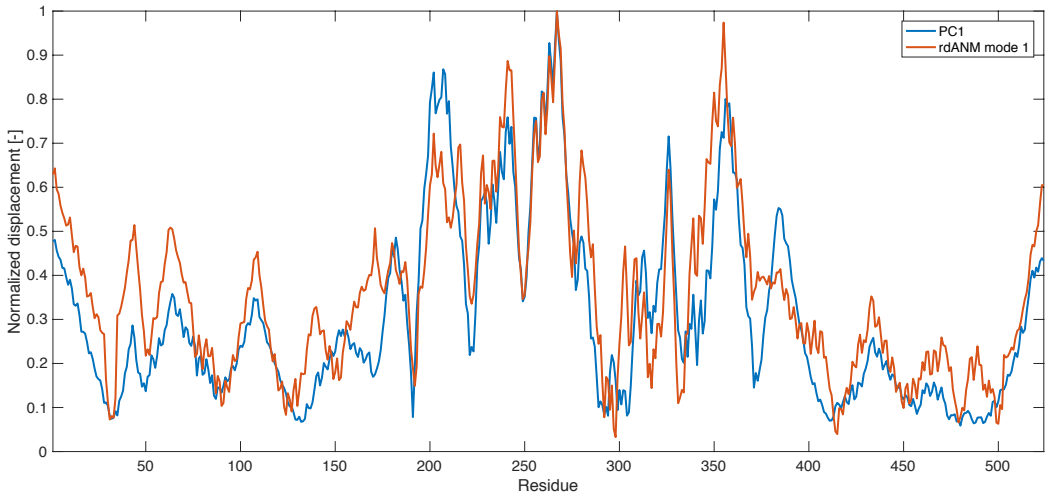

Figure 2.20. PC1 vs. the first hdANM mode of GroEL subunit.

The results shown above regarding the application of the hdANM to the LAO-binding protein and GroEL subunit show that this new model is indeed able to identify correctly the biological mechanism of these proteins. Moreover, being grounded on the coarse-graining of entire domains into their COM, it turns out to be much more computationally effective than traditional models, such as ANM. As a matter of fact, by considering only six DOFs per rigid domain, the whole dimension of the hdANM stiffness and mass matrices is much lower than the ANM ones. In turn, their diagonalization can take place with much less amount of time, allowing to carry out fast analyses even for large macromolecular assemblies.

Nevertheless, this method still has some limitations. Firstly, it derives from the ANM, thus it contains only the information about the three-dimensional shape

and connectivity of the protein structure. Although coarse-grained models based only on protein topology (GNM, ANM, RTB, etc.) have been shown to be powerful in describing protein fluctuations and conformational transitions, their inherent simplicity might prevent the successful application to those proteins where the chemo-physical properties of certain amino acids in specific regions play a key role in defining the protein dynamics. Secondly, being based on the diagonalization of matrices and modal analysis, it allows the computation of the linear normal modes, that identify the small-amplitude protein vibrations. In some cases, these modes might fail to describe the large-scale conformational transitions that are involved in the biological mechanism.

Although the first aspect is common to all the ELMs and constitutes their fundamental feature, the second issue could be overcome by extrapolating the linear normal modes, which are related to the small-amplitude protein vibrations, to obtain large-scale curvilinear transition pathways. This strategy has been recently adopted by Hoffmann and Grudinin [38] and might generate much more realistic motions, rather than simply re-scaling the small-amplitude normal modes for larger scales, which can induce unrealistic distortions within the domains. The hdANM is certainly suitable for that, since the rotational component of the domain motion can be easily extrapolated to generate large-scale curvilinear pathways of the conformational transition. This aspect will be treated in further contributions and it is believed to become a powerful yet simple tool for the evaluation of protein biological mechanisms.

2.4 Conclusions

In this Chapter, the subject of protein dynamics and biological mechanisms has been addressed through a pure Structural Mechanics approach. Specifically, after a brief overview of the protein structure presented at the beginning of the Chapter, together with the discussion of protein folding and the sequence-structure-dynamics-function paradigm, the use of the Elastic Lattice Models (ELMs) for the investigation of protein dynamics has been discussed.

Based on the seminal work of Tirion's [29] and the subsequent development of the first Elastic Network Models (ENMs), such as the Gaussian Network Model (GNM) [30] and the Anisotropic Network Model (ANM) [31], the Structural Mechanics foundation of the ELMs for the analysis of protein vibrations has been thoroughly addressed. To the purpose, a FE-based ELM has been presented which is the counterpart of the ANM by following a pure Structural Mechanics approach, focuses on the low-frequency protein dynamics and is easily accessible to the engineering community. Despite the simplified nature of these models, they are shown to provide good estimate of the protein flexibility, by comparison with the experimental B-factors.

Furthermore, the ELMs have been shown to be effective to investigate and predict the protein conformational changes, which are involved into the protein biological mechanisms. As a matter of fact, traditional ELMs, such as the ANM, allow to obtain a good prediction of the protein conformational transition through the computation of the low-frequency normal modes. Moreover, the ELM modes are also found to match fairly accurately with the Principal Components (PCs) arising from the Principal Component Analysis (PCA) on a set of known crystal structures.

Consequently, a new ELM has been recently developed and presented at the end of this Chapter. It has been called the hinge-domain ANM (hdANM), since it

is based on a further coarse-graining of the protein ELM, which treats hinge regions as flexible and rigid domains as rigid bodies that translate and rotate around their center of mass (COM). This new model has been applied to extract the low-frequency motions of the protein structure, which in turn have been compared to the conformational changes and the PCs arising from sets of known crystal structures. From the analysis regarding LAO-binding protein and GroEL subunit, the hdANM is shown to provide good matches between the low-frequency motions and the lowest PCs, thus confirming that it can predict fairly accurately the protein biological mechanisms.

The results presented in this Chapter are very interesting as they suggest that even very complex entities, such as proteins, can be successfully modeled – and their behavior can be accurately analyzed – by means of simplified structural models, such as the ELMs. Despite being extremely complicated, protein dynamics and behavior can thus be analyzed by models that exploit purely Structural Mechanics concepts, without tackling the problem by using very byzantine approaches that include complex chemo-physical formulations. Obviously, this does not mean that complex models are not useful. For example, thinking about Molecular Dynamics (MD) simulations, it is clear that these are very sophisticated models where the Newton's laws of motion are solved at the atomic scale, with the use of complex energetical potentials that require the knowledge of the chemo-physical interaction among all the atoms. Of course, MD simulations can reveal crucial information about the behavior of complex systems. However, their complexity can sometimes prevent the success of the analysis or the reliability of the results. Conversely, simplified yet powerful models, such as the ELMs, can shed light on the overall behavior of the system and can make the analysis and results interpretation much easier and accessible to the scientific community.

Chapter 3

ELMs and Proteins: Force Application Patterns and Geometrical Non-Linearities

In the previous Chapter, it has been shown that protein flexibility and mechanisms can be predicted by using simplified ELMs coupled with the Structural Mechanics concept of modal analysis. Low-frequency modes are often related to the conformational changes and their fluctuations are frequently in agreement with the experimental B-factors, which in turn are the experimental fingerprints of protein flexibility. Besides, in the last decades, some other works exploited the potential of the protein ELMs through the concept of force application.

In the first Section of this Chapter, the novel results arising from novel force application patterns on the protein ELMs are reported, which are found to provide useful insight into protein flexibility. Then, in Section 3.2, the geometrical non-linear analysis is also applied to the protein ELM, which is meant to investigate the possible role of geometrical non-linearities in the definition and characterization of the conformational change pathway.

3.1 Force Application on Protein ELMs

The fundamental assumption for the development of the first force application methodologies on protein ELMs relies on the linear response theory, that assumes that the protein structural change upon ligand-binding can be predicted by means of a linear deformation process [87]. Note that the concept of linearity has already been exploited in all the analyses reported above dealing with the use of modal analysis, since this aims at evaluating the mode shapes under the assumption of small displacements and linear elastic behavior.

Based on the linear approach, Atilgan and Atilgan [88] developed a force application methodology called the Perturbation-Response Scanning (PRS). The PRS relies on the sequential application of directional forces (perturbations) on single residues and record the resulting changes in the protein configuration. The

PRS starts from the fundamental equilibrium equation that relates the vector of forces acting on the structure $\boldsymbol{F}$ to the corresponding displacements $\boldsymbol{\delta}$ through the Hessian matrix $\boldsymbol{H}$:

$$\boldsymbol{F} = \boldsymbol{H}\boldsymbol{\delta}. \tag{3.1}$$

By calculating the pseudo-inverse of the Hessian matrix, e.g. from Eq. (2.13), one can obtain the displacements of the nodes for any given applied forces:

$$\boldsymbol{\delta} = \widetilde{\boldsymbol{H}}^{-1}\boldsymbol{F}. \tag{3.2}$$

The PRS sequentially applies point forces, randomly oriented in the three-dimensional space, at single residues and compute the corresponding displacements of the protein structure. Applying this methodology to the bacterial ferric binding protein (FBT), the researchers found that the residue-by-residue displacements between the open and closed forms are faithfully reproduced by perturbations applied on the majority of residues [88]. Subsequently, the PRS was applied to study a set of 25 proteins and it was found that, in most cases, there are single key residues that can be manipulated to accurately describe the whole conformational change. Conversely, in other cases, the transitions are achieved by perturbating several residues scattered throughout the protein chain [89]. The method was also successfully applied to investigate the allosteric mechanism of PDZ domains [90] and, more recently, to predict the closed-to-open transition of the GroEL subunit originating from ATP hydrolysis [86].

Another methodology based on force application and the linear response theory was developed by Eyal and Bahar [91]. The work aims at evaluating the anisotropic mechanical behavior of the protein elastic network in order to understand the response of proteins to external applied forces. This behavior can be experimentally analyzed through single-molecule manipulation techniques, such as Optical Tweezers (OT) and Atomic Force Microscopy (AFM). The force application methodology proposed by the authors relies on the calculation of the quantity $\langle \kappa_{ij} \rangle$, called effective spring constant or mechanical resistance, that quantifies the resistance of the protein network against pulling forces applied on residues i and j. The mathematical framework for the calculation of $\langle \kappa_{ij} \rangle$ is based on the normal modes extracted from the ANM Hessian and it was found that, despite the simplicity of the model, the results are able to capture the anisotropic mechanical response observed in single-molecule pulling experiments [91].

Based on the works described above, two methodologies based on force application patterns on the protein ELM have been proposed and will be shown in the remaining of this Section. The first is based on the pairwise pulling pattern shown by Eyal and Bahar [91], but aimed at defining two new metrics, called the structural compliance and structural stiffness, that are found to provide a faithful estimate of the protein flexibility upon comparison with the experimental B-factors (see Section 3.1.1). The second approach is a further generalization of the previous method, as it relies on random forces applied on several surface residues or the entire protein structure, and it is shown to provide a good agreement with the protein flexibility extracted from the experimental B-factors (see Section 3.1.2).

3.1.1 Pairwise force application: Structural compliance and stiffness as new metrics of protein flexibility

The Structural Mechanics approach of force application on the protein ELM has been recently applied by Scaramozzino et al. [92] for the definition of new structural metrics that provide information about protein flexibility. The procedure is based on pairwise force application, i.e. a couple of equal and opposite forces are applied to each couplet of residues, as shown in Figure 3.1.

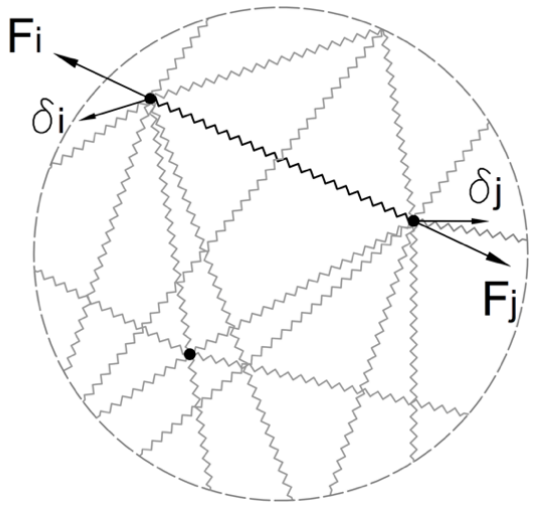

Figure 3.1. Scheme for the pairwise force application. The figure shows a zoomed picture of the protein ELM, made up of nodes and connecting springs. For each couplet of residues *i* and *j*, two force vectors $\boldsymbol{F_i}$ and $\boldsymbol{F_j}$ are applied along the *i-j* direction to pull the residues apart probing the directional deformability. Adapted with permission from [92].

The forces are assumed to have unit magnitude and act along the *i-j* direction for each couplet of residues *i* and *j*. Based on the XYZ coordinates of these nodes, the 3 × 1 force vectors $\boldsymbol{F_i}$ and $\boldsymbol{F_j}$ can be formulated as follows:

$$\boldsymbol{F_i} = -\frac{\boldsymbol{R_{i,j}}}{\left|\boldsymbol{R_{i,j}}\right|}, \tag{3.3a}$$

$$\boldsymbol{F_j} = \frac{\boldsymbol{R_{i,j}}}{\left|\boldsymbol{R_{i,j}}\right|}, \tag{3.3b}$$

being $\boldsymbol{R_{i,j}} = \{x_j - x_i, y_j - y_i, z_j - z_i\}^{\boldsymbol{T}}$ the vector connecting residue *i* to residue *j* and $\left|\boldsymbol{R_{i,j}}\right| = \sqrt{(x_j - x_i)^2 + (y_j - y_i)^2 + (z_j - z_i)^2}$ their initial distance. The force vectors $\boldsymbol{F_i}$ and $\boldsymbol{F_j}$ are then inserted into the $3N \times 1$ global force vector $\boldsymbol{F}$ in Eq. (3.1). Based on the pairwise force application pattern, it follows that the vector $\boldsymbol{F}$ has only six non-zero components, as calculated from Eqs. (3.3). Once the Hessian matrix of the protein ELM is evaluated according to the ANM or the FE-based methodology, its pseudo-inverse is calculated from Eq. (2.13). Equation (3.2) is then applied to obtain the structure displacements $\boldsymbol{\delta}$ due to the pairwise force application.

Based on the obtained displacements, two new structural metrics are then introduced to describe the deformability of the protein structure along the *i-j* direction, which have been called the structural compliance and the structural stiffness. Both are classical measures of the deformability and rigidity of civil and mechanical systems, but they are applied for the first time to the case of proteins by Scaramozzino et al. [92]. The former is defined as the total displacement along the force direction divided by the absolute magnitude of the applied force, while the latter can be simply evaluated as the inverse of compliance. Based on this definition, for the case under investigation one obtains the values of the pairwise compliance $C_{i,j}$ and stiffness $S_{i,j}$ related to nodes *i* and *j*:

$$C_{i,j} = \frac{\left(\boldsymbol{\delta_j} - \boldsymbol{\delta_i}\right)^T \boldsymbol{F_j}}{|\boldsymbol{F_j}|} = \frac{(\boldsymbol{\delta_j} - \boldsymbol{\delta_i})^T \boldsymbol{R_{i,j}}}{\sqrt{(x_j - x_i)^2 + (y_j - y_i)^2 + (z_j - z_i)^2}}, \tag{3.4a}$$

$$S_{i,j} = \frac{1}{C_{i,j}} = \frac{\sqrt{(x_j - x_i)^2 + (y_j - y_i)^2 + (z_j - z_i)^2}}{(\boldsymbol{\delta_j} - \boldsymbol{\delta_i})^T \boldsymbol{R_{i,j}}}. \tag{3.4b}$$

Applying the pairwise force application pattern for each couplet of residues *i* and *j*, one obtains the complete description of the distribution of these structural metrics throughout the protein structure. For each residue *i*, a unique value of compliance C_i and stiffness S_i can then be defined as the average across all the *i-j* interactions, namely:

$$C_i = \frac{1}{N-1} \sum_{j=1, j \neq i}^{N} C_{i,j}, \tag{3.5a}$$

$$S_i = \frac{1}{N-1} \sum_{j=1, j \neq i}^{N} S_{i,j}. \tag{3.5b}$$

The average procedure reported in Eqs. (3.5) is not the only possible to achieve a single value that provides information about the flexibility of the protein structure in the i^{th} node, but it seems the most reasonable one. Of course, other average procedures are possible, that take into account the effective position of the i^{th} residue within the protein structure or its chemical species.

Remarkably, the compliance and stiffness distributions along the protein chain are found to exhibit a very good correlation with the experimental B-factors. In Figure 3.2, this comparison is shown for the case of HEW lysozyme (PDB: 4ym8), modeled through the pfANM [32] by using a value of p equal to 3 from Eq. (2.15). Figure 3.2a shows the comparison of the experimental B-factors against the computed fluctuations obtained from the normal modes as from Eq. (2.14), leading to a Pearson correlation coefficient of 0.73. Instead, Figure 3.2b shows the comparison of the experimental B-factors against the compliance and stiffness distributions from Eqs. (3.5) that lead to correlation coefficients of 0.70 and –0.69. As can be seen, despite the simplicity of the model and of the methodology for the derivation of these structural metrics, the results show a good agreement with the experimental data. This confirms that the proposed structural metrics are indeed able to describe fairly accurately the protein flexibility, as extracted from the crystallographic B-factors.

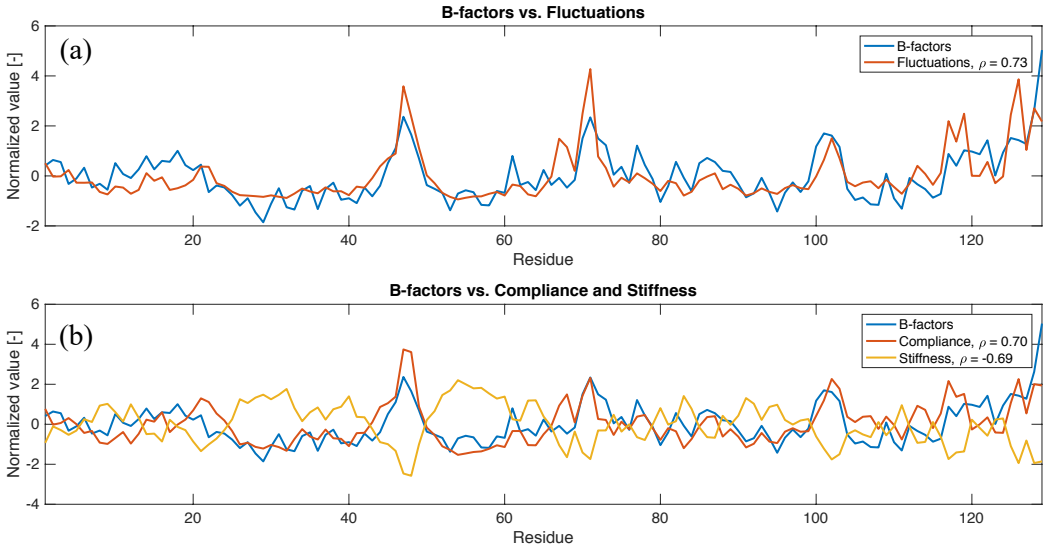

Figure 3.2. HEW lysozyme (PDB: 4ym8), modeled with pfANM (p = 3): (a) experimental B-factors vs. fluctuations computed from normal modes; (b) experimental B-factors vs. compliance and stiffness distribution computed from the pairwise force application pattern.

As can be seen from Figure 3.2, the compliance profile shows a positive correlation with the B-factors distribution, meaning that peaks in the B-factors profile, i.e. peaks of protein flexibility, correspond to higher values in the compliance distribution. Conversely, the stiffness distribution exhibits a negative correlation with the B-factors, so that regions with greater B-factors tend to have lower stiffness values.

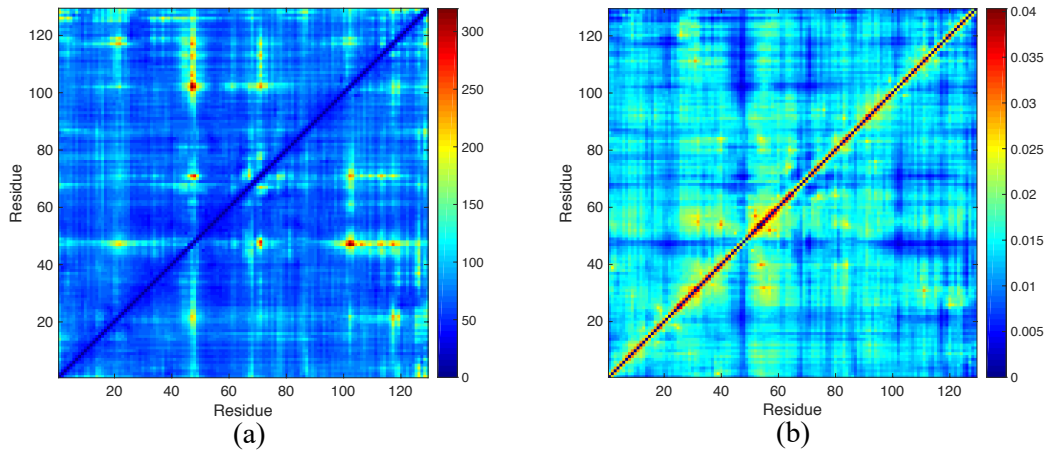

Figure 3.3. HEW lysozyme (PDB: 4ym8), modeled with pfANM (p = 3): (a) compliance map; (b) stiffness map.

Besides the evaluation of the linear distributions, the approach presented here based on the pairwise force application also allows the derivation of residue-residue interaction information, through the evaluation of the pairwise compliance and stiffness values, i.e. $C_{i,j}$ and $S_{i,j}$. These values can be plotted in map representations, as reported in Figure 3.3 for the case of HEW lysozyme analyzed above. Figure 3.3a shows the map of compliance values from Eq. (3.4a), while Figure 3.3b plots the stiffness values from Eq. (3.4b). These maps are useful to investigate the anisotropic distribution of the protein flexibility-rigidity based on

the internal residue-residue interactions. High values of compliance and low values of stiffness mean high flexibility in the considered direction, whereas low compliance and high stiffness values denote high rigidity in that direction. Similarly to the maps of mechanical resistance obtained from Eyal and Bahar [91], the ones reported here can be used as well to predict the anisotropic response of proteins against external pulling forces.

The analysis shown above for HEW lysozyme has been run for several protein structures, modeled by means of the pfANM using a value of p equal to 3, which is found to provide the best results. High-resolution structures have been considered from the PDB [14], and divided into two datasets. Dataset 1 contains single-chain proteins, while dataset 2 contains proteins with more than one polypeptide chain. The characteristics of the datasets used for the analysis are shown in Table 3.1. The former contains 921 single-chain protein structures, whereas the latter 149 multi-chain proteins. More details can be found in [92].

Table 3.1. Datasets characteristics. Used with permission from [92].

Dataset	**1**	**2**
Number of chains [-]	Single (1)	Multiple (2-10)
Resolution [Å]	0.0 – 1.3	0.0 – 1.1
Sequence identity [%]	30	50
Number of structures [-]	921	149
Protein size (number of residues) [min – max]	101 – 1174	104 – 2484

For each protein structure, the experimental B-factors available in the PDB record are compared to the fluctuations calculated from the pfANM normal modes from Eq. (2.14), and to the compliance and stiffness profiles defined above. The Pearson correlation coefficients are computed for each comparison and the results are shown in Figure 3.4 and 3.5 for dataset 1 and 2, respectively.

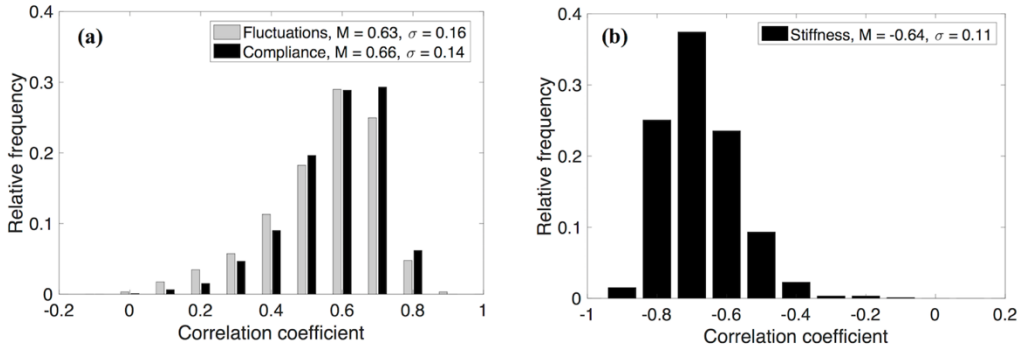

Figure 3.4. Comparison of the fluctuation, compliance and stiffness correlations with the experimental B-factors for dataset 1. (a) Distribution of the correlation coefficients for fluctuations (grey histogram) and compliance (black histogram). (b) Distribution of the correlation coefficients for stiffness. Median values (M) and standard deviations (σ) are reported in the keys. Used with permission from [92].

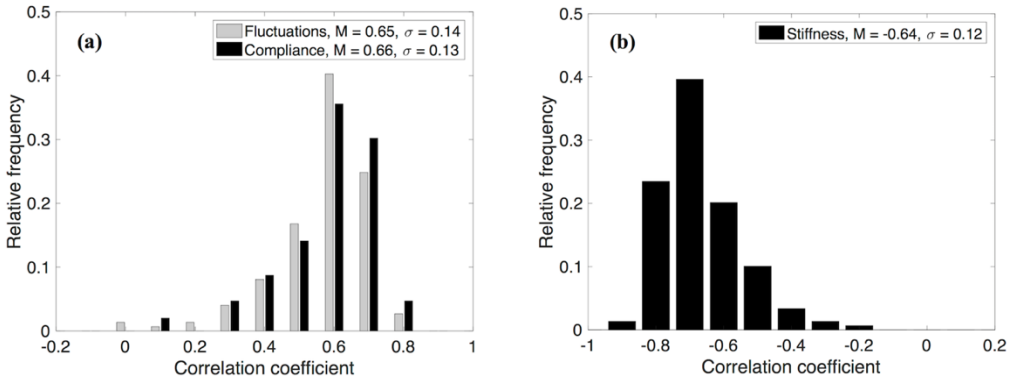

Figure 3.5. Comparison of the fluctuation, compliance and stiffness correlations with the experimental B-factors for dataset 2. (a) Distribution of the correlation coefficients for fluctuations (grey histogram) and compliance (black histogram). (b) Distribution of the correlation coefficients for stiffness. Median values (M) and standard deviations (σ) are reported in the keys. Used with permission from [92].

As can be seen from Figures 3.4a and 3.5a, the statistical distributions of the Pearson correlation coefficients resembles a log-normal distribution centered around 0.65. Also, for both dataset 1 and 2, the distributions of the correlation coefficients of the compliance metric are similar to the ones of the traditional fluctuations. This means that compliance based on pairwise force application is indeed a valid metric for the prediction of the experimental B-factors. Similarly, from Figures 3.4b and 3.5b, it is found that the statistical distribution of the correlation coefficients obtained by comparing the B-factors against stiffness values resembles a log-normal distribution centered around –0.65, confirming that the stiffness profile generally shows a good anti-correlation with the experimental B-factors.

From the analysis performed on the extensive dataset shown in Table 3.1, it is also found that, in most cases, compliance and stiffness profiles outperform the traditional fluctuations in the correlation with experimental data. For example, in Figure 3.6, the case of the single-chain Human Complement Protein C8γ (PDB: 1lf7) is shown, whereas Figure 3.7 reports the results from the multi-chain dimeric *Clitocybe nebularis* ricin B-like lectin (PDB: 3nbc).

Figures 3.6a and 3.7a report the comparison between the B-factors and fluctuations, Figures 3.6b and 3.7b show the comparison with the compliance and stiffness metrics, while Figures 3.6c and 3.7c map the compliance, experimental B-factors and fluctuations onto the tertiary structure of the protein. As can be seen, in the first case, compliance and stiffness profiles show a correlation with the experimental data 15% higher than the one found with the usual fluctuations. In the second case, the improvement of the correlation is around 5–7%. In both cases, the compliance profile closely align to the experimental data, whereas the stiffness distribution is someway mirrored with respect to the experimental B-factors.

However, it must be also said that in some cases the compliance and stiffness metrics provide lower correlation coefficients than the ones obtained from the traditional fluctuations. However, as demonstrated from Figures 3.4–3.7, they can certainly be used as a novel valid metric to predict the experimental B-factors and then measure the protein flexibility.

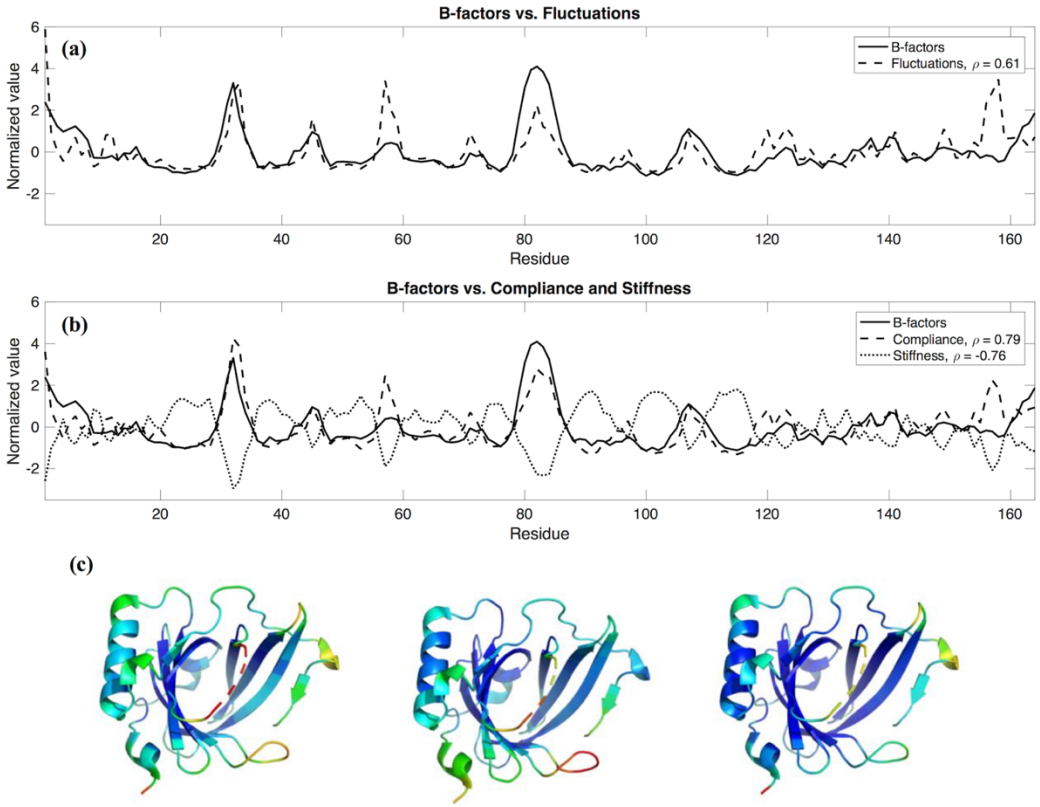

Figure 3.6. Comparison of the fluctuation, compliance and stiffness correlations with the experimental B-factors for Human Complement Protein C8γ (PDB: 1lf7). (a) Fluctuations; (b) compliance and stiffness; (c) graphical versions of these values mapped on the structure – left, compliance; center, normalized B-factors; and right, normalized fluctuations. Coloring is spectral with red for higher values and dark blue for lower values. Used with permission from [92].

Traditionally, the uncertainty of the atom position in macromolecular structures, which is measured by the crystallographic B-factors, has been associated with the thermal fluctuations. These can be computed from the internal protein dynamics, e.g. as reported in Eqs. (2.7), (2.14) and (2.23). The pairwise force application approach presented here sheds a different light on the nature of the experimental B-factors. As a matter of fact, these can therefore be explained under a new perspective, as they are found to result from the intramolecular mechanical interactions arising between each couplet of residues. In this respect, the pairwise force application methodology seems the most rational choice to probe the residue-residue interaction and, as shown above, it has provided good results in measuring the protein flexibility.

This mechanical perspective is rather new in the field of computational biology. Still, the pairwise force application method presented above has some limitations, as it focuses only on the internal residue-residue interactions neglecting the effect that the external environment can have on the protein flexibility. Moreover, B-factors should be the consequence of stochastic processes, that result from the intrinsic protein dynamics as well as from the interaction between the protein residues and external particles, e.g. water molecules, ions, etc. The latter are constantly jiggling in the protein environment and are likely to create continuous random collisions with the protein structure. For these reasons, an additional force application methodology was developed to

predict the protein flexibility and the experimental B-factors, by considering a random force pattern on the protein ELM, which is presented in the next Section.

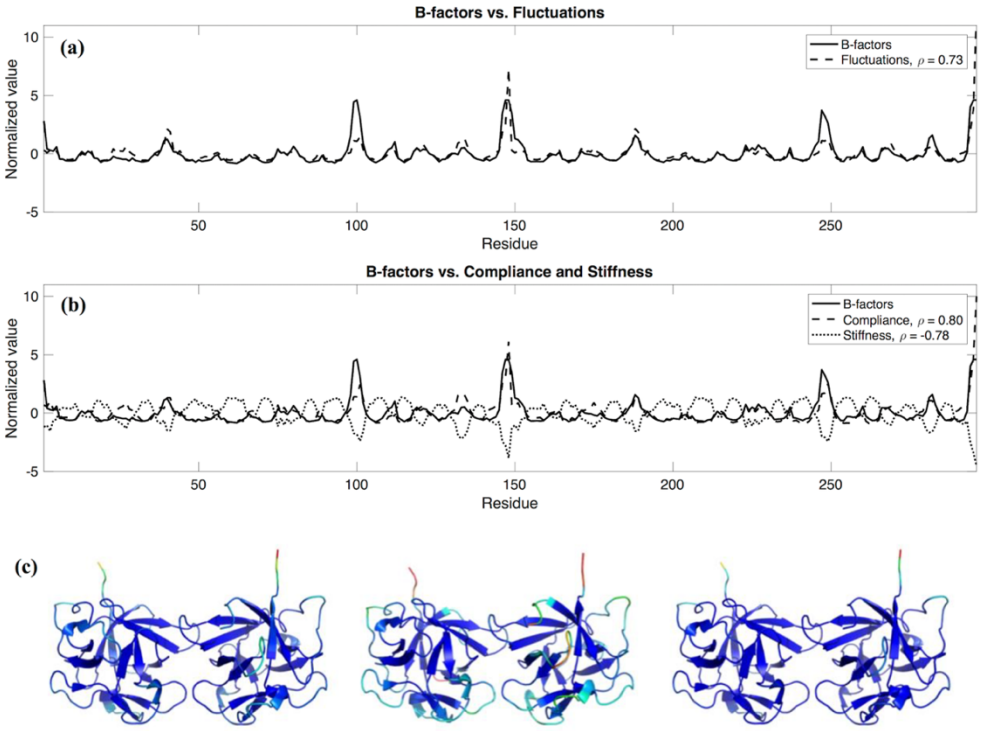

Figure 3.7. Comparison of the fluctuation, compliance and stiffness correlations with the experimental B-factors for *Clitocybe nebularis* ricin B-like lectin (PDB: 3nbc). (a) Fluctuations; (b) compliance and stiffness; (c) graphical versions of these values mapped on the structure – left, compliance; center, normalized B-factors; and right, normalized fluctuations. Coloring is spectral with red for higher values and dark blue for lower values. Used with permission from [92].

3.1.2 Random force bombardment on the protein ELM

The random force application pattern is meant to simulate the effect of the bombardment process that results from the random collisions of external particles onto the protein structure [93]. As a matter of fact, water molecules, ions and other particles are always present in the environment where proteins exist and are constantly vibrating, generating continuous collisions with the protein structure. Therefore, the protein-environment interaction can have a not negligible influence on protein behavior and flexibility.

Differently from the pairwise force application method presented above, where only two residues are pulled apart independently, this approach consists of applying random forces to the whole protein ELM. The randomness of the force is considered both in magnitude and directionality. Each node i of the protein structure is subjected to a 3 × 1 force vector $\boldsymbol{F_i}$. The three vector components, i.e. $F_{i,x}$, $F_{i,y}$ and $F_{i,z}$, are randomly sampled from a uniform distribution between –1 and +1:

$$F_{i,x} \sim U(-1,1), \tag{3.6a}$$
$$F_{i,y} \sim U(-1,1), \tag{3.6b}$$
$$F_{i,z} \sim U(-1,1). \tag{3.6c}$$

As a result, one obtains random force application patterns similar to the one shown in Figure 3.8. The figure reports the ELM of HEW lysozyme (PDB: 4ym8), with random forces applied to all the C^{α} atoms.

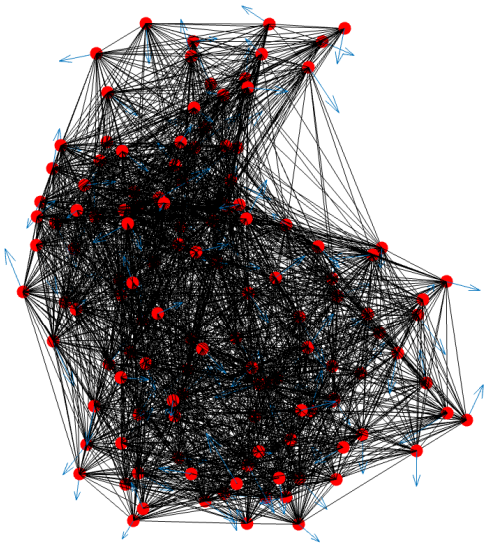

Figure 3.8. Random force application pattern on the HEW lysozyme (PDB: 4ym8) ELM. Red dots represent C^{α} atoms, black lines the elastic connections generated with a geometrical cutoff of 15 Å, and blue arrows the random forces. In this case, random forces are applied to each node.

The N nodal random force vectors $\boldsymbol{F_i}$ are then grouped into the global $3N \times 1$ force vector $\boldsymbol{F^s}$. This vector is defined as $\boldsymbol{F^s}$ since it refers to the s^{th} random pattern. Based on the calculation of the Hessian matrix of the protein ELM and its pseudo-inverse, the application of the s^{th} random pattern $\boldsymbol{F^s}$ leads to the evaluation of the global $3N \times 1$ displacement vector $\boldsymbol{\delta^s}$ as follows:

$$\boldsymbol{\delta^s} = \widetilde{\boldsymbol{H}}^{-1}\boldsymbol{F^s}. \tag{3.7}$$

From the global displacement vector $\boldsymbol{\delta^s}$, it is straightforward to evaluate the total absolute displacement related to the i^{th} node as follows:

$$\delta^s{}_i = \sqrt{\delta^s{}_{3i-2}{}^2 + \delta^s{}_{3i-1}{}^2 + \delta^s{}_{3i}{}^2}. \tag{3.8}$$

being $\delta^s{}_{3i-2}$, $\delta^s{}_{3i-1}$ and $\delta^s{}_{3i}$ the three Cartesian components along the X, Y and Z axes of the displacements of the i^{th} node.

The procedure explained so far is repeated several times, thus generating several randomly sampled force vectors and evaluating the corresponding nodal displacements through Eqs. (3.7) and (3.8). In Figure 3.9 three different displacement profiles based on three different random force patterns are shown for the case of HEW lysozyme. The results refer to the pfANM of the protein structure, with a value of p equal to 3. By looking at Figure 3.9, it is interesting to observe that, although the specific displacement profiles are obviously different as they result from different force patterns (s = 1, 2, 3), they exhibit a certain similarity. This similarity should be due to the intrinsic protein flexibility, that

ultimately depends only on the three-dimensional structure and the features of the ELM. From this observation, it follows that the random force application pattern can provide useful information to unravel the flexibility characteristics of the protein structure [93].

Based on these considerations, the total nodal displacement δ_i is defined as the average value of all the absolute displacements $\delta^s{}_i$ resulting from the different random force patterns $\boldsymbol{F^s}$:

$$\delta_i = \frac{1}{S}\sum_{s=1}^{S} \delta^s{}_i. \tag{3.9}$$

being S the total number of force patterns applied to the ELM. Remarkably, it is found that the profile of absolute displacements found from the procedure reported in Eqs. (3.7), (3.8) and (3.9) shows good agreement with the experimental B-factors. This confirms the previous observation that, similarly to the pairwise force application methodology reported above, the random force bombardment is able to provide correct information about the flexibility of the protein structure. In Figure 3.10, the comparison between the experimental B-factors and total average displacements resulting from S = 10000 random force patterns is shown for the pfANM of HEW lysozyme. As can be seen, a correlation coefficient of 0.73 is obtained, showing that the proposed random force application methodology can well predict the experimental flexibility.

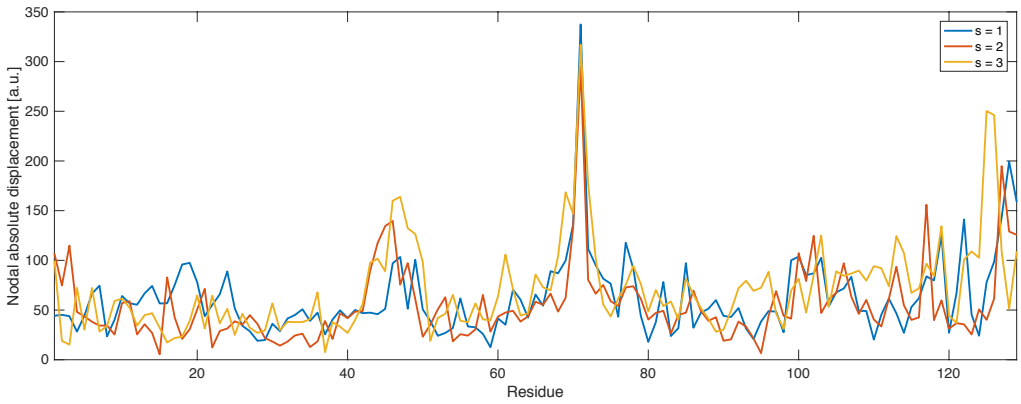

Figure 3.9. Nodal absolute displacements of the HEW lysozyme (PDB: 4ym8) ELM (pfANM, p = 3) under three different random force application patterns.

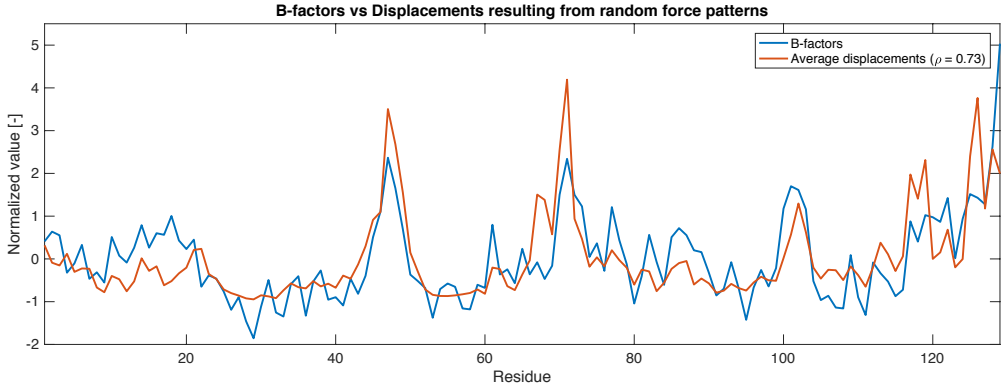

Figure 3.10. Average displacements of the HEW lysozyme (PDB: 4ym8) ELM (pfANM, p = 3) from 10,000 random force application patterns compared to experimental B-factors.

Interestingly, although the total number of random force patterns S should be as high as possible to have results that are accurate and that can be replicated in subsequent analyses, it is found that after almost one hundred runs the profile of average displacements from Eq. (3.9) matches the experimental B-factors basically with the same correlation coefficient that is obtained after 10000 runs. Figure 3.11 shows the convergence curve of the correlation coefficient depending on the total number of runs S.

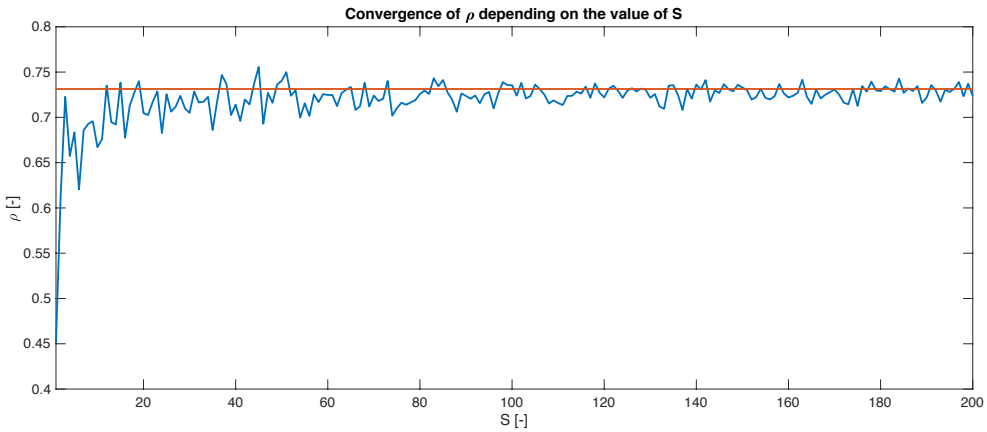

Figure 3.11. Convergence of the correlation coefficient between experimental B-factors and average displacements of the HEW lysozyme (PDB: 4ym8) ELM (pfANM, p = 3), based on variable total number S of random force application patterns. Blue line represents the convergence curve, while the orange line is the correlation coefficient (0.73) found after 10000 runs.

The previous results allow to draw an interesting conclusions about the nature of the protein flexibility, that is reflected by the experimental B-factors. In the previous Chapter, we have seen that B-factors can fairly accurately be predicted from the fluctuations derived from the normal modes, meaning that the B-factors should reflect the intrinsic dynamics of the protein. Furthermore, in Section 3.1.1, we have also seen that a pairwise force application pattern, simulating the residue-residue interactions, also leads to good correlations with the experimental B-factors, meaning that these can also reflect the effect of the internal residue-residue mechanical strength of the protein structure. Finally, in this Section, we find that a random force application pattern, that is meant to simulate the bombardment of the external particles on the protein structure, still provides good results in terms of B-factors prediction. Eventually, this suggests that the experimental B-factors can be described not only as the fingerprint of the internal protein dynamics and mechanical strength, but also as the result of the external collisions that characterize the protein-environment interaction.

Based on the consideration that the effect of random forces due to the external collisions should be greater on the protein surface rather than on the interior core, one might wonder whether it is really necessary to apply forces all over the protein structure. To verify this hypothesis, an additional random force pattern is defined, where the random force vectors are applied only on the residues lying on the protein surface. For this purpose, a methodology to define the protein surface is needed.

This is based on the boundary function, that is available in the MATLAB® environment. This function works based on the Delaunay triangulation of a set of points, and is dependent on a single parameter which is called the shrink factor.

The shrink factor is a scalar value between 0 and 1: setting the shrink factor to 0 gives rise to the convex hull, while setting it to 1 gives rise to the most compact boundary that envelops the points. Points on the surface are then considered the external nodes of the protein, whereas points lying in the interior space are the core nodes. In Figure 3.12 the generation of the external surface of HEW lysozyme (PDB: 4ym8) is shown for three different values of the shrink factors, i.e. 0.0, 0.5 and 1.0. As can be seen, higher shrink factors lead to more shrunk surfaces, thus higher numbers of external nodes. For shrink factors equal to 0.0, 0.5 and 1.0, one obtains 44, 83 and 109 external nodes, respectively, out of a total of 129 nodes for HEW lysozyme (Figure 3.12).

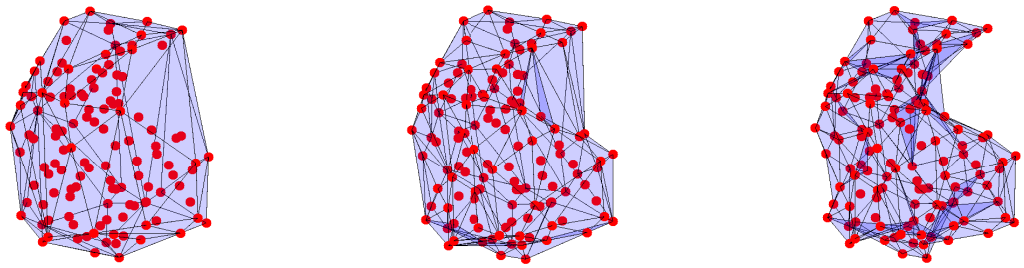

(a) (b) (c)

Figure 3.12. Generation of external surface of HEW lysozyme (PDB: 4ym8), depending on the shrink factor: (a) shrink factor = 0.0; (b) shrink factor = 0.5; (c) shrink factor = 1.0. Red dots represent the 129 C^{α} atoms of the protein, blue surface represents the external surface generated by Delaunay triangulation with different shrink factors.

Once the external surface is defined based on the boundary function and the selected shrink factor, the force vectors $\boldsymbol{F_i}$ are randomly generated from Eqs. (3.6) only for the nodes that lie on the external surface. As a consequence, the force vectors $\boldsymbol{F_i}$ are null for all the internal nodes. Based on this, the global force vector $3N \times 1$ $\boldsymbol{F^s}$ is generated for each random simulation s, and the corresponding nodal displacements $\boldsymbol{\delta^s}$ are computed as from Eq. (3.7). Equations (3.8) and (3.9) are then applied as explained above to find the average displacements of the protein residues, that results from 10000 runs.

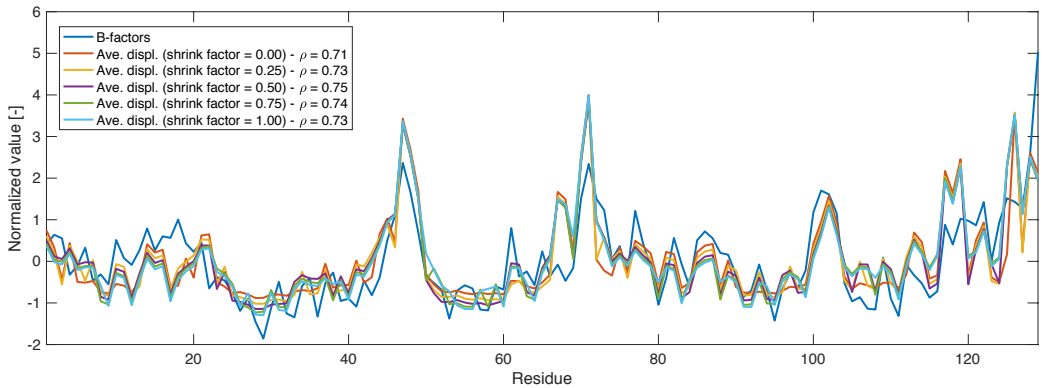

Figure 3.13. Experimental B-factors vs. average displacements of the HEW lysozyme (PDB: 4ym8) ELM (pfANM, $p = 3$), resulting from 10000 random force application only on the external nodes depending on the selected shrink factor.

In Figure 3.13 the profile of experimental B-factors of HEW lysozyme is compared to the average displacements resulting from random forces applied only on the external surface, based on different selected shrink factors, i.e. 0.00, 0.25,

0.50, 0.75 and 1.00. Obviously, the results depend on the selected shrink factor, that in turn affects the generated surface. In this case, an optimal shrink factor of 0.50 is found (Figure 3.12b), that leads to the maximum correlation coefficient with the experimental data of 0.75. Note that this result confirms the hypothesis above, that random forces only on the external surface, without applying any perturbation on the protein core, is sufficient to explain the experimental B-factors of the whole protein structure.

To further verify that the random bombardment only on the external surface of the protein is strongly related to the experimental B-factors, one might also wonder what happens if the random bombardment is applied only on the protein internal nodes. This should simulate an unrealistic phenomenon, the protein being punched on its core whereas no perturbations are found on the external surface. By repeating the procedure reported above applying forces only on the internal nodes, the average displacements of the protein residues show no meaningful correlation with the experimental B-factors, as shown in Figure 3.14. This confirms that the random bombardment methodology is meaningful to predict protein flexibility as long as forces are applied on the protein surface.

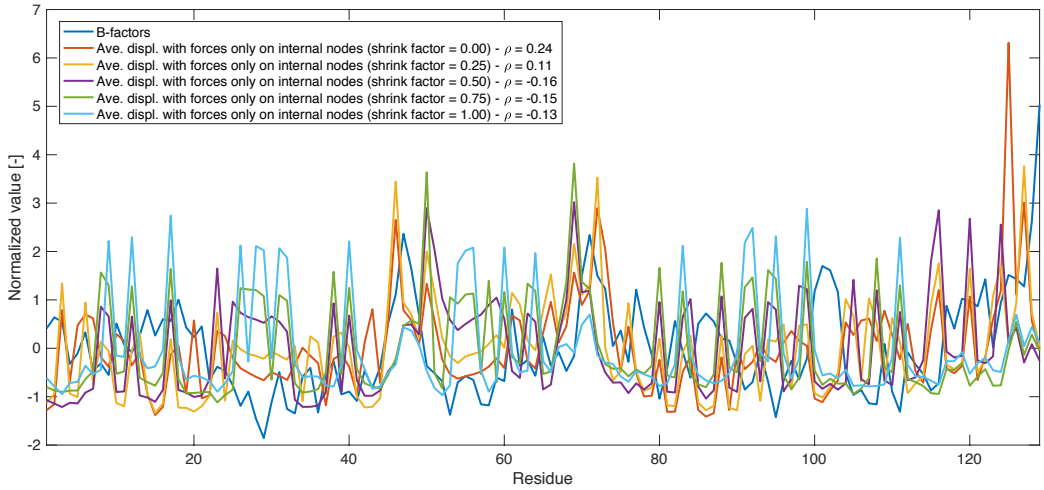

Figure 3.14. Experimental B-factors vs. average displacements of the HEW lysozyme (PDB: 4ym8) ELM (pfANM, p = 3), resulting from 10000 random force application only on the internal nodes depending on the selected shrink factor.

The results found above in terms of correlation coefficients with the experimental B-factors for HEW lysozyme are summarized in Figure 3.15. Figure 3.15a shows the correlation coefficient obtained with the pfANM mode-based fluctuations (orange line, ρ = 0.73), with the average displacements resulting from random bombardment on all the residues (yellow line, ρ = 0.73), and with the average displacements resulting from random forces applied only on the external surface (blue line, ρ depends on the shrink factor). The numbers reported close to the markers of the blue line, represent the fraction of the external nodes out of the total protein residues, which obviously increases as the shrink factor increases. As can be seen, applying forces on the whole protein structure leads to good agreement with experimental data, similarly to that obtained considering the traditional mode-based fluctuations. Applying the random forces only on the external surface can in turn lead to greater correlation coefficients, depending on the selected shrink factor. In the case of HEW lysozyme, a shrink factor of 0.50, that results in perturbing only the 64% of the protein residues, leads to a correlation with experimental data of 0.75.

In Figure 3.15b, the correlations found with the average displacements resulting from random forces applied only on the internal nodes are reported. In this case, the numbers reported close to the markers, represent the fraction of the internal nodes out of the total protein residues. As already reported above, random perturbations on the protein core lead to poor correlation coefficients, therefore they do not explain the experimental flexibility, i.e. the experimental B-factors.

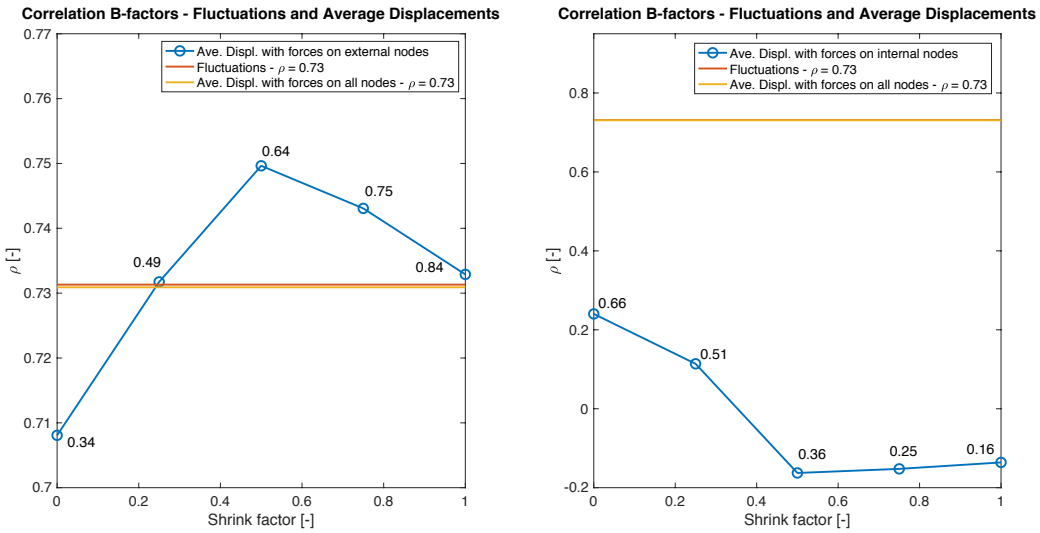

Figure 3.15. Experimental B-factors vs. fluctuations and average displacements of the HEW lysozyme (PDB: 4ym8) ELM (pfANM, p = 3) due to random force application. Orange lines refer to the mode-based fluctuations, yellow lines refer to the average displacements resulting from random forces applied on all the protein residues, blue lines refer to the average displacements from random forces applied only on (a) external nodes or (b) internal nodes. In both cases, the numbers reported close to the blue markers represent the fraction of (a) external or (b) internal nodes, depending on the selected shrink factor.

The analysis based on the random bombardment on the protein ELM presented above for the single case of HEW lysozyme has been carried out for a large dataset of highly refined protein structures extracted from the PDB [14]. The dataset is the same dataset 1 containing single-chain proteins that has been reported in Table 3.1 and considered for the pairwise force application presented in Section 3.1.1. Based on the analysis presented in this Section, the experimental B-factors of more than 900 proteins are compared to the mode-based fluctuations, the average displacements resulting from random forces applied on the whole ELM, and the average displacements resulting from random forces applied only on the external surface. For each protein, different external surfaces are generated based on various values of the shrink factor, namely 0.0, 0.1, 0.2, …, 0.9, 1.0. The optimal value of the shrink factor giving rise to the highest correlation with the experimental data is then considered for further comments.

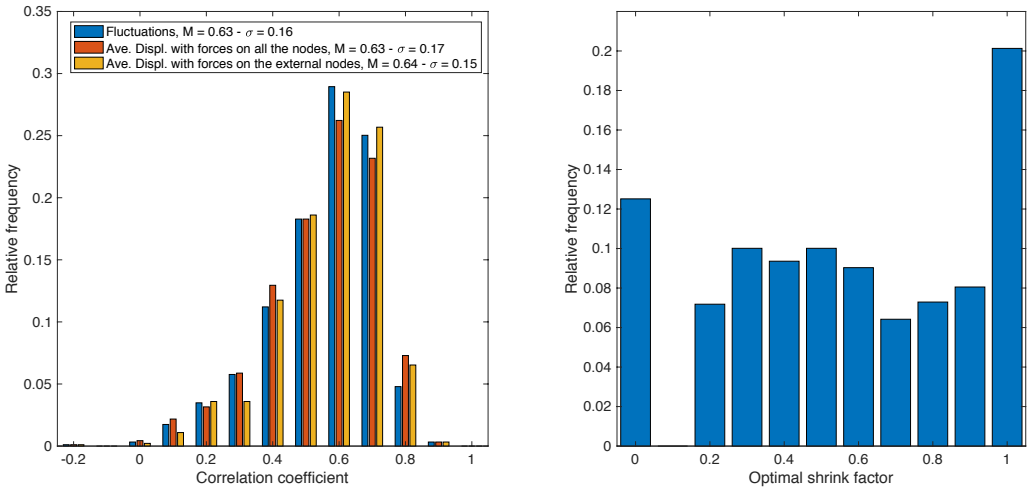

(a) (b)

Figure 3.16. Comparison of the fluctuation and force-based average displacements correlations with the experimental B-factors for dataset 1. (a) Distribution of the correlation coefficients for fluctuations (blue histogram), average displacements resulting from forces applied on all the nodes (red histogram), and average displacements resulting from forces applied only on the external nodes (orange histogram). Median values (M) and standard deviations (σ) are reported in the keys. (b) Distribution of the optimal shrink factors for the external force application pattern [93].

Similarly to Figures 3.4 and 3.5, Figure 3.16a reports the histogram of the correlation coefficients obtained from the comparison with experimental B-factors based on normal mode fluctuations (blue bars), random forces applied on all the nodes (red bars), and random forces applied only on external nodes (orange bars). The three distributions are comparable, which means that the random force application pattern is indeed able to describe the protein flexibility and can be used as an additional method, besides the traditional mode-based fluctuations, to predict the experimental B-factors. Figure 3.16b also reports the statistical distribution of the optimal shrink factors, that provide the best agreements with the experimental B-factors, when perturbing only the external surface. Based on the shape of this distribution, it can be inferred how the optimal shrink factor strongly depends on the specific protein and can assume each value between 0.0 and 1.0.

From the extensive analysis carried out on dataset 1, for various cases it is found that the average displacements based on the random force bombardment show enhanced correlation with the experimental B-factors, with respect to the traditional fluctuations. As an example, Figure 3.17 reports the case of the yeast Ent2 ENTH domain (PDB: 4gzc). By using a pfANM with p = 3, one obtains a correlation with traditional fluctuations of 0.63, whereas a correlation coefficient of 0.73 is found with the average displacements based on random force bombardment on the entire structure as well as only on the external nodes. In this case the optimal shrink factor is found to be equal to 1.0, corresponding to the perturbation of the 69% of total nodes.

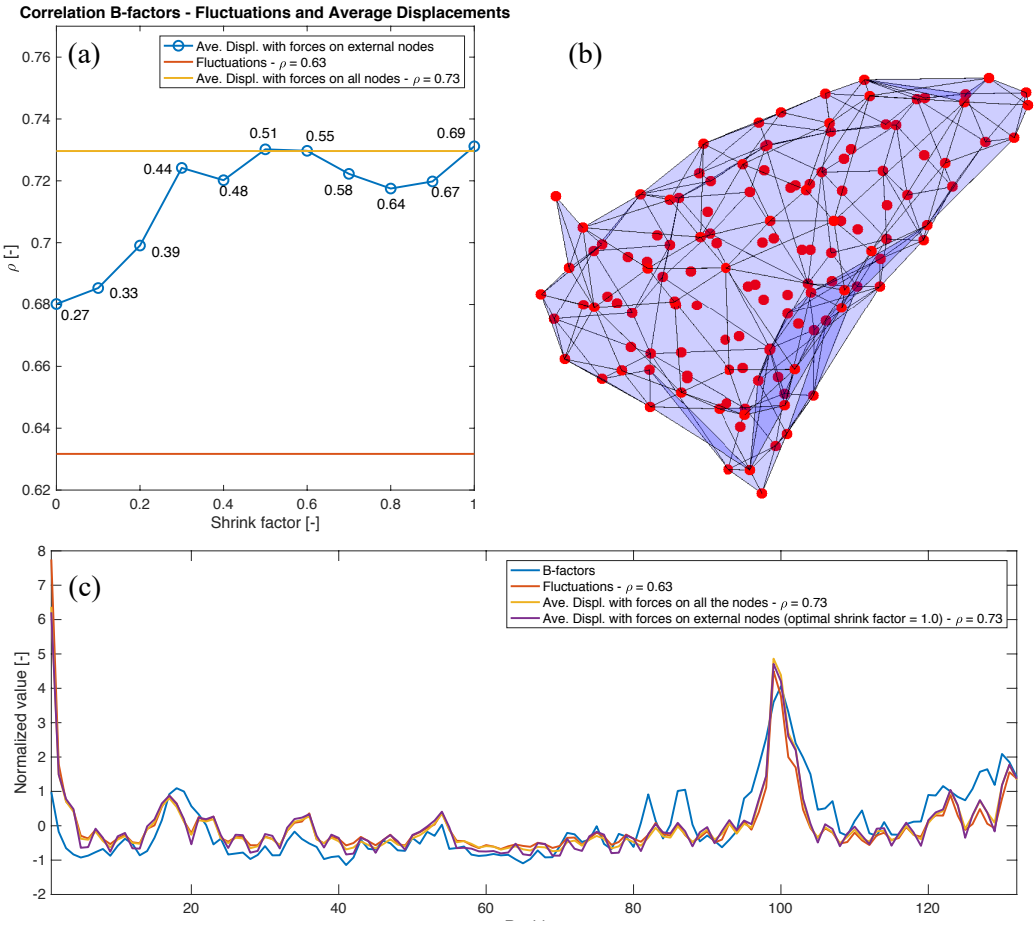

Figure 3.17. (a) Experimental B-factors vs. fluctuations and average displacements of the yeast Ent2 ENTH domain (PDB: 4gzc) ELM (pfANM, p = 3) due to random force application. Orange lines refer to the mode-based fluctuations, yellow lines refer to the average displacements resulting from random forces applied on all the protein residues, blue lines refer to the average displacements from random forces applied only on the external nodes. The numbers reported close to the blue markers represent the fraction of external nodes depending on the selected shrink factor. (b) External surface generated for the optimal shrink factor, equal to 1.0. (c) Experimental B-factors vs. fluctuations (ρ = 0.63) and average displacements resulting from 10000 random force applications on the whole structure (ρ = 0.73) and only on the external nodes with the optimal shrink factor (ρ = 0.73).

Similarly to what already found in the analysis on dataset 1 for the pairwise force application pattern, it was found also in this case that for certain proteins the mode-based fluctuations correlate to the experimental B-factors slightly better or comparably than the average displacements resulting from the random force pattern. This seems to be very dependent on the protein structure and in turn on the geometrical and mechanical characteristics of the ELM. In any case, from the analysis performed here, it can be concluded that experimental B-factors cannot only be explained as the result of the vibrational fluctuations that arise from the intrinsic dynamics (Section 2.2) or the result of the pairwise mechanical interactions among the protein residues (Section 3.1.1), but also as the results of the random bombardment on the protein structure. This bombardment reflects the collisions of external particles on the protein structures, thus simulating the protein-environment interaction. This explains why perturbing only the external surface leads to more accurate results in terms of protein flexibility predictions.

3.2 Protein Conformational Changes and Geometrical Non-linearities

In the previous Sections of this Chapter, we have seen that applying various force patterns on the ELM can accurately explain the experimental B-factors and the protein flexibility, that ultimately affects the biological behavior. Note that both the pairwise and random force application approaches were developed within the framework of linear structural analysis, as they rely on the linear matrix relationships from Eqs. (3.1) and (3.2). This is reasonable for B-factors prediction, as these are the results of small-amplitude displacements around the equilibrium position.

In the previous Chapter, we have also seen that the protein biological mechanism is usually driven by the protein flexibility and often carried out through conformational changes. From the works of the Atilgan's group [88–90] and Liu et al. [86], which exploit the PRS methodology, it has already been shown that force applications based on the linear response theory provide a good estimate of the conformational change directionality. The ELMs were also used in the last decades not only to predict the directionality of the protein conformational changes, but also to evaluate the pathway of the conformational transitions that occur between two known crystal structures. Based on the minimization of the elastic energy of the deformed spring network, Kim et al. [94,95] proposed a numerical method to generate feasible pathways of the protein transition, that interpolates the two end conformations while avoiding steric clashes in the intermediate states. Few years later, Maragakis and Karplus [96] proposed a plastic network model (PNM) to generate the large-amplitude transition pathway of *Escherichia Coli* adenylate kinase. The results revealed the presence of hinges that contribute to the protein mechanism and pronounced curvilinear motions.

Linear response theories based on Eqs. (3.1) and (3.2) imply that both the displacement field and mechanical behavior of the system remain linear as the deformation proceeds. The linearity of the displacement field implies that, given the initial direction of motion, the direction remains the same while the transition proceeds. Although this is often reasonable for the first steps of the transition, the displacement linearity usually gets lost as the protein begins to follow curvilinear pathways. Conversely, the linearity in the mechanical behavior implies that, given the initial displacements obtained for small forces, the displacements increase proportionally as the magnitude of the external perturbations increases. This aspect is supposed to play an important role in the analysis of protein conformational changes, as these can often imply large-scale motions. Moreover, from Structural Mechanics, it is well-know that the ELMs are usually prone to exhibit non-linearities in the structural response due to the effect of geometrical non-linearities (Figure 1.3) [6]. As a matter of fact, the presence of non-linear effects in the relaxation dynamics of the protein ENMs has been already suggested by Togashi et al. [97,98]. For this reason, in this Section, the possible role of the ELM geometrical non-linearities in the protein conformational changes is investigated.

3.2.1 Geometrical non-linearities: Equilibrium on the undeformed and deformed conformations

To investigate the possible presence of geometrical non-linearities in the protein conformational transition, known the two end crystal conformations, one of the possible strategies consists of applying the equilibrium equations in the undeformed and deformed conformations and comparing the results, as shown in Scaramozzino et al. [99].

As explained in Section 2.3.1, known the initial conformation $\boldsymbol{A}$ and final conformation $\boldsymbol{B}$, the superimposition procedure yields the evaluation of the displacements of the conformational change $\boldsymbol{CC}$, as from Eq. (2.27). Note that these represents the total linear displacements that lead the starting configuration to match the final one, but do not represent the actual displacements that the protein undergoes within the transition pathway, since this can be curvilinear. However, known the total displacements and assuming that the linear response theory is valid for the large-scale motion (linearity in the displacement field and mechanical behavior), Eq. (3.1) can be used to relate the nodal displacements to the nodal forces. Note that using Eq. (3.1) for the equilibrium implicitly means considering the equilibrium in the initial undeformed configuration, i.e. $\boldsymbol{A}$. By substituting the total conformational change vector $\boldsymbol{CC}$ in Eq. (3.1), one obtains the forces $\boldsymbol{F}$ needed to guarantee the equilibrium in the undeformed configuration:

$$\boldsymbol{F} = \boldsymbol{H}\,\boldsymbol{CC}, \tag{3.10}$$

being $\boldsymbol{H}$ the Hessian matrix of the ELM.

Conversely, if configurations $\boldsymbol{A}$ and $\boldsymbol{B}$ are the result of a large-scale conformational transition, the effect of geometrical non-linearities can be revealed by applying the equilibrium equations in the final deformed configuration $\boldsymbol{B}$. These equations can be expressed in compact form as:

$$\boldsymbol{F} = \boldsymbol{f}(\boldsymbol{CC}), \tag{3.11}$$

where $\boldsymbol{f}$ represents the system of non-linear equations relating the displacements to the equilibrating nodal forces. The non-linear system reported in Eq. (3.11) can be written analytically by considering the equilibrium conditions in the final deformed configuration, through the following steps: (1) the elongation of each connection of the ELM is computed based on the effective positions of the nodes in the initial and final configuration (kinematic equations); (2) the internal force within each connection is computed based on the stiffness value of the connection and calculated elongation (constitutive equations); (3) the total force on each node is finally computed by equilibrating all the internal forces acting on the node deriving from the deformed connections, with reference to the final deformed configuration (equilibrium equations) [99]. It is clear that, if the linearity hypothesis holds true, the two force fields that guarantee the equilibrium obtained from Eqs. (3.10) and (3.11) should match. Conversely, the higher the deviation of the force values (in terms of both magnitude and directionality), the greater the possible effect of geometrical non-linearities.

Two examples are analyzed here. The first one is related to HIV-1 protease, whose biological activity is pivotal for the replication of the AIDS virus. Two crystal structures are considered, namely the open form (PDB: 1hhp) and the

closed form (1ajx). Note that HIV-1 protease is a dimer, made up of two chains of 99 amino acids each. However, for simplicity, the single monomer is analyzed here. The two monomers are reported in Figure 3.18a, after the superimposition. Figure 3.18b shows the profile of the conformational change displacements, as evaluated from Eq. (2.27). As can be seen, the monomer exhibits a maximum displacement of 4 Å near the central portion of the protein and 2 Å close to the C-terminus. The other regions of the proteins exhibit rather small displacements.

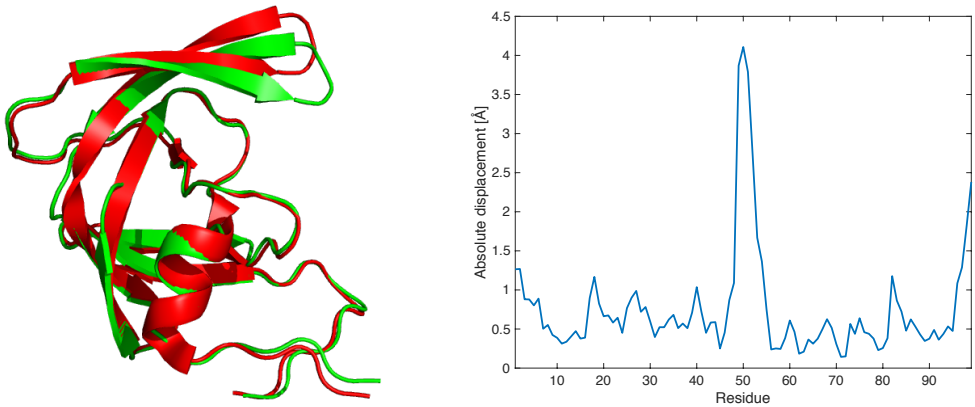

(a) (b)

Figure 3.18. HIV-1 protease conformational change: (a) Open form in red (PDB: 1hhp) and closed form in green (PDB: 1ajx) after superimposition; (b) Profile of the absolute displacements.

Figure 3.19 shows the comparison between the forces evaluated through the linear relationship in Eq. (3.10) and the non-linear system in Eq. (3.11), for the open-to-closed conformational change, i.e. taking the open form as the initial structure. Figure 3.20 shows the same comparison for the closed-to-open transition, i.e. taking the closed form as reference. The calculations are carried out by considering the ELM of the HIV-1 protease monomer, with the geometrical cutoff limit of 15 Å, with spring constants that do not depend on the residue-residue distance, i.e. with a value of p equal to 0 from Eq. (2.15).

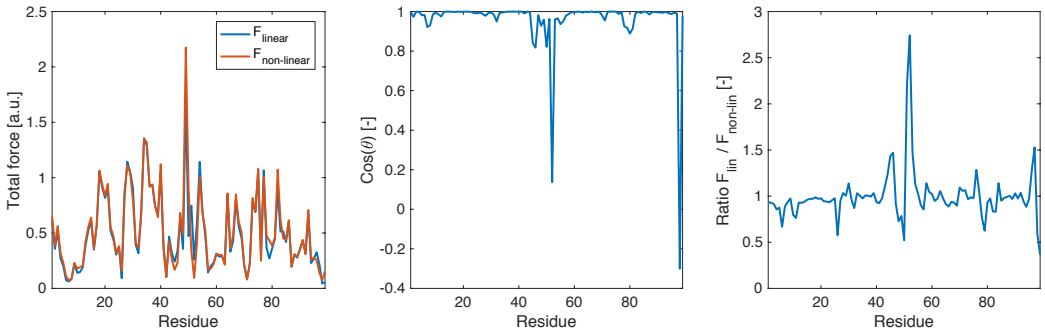

(a) (b) (c)

Figure 3.19. HIV-1 protease open-to-closed conformational change: (a) comparison between absolute values of nodal forces (linear vs. non-linear analysis); (b) comparison between directionality of nodal forces; (c) ratio between absolute values of nodal forces.

Figures 3.19a and 3.20a show the comparison of the absolute values of nodal forces, Figures 3.19b and 3.20b show the difference in directionality (measuring the cosine of the angle between the nodal vectors) and Figures 3.19c and 3.20c show the ratio between the absolute values of the forces. From these figures, it is

evident that the profiles of the forces calculated via the equilibrium in the undeformed structure (linear analysis) or deformed configuration (non-linear analysis) share many common features for most parts of the protein chain. However, for both the open-to-closed and closed-to-open transition, in the regions where the protein exhibits the highest displacements of the conformational change (Figure 3.18b), the forces show differences both in directionality (Figures 3.19b and 3.20b) and magnitude (Figures 3.19c and 3.20c). This seems to confirm that geometrical non-linearities can affect the structural response of the protein ELM when investigating conformational changes.

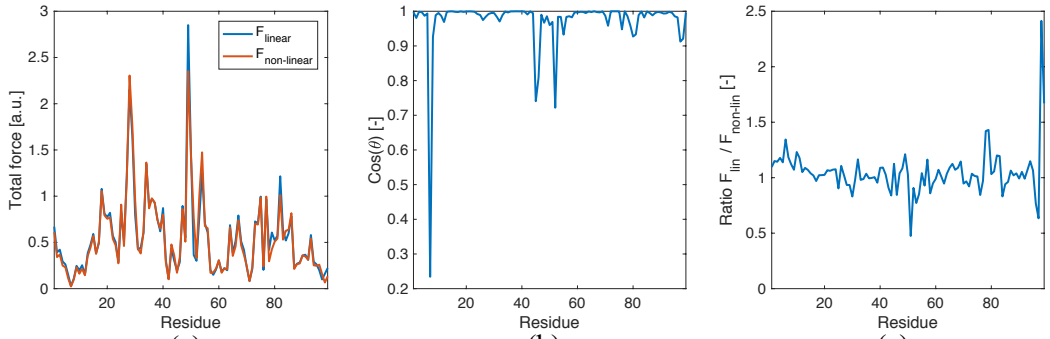

(a) (b) (c)

Figure 3.20. HIV-1 protease closed-to-open conformational change: (a) comparison between absolute values of nodal forces (linear vs. non-linear analysis); (b) comparison between directionality of nodal forces; (c) ratio between absolute values of nodal forces.

The example of HIV-1 protease treated above is informative because it exhibits a rather localized conformational change and involves quite small displacements, being the maximum value around 4 Å (Figure 3.18). Nevertheless, from the analysis carried out above it is found that, in the regions where the proteins undergoes the maximum displacements, the forces experiences by the ELM are potentially affected by the geometrical non-linearities. In most cases, proteins exhibit conformational changes which are more collective, i.e. more atoms participate to the transition in a concerted way, and the absolute displacements are greater than the ones found in the HIV-1 protease. For example, Figure 3.21 reports the case of LAO-binding protein, already seen in Section 2.3. As can be seen from the displacements in Figure 3.21b, the conformational change is rather collective and the maximum displacement is around 10 Å.

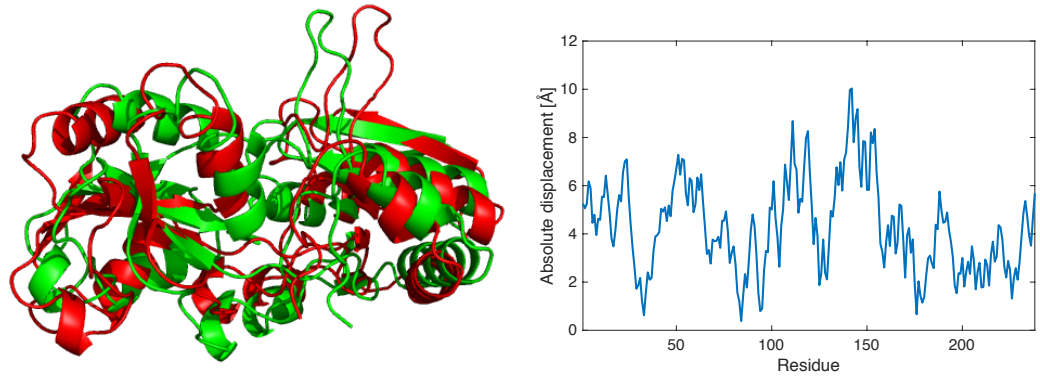

(a) (b)

Figure 3.21. LAO-binding protein conformational change: (a) Open form in red (PDB: 2loa) and closed form in green (PDB: 1lst) after superimposition; (b) Profile of the absolute displacements.

Figures 3.22 and 3.23 show the results for the open-to-closed and closed-to-open conformational change, respectively. As can be seen, in this case, the forces that provide the equilibrium of the ELM are remarkably different (both in magnitude and directionality) whether they are calculated from the linear response theory from Eq. (3.10) or whether one applies the equilibrium on the final deformed configuration from Eq. (3.11). This suggests that, for large-scale collective conformational changes, the linear response theory is appropriate for analyzing the first steps of the conformational transition, but it might not be enough for the whole transition pathway, as the presence of geometrical non-linearities might play an important role [99].

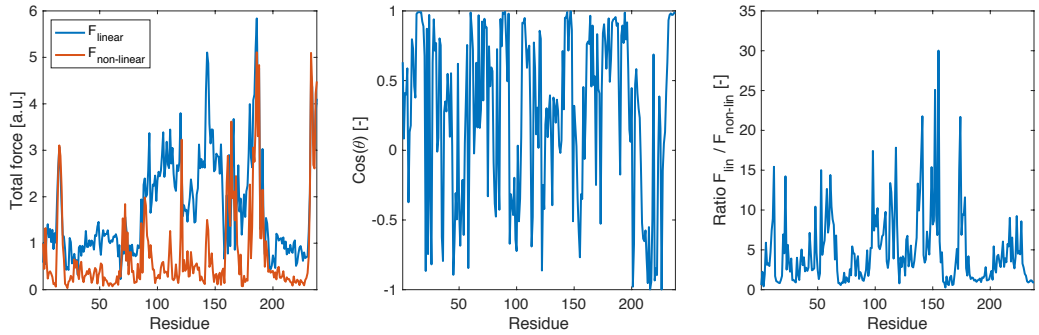

(a) (b) (c)

Figure 3.22. LAO-binding protein open-to-closed conformational change: (a) comparison between absolute values of nodal forces (linear vs. non-linear analysis); (b) comparison between directionality of nodal forces; (c) ratio between absolute values of nodal forces.

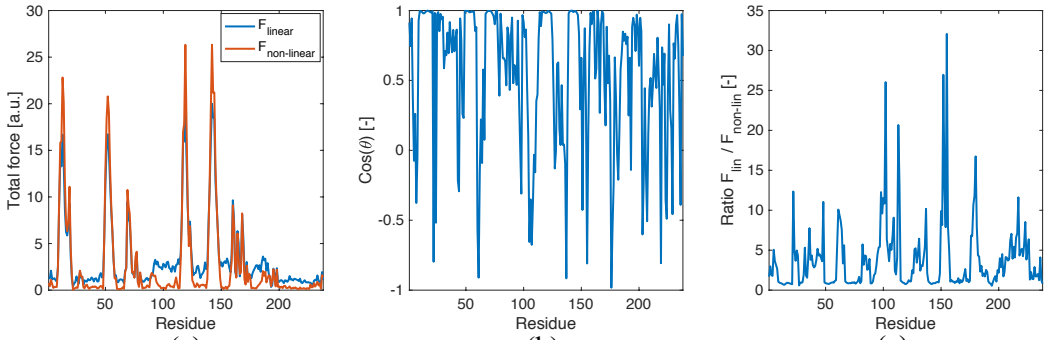

(a) (b) (c)

Figure 3.23. LAO-binding protein closed-to-open conformational change: (a) comparison between absolute values of nodal forces (linear vs. non-linear analysis); (b) comparison between directionality of nodal forces; (c) ratio between absolute values of nodal forces.

3.2.2 Geometrical non-linear analysis throughout the protein transition pathway

Based on the results of Section 3.2.1, it is found that the linear response theory might not be enough for the entire conformational transition pathway. However, as mentioned at the beginning of Section 3.2, this might be due to the non-linearity of the displacement field, non-linearity of the structural response, or both. The former basically means that proteins might exhibit curvilinear pathways, which in turn is known to be true for several cases, e.g. [96]. Conversely, the latter implies that there is a non-linear relationship between the

increase of external perturbations (forces) and corresponding structural modifications (displacements). To further investigate this aspect, the geometrical non-linear analysis can be applied in all the intermediate states of the conformational transition, i.e. in a step-by-step fashion, to seek the equilibrium between the acting forces and corresponding nodal displacements at each step. In this way, from the assessment of the force evolution throughout the transition pathways, one can estimate whether the linear response theory is not adequate for the entire conformational change just because of the tortuosity of the pathway or because of the underlying ELM geometrical non-linearities.

To carry out this analysis, one needs to have the information about the transition pathway, in order to further apply the non-linear equilibrium equations from:

$$\boldsymbol{F_k} = \boldsymbol{f}(\boldsymbol{\delta_k}), \tag{3.12}$$

being $\boldsymbol{F_k}$ and $\boldsymbol{\delta_k}$ the force and displacement vectors at each intermediate step *k*, and $\boldsymbol{f}$ the non-linear system already reported in Eq. (3.11). The approach from Kim et al. [94,95] has been used here to generate the intermediate states of the protein ELM, given the two known configurations, and thus the nodal displacement vector at each step $\boldsymbol{\delta_k}$.

The step-by-step geometrical non-linear analysis has been applied to the conformational change of LAO-binding protein (Figure 3.21), by using an ELM with cutoff of 15 Å and no distance-dependence for the spring constant. Known the open (PDB: 2lao) and closed form (PDB: 1lst), the interpolation based on elastic energy minimization is applied according to Kim et al. [94,95] to find the intermediate configurations, and thus the displacements at each step $\boldsymbol{\delta_k}$.

Based on the obtained pathway, the analysis of the displacement evolution has been first carried out, as reported in Figure 3.24a. At each subsequent steps *k* and *k+1*, the incremental vector $\boldsymbol{\delta_{k,k+1}}$ is evaluated as the difference of the XYZ coordinates of the intermediate conformation at step *k+1* and those at step *k*. For each node *i*, the normalized cosine between vectors $\boldsymbol{\delta_{k,k+1}}$ and $\boldsymbol{\delta_{0,1}}$ is then evaluated as follows:

$$\cos\theta_{k,i} = \frac{\left(\boldsymbol{\delta_{k,k+1}}\right)_i \cdot \left(\boldsymbol{\delta_{0,1}}\right)_i}{\sqrt{\left(\boldsymbol{\delta_{k,k+1}}\right)_i \cdot \left(\boldsymbol{\delta_{k,k+1}}\right)_i}\sqrt{\left(\boldsymbol{\delta_{0,1}}\right)_i \cdot \left(\boldsymbol{\delta_{0,1}}\right)_i}}, \tag{3.13}$$

being $\boldsymbol{\delta_{0,1}}$ the incremental displacement vector at the first step of the transition pathway. The cosine defined in Eq. (3.13) provides a simple estimate of the non-linearity in the transition pathway. If $\cos\theta_{k,i}$ is equal or proximal to 1 for each step *k*, it means that the i^{th} residue follows a straight line between the two end conformations. Conversely, $\cos\theta_{k,i}$ different from 1 implies that the i^{th} residue is undergoing a curvilinear pathway within the transition. A mean value of $\cos\theta_{k,i}$ can be ultimately defined for each residue *i* to provide a unique numerical estimate of the average non-linearity of the transition pathway at each position of the protein chain:

$$\cos\theta_i = \frac{1}{100}\sum_{k=0}^{99}\cos\theta_{k,i}, \tag{3.14}$$

being 100 the total number of conformations considered in the transition pathway. Figure 3.25a shows the values of the mean cosine for the LAO-binding protein open-to-closed conformational change. As can be seen, in several residues the mean cosine exhibits values sensibly lower than 1, which confirms that the transition involves curvilinear pathways for various portion of the protein.

Besides the non-linearity in the displacement field, it is interesting to investigate whether the non-linearity affects the structural response as well. To do so, the scheme reported in Figure 3.24b is followed. The figure shows a generical non-linear force-displacement curve. Applied to the case under investigation, the displacement on the X-axis represents the absolute value of the change of coordinates that each residue exhibits during the transition, whereas the force on the Y-axis is the absolute value of the nodal force calculated from Eq. (3.12). By tracing curves like the one reported in Figure 3.24b for each residue *i*, one can evaluate the tangential stiffness $TS_{k,i}$ at each step *k* as:

$$TS_{k,i} = \frac{\left(F_{k,k+1}\right)_i}{\left(\delta_{k,k+1}\right)_i}, \tag{3.15}$$

being $F_{k,k+1}$ and $\delta_{k,k+1}$ the increment of absolute force and absolute displacement between steps *k* and *k+1*.

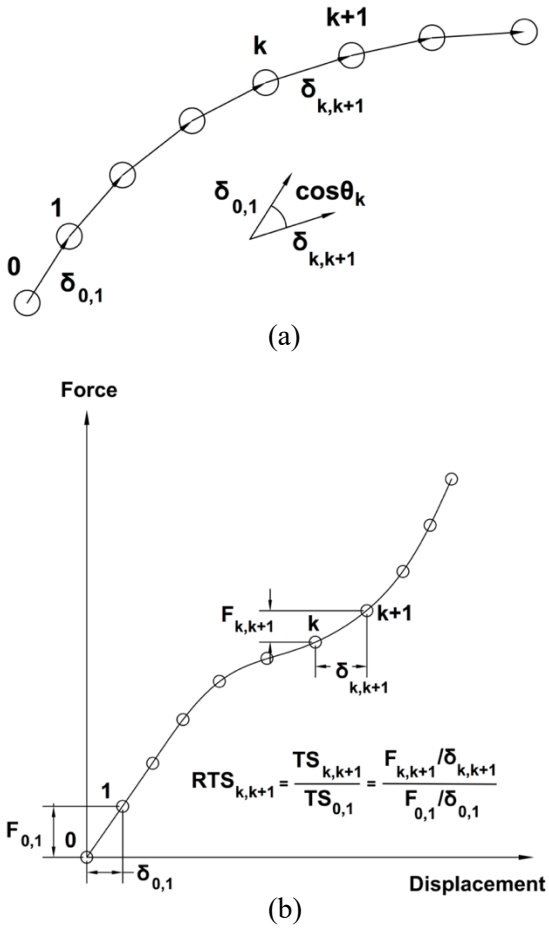

Figure 3.24. Scheme for the evaluation of non-linearities in the protein conformational transitions: (a) non-linearity of the displacement field; (b) the non-linearity of the structural response.

At this point, the relative tangential stiffness can be defined as the ratio of the tangential stiffness at each step k and the one at the beginning of the transition ($k = 0$):

$$RTS_{k,i} = \frac{TS_{k,i}}{TS_{0,i}}. \tag{3.16}$$

It is clear that, if $RTS_{k,i}$ is equal to 1 for the entire transition, the force-displacement curve for the i^{th} residue is completely linear. Conversely, values of $RTS_{k,i}$ different from 1 are the fingerprints of non-linearities in the structural response of the ELM during the transition. Similarly to Eqs. (3.13) and (3.14), the mean value of $RTS_{k,i}$ across all the steps can be defined, which has been called the non-linearity index NLI_i:

$$NLI_i = \frac{1}{100}\sum_{k=0}^{99} RTS_{k,i}. \tag{3.17}$$

Figure 3.25b shows the non-linearity index for the LAO-binding protein open-to-closed conformational transition. As can be seen, values different from 1 (both greater and lower) are found throughout the protein structure, meaning that the force-displacement curves of these residues exhibit non-linear features. Ultimately, this confirms that geometrical non-linearities occur and can play a role during the conformational transition, inducing both the pathway to be curvilinear at certain locations (Figure 3.25a) and the structural response to exhibit non-linearities in the force-displacements curves (Figure 3.25b).

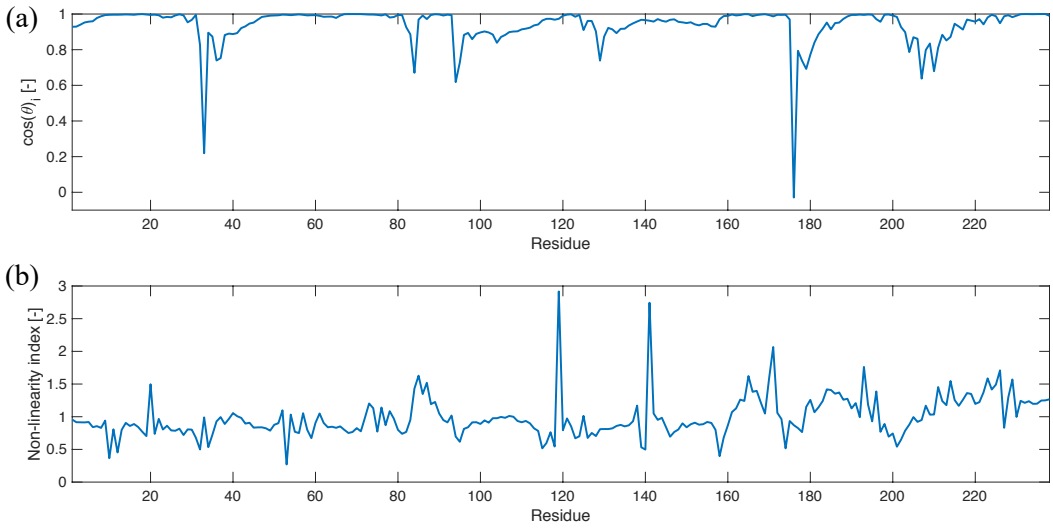

Figure 3.25. Non-linearities in the LAO-binding protein open-to-closed conformational change: (a) non-linearity in the displacement field; (b) non-linearity in the structural response.

Figure 3.26 shows the same analysis (mean cosine and non-linearity index) for the closed-to-open conformational change of LAO-binding protein. Again, Figure 3.26a confirms that the pathway is not completely linear in various

portions of the proteins and Figure 3.26b demonstrates that non-linearities occur in the force-displacement curves of several protein residues.

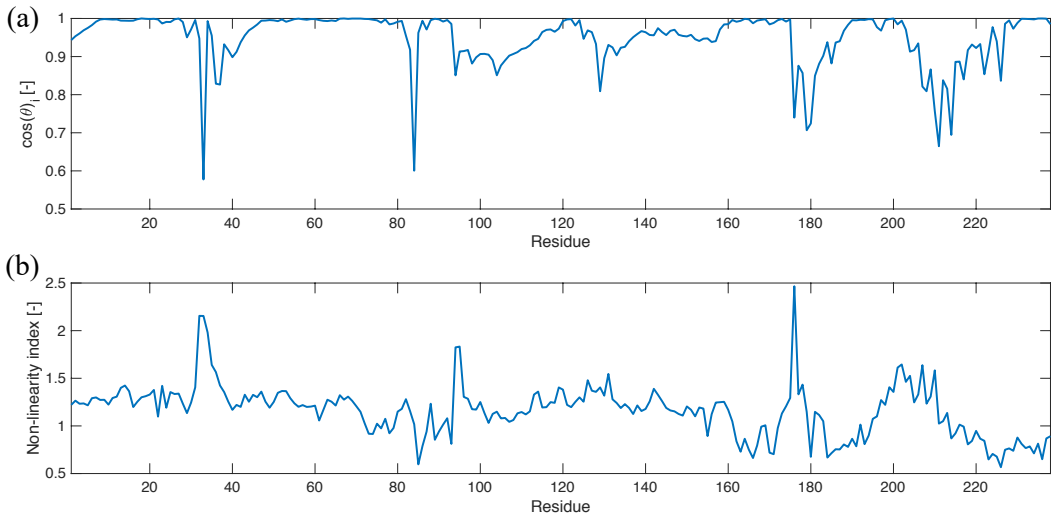

Figure 3.26. Non-linearities in the LAO-binding protein closed-to-open conformational change: (a) non-linearity in the displacement field; (b) non-linearity in the structural response.

3.3 Conclusions

In this Chapter, the subject of force application on the protein ELMs has been addressed under novel perspectives. Specifically, in Section 3.1 two different force patterns have been proposed to predict the experimental B-factors, i.e. protein flexibility. B-factors can be seen as the result of small-amplitude displacements of the protein residues around the equilibrium position. For this reason, the force application patterns were developed within the framework of linear response theory, i.e. linear structural analysis.

The first pattern is based on pairwise pulling forces applied iteratively on the residue-residue couplets to probe the distribution of the mechanical resistance within the protein ELM. Two novel structural metrics, namely the structural compliance and stiffness, have been defined based on the pairwise force pattern and they were found to accurately match with the experimental B-factors. These results shed new light on the nature of the experimental B-factors: these are then not only seen as the result of the dynamic fluctuations, but also as the result of the inter-molecular mechanical interactions among the protein residues. The second force application pattern considers random collisions of external particles (water molecules, ions, etc.), simulated via random force bombardment on the protein ELM. By applying random forces on the ELM, it is found that the resulting average displacements are well correlated with the experimental B-factors. Moreover, it was found that the application of random forces only on the external protein surface enhances the good correlation with the experimental flexibility. This second force pattern implies that the B-factors can also be described as the result of the protein-environment interaction, the protein being randomly perturbated by the external particles and undergoing internal deformations.

Future improvements of these methodologies will mainly address at least two points. Exploit the force application patterns to predict the entire anisotropic part of the B-factors, and not only the isotropic values as done in these analyses. Add

the layer of external water molecules in the protein ELM, as it is believed to affect the ELM behavior, especially when forces are applied on the external surface.

The force application patterns shown above are based on the linear response theory since the goal was to simulate small-amplitude protein displacements. However, when proteins undergo conformational transition, that might be highly collective and large-scale, one might wonder whether the linear response theory is sufficient to describe the structural behavior of the protein ELM throughout the transition. As a matter of fact, from Structural Mechanics, we know that spatial ELMs are usually likely to exhibit geometrical non-linearities. For this reason, in Section 3.2, the possible role of geometrical non-linearities was investigated.

Firstly, given the two known end conformations, equilibrium equations were applied on the undeformed (initial) or deformed (final) structure and the results in terms of force fields were compared. From the comparison, it was found that the force fields only match if the involved displacements are very small; conversely, when the displacements are rather high, the forces that equilibrate the structures often differ both in magnitude and directionality. This suggests that non-linearities can indeed be significant within the protein transition. Secondly, to understand whether these non-linearities are only the results of the curvilinear transition pathways (non-linearity of the displacement field) or also the results of a non-linear structural response (non-linearity of the force-displacement curve), the geometrical non-linear analysis has been applied in a step-by-step fashion to the whole transition pathway. Specifically, equilibrium equations have been applied to all the intermediate configurations and the evolution of the force values has been analyzed with respect to the increasing displacements. From the results, it was found that for collective and large-scale conformational changes, e.g. LAO-binding protein, non-linearities can occur both in the displacement field (curvilinear pathways) and structural response (non-linear force-displacement curves for various residues).

These analyses tell us that, in order to fully comprehend and describe protein transitions throughout their entire pathway, geometrical non-linearities should be taken into account when making use of ELMs. However, in this Chapter, the non-linear analysis was carried out under static conditions, i.e. without considering the dynamical features of the ELM. This aspect, i.e. coupling the static non-linear equilibrium equations with the dynamic equations, should be addressed in future works to have a complete comprehension of the dynamic (non-linear) conformational changes of the protein ELM. A further investigation might also include the calculation of stresses and strains developed within the protein structure and see how these are related to biophysical stimuli coming from the surrounding environment. To do this, one might use the ELMs or continuum models such as the ones developed by Bathe [51], where the protein is treated as an elastic continuum solid.

Chapter 4

ELMs and Diagrid Tall Buildings: Introduction and Matrix-Based Method for the Structural Analysis

In the previous Chapters, the ELMs were extensively used to investigate the flexibility and biological behavior of the protein structures. Conversely, in this and the following Chapter, we will move to a completely different research field, which is the field of tall buildings. In particular, the focus of these Chapters will be about a new structural system which is emerging in recent years for tall building design and construction: the diagrids. The diagrid is a tubular structural system placed over the exterior of the building which is composed by an assembly of inclined bars. For this reason, the diagrids can be analyzed via the fundamental equations and characteristics of the ELMs.

In the first Section of this Chapter, a brief overview of the diagrid structural system will be provided. Moreover, a review of the most recent research works about the diagrid preliminary design and structural analysis will be reported. This Section is largely derived from the open-access recent review paper by Scaramozzino et al. [100]. In the remaining part of the Chapter, a dedicated matrix-based method (MBM) will be described, which has been developed in recent years based on the Elastic Lattice modeling, in order to carry out a simplified structural analysis of diagrid systems.

4.1 Overview of the Diagrid Structural Systems

The evolution of tall buildings has experienced a remarkable development in the last century. The first buildings reaching a few tens of stories were built in the United States in the late 19th century, mostly in the cities of New York and Chicago. At the beginning of the 20th century, the race for the realization of the tallest skyscrapers led to the completion of the 102-story tall Empire State Building in 1931 (Figure 4.1a) [100]. Although at that time the height of those buildings was worthy of note, their realization was not achieved by means of significant technological innovations. They usually employed the same steel

frames which were adopted for shorter buildings, leading to excessive material usage and rather over-designed solutions [101]. Bracings were employed to withstand lateral loads arising from wind pressures and earthquake actions. It was already recognized that lateral actions usually govern the design solutions in tall buildings. In fact, as the building becomes taller, the lateral drifts turn out to be more critical, and there is greater demand for suitable structural systems to carry lateral forces. This leads to a dramatic increase of material consumption with the increase in the number of stories, which is usually referred to as the "premium for height" [101,102].

Due to aesthetic and constructability considerations, the bracings were usually embedded within the interior core of the building. Although their shear resistance, based on the axial deformation of the diagonals, was beneficial in resisting the lateral actions, their placement within the interior of the building prevented their effective employment in withstanding the overturning moment. Therefore, new solutions exploiting bracings on the external perimeter of the building were developed. One of the first examples was the 100-story tall John Hancock Center built in Chicago in 1970 (Figure 4.1b). The John Hancock is an example of braced tube, where the mega-diagonals spanning over several stories are effective in resisting the shear and bending moment deriving from lateral actions. The braced tube was a variation of the typical framed tube, where closely spaced perimeter columns were in charge of providing the necessary lateral stiffness. The adoption of mega-diagonals on the external surface offered higher lateral stiffness, while reducing some detrimental phenomena of the framed tube, such as the shear-lag effect. With this new solution, a greater number of stories and an overall enhanced structural performance could be achieved, leading also to important advantages from a material consumption perspective.

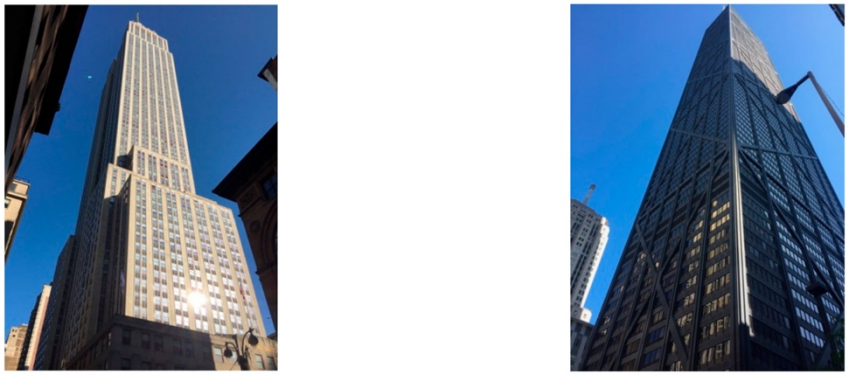

(a) (b)

Figure 4.1. Different structural systems for 20th century tall buildings: (a) moment resisting frame (Empire State Building, New York, NY, USA); (b) braced tube (John Hancock Center, Chicago, IL, USA) [100].

Based on the structural behavior of the braced tube, where vertical columns and external bracings were designed to carry gravity and lateral loads respectively, it was realized that the external mega-diagonals were able to resist vertical and horizontal loads simultaneously, without the need for conventional vertical columns. This led to the realization of the diagrid ("diagonal" + "grid") structural system.

The idea of removing vertical columns and considering only inclined diagonals was not new. As a matter of fact, the first diagrid structure was realized before the construction of the John Hancock braced tube, in the 1920s, by the

Russian architect Vladimir Shukhov, for the realization of a broadcasting tower in Moscow [103]. The external pattern, made up of a triangular tessellation, allowed the reduction of the wind load while reaching a stable stiff configuration. The first application of a diagrid system in building design occurred in the 1960s, with the completion of the 13-story tall IBM Building (Pittsburgh, USA). The steel diagrid exoskeleton was integrated with the glazing system, and assisted in the overall stability of the building [96].

However, it was not until the early 21st century that diagrid systems started to be thoroughly applied in the design and construction of tall buildings. The first examples are the Hearst Tower in New York (Figure 4.2a) and the 30 St. Mary Axe (also known as Swiss Re Tower or The Gherkin) in London (Figure 4.2b), both by Sir Norman Foster. These buildings reached 180 m and provided the first references for the suitability of diagrid systems in tall building design. Thanks to the stiff diagrid façades, which create a pleasant diamond-like pattern, the Hearst Tower was realized using 20% less steel than an equivalent conventional moment frame structure [104]. The aerodynamic form of the Swiss Re Tower, obtained through an external free-form diagrid envelope, allowed the reduction of wind actions on the building, and led to column-free flexible internal spaces [105]. These two examples already showed the valuable features of diagrids for tall buildings: enhanced structural performance, saving of material consumption compared to traditional solutions, and significant aesthetic potential.

Many diagrid structures were realized worldwide in the following years, where various forms and shapes were adopted for the external diagrid façades. Among others, examples worthy of note are the Guangzhou Financial Center, the CCTV Tower and the Poly International Plaza in China, the Tornado Tower (Figure 4.2c) in Qatar, the Capital Gate in Arab Emirates, and the Bow Tower in Canada [103]. Nowadays, most of the built diagrid structures are made of steel, mostly due to the easier and faster construction, simpler joints and less expensive formworks [103]. However, concrete and composite diagrids are also experiencing an increasing popularity, as they allow the realization of even more complex-shaped diagrid patterns, e.g. the O-14 Building in Dubai.

(a) (b) (c)

Figure 4.2. Examples of diagrid systems in tall buildings: (a) Hearst Tower (New York, USA); (b) Swiss Re Tower (London, UK), from https://larryspeck.com/; (c) Tornado Tower (Doha, Qatar), from http://www.asergeev.com/.

The significant use of diagrid systems in recent tall buildings is mainly due to the following reasons: high lateral stiffness (thus low lateral deformability), which allowed to reach the lateral deflection limit target using a lower amount of structural material compared to other conventional systems; architectural

flexibility, allowing a more rational use of the interior space with fewer columns; modularity, which led to the realization of complex-shaped structures of various forms.

These three points arise from the successful use of the triangular module coupled with the inherent structural performance of the tubular structure [106,107]. The triangular element, which is made up of two inclined diagonals and a ring beam, is the basic component of the diagrid façade. The diagonals carry the vertical and lateral loads mostly by axial forces (compression or tension). For this reason, they are usually pinned at the panel nodes, as reflected in Figure 4.3a. Since the inclined diagonals often extend over multiple stories, the external floor beams of the intermediate stories are often supported by the diagonals, which consequently induces slight shear and bending stresses on them. However, in preliminary design stages, these are usually neglected when compared to the high axial stresses arising from the vertical and lateral loads on the building.

In Figure 4.3b, the three-dimensional view of the tubular diagrid structure is shown, as reported in [108]. Usually, the tube-in-tube configuration is found in real diagrid buildings, where an internal (concrete or steel braced) core is coupled with the external diagrid tube. In preliminary design stages, the diagrid is usually designed to carry the lateral actions alone, while the internal core is designed only for gravity loads. Hence, it is the combination of the axial resisting mechanism of the triangular element (Figure 4.3a), characterized by modularity and arrangement flexibility, coupled with the structural efficiency of the tubular configuration (Figure 4.3b), that has ultimately led to the success of the diagrids in recent times.

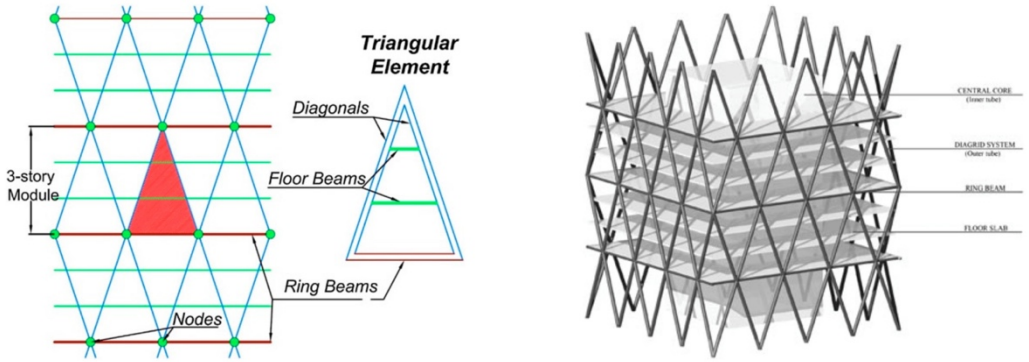

(a) (b)

Figure 4.3. Fundamental diagrid geometrical features: (a) diagrid module and basic triangular element, used with permission from Asadi and Adeli [107]; (b) diagrid tubular configuration, used with permission from Angelucci and Mollaioli [108].

4.1.1 Simplified approaches for the preliminary design of diagrids

The first simplified stiffness-based approach to the preliminary design of diagrid systems was proposed by Moon et al. in 2007 [109]. It is based on the evaluation of the shear and bending stiffness of the diagrid modules, aimed at limiting the lateral deflection of the structure. The building is treated as a vertical cantilever beam, fixed on the ground and subjected to lateral loads. Accordingly, the building undergoes horizontal displacements, which depend on the stiffness of the diagrid tubular structure. For the sake of the preliminary design, the contribution of the internal cores to the lateral stiffness of the building is neglected, as they are only designed to carry gravity loads.

The elementary diagrid module is depicted in Figure 4.4. The diagrid module covers a height h with two triangular elements. The diagonals have a length L_d, and their inclination with respect to the horizontal plane is θ. Depending on the loading direction, each façade can act either as a web or a flange. V_i and M_i are the shear force and bending moment acting on the level of the i^{th} module. These are carried by the web and flange diagonals, respectively. Diagonals are assumed to be pinned at their end, thus carrying only axial force, and remain in the linear elastic regime. In this way, the cross-sectional areas of the web and flange members are the only factors that need to be obtained in order to accomplish the preliminary design.

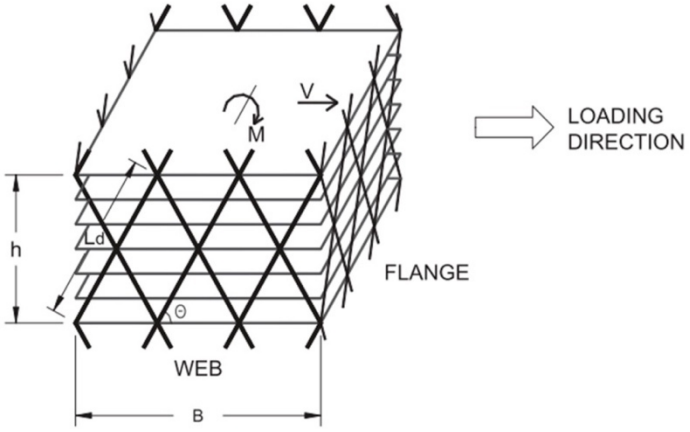

Figure 4.4. Scheme of the elementary diagrid module for the definition of the stiffness-based approach to the diagrid preliminary design. Used with permission from Moon et al. [109].

The shear stiffness $K_{T,i}$ and bending stiffness $K_{B,i}$ of the i^{th} diagrid module link the shear force V_i and bending moment M_i to the module displacement Δu_i and rotation $\Delta\beta_i$, respectively. By applying compatibility, constitutive and equilibrium equations, $K_{T,i}$ and $K_{B,i}$ are obtained as follows:

$$K_{T,i} = 2N_w \left(\frac{A_{d,w,i}E}{L_d}\right) \cos^2\theta, \tag{4.1a}$$

$$K_{M,i} = N_f \left(\frac{B^2 A_{d,f,i}E}{2L_d}\right) \sin^2\theta, \tag{4.1b}$$

where N_w and N_f are the total number of diagonals in the web and flange façade, respectively, $A_{d,w,i}$ and $A_{d,f,i}$ the cross-sectional area of the web and flange members, E the elastic modulus of the diagonals and B the web dimension. The displacement Δu_i and rotation $\Delta\beta_i$ are equal to the product of the module height h and the shear and bending deformation, γ and χ, respectively. Specifying the desired values of shear and bending deformation, γ^* and χ^*, the member dimensions can be easily obtained as [109]:

$$A_{d,w,i} = \frac{V_i L_d}{2N_w Eh\gamma^* \cos^2\theta}, \tag{4.2a}$$

$$A_{d,f,i} = \frac{2M_i L_d}{N_f B^2 Eh\chi^* \sin^2\theta}. \tag{4.2b}$$

Since the horizontal load can act in either direction, the maximum value of the cross-sectional areas from Eqs. (4.2a) and (4.2b) should be assigned to each diagonal, which can act as either a web or flange member. The desired values of γ^* and χ^* are specified based on the desired deformation mode of the building. Assuming that the building sway mechanism is equivalent to the deformation of a cantilever beam, the lateral deflection at the top of the building *u(H)* can be written as follows:

$$u(H) = \gamma^* H + \frac{\chi^* H^2}{2}, \tag{4.3}$$

where $\gamma^* H$ and $\chi^* H^2/2$ are the shear and bending contribution, respectively. In order to assess the relative contribution of bending versus shear deformation, Moon et al. [109] introduce a non-dimensional parameter *s*, given by the ratio of the bending to the shear contribution, i.e.:

$$s = \frac{\chi^* H^2}{2\gamma^* H} = \frac{\chi^* H}{2\gamma^*}. \tag{4.4}$$

Combining Eqs. (4.3) and (4.4), and considering that the top lateral displacement is usually specified as a fraction of the total building height, i.e. $u(H) = H/\alpha$ (α usually being 500), one obtains the following relations between γ^*, χ^* and *s*:

$$\gamma^* = \frac{1}{(1+s)\alpha}, \tag{4.5a}$$

$$\chi^* = \frac{2\gamma^* s}{H} = \frac{2s}{(1+s)\alpha H}. \tag{4.5b}$$

Substituting Eqs. (4.5a) and (4.5b) into Eqs. (4.2a) and (4.2b), the member sizes can be obtained for the different values of the parameters.

Adopting different *s* values leads to different preliminary sizing for the external diagonals. When *s* is extremely low, the shear deformation mode of the structure prevails over the bending mode, and this leads to excessive material usage in the flange members to limit the bending deflection. Conversely, when *s* is high, the bending deformation prevails, and the obtained cross-sectional areas are mainly governed by the web façades to limit the shear deformability. Therefore, an optimal value of *s* is shown to exist, s_{opt}, which balances the need to limit both shear and bending deformability [109]. In this case, the member sizes at the higher stories are usually governed by the shear deformation, while the ones at the lower stories are mostly controlled by the bending deformation. The s_{opt} depends on the building aspect ratio (*H/B*) and leads to the most efficient solutions that comply with the target maximum displacement while employing the minimum amount of material. For diagrid structures taller than 40 stories, with *H/B* greater than 5 and diagonal angles between 60° and 70°, the empirical equation $s_{opt} = H/B - 3$ is proposed [109].

The other fundamental parameter that plays a key role in the preliminary design of diagrids is the diagonal inclination. Investigating a set of 20- to 60-story tall buildings, Moon et al. [109] show that, for diagrid structures with aspect ratios of about 7, the optimal angle is between 65° and 75°, whereas for diagrids with aspect ratios of about 5 the optimal angle is lower, at around 10°. This is due to

the competition between shear and bending stiffnesses in governing the deformation mode, and their dependence on the diagonal angle. Shear rigidity is maximum when the diagonal inclination is about 35°, while bending rigidity achieves its maximum value when the elements are vertical, i.e. $\theta = 90°$. The optimal value for maximizing both shear and bending rigidity lies between these two. Since shear mechanism prevails in shorter buildings and bending prevails in taller ones, it is expected that, as the aspect ratio increases, the building behaves more like a bending beam, and the optimal angle thus increases [109]. This consideration has been strongly exploited in the analysis and design of diagrid systems, by considering various angle-based strategies and patterns for optimizing the diagrid performance, as will be shown in the next Chapter.

The same stiffness-based approach reported in the previous paragraphs is also applied by Moon to braced tubes in [110]. In this case, the shear force is carried by the external mega-diagonals, while the bending moment is carried by the perimeter vertical columns. Analyses based on 40- to 100-story tall braced tubes show that the optimal angle in this case is close to 45°, and is less dependent on the building aspect ratio. This is due to the negligible involvement of external diagonals in carrying bending moment. For braced tubes with an aspect ratio greater than 6, Moon suggests a different empirical equation for the optimal s value, i.e. $s_{opt} = (H/B)/2 - 1$ [110]. It has to be noted that, in the same paper, the same analysis has been applied to diagrids with a broader range of heights than previously analyzed, i.e. from 40 to 100 stories. As a result, the author proposes a new empirical equation for the s_{opt} for diagrid structures with aspect ratios greater than 6, i.e. $s_{opt} = H/B - 2$.

In the cases investigated by Moon [109,110], it is found that the stiffness requirements drive the preliminary design, and the strength criteria are usually fulfilled. Only a few members in the leeward façade of the building are found to fail when the maximum allowable displacement is increased, i.e. $\alpha < 500$. However, thanks to the high rigidity of the diagonalized façades, which make the diagrid structure highly efficient, strength requirements may be of paramount importance, and in specific cases, they might even govern the design criteria, as suggested by Montuori et al. in [111]. In this paper, a simplified strength-based methodology for the preliminary design of diagrid tubes is provided. Figure 4.5 shows the adopted scheme for the development of the strength-based approach. Both gravity and lateral loads are applied to the building.

Assuming that the internal core occupies 25% of the floor area, the diagrid carries 37.5% of the gravity load at the level of the m^{th} module, Q_m (Figure 4.5a). This vertical loading condition generates a uniform compression state in all the n_k diagonals of the module, $N_{m,k,Q} = 0.375 Q_m \sin\theta / 2 n_k$. Conversely, the lateral loads generate the bending moment M_m and shear force V_m at the module level. The former induces a uniform compression state in the diagonals of the leeward flange, a uniform tension state in the windward flange and a linear distribution of tension–compression axial forces in the webs, depending on the distance d_i of the i^{th} diagonal from the center of the floor (Figure 4.5b). This leads to the expression of the axial force $N_{m,k,M} = \pm M_m d_k \sin\theta / 2\Sigma d_i$. Conversely, the shear force induces only tension–compression stresses in the web diagonals, therefore $N_{m,k,V} = \pm V_m \cos\alpha_k \cos\theta / 2\Sigma\cos\alpha_i$, α being the direction of the horizontal force with respect to the orientation of the diagrid module (Figure 4.5c).

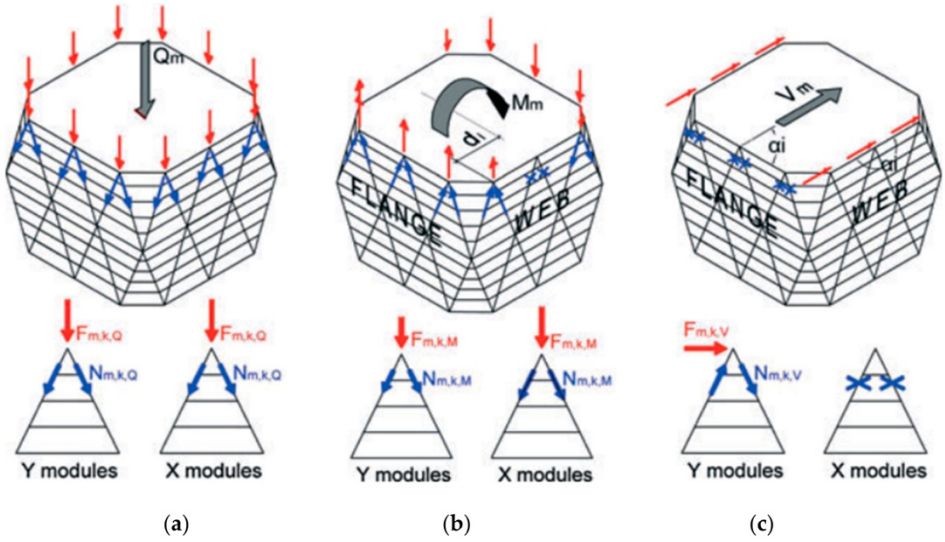

Figure 4.5. Scheme of the elementary diagrid module for the definition of the strength-based approach to the diagrid preliminary design, under: (a) gravity loads; (b) overturning moment; (c) shear force. Used with permission from Montuori et al. [111].

Considering all the loading conditions, one obtains the total axial force in the generic diagonal, as $N_{m,k} = N_{m,k,Q} + N_{m,k,M} + N_{m,k,V}$. This value is finally used to define the member size, based on the tensile strength and the buckling compressive resistance of the diagonal. In the same paper, the authors also propose an analytical formulation, based on the Euler–Bernoulli and Timoshenko beam theories, to obtain an alternative optimal s value for the stiffness-based approach, i.e. $s_{opt} = 0.19H^2/\tan\theta L^2$.

The strength- and stiffness-based approaches are simultaneously applied in the preliminary design of a rectangular, 100-story tall diagrid tube, considering three different diagonal angles (64°, 69° and 79°), under both gravity and wind loads. The results show that, on the broad side of the building, strength requirements always prevail at the upper modules, whereas stiffness criteria drive the design of the lower modules. Conversely, on the shorter side, strength prevails over stiffness for the entire height of the building with θ = 64°, and stiffness prevails for θ = 79°, while in the case of 69° (which is close to the optimal angle inclination) the stiffness- and strength-based approaches provide almost the same result [111].

After carrying out the structural analyses on the designed buildings, it is found that the stiffness-based methodology leads to very efficient structures as regards the top lateral deflection, which is very close to the target value. However, this approach usually leads to unsatisfactory results in terms of the inter-story drift of the upper modules, as well as in terms of member strength demand-to-capacity ratio (DCR). In fact, besides the case of θ = 79°, where only 0.3% of the diagonals fail the strength requirements, 26% and 23% of them exhibit DCR greater than 1, for θ = 64° and 69°, respectively. On the contrary, adopting the strength-based design, the fraction of elements with DCR greater than 1 is 0%, 0.5% and 0.3%, for θ = 64°, 69° and 79°, respectively. However, with this approach, unsatisfactory results are obtained in terms of lateral deformability, especially in the case of 69° and 79° [111]. Therefore, stiffness-based approaches might lead to unsatisfactory strength results, while strength criteria might fail stiffness requirements. A compromise should then be found depending on the specific building characteristics. In both cases, large inter-story drifts are usually found at the upper modules.

Further investigation regarding the suitability of stiffness- and strength-based criteria for the preliminary design is subsequently developed for a broader range of diagrid structures [112,113]. In [112], Mele investigates the effect of both approaches on 90-story tall diagrid tubes, with diagonal angles of 60°, 70° and 80°. The results are in line with the previous findings. For smaller diagonal angles, strength usually drives the design, while the stiffness-based approach leads to inadequate DCR values. For greater angles, the stiffness-based design prevails, while strength criteria lead to excessive lateral deflections. In the range of the optimal angle, both criteria concur in defining the member sizes.

More recently, the effect of both slenderness and diagonal angle has been taken into account simultaneously for the preliminary design [113]. Diagrids with aspect ratios ranging from 2 to 8, and diagonal angles from 50° to 80°, are considered. It is found that, for those with an aspect ratio from 2 to 4, the design is mainly governed by strength requirements, independently of the diagrid angle, and the "premium for height" is mostly linear with the increase of slenderness. Conversely, for aspect ratios greater than 6, the design is mainly driven by stiffness, and the weight increases more than linearly with the slenderness. Aspect ratios around 5 are found to be the threshold, where stiffness- and strength-based designs provide comparable solutions [113]. Based on these results, it is concluded that, due to the extreme rigidity of the diagrid tubular system, it is not always possible to know a priori whether stiffness- or strength-based criteria should be considered for the preliminary design. Both approaches are necessary and unavoidable, and none of them should be used without the other [111]. The geometrical diagrid parameters, e.g. building aspect ratio and diagonal angle, drive the prevalence of one over the other.

In any case, simplified approaches for the preliminary design represent an effective way to quickly define and assess the structural characteristics and performance of the diagrid.

4.1.2 Methods for the structural analysis of diagrid systems

In the academic literature, the most common procedure to deal with the structural analysis of diagrid systems is the Finite Element Method (FEM). However, simplified methodologies have also been developed for a quick evaluation of the diagrid overall structural behavior.

Mele et al. [114] have proposed a hand-based method for the evaluation of the axial stress in the diagrid members. The method is based on the analysis of the internal forces arising in the basic triangular element due to gravity and vertical loads, taking also into account the effect of the horizontal and vertical curvatures of the diagrid façade. Although it does not allow the direct calculation of the displacements of the structure, this methodology has proven effective in the computation of the axial forces in the diagonals. It is applied to three real case studies, the Swiss Re Building (London), the Hearst Headquarters (New York) and West Tower (Guangzhou), and the axial stresses arising from hand-calculations show a very good correspondence with FEM results. Design considerations regarding the optimal diagonal inclination for the investigated cases are also provided.

More recently, Liu and Ma have developed a simplified methodology, called the modular method (MM), to perform the structural analysis of diagrid tubes with an arbitrary polygonal shape [115]. So far, most of the research has been focused on rectangular diagrids, having vertical façades acting as webs or flanges (Figures

4.4 and 4.5); however, little attention has been paid to diagrids with polygonal shapes.

The modular method relies on the modularization of the diagrid and the calculation of the lateral stiffness of the diagrid modules in order to compute the total lateral deflection. The lateral displacement u_i of the i^{th} module can be obtained by superimposing the contribution of the shear displacement $u_{V,i}$ and bending displacement $u_{M,i}$. Based on the evaluation of the shear and bending rigidity of the i^{th} module, $K_{V,i}$ and $K_{M,i}$, the two contributions can be computed as follows:

$$u_{V,i} = \frac{V_1}{K_{V,1}} + \frac{V_2}{K_{V,2}} + \cdots + \frac{V_i}{K_{V,i}}, \tag{4.6a}$$

$$u_{M,i} = \frac{M_1}{K_{M,1}} hi + \frac{M_2}{K_{M,2}} h(i-1) + \cdots + \frac{M_i}{K_{M,i}} h[i-(i-1)], \tag{4.6b}$$

where V_i and M_i are the shear force and bending moment at the level of the i^{th} module, respectively, and h the height of the module. The key to the MM is the calculation of the shear and bending rigidities, $K_{V,i}$ and $K_{M,i}$, which is based on the usual assumptions for diagrid tubes: the diagonals are only subjected to axial stress and remain in the linear elastic regime; the building floors behave as rigid bodies without any internal deformation; the intra-module floors are neglected for the calculation of the modular rigidities.

Shear rigidity is defined as the total shear force F_V required for unitary horizontal displacement of the module Δv (Figure 4.6a), and bending rigidity is defined as the bending moment M required for unitary floor rotation $\Delta\beta$ (Figure 4.6b). Applying independently unitary floor displacements and rotations, and computing the total shear force and bending moment, leads to the direct evaluation of $K_{V,i}$ and $K_{M,i}$. The calculation of the shear force and bending moment is based on the geometrical compatibility equations, the constitutive relations of the diagonals, and finally the equilibrium equations at the level of the floor. This finally allows one to obtain the following formulations for K_V and K_M:

$$K_V = \frac{EA\cos^2\theta\sin\theta\sin\gamma}{h}\sum_{d=1}^{N}\cos^2\alpha_d + \frac{EA\sin^3\theta\cos^2\gamma\sin\gamma}{h}\sum_{d=1}^{N}\sin^2\alpha_d, \tag{4.7a}$$

$$K_M = \frac{EA\sin^3\theta\sin^3\gamma}{h}\sum_{d=1}^{N}{B_d}^2, \tag{4.7b}$$

where E and A are the Young modulus and cross-sectional areas of the diagonals, θ the angle between the diagonal and the main ring beam in the façade, γ the angle between the ring beam plane and the façade, N the number of total diagonals in the module, α the angle between the ring beam and shear direction, and B_d is the distance between the diagonal d and the neutral axis in the main ring beam plane [115]. Note that Eqs. (4.7a) and (4.7b) resemble Eqs. (4.1a) and (4.1b), but they also include the effect of not-vertical façades (γ angle) and polygonal planar shapes (α angle). Making use of Equations (4.7a) and (4.7b) for each module, together with the application of Equations (4.6a) and (4.6b), one can finally evaluate the lateral deformation of the diagrid building under horizontal loads.

The MM is verified against FEM calculations, analyzing square, hexagonal and octagonal diagrid tubes with vertical and inclined façades under different

horizontal loading conditions. The variations, in terms of top displacement, from the FEM results are always within 10%, which verifies the proposed methodology. Based on the evaluation of the shear and bending rigidities, the MM is also employed to define the analytical framework for the preliminary design of diagrids [115].

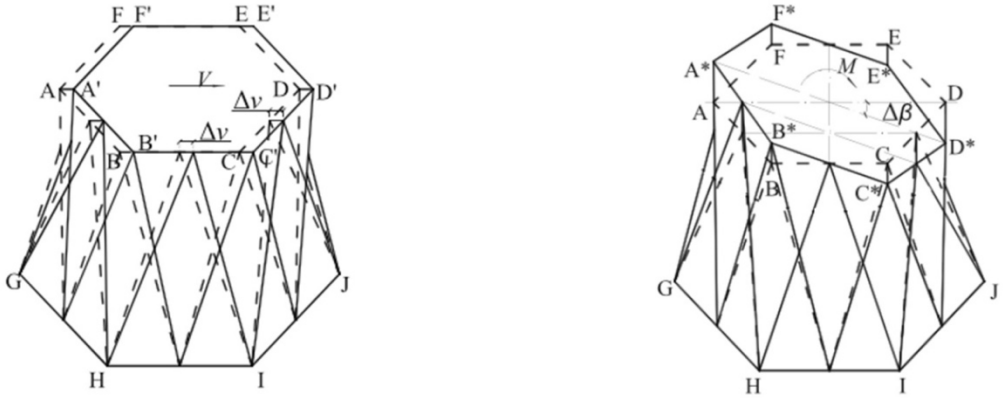

Figure 4.6. Scheme for the calculation of (a) shear rigidity and (b) bending rigidity, according to the modular method (MM). Used with permission from Liu and Ma [115].

Subsequently, a new method has been developed for the structural analysis of diagrids by Scaramozzino [116] and subsequently published by Lacidogna et al. [117], which has been called the matrix-based method (MBM). This methodology is grounded on the matrix calculus applied to the ELMs. This strategy drastically reduces the degrees of freedom (DOFs) of the diagrid structure with respect to the FE calculations, while capturing the overall building behavior. The method will be thoroughly described in the following Section.

4.2 Matrix-based Method (MBM) for the Structural Analysis of Diagrid Systems

The matrix-based method (MBM) shown in this Section has been recently developed for the structural analysis of diagrid systems in [116,117]. It is based on the direct calculation of the stiffness matrix of the structure with respect to the DOFs of the floors. In order to focus on the global behavior of the building and coherently with the other studies in the literature [109,114,115], the floors are considered as rigid bodies in the three-dimensional space. Their motion can then be described by means of six DOFs, i.e. three displacements and three rotations. Therefore, for the most general case of a three-dimensional diagrid structure counting N floors, the MBM yields the consideration of a total of $6N$ DOFs.

The hypotheses behind the formulation of the MBM, that allows to reduce the computational cost of the structural problem, are the same considered by the previous researchers: the external diagonals are only subjected to the axial stress and remain within the linear elastic regime; the floors are considered as rigid bodies with no internal deformation; the floors included within the triangular module of the diagrid (the green ones in Figure 4.3a) are neglected. As a consequence of the last assumption, the total number of floors N only refers to the ones lying at the end of the pinned diagonals (the red ones in Figure 4.3a).

Based on these hypotheses, the general structural problem in the linear elastic regime can be formulated by means of the following matrix relationship:

$$\boldsymbol{F} = \boldsymbol{K}\boldsymbol{\delta}, \tag{4.8}$$

being $\boldsymbol{F}$ and $\boldsymbol{\delta}$ the $6N \times 1$ generalized force and displacement vector, respectively, and $\boldsymbol{K}$ the $6N \times 6N$ stiffness matrix of the entire diagrid structure. $\boldsymbol{F}$ contains the forces and moments applied to the floor centroids, while $\boldsymbol{\delta}$ contains the corresponding displacements and rotations. Equation (4.8) can be further expanded by distinguishing the translational and rotational DOFs of the floors as follows:

$$\begin{Bmatrix} \boldsymbol{F_x} \\ \boldsymbol{F_y} \\ \boldsymbol{M_z} \\ \boldsymbol{M_x} \\ \boldsymbol{M_y} \\ \boldsymbol{F_z} \end{Bmatrix} = \begin{bmatrix} \boldsymbol{K_{F_x\delta_x}} & \boldsymbol{K_{F_x\delta_y}} & \boldsymbol{K_{F_x\varphi_z}} & \boldsymbol{K_{F_x\varphi_x}} & \boldsymbol{K_{F_x\varphi_y}} & \boldsymbol{K_{F_x\delta_z}} \\ \boldsymbol{K_{F_y\delta_x}} & \boldsymbol{K_{F_y\delta_y}} & \boldsymbol{K_{F_y\varphi_z}} & \boldsymbol{K_{F_y\varphi_x}} & \boldsymbol{K_{F_y\varphi_y}} & \boldsymbol{K_{F_y\delta_z}} \\ \boldsymbol{K_{M_z\delta_x}} & \boldsymbol{K_{M_z\delta_y}} & \boldsymbol{K_{M_z\varphi_z}} & \boldsymbol{K_{M_z\varphi_x}} & \boldsymbol{K_{M_z\varphi_y}} & \boldsymbol{K_{M_z\delta_z}} \\ \boldsymbol{K_{M_x\delta_x}} & \boldsymbol{K_{M_x\delta_y}} & \boldsymbol{K_{M_x\varphi_z}} & \boldsymbol{K_{M_x\varphi_x}} & \boldsymbol{K_{M_x\varphi_y}} & \boldsymbol{K_{M_x\delta_z}} \\ \boldsymbol{K_{M_y\delta_x}} & \boldsymbol{K_{M_y\delta_y}} & \boldsymbol{K_{M_y\varphi_z}} & \boldsymbol{K_{M_y\varphi_x}} & \boldsymbol{K_{M_y\varphi_y}} & \boldsymbol{K_{M_y\delta_z}} \\ \boldsymbol{K_{F_z\delta_x}} & \boldsymbol{K_{F_z\delta_y}} & \boldsymbol{K_{F_z\varphi_z}} & \boldsymbol{K_{F_z\varphi_x}} & \boldsymbol{K_{F_z\varphi_y}} & \boldsymbol{K_{F_z\delta_z}} \end{bmatrix} \begin{Bmatrix} \boldsymbol{\delta_x} \\ \boldsymbol{\delta_y} \\ \boldsymbol{\varphi_z} \\ \boldsymbol{\varphi_x} \\ \boldsymbol{\varphi_y} \\ \boldsymbol{\delta_z} \end{Bmatrix}, \tag{4.9}$$

being $\boldsymbol{F_x}$, $\boldsymbol{F_y}$ and $\boldsymbol{F_z}$ the floor forces along the axes X, Y and Z, respectively, and $\boldsymbol{\delta_x}$, $\boldsymbol{\delta_y}$ and $\boldsymbol{\delta_z}$ the corresponding displacements, $\boldsymbol{M_z}$ the in-plane torque moments acting around the vertical axis Z and $\boldsymbol{\varphi_z}$ the corresponding torsional rotations, $\boldsymbol{M_x}$ and $\boldsymbol{M_y}$ the out-of-plane moments acting along the horizontal axes X and Y and $\boldsymbol{\varphi_x}$ and $\boldsymbol{\varphi_y}$ the corresponding out-of-plane rotations. Figure 4.7a reports the convention adopted for the axes, displacements and rotations in the three-dimensional reference system.

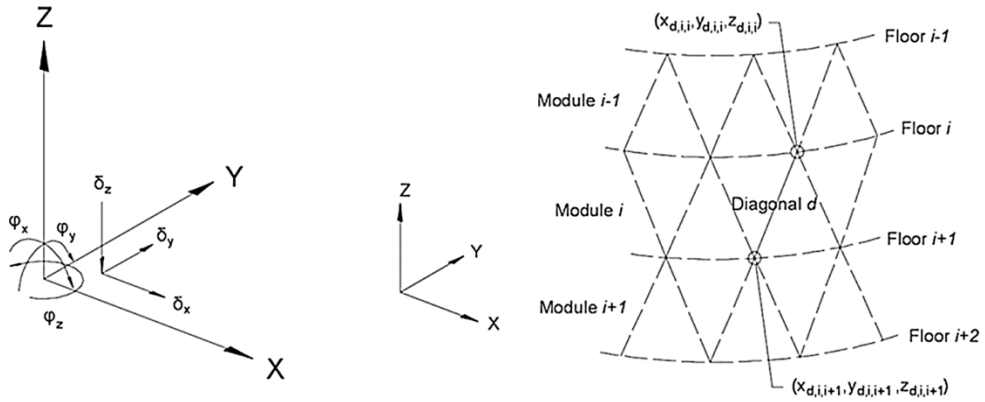

(a) (b)

Figure 4.7. Conventions for three-dimensional diagrid structure: (a) displacements and rotations of the floors; (b) floors and modules numbering and subscripts of diagonal coordinates. Used with permission from Lacidogna et al. [117].

In Eq. (4.9), the $6N \times 6N$ stiffness matrix $\boldsymbol{K}$ is represented through the partitioning based on the translational and rotational DOFs of the system. In this way, it can be written as a 6×6 matrix made up of $N \times N$ sub-matrices $\boldsymbol{K_{\alpha,\beta}}$, where $\boldsymbol{\alpha}$ and $\boldsymbol{\beta}$ represent one of the entries of the force and displacement vector, respectively. For example, $\boldsymbol{K_{F_x\delta_x}}$ represents the $N \times N$ stiffness matrix that relates the horizontal forces along the X direction with the corresponding horizontal displacements. The thirty-six matrices reported in Eq. (4.9) constitute all the

combination between the forces and moments acting on the floors and the corresponding translational and rotational DOFs.

As reported in [116,117], the MBM relies on the direct calculation of the stiffness matrix $\boldsymbol{K}$ in Eq. (4.9), by means of the displacement method. This is applied in the following way to compute each element *i-j* of the generic sub-matrix $\boldsymbol{K_{\alpha,\beta}}$: (1) a unitary displacement or a unitary rotation (depending on $\boldsymbol{\beta}$) is applied to the j^{th} floor; (2) based on the imposed displacements, the deformations and the axial forces of the diagonals included within the deformed modules are computed, through the kinematic and constitutive relationships; (3) the total reactive force or the total reactive moments (depending on $\boldsymbol{\alpha}$) at the i^{th} floor is evaluated, through equilibrium equations. By means of this procedure, one is able to analytically compute all the stiffness coefficients in each sub-matrix in Eq. (4.9), and finally evaluate the whole stiffness matrix of the diagrid structure. Note that, due to the property of symmetry of the stiffness matrices, $\boldsymbol{K}$ is symmetric, therefore only twenty-one sub-matrices need to be actually calculated, out of the thirty-six reported in Eq. (4.9).

Equation (4.9) can be presented in a simplified way to separate the DOFs that generate horizontal displacements of the floors, i.e. $\boldsymbol{\delta_x}$, $\boldsymbol{\delta_y}$ and $\boldsymbol{\varphi_z}$, and the ones generating vertical displacements, i.e. $\boldsymbol{\varphi_x}$, $\boldsymbol{\varphi_y}$ and $\boldsymbol{\delta_z}$:

$$\begin{Bmatrix} \boldsymbol{F_H} \\ \boldsymbol{F_V} \end{Bmatrix} = \begin{bmatrix} \boldsymbol{K_{HH}} & \boldsymbol{K_{HV}} \\ \boldsymbol{K_{VH}} & \boldsymbol{K_{VV}} \end{bmatrix} \begin{Bmatrix} \boldsymbol{\delta_H} \\ \boldsymbol{\delta_V} \end{Bmatrix}, \tag{4.10}$$

being $\boldsymbol{F_H}$ the $3N \times 1$ vector of generalized horizontal forces ($\boldsymbol{F_x}$, $\boldsymbol{F_y}$ and $\boldsymbol{M_z}$) and $\boldsymbol{\delta_H}$ the generalized horizontal displacements ($\boldsymbol{\delta_x}$, $\boldsymbol{\delta_y}$ and $\boldsymbol{\varphi_z}$), $\boldsymbol{F_V}$ the $3N \times 1$ vector of generalized vertical forces ($\boldsymbol{M_x}$, $\boldsymbol{M_y}$ and $\boldsymbol{F_z}$) and $\boldsymbol{\delta_V}$ the generalized horizontal displacements ($\boldsymbol{\varphi_x}$, $\boldsymbol{\varphi_y}$ and $\boldsymbol{\delta_z}$).

Based on this partitioning, the stiffness matrix is a formal 2×2 matrix, where the four sub-matrices are $3N \times 3N$ stiffness sub-matrices relating the horizontal and vertical DOFs to the generalized horizontal and vertical force vectors. Based on the symmetry of the stiffness matrix, it follows that $\boldsymbol{K_{VH}} = \boldsymbol{K_{HV}}^{\boldsymbol{T}}$. In the following paragraphs, the analytical equations for the computation of the stiffness coefficients of $\boldsymbol{K_{HH}}$, $\boldsymbol{K_{VV}}$ and $\boldsymbol{K_{HV}}$ will be reported.

4.2.1 Direct calculation of the stiffness coefficients

As mentioned above, the coefficients within each stiffness matrix are directly computed through the displacement method, which relies on the application of unitary displacements/rotations, subsequent evaluation of the axial stresses in the deformed diagonals and final calculation of the total equilibrium forces/moments acting at the level of the floor centroids [117].

4.2.1.1 Calculation of the K_{HH} sub-matrix

Based on the partitioning of the stiffness matrix presented in Eqs. (4.9) and (4.10), $\boldsymbol{K_{HH}}$ contains nine sub-matrices which relate the horizontal forces $\boldsymbol{F_x}$ and $\boldsymbol{F_y}$ and torque moments $\boldsymbol{M_z}$ to the corresponding horizontal displacements $\boldsymbol{\delta_x}$ and $\boldsymbol{\delta_y}$ and torsional rotations $\boldsymbol{\varphi_z}$. Due to the symmetry of the matrix $\boldsymbol{K_{HH}}$, only six

sub-matrices need to be calculated, e.g. $\boldsymbol{K_{F_x\delta_x}}$, $\boldsymbol{K_{F_y\delta_y}}$, $\boldsymbol{K_{F_x\delta_y}}$, $\boldsymbol{K_{M_z\varphi_z}}$, $\boldsymbol{K_{F_x\varphi_z}}$, $\boldsymbol{K_{F_y\varphi_z}}$.

Based on the methodology explained above, the generic *i-j* element of $\boldsymbol{K_{F_x\delta_x}}$ is calculated by applying an unitary displacement along the X axis on the j^{th} floor, while keeping all the other floors fixed, and computing the total reactive force along the X direction at the i^{th} floor. Consequently, it is easy to show that $\boldsymbol{K_{F_x\delta_x}}$ is a tri-diagonal matrix, whit values different from zero only for $i = j - 1$, j and $j + 1$. Note that this holds true for all the thirty-six matrices in Eq. (4.8). Eventually, one obtains:

$$\left(K_{F_x\delta_x}\right)_{j-1,j} = -\sum_{d=1}^{n_{j-1}} E_{d,j-1}A_{d,j-1}\frac{{\Delta x_{d,j-1}}^2}{{L_{d,j-1}}^3}, \tag{4.11a}$$

$$\left(K_{F_x\delta_x}\right)_{j,j} = \sum_{d=1}^{n_{j-1}} E_{d,j-1}A_{d,j-1}\frac{{\Delta x_{d,j-1}}^2}{{L_{d,j-1}}^3} + \sum_{d=1}^{n_j} E_{d,j}A_{d,j}\frac{{\Delta x_{d,j}}^2}{{L_{d,j}}^3}, \tag{4.11b}$$

$$\left(K_{F_x\delta_x}\right)_{j+1,j} = -\sum_{d=1}^{n_j} E_{d,j}A_{d,j}\frac{{\Delta x_{d,j}}^2}{{L_{d,j}}^3}, \tag{4.11c}$$

being $E_{d,j}$, $A_{d,j}$ and $L_{d,j}$ the Young's Modulus, cross-sectional area and length of the d^{th} diagonal in the j^{th} module, $\Delta x_{d,j}$ the difference of the X-coordinates of the diagonal end nodes referred to the j^{th} module. See Figure 4.7b and [116,117] for more details about the numberings of the floors and diagrid modules. Similarly to Eqs. (4.11), the stiffness coefficients of $\boldsymbol{K_{F_y\delta_y}}$ can be obtained as:

$$\left(K_{F_y\delta_y}\right)_{j-1,j} = -\sum_{d=1}^{n_{j-1}} E_{d,j-1}A_{d,j-1}\frac{{\Delta y_{d,j-1}}^2}{{L_{d,j-1}}^3}, \tag{4.12a}$$

$$\left(K_{F_y\delta_y}\right)_{j,j} = \sum_{d=1}^{n_{j-1}} E_{d,j-1}A_{d,j-1}\frac{{\Delta y_{d,j-1}}^2}{{L_{d,j-1}}^3} + \sum_{d=1}^{n_j} E_{d,j}A_{d,j}\frac{{\Delta y_{d,j}}^2}{{L_{d,j}}^3}, \tag{4.12b}$$

$$\left(K_{F_y\delta_y}\right)_{j+1,j} = -\sum_{d=1}^{n_j} E_{d,j}A_{d,j}\frac{{\Delta y_{d,j}}^2}{{L_{d,j}}^3}, \tag{4.12c}$$

being $\Delta y_{d,j}$ the difference of the Y-coordinates of the d^{th} diagonal end nodes referred to the j^{th} module.

The stiffness coefficients of the out-of-diagonal sub-matrix $\boldsymbol{K_{F_x\delta_y}}$ can be obtained by applying displacements along the Y direction and computing the total reacting force along the X direction, obtaining:

$$\left(K_{F_x\delta_y}\right)_{j-1,j} = -\sum_{d=1}^{n_{j-1}} E_{d,j-1}A_{d,j-1}\frac{\Delta x_{d,j-1}\Delta y_{d,j-1}}{{L_{d,j-1}}^3}, \tag{4.13a}$$

$$\left(K_{F_x\delta_y}\right)_{j,j} = \sum_{d=1}^{n_{j-1}} E_{d,j-1}A_{d,j-1}\frac{\Delta x_{d,j-1}\Delta y_{d,j-1}}{{L_{d,j-1}}^3} + \sum_{d=1}^{n_j} E_{d,j}A_{d,j}\frac{\Delta x_{d,j}\Delta y_{d,j}}{{L_{d,j}}^3}, \tag{4.13b}$$

$$\left(K_{F_x\delta_y}\right)_{j+1,j} = -\sum_{d=1}^{n_j} E_{d,j}A_{d,j}\frac{\Delta x_{d,j}\Delta y_{d,j}}{{L_{d,j}}^3}. \tag{4.13c}$$

Note that for symmetric buildings, it follows that $\boldsymbol{K_{F_x\delta_y}}$ is completely null.

The calculation of $\boldsymbol{K_{M_z\varphi_z}}$, $\boldsymbol{K_{F_x\varphi_z}}$ and $\boldsymbol{K_{F_y\varphi_z}}$ is a bit more complicated, from an analytical point of view, as the MBM relies on the application of unitary torsional rotations $\boldsymbol{\varphi_z}$ and consequent calculation of torque moments $\boldsymbol{M_z}$ and horizontal forces $\boldsymbol{F_x}$ and $\boldsymbol{F_y}$. Accordingly, one obtains the following expressions for the coefficients of $\boldsymbol{K_{M_z\varphi_z}}$:

$$\begin{aligned}\left(K_{M_z\varphi_z}\right)_{j-1,j} = -\sum_{d=1}^{n_{j-1}} \frac{E_{d,j-1}A_{d,j-1}}{{L_{d,j-1}}^3}\big[&(x_{d,j-1,j-1}-x_{C,j-1})(x_{d,j-1,j}-x_{C,j})\Delta {y_{d,j-1}}^2\\ &+(y_{d,j-1,j-1}-y_{C,j-1})(y_{d,j-1,j}-y_{C,j})\Delta {x_{d,j-1}}^2\\ &-(x_{d,j-1,j-1}-x_{C,j-1})(y_{d,j-1,j}-y_{C,j})\Delta x_{d,j-1}\Delta y_{d,j-1}\\ &-(y_{d,j-1,j-1}-y_{C,j-1})(x_{d,j-1,j}-x_{C,j})\Delta x_{d,j-1}\Delta y_{d,j-1}\big],\end{aligned} \tag{4.14a}$$

$$\begin{aligned}\left(K_{M_z\varphi_z}\right)_{j,j} = &\sum_{d=1}^{n_{j-1}} \frac{E_{d,j-1}A_{d,j-1}}{{L_{d,j-1}}^3}\big[(x_{d,j-1,j}-x_{C,j})\Delta y_{d,j-1}-(y_{d,j-1,j}-y_{C,j})\Delta x_{d,j-1}\big]^2\\ &+\sum_{d=1}^{n_j} \frac{E_{d,j}A_{d,j}}{{L_{d,j}}^3}\big[(x_{d,j,j}-x_{C,j})\Delta y_{d,j}-(y_{d,j,j}-y_{C,j})\Delta x_{d,j}\big]^2,\end{aligned} \tag{4.14b}$$

$$\begin{aligned}\left(K_{M_z\varphi_z}\right)_{j+1,j} = -\sum_{d=1}^{n_j} \frac{E_{d,j}A_{d,j}}{{L_{d,j}}^3}\big[&(x_{d,j,j}-x_{C,j})(x_{d,j,j+1}-x_{C,j+1})\Delta {y_{d,j}}^2\\ &+(y_{d,j,j}-y_{C,j})(y_{d,j,j+1}-y_{C,j+1})\Delta {x_{d,j}}^2\\ &-(x_{d,j,j}-x_{C,j})(y_{d,j,j+1}-y_{C,j+1})\Delta x_{d,j}\Delta y_{d,j}\\ &-(y_{d,j,j}-y_{C,j})(x_{d,j,j+1}-x_{C,j+1})\Delta x_{d,j}\Delta y_{d,j}\big],\end{aligned} \tag{4.14c}$$

being $x_{C,j}$ and $y_{C,j}$ the X and Y coordinate of the centroid of the j^{th} floor, while $x_{d,j,j}$ and $y_{d,j,j}$ are the X and Y coordinate of the end nodes of the d^{th} diagonal contained within the j^{th} module and referring to the j^{th} floor (see Figure 4.7b). Similarly, the analytical expression of the coefficients of $\boldsymbol{K_{F_x\varphi_z}}$ and $\boldsymbol{K_{F_y\varphi_z}}$ is obtained as follows:

$$\begin{aligned}\left(K_{F_x\varphi_z}\right)_{j-1,j} = \sum_{d=1}^{n_{j-1}} \frac{E_{d,j-1}A_{d,j-1}}{{L_{d,j-1}}^3}\big[&(y_{d,j-1,j}-y_{C,j})\Delta {x_{d,j-1}}^2\\ &-(x_{d,j-1,j}-x_{C,j})\Delta x_{d,j-1}\Delta y_{d,j-1}\big],\end{aligned} \tag{4.15a}$$

$$\begin{aligned}\left(K_{F_x\varphi_z}\right)_{j,j} = &\sum_{d=1}^{n_{j-1}} \frac{E_{d,j-1}A_{d,j-1}}{{L_{d,j-1}}^3}\big[(x_{d,j-1,j}-x_{C,j})\Delta x_{d,j-1}\Delta y_{d,j-1}\\ &-(y_{d,j-1,j}-y_{C,j})\Delta {x_{d,j-1}}^2\big]\\ &+\sum_{d=1}^{n_j} \frac{E_{d,j}A_{d,j}}{{L_{d,j}}^3}\big[(x_{d,j,j}-x_{C,j})\Delta x_{d,j}\Delta y_{d,j}-(y_{d,j,j}-y_{C,j})\Delta {x_{d,j}}^2\big],\end{aligned} \tag{4.15b}$$

$$\left(K_{F_x\varphi_z}\right)_{j+1,j} = \sum_{d=1}^{n_j} \frac{E_{d,j}A_{d,j}}{{L_{d,j}}^3}\big[(y_{d,j,j}-y_{C,j})\Delta {x_{d,j}}^2-(x_{d,j,j}-x_{C,j})\Delta x_{d,j}\Delta y_{d,j}\big], \tag{4.15c}$$

$$\begin{aligned}\left(K_{F_y\varphi_z}\right)_{j-1,j} = \sum_{d=1}^{n_{j-1}} \frac{E_{d,j-1}A_{d,j-1}}{{L_{d,j-1}}^3}\big[&(y_{d,j-1,j}-y_{C,j})\Delta x_{d,j-1}\Delta y_{d,j-1}\\ &-(x_{d,j-1,j}-x_{C,j})\Delta {y_{d,j-1}}^2\big],\end{aligned} \tag{4.16a}$$

$$\left(K_{F_y\varphi_z}\right)_{j,j} = \sum_{d=1}^{n_{j-1}} \frac{E_{d,j-1}A_{d,j-1}}{{L_{d,j-1}}^3}\left[\left(x_{d,j-1,j} - x_{C,j}\right)\Delta {y_{d,j-1}}^2 - \left(y_{d,j-1,j} - y_{C,j}\right)\Delta x_{d,j-1}\Delta y_{d,j-1}\right] + \sum_{d=1}^{n_j} \frac{E_{d,j}A_{d,j}}{{L_{d,j}}^3}\left[\left(x_{d,j,j} - x_{C,j}\right)\Delta {y_{d,j}}^2 - \left(y_{d,j,j} - y_{C,j}\right)\Delta x_{d,j}\Delta y_{d,j}\right], \quad (4.16b)$$

$$\left(K_{F_y\varphi_z}\right)_{j+1,j} = \sum_{d=1}^{n_j} \frac{E_{d,j}A_{d,j}}{{L_{d,j}}^3}\left[\left(y_{d,j,j} - y_{C,j}\right)\Delta x_{d,j}\Delta y_{d,j} - \left(x_{d,j,j} - x_{C,j}\right)\Delta {y_{d,j}}^2\right], \quad (4.16c)$$

The application of Eqs. (4.11)-(4.16) finally allows the direct computation of the whole $\boldsymbol{K_{HH}}$ matrix in Eq. (4.10).

4.2.1.2 Calculation of the K_{VV} sub-matrix

According to Eqs. (4.9) and (4.10), the stiffness matrix $\boldsymbol{K_{VV}}$ contains nine sub-matrices that relate the out-of-plane moments $\boldsymbol{M_x}$ and $\boldsymbol{M_y}$ and vertical forces $\boldsymbol{F_z}$ to the corresponding out-of-plane rotations $\boldsymbol{\varphi_x}$ and $\boldsymbol{\varphi_y}$ and vertical displacements $\boldsymbol{\delta_z}$. Due to the symmetry of the matrix $\boldsymbol{K_{VV}}$, only six sub-matrices need to be calculated, e.g. $\boldsymbol{K_{M_x\varphi_x}}$, $\boldsymbol{K_{M_y\varphi_y}}$, $\boldsymbol{K_{M_x\varphi_y}}$, $\boldsymbol{K_{F_z\delta_z}}$, $\boldsymbol{K_{M_x\delta_z}}$, $\boldsymbol{K_{M_y\delta_z}}$.

By applying the same methodology explained above, the stiffness coefficients of $\boldsymbol{K_{M_x\varphi_x}}$ can be obtained as:

$$\left(K_{M_x\varphi_x}\right)_{j-1,j} = -\sum_{d=1}^{n_{j-1}} E_{d,j-1}A_{d,j-1}\frac{{\Delta z_{d,j-1}}^2}{{L_{d,j-1}}^3}\left(x_{d,j-1,j} - x_{C,j}\right)\left(x_{d,j-1,j-1} - x_{C,j-1}\right), \quad (4.17a)$$

$$\left(K_{M_x\varphi_x}\right)_{j,j} = \sum_{d=1}^{n_{j-1}} E_{d,j-1}A_{d,j-1}\frac{{\Delta z_{d,j-1}}^2}{{L_{d,j-1}}^3}\left(x_{d,j-1,j} - x_{C,j}\right)^2 + \sum_{d=1}^{n_j} E_{d,j}A_{d,j}\frac{{\Delta z_{d,j}}^2}{{L_{d,j}}^3}\left(x_{d,j,j} - x_{C,j}\right)^2, \quad (4.17b)$$

$$\left(K_{M_x\varphi_x}\right)_{j+1,j} = -\sum_{d=1}^{n_j} E_{d,j}A_{d,j}\frac{{\Delta z_{d,j}}^2}{{L_{d,j}}^3}\left(x_{d,j,j} - x_{C,j}\right)\left(x_{d,j,j+1} - x_{C,j+1}\right), \quad (4.17c)$$

being $\Delta z_{d,j}$ the difference of the X-coordinates of the diagonal end nodes referred to the j^{th} module and the other terms have the same meaning explained in Section 4.2.1.1. Similarly, to Eqs. (4.17), the stiffness coefficients of $\boldsymbol{K_{M_y\varphi_y}}$ can be obtained as:

$$\left(K_{M_y\varphi_y}\right)_{j-1,j} = -\sum_{d=1}^{n_{j-1}} E_{d,j-1}A_{d,j-1}\frac{{\Delta z_{d,j-1}}^2}{{L_{d,j-1}}^3}\left(y_{d,j-1,j} - y_{C,j}\right)\left(y_{d,j-1,j-1} - y_{C,j-1}\right), \quad (4.18a)$$

$$\left(K_{M_y\varphi_y}\right)_{j,j} = \sum_{d=1}^{n_{j-1}} E_{d,j-1}A_{d,j-1}\frac{{\Delta z_{d,j-1}}^2}{{L_{d,j-1}}^3}\left(y_{d,j-1,j} - y_{C,j}\right)^2 + \sum_{d=1}^{n_j} E_{d,j}A_{d,j}\frac{{\Delta z_{d,j}}^2}{{L_{d,j}}^3}\left(y_{d,j,j} - y_{C,j}\right)^2, \quad (4.18b)$$

$$\left(K_{M_y\varphi_y}\right)_{j+1,j} = -\sum_{d=1}^{n_j} E_{d,j}A_{d,j}\frac{{\Delta z_{d,j}}^2}{{L_{d,j}}^3}\left(y_{d,j,j} - y_{C,j}\right)\left(y_{d,j,j+1} - y_{C,j+1}\right). \quad (4.18c)$$

The stiffness coefficients of the out-of-diagonal sub-matrix $\boldsymbol{K_{M_x\varphi_y}}$ can be obtained by applying rotations along the Y direction and computing the total reacting moments along the X direction, obtaining:

$$\left(K_{M_x\varphi_y}\right)_{j-1,j} = -\sum_{d=1}^{n_{j-1}} E_{d,j-1}A_{d,j-1}\frac{\Delta z_{d,j-1}{}^2}{L_{d,j-1}{}^3}\left(y_{d,j-1,j}-y_{C,j}\right)\left(x_{d,j-1,j-1}-x_{C,j-1}\right), \tag{4.19a}$$

$$\begin{aligned}\left(K_{M_x\varphi_y}\right)_{j,j} = &\sum_{d=1}^{n_{j-1}} E_{d,j-1}A_{d,j-1}\frac{\Delta z_{d,j-1}{}^2}{L_{d,j-1}{}^3}\left(y_{d,j-1,j}-y_{C,j}\right)\left(x_{d,j-1,j}-x_{C,j}\right)\\ &+\sum_{d=1}^{n_j} E_{d,j}A_{d,j}\frac{\Delta z_{d,j}{}^2}{L_{d,j}{}^3}\left(y_{d,j,j}-y_{C,j}\right)\left(x_{d,j,j}-x_{C,j}\right),\end{aligned} \tag{4.19b}$$

$$\left(K_{M_x\varphi_y}\right)_{j+1,j} = -\sum_{d=1}^{n_j} E_{d,j}A_{d,j}\frac{\Delta z_{d,j}{}^2}{L_{d,j}{}^3}\left(y_{d,j,j}-y_{C,j}\right)\left(x_{d,j,j+1}-x_{C,j+1}\right). \tag{4.19c}$$

Finally, by applying unitary vertical displacements $\boldsymbol{\delta_z}$ and computing the resulting vertical forces and $\boldsymbol{F_z}$ and out-of-plane moments $\boldsymbol{M_x}$ and $\boldsymbol{M_y}$, one directly obtains the following expressions for the coefficients of $\boldsymbol{K_{F_z\delta_z}}$, $\boldsymbol{K_{M_x\delta_z}}$ and $\boldsymbol{K_{M_y\delta_z}}$:

$$\left(K_{F_z\delta_z}\right)_{j-1,j} = -\sum_{d=1}^{n_{j-1}} E_{d,j-1}A_{d,j-1}\frac{\Delta z_{d,j-1}{}^2}{L_{d,j-1}{}^3}, \tag{4.20a}$$

$$\left(K_{F_z\delta_z}\right)_{j,j} = \sum_{d=1}^{n_{j-1}} E_{d,j-1}A_{d,j-1}\frac{\Delta z_{d,j-1}{}^2}{L_{d,j-1}{}^3} + \sum_{d=1}^{n_j} E_{d,j}A_{d,j}\frac{\Delta z_{d,j}{}^2}{L_{d,j}{}^3}, \tag{4.20b}$$

$$\left(K_{F_z\delta_z}\right)_{j+1,j} = -\sum_{d=1}^{n_j} E_{d,j}A_{d,j}\frac{\Delta z_{d,j}{}^2}{L_{d,j}{}^3}, \tag{4.20c}$$

$$\left(K_{M_x\delta_z}\right)_{j-1,j} = -\sum_{d=1}^{n_{j-1}} E_{d,j-1}A_{d,j-1}\frac{\Delta z_{d,j-1}{}^2}{L_{d,j-1}{}^3}\left(x_{d,j-1,j-1}-x_{C,j-1}\right), \tag{4.21a}$$

$$\begin{aligned}\left(K_{M_x\delta_z}\right)_{j,j} = &\sum_{d=1}^{n_{j-1}} E_{d,j-1}A_{d,j-1}\frac{\Delta z_{d,j-1}{}^2}{L_{d,j-1}{}^3}\left(x_{d,j-1,j}-x_{C,j}\right)\\ &+\sum_{d=1}^{n_j} E_{d,j}A_{d,j}\frac{\Delta z_{d,j}{}^2}{L_{d,j}{}^3}\left(x_{d,j,j}-x_{C,j}\right),\end{aligned} \tag{4.21b}$$

$$\left(K_{M_x\delta_z}\right)_{j+1,j} = -\sum_{d=1}^{n_j} E_{d,j}A_{d,j}\frac{\Delta z_{d,j}{}^2}{L_{d,j}{}^3}\left(x_{d,j,j+1}-x_{C,j+1}\right), \tag{4.21c}$$

$$\left(K_{M_y\delta_z}\right)_{j-1,j} = -\sum_{d=1}^{n_{j-1}} E_{d,j-1}A_{d,j-1}\frac{\Delta z_{d,j-1}{}^2}{L_{d,j-1}{}^3}\left(y_{d,j-1,j-1}-y_{C,j-1}\right), \tag{4.22a}$$

$$\begin{aligned}\left(K_{M_y\delta_z}\right)_{j,j} = &\sum_{d=1}^{n_{j-1}} E_{d,j-1}A_{d,j-1}\frac{\Delta z_{d,j-1}{}^2}{L_{d,j-1}{}^3}\left(y_{d,j-1,j}-y_{C,j}\right)\\ &+\sum_{d=1}^{n_j} E_{d,j}A_{d,j}\frac{\Delta z_{d,j}{}^2}{L_{d,j}{}^3}\left(y_{d,j,j}-y_{C,j}\right),\end{aligned} \tag{4.22b}$$

$$\left(K_{M_y\delta_z}\right)_{j+1,j} = -\sum_{d=1}^{n_j} E_{d,j}A_{d,j}\frac{{\Delta z_{d,j}}^2}{{L_{d,j}}^3}\left(y_{d,j,j+1} - y_{C,j+1}\right), \tag{4.22c}$$

The application of Eqs. (4.17)-(4.22) finally allows the direct computation of the whole $\boldsymbol{K_{VV}}$ matrix in Eq. (4.10).

4.2.1.3 Calculation of the K_{HV} sub-matrix

Finally, the stiffness matrix $\boldsymbol{K_{HV}}$ contains the nine sub-matrices that relate the horizontal forces $\boldsymbol{F_x}$ and $\boldsymbol{F_y}$ and torque moments $\boldsymbol{M_z}$ to the out-of-plane rotations $\boldsymbol{\varphi_x}$ and $\boldsymbol{\varphi_y}$ and vertical displacements $\boldsymbol{\delta_z}$. Due to the fact that this matrix is not on the diagonal of the global stiffness matrix, it is not necessarily symmetric, therefore all the nine sub-matrices need to be calculated, i.e. $\boldsymbol{K_{F_x\varphi_x}}$, $\boldsymbol{K_{F_x\varphi_y}}$, $\boldsymbol{K_{F_x\delta_z}}$, $\boldsymbol{K_{F_y\varphi_x}}$, $\boldsymbol{K_{F_y\varphi_y}}$, $\boldsymbol{K_{F_y\delta_z}}$, $\boldsymbol{K_{M_z\varphi_x}}$, $\boldsymbol{K_{M_z\varphi_y}}$, $\boldsymbol{K_{M_z\delta_z}}$.

By applying the same methodology explained above, the stiffness coefficients of these sub-matrices can be obtained as:

$$\left(K_{F_x\varphi_x}\right)_{j-1,j} = \sum_{d=1}^{n_{j-1}} E_{d,j-1}A_{d,j-1}\frac{\Delta x_{d,j-1}\Delta z_{d,j-1}}{{L_{d,j-1}}^3}\left(x_{d,j-1,j} - x_{C,j}\right), \tag{4.23a}$$

$$\begin{aligned}\left(K_{F_x\varphi_x}\right)_{j,j} = &-\sum_{d=1}^{n_{j-1}} E_{d,j-1}A_{d,j-1}\frac{\Delta x_{d,j-1}\Delta z_{d,j-1}}{{L_{d,j-1}}^3}\left(x_{d,j-1,j} - x_{C,j}\right)\\ &-\sum_{d=1}^{n_j} E_{d,j}A_{d,j}\frac{\Delta x_{d,j}\Delta z_{d,j}}{{L_{d,j}}^3}\left(x_{d,j,j} - x_{C,j}\right),\end{aligned} \tag{4.23b}$$

$$\left(K_{F_x\varphi_x}\right)_{j+1,j} = \sum_{d=1}^{n_j} E_{d,j}A_{d,j}\frac{\Delta x_{d,j}\Delta z_{d,j}}{{L_{d,j}}^3}\left(x_{d,j,j} - x_{C,j}\right), \tag{4.23c}$$

$$\left(K_{F_x\varphi_y}\right)_{j-1,j} = \sum_{d=1}^{n_{j-1}} E_{d,j-1}A_{d,j-1}\frac{\Delta x_{d,j-1}\Delta z_{d,j-1}}{{L_{d,j-1}}^3}\left(y_{d,j-1,j} - y_{C,j}\right), \tag{4.24a}$$

$$\begin{aligned}\left(K_{F_x\varphi_y}\right)_{j,j} = &-\sum_{d=1}^{n_{j-1}} E_{d,j-1}A_{d,j-1}\frac{\Delta x_{d,j-1}\Delta z_{d,j-1}}{{L_{d,j-1}}^3}\left(y_{d,j-1,j} - y_{C,j}\right)\\ &-\sum_{d=1}^{n_j} E_{d,j}A_{d,j}\frac{\Delta x_{d,j}\Delta z_{d,j}}{{L_{d,j}}^3}\left(y_{d,j,j} - y_{C,j}\right),\end{aligned} \tag{4.24b}$$

$$\left(K_{F_x\varphi_y}\right)_{j+1,j} = \sum_{d=1}^{n_j} E_{d,j}A_{d,j}\frac{\Delta x_{d,j}\Delta z_{d,j}}{{L_{d,j}}^3}\left(y_{d,j,j} - y_{C,j}\right), \tag{4.24c}$$

$$\left(K_{F_x\delta_z}\right)_{j-1,j} = \sum_{d=1}^{n_{j-1}} E_{d,j-1}A_{d,j-1}\frac{\Delta x_{d,j-1}\Delta z_{d,j-1}}{{L_{d,j-1}}^3}, \tag{4.25a}$$

$$\left(K_{F_x\delta_z}\right)_{j,j} = -\sum_{d=1}^{n_{j-1}} E_{d,j-1}A_{d,j-1}\frac{\Delta x_{d,j-1}\Delta z_{d,j-1}}{{L_{d,j-1}}^3} - \sum_{d=1}^{n_j} E_{d,j}A_{d,j}\frac{\Delta x_{d,j}\Delta z_{d,j}}{{L_{d,j}}^3}, \tag{4.25b}$$

$$\left(K_{F_x\delta_z}\right)_{j+1,j} = \sum_{d=1}^{n_j} E_{d,j}A_{d,j}\frac{\Delta x_{d,j}\Delta z_{d,j}}{{L_{d,j}}^3}, \tag{4.25c}$$

$$\left(K_{F_y\varphi_x}\right)_{j-1,j} = \sum_{d=1}^{n_{j-1}} E_{d,j-1}A_{d,j-1}\frac{\Delta y_{d,j-1}\Delta z_{d,j-1}}{{L_{d,j-1}}^3}\left(x_{d,j-1,j} - x_{C,j}\right), \tag{4.26a}$$

$$\left(K_{F_y\varphi_x}\right)_{j,j} = -\sum_{d=1}^{n_{j-1}} E_{d,j-1}A_{d,j-1}\frac{\Delta y_{d,j-1}\Delta z_{d,j-1}}{{L_{d,j-1}}^3}\left(x_{d,j-1,j} - x_{C,j}\right) - \sum_{d=1}^{n_j} E_{d,j}A_{d,j}\frac{\Delta y_{d,j}\Delta z_{d,j}}{{L_{d,j}}^3}\left(x_{d,j,j} - x_{C,j}\right), \tag{4.26b}$$

$$\left(K_{F_y\varphi_x}\right)_{j+1,j} = \sum_{d=1}^{n_j} E_{d,j}A_{d,j}\frac{\Delta y_{d,j}\Delta z_{d,j}}{{L_{d,j}}^3}\left(x_{d,j,j} - x_{C,j}\right), \tag{4.26c}$$

$$\left(K_{F_y\varphi_y}\right)_{j-1,j} = \sum_{d=1}^{n_{j-1}} E_{d,j-1}A_{d,j-1}\frac{\Delta y_{d,j-1}\Delta z_{d,j-1}}{{L_{d,j-1}}^3}\left(y_{d,j-1,j} - y_{C,j}\right), \tag{4.27a}$$

$$\left(K_{F_y\varphi_y}\right)_{j,j} = -\sum_{d=1}^{n_{j-1}} E_{d,j-1}A_{d,j-1}\frac{\Delta y_{d,j-1}\Delta z_{d,j-1}}{{L_{d,j-1}}^3}\left(y_{d,j-1,j} - y_{C,j}\right) - \sum_{d=1}^{n_j} E_{d,j}A_{d,j}\frac{\Delta y_{d,j}\Delta z_{d,j}}{{L_{d,j}}^3}\left(y_{d,j,j} - y_{C,j}\right), \tag{4.27b}$$

$$\left(K_{F_y\varphi_y}\right)_{j+1,j} = \sum_{d=1}^{n_j} E_{d,j}A_{d,j}\frac{\Delta y_{d,j}\Delta z_{d,j}}{{L_{d,j}}^3}\left(y_{d,j,j} - y_{C,j}\right), \tag{4.27c}$$

$$\left(K_{F_y\delta_z}\right)_{j-1,j} = \sum_{d=1}^{n_{j-1}} E_{d,j-1}A_{d,j-1}\frac{\Delta y_{d,j-1}\Delta z_{d,j-1}}{{L_{d,j-1}}^3}, \tag{4.28a}$$

$$\left(K_{F_y\delta_z}\right)_{j,j} = -\sum_{d=1}^{n_{j-1}} E_{d,j-1}A_{d,j-1}\frac{\Delta y_{d,j-1}\Delta z_{d,j-1}}{{L_{d,j-1}}^3} - \sum_{d=1}^{n_j} E_{d,j}A_{d,j}\frac{\Delta y_{d,j}\Delta z_{d,j}}{{L_{d,j}}^3}, \tag{4.28b}$$

$$\left(K_{F_y\delta_z}\right)_{j+1,j} = \sum_{d=1}^{n_j} E_{d,j}A_{d,j}\frac{\Delta y_{d,j}\Delta z_{d,j}}{{L_{d,j}}^3}, \tag{4.28c}$$

$$\left(K_{M_z\varphi_x}\right)_{j-1,j} = \sum_{d=1}^{n_{j-1}} E_{d,j-1}A_{d,j-1}\frac{\Delta z_{d,j-1}}{{L_{d,j-1}}^3}\left[\left(x_{d,j-1,j} - x_{C,j}\right)\left(x_{d,j-1,j-1} - x_{C,j-1}\right)\Delta y_{d,j-1} - \left(y_{d,j-1,j-1} - y_{C,j-1}\right)\left(x_{d,j-1,j} - x_{C,j}\right)\Delta x_{d,j-1}\right], \tag{4.29a}$$

$$\left(K_{M_z\varphi_x}\right)_{j,j} = \sum_{d=1}^{n_{j-1}} E_{d,j-1}A_{d,j-1}\frac{\Delta z_{d,j-1}}{{L_{d,j-1}}^3}\left[\left(x_{d,j-1,j} - x_{C,j}\right)\left(y_{d,j-1,j} - y_{C,j}\right)\Delta x_{d,j-1} - \left(x_{d,j-1,j} - x_{C,j}\right)^2\Delta y_{d,j-1}\right] + \sum_{d=1}^{n_j} E_{d,j}A_{d,j}\frac{\Delta z_{d,j}}{{L_{d,j}}^3}\left[\left(x_{d,j,j} - x_{C,j}\right)\left(y_{d,j,j} - y_{C,j}\right)\Delta x_{d,j} - \left(x_{d,j,j} - x_{C,j}\right)^2\Delta y_{d,j}\right], \tag{4.29b}$$

$$\left(K_{M_z\varphi_x}\right)_{j+1,j} = \sum_{d=1}^{n_{j-1}} E_{d,j}A_{d,j}\frac{\Delta z_{d,j}}{{L_{d,j}}^3}\left[\left(x_{d,j,j} - x_{C,j}\right)\left(x_{d,j,j+1} - x_{C,j+1}\right)\Delta y_{d,j} - \left(y_{d,j,j+1} - y_{C,j+1}\right)\left(x_{d,j,j} - x_{C,j}\right)\Delta x_{d,j}\right], \tag{4.29c}$$

$$\left(K_{M_z\varphi_y}\right)_{j-1,j} = \sum_{d=1}^{n_{j-1}} E_{d,j-1}A_{d,j-1}\frac{\Delta z_{d,j-1}}{{L_{d,j-1}}^3}\left[\left(y_{d,j-1,j} - y_{C,j}\right)\left(x_{d,j-1,j-1} - x_{C,j-1}\right)\Delta y_{d,j-1} - \left(y_{d,j-1,j-1} - y_{C,j-1}\right)\left(y_{d,j-1,j} - y_{C,j}\right)\Delta x_{d,j-1}\right], \tag{4.30a}$$

$$\left(K_{M_z\varphi_y}\right)_{j,j} = \sum_{d=1}^{n_{j-1}} E_{d,j-1}A_{d,j-1}\frac{\Delta z_{d,j-1}}{L_{d,j-1}^{\,3}}\Big[\left(y_{d,j-1,j}-y_{C,j}\right)^2\Delta x_{d,j-1} - \left(x_{d,j-1,j}-x_{C,j}\right)\left(y_{d,j-1,j}-y_{C,j}\right)\Delta y_{d,j-1}\Big] + \sum_{d=1}^{n_j} E_{d,j}A_{d,j}\frac{\Delta z_{d,j}}{L_{d,j}^{\,3}}\Big[\left(y_{d,j,j}-y_{C,j}\right)^2\Delta x_{d,j} - \left(x_{d,j,j}-x_{C,j}\right)\left(y_{d,j,j}-y_{C,j}\right)\Delta y_{d,j}\Big], \tag{4.30b}$$

$$\left(K_{M_z\varphi_y}\right)_{j+1,j} = \sum_{d=1}^{n_{j-1}} E_{d,j}A_{d,j}\frac{\Delta z_{d,j}}{L_{d,j}^{\,3}}\left[\left(y_{d,j,j}-y_{C,j}\right)\left(x_{d,j,j+1}-x_{C,j+1}\right)\Delta y_{d,j} - \left(y_{d,j,j+1}-y_{C,j+1}\right)\left(y_{d,j,j}-y_{C,j}\right)\Delta x_{d,j}\right], \tag{4.30c}$$

$$\left(K_{M_z\delta_Z}\right)_{j-1,j} = \sum_{d=1}^{n_{j-1}} E_{d,j-1}A_{d,j-1}\frac{\Delta z_{d,j-1}}{L_{d,j-1}^{\,3}}\left[\left(x_{d,j-1,j-1}-x_{C,j-1}\right)\Delta y_{d,j-1} - \left(y_{d,j-1,j-1}-y_{C,j-1}\right)\Delta x_{d,j-1}\right], \tag{4.31a}$$

$$\left(K_{M_z\delta_Z}\right)_{j,j} = \sum_{d=1}^{n_{j-1}} E_{d,j-1}A_{d,j-1}\frac{\Delta z_{d,j-1}}{L_{d,j-1}^{\,3}}\left[\left(y_{d,j-1,j}-y_{C,j}\right)\Delta x_{d,j-1} - \left(x_{d,j-1,j}-x_{C,j}\right)\Delta y_{d,j-1}\right] + \sum_{d=1}^{n_j} E_{d,j}A_{d,j}\frac{\Delta z_{d,j}}{L_{d,j}^{\,3}}\left[\left(y_{d,j,j}-y_{C,j}\right)\Delta x_{d,j} - \left(x_{d,j,j}-x_{C,j}\right)\Delta y_{d,j}\right], \tag{4.31b}$$

$$\left(K_{M_z\delta_Z}\right)_{j+1,j} = \sum_{d=1}^{n_{j-1}} E_{d,j}A_{d,j}\frac{\Delta z_{d,j}}{L_{d,j}^{\,3}}\left[\left(x_{d,j,j+1}-x_{C,j+1}\right)\Delta y_{d,j} - \left(y_{d,j,j+1}-y_{C,j+1}\right)\Delta x_{d,j}\right], \tag{4.31c}$$

The application of Eqs. (4.23)-(4.31) finally allows the direct computation of the whole $\boldsymbol{K_{HV}}$ matrix in Eq. (4.10) Eventually, remembering that $\boldsymbol{K_{VH}}$ is the transpose of $\boldsymbol{K_{HV}}$, one obtains the whole stiffness matrix of the diagrid structure $\boldsymbol{K}$ in Eqs. (4.8), that allows to solve the structural analysis.

4.2.2 MBM for the structural analysis and insertion into the General Algorithm

Once the coefficients of the diagrid stiffness matrix are computed based on the equations presented in Section 4.2.1, the matrix relationships reported in Eqs. (4.8) and (4.9) can be simply inverted to obtain all the displacements and rotations of the floors under the given external forces and moments acting at the level of the floor centroids:

$$\boldsymbol{\delta} = \boldsymbol{K^{-1}F}. \tag{4.32}$$

Ultimately, these allow to evaluate the flexibility of the diagrid structure, in terms of both lateral and vertical displacements, as well as torsional and bending rotations. Based on the obtained displacements and rotations of each floor, the final step of the linear structural analysis yields the calculation of the axial force $N_{d,j}$ in the generic d^{th} diagonal lying within the j^{th} diagrid module, as follows:

$$
\begin{aligned}
N_{d,j} = \frac{E_{d,j}A_{d,j}}{{L_{d,j}}^2}\{&[\delta_{x,j} - \delta_{x,j+1}]\Delta x_{d,j} + [\delta_{y,j} - \delta_{y,j+1}]\Delta y_{d,j} - [\delta_{z,j} - \delta_{z,j+1}]\Delta z_{d,j} \\
&+ \varphi_{z,j}[-(y_{d,j,j} - y_{C,j})\Delta x_{d,j} + (x_{d,j,j} - x_{C,j})\Delta y_{d,j}] \\
&- \varphi_{z,j+1}[-(y_{d,j,j+1} - y_{C,j+1})\Delta x_{d,j} \\
&+ (x_{d,j,j+1} - x_{C,j+1})\Delta y_{d,j}] - \varphi_{x,j}(x_{d,j,j} - x_{C,j})\Delta z_{d,j} \\
&+ \varphi_{x,j+1}(x_{d,j,j+1} - x_{C,j+1})\Delta z_{d,j} - \varphi_{y,j}(y_{d,j,j} - y_{C,j})\Delta z_{d,j} \\
&+ \varphi_{y,j+1}(y_{d,j,j+1} - y_{C,j+1})\Delta z_{d,j}\},
\end{aligned}
\tag{4.33}
$$

where the symbols have the same meaning provided in the previous Section. Note that the axial force in the diagonal is generated by the three displacements and three rotations of the j^{th} and $(j + 1)^{th}$ floors (Figure 4.7b).

By applying the methodology developed in Section 4.2.1 for the calculation of the diagrid stiffness matrix and the Eqs. (4.32) and (4.33) to solve the structural problem, the structural analysis of the diagrid tall building can be ultimately carried out. In [116,117], the MBM has been applied to perform the structural analysis of the Swiss Re Tower (Figure 4.2b). Lateral and vertical loads have been considered, as well as torque moments acting at the level of the floors. The results that arise from the MBM, in terms of both floor displacement and rotations and axial forces in the diagonals, have been compared to the ones deriving from FE calculations, carried out on the commercial code LUSAS [72]. The comparison showed that the MBM is indeed able to perform the structural analysis under the above mentioned hypotheses, being the results from the MBM completely matching the ones arising from FE calculations [116,117]. Note that the Swiss Re Tower is a freeform diagrid, having a curvature both on the horizontal and vertical plane (Figure 4.3b). Therefore, the MBM has proven to be effective in investigating diagrid buildings with generic geometries.

Despite the other methods presented in the literature for the analysis of diagrids, which aim at calculating the lateral shear and bending rigidity of the diagrid tube [102,108], the MBM allows also to obtain information about the vertical and torsional flexibility of the diagrid structure. This is due to the fact that all the six generalized displacements have been taken into account during the development of the model, as reported in Eq. (4.9). Moreover, despite the MBM is more simplified than complete FE models, it focuses on the global behavior of the structure neglecting the local deformability, therefore it allows to obtain a faster assessment of the overall structural behavior, without the need to insert detailed information. This is particularly beneficial for the preliminary design stages, where the designer is interested on the global structural response, rather than on the local structural issues that are usually addressed in subsequent design stages.

4.2.2.1 The General Algorithm

One of the main reasons why the MBM has been developed in this form, i.e. based on matrix calculus, is that it is also suitable to be inserted into the so-called General Algorithm (GA) for the investigation of the force distribution among different resisting elements within a complex tall building. The GA has been firstly developed as a semi-analytical approach by Carpinteri and Carpinteri in 1985 [6,118], for the analysis of the lateral loading distribution between the elements of a three-dimensional civil structure, such as frames and shear walls.

The GA formulation takes into account an *N*-story building that has *M* vertical bracings, each defined by an arbitrary position in the floor plan. Since the floor slabs are considered to be infinitely rigid in their own planes, the DOFs are

represented by the transverse displacements of the single floors: the translations ξ and η in the directions X and Y, respectively, and the torsional rotation ϑ for each story. In the same way, the external load applied to the origin of the reference system is expressed by a 3*N*-vector $\boldsymbol{F}$, in which 2*N* shearing forces $\boldsymbol{p_x}$ and $\boldsymbol{p_y}$ and *N* torque moments $\boldsymbol{m_z}$ are included (Figure 4.8a):

$$\boldsymbol{F_i} = \begin{Bmatrix} \boldsymbol{p_i} \\ \boldsymbol{m_{z,i}} \end{Bmatrix} = \begin{Bmatrix} \boldsymbol{p_{x,i}} \\ \boldsymbol{p_{y,i}} \\ \boldsymbol{m_{z,i}} \end{Bmatrix}. \tag{4.34}$$

Within the local reference system of the i^{th} resisting element, i.e. $X_i^* Y_i^* Z_i^*$, the 3*N*-load vector $\boldsymbol{F_i}^*$ and the 3*N*-displacement vector $\boldsymbol{\delta_i}^*$describe the amount of external load carried by the i^{th} element and its transverse displacements, respectively. The loading vector $\boldsymbol{F_i}^*$ can be reduced to $\boldsymbol{F_i}$, which refers to the global reference system XYZ (Figure 4.8b), by means of the following expressions valid for each bracing [118]:

$$\boldsymbol{p_i}^* = \boldsymbol{N_i p_i}, \tag{4.35a}$$

$$\boldsymbol{m_{z,i}}^* = \boldsymbol{m_{z,i}} - \boldsymbol{\psi_i} \wedge \boldsymbol{p_i} \times \boldsymbol{u_z}. \tag{4.35b}$$

In matrix form:

$$\begin{Bmatrix} \boldsymbol{p_{x,i}}^* \\ \boldsymbol{p_{y,i}}^* \\ \boldsymbol{m_{z,i}}^* \end{Bmatrix} = \begin{bmatrix} \boldsymbol{N_i} & \boldsymbol{0} \\ -\boldsymbol{u_z} \wedge \boldsymbol{\psi_i} & \boldsymbol{I} \end{bmatrix} \begin{Bmatrix} \boldsymbol{p_{x,i}} \\ \boldsymbol{p_{y,i}} \\ \boldsymbol{m_{z,i}} \end{Bmatrix}, \tag{4.36}$$

where $\boldsymbol{N_i}$ represents the orthogonal rotation matrix from the global system XY to the local system $X_i^* Y_i^*$, $\boldsymbol{\psi_i}$ is the coordinate vector of the origin of the local system in the global one, $\boldsymbol{u_z}$ is the unit vector associated with the direction Z and $\boldsymbol{I}$ is the identity matrix.

The orthogonal matrix $\boldsymbol{N_i}$, extended to consider all the floors, can be represented by means of the angle φ_i between the Y and Y_i^* axes:

$$\boldsymbol{N_i} = \begin{bmatrix} [cos\varphi_i] & [sin\varphi_i] \\ -[sin\varphi_i] & [cos\varphi_i] \end{bmatrix}, \tag{4.37}$$

where each term is a diagonal $N \times N$ submatrix. Taking into account all the floors, Eq. (4.36) can be rewritten in the following form:

$$\boldsymbol{F_i}^* = \boldsymbol{A_i F_i}, \tag{4.38}$$

where the $3N \times 3N$ submatrix $\boldsymbol{A_i}$ gathers the information about the reciprocal rotation between the local and global reference systems and the location of the i^{th} resisting element in the global system XY:

$$\boldsymbol{A_i} = \begin{bmatrix} \boldsymbol{N_i} & \boldsymbol{0} \\ -\boldsymbol{u_z} \wedge \boldsymbol{\psi_i} & \boldsymbol{I} \end{bmatrix}. \tag{4.39}$$

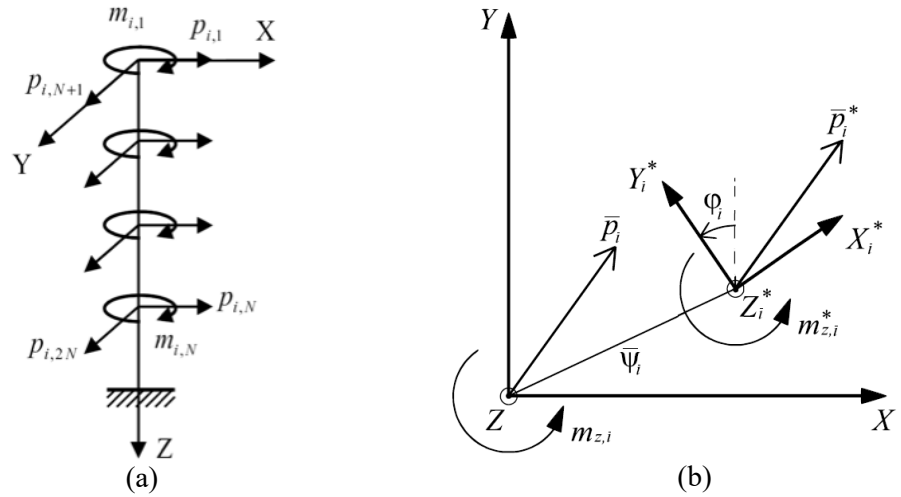

Figure 4.8. (a) Internal loadings S_i transmitted to the i^{th} bracing in the global reference system; (b) global and local reference systems. Used with permission from Carpinteri [6].

The component $-\boldsymbol{u_z} \wedge \boldsymbol{\psi_i}$ is obtained from Eq. (4.35b) exploiting the fact that the scalar triple product is invariant under any cyclic permutation of its factors [6]. For the sake of simplicity, to take into account the N floors of the structure, this vector product can be written as a $2N \times N$ matrix $\boldsymbol{C_i}$ composed of two diagonal submatrices containing the coordinates (x_i, y_i) of the origin of the local system $X_i^*Y_i^*$ (Figure 4.8b):

$$-\boldsymbol{u_z} \wedge \boldsymbol{\psi_i} = \begin{vmatrix} \bar{\imath} & \bar{\jmath} & \bar{k} \\ 0 & 0 & 1 \\ x_i & y_i & 0 \end{vmatrix} = -[-y_i \quad x_i] = -\boldsymbol{C_i}^{\boldsymbol{T}}. \tag{4.40}$$

Thus, the final expression for $\boldsymbol{A_i}$ is:

$$\boldsymbol{A_i} = \begin{bmatrix} \boldsymbol{N_i} & \boldsymbol{0} \\ -\boldsymbol{C_i}^{\boldsymbol{T}} & \boldsymbol{I} \end{bmatrix}. \tag{4.41}$$

In the same way, the vector $\boldsymbol{\delta_i}^*$, constituted by $2N$ translations ξ_i^*, η_i^* and N rotations ϑ_i^*, can be connected to the corresponding $\boldsymbol{\delta_i}$, which is referred to the global reference system, by means of the orthogonal matrix $\boldsymbol{N_i}$:

$$\begin{Bmatrix} \boldsymbol{\xi_i}^* \\ \boldsymbol{\eta_i}^* \end{Bmatrix} = \boldsymbol{N_i} \begin{Bmatrix} \boldsymbol{\xi_i} \\ \boldsymbol{\eta_i} \end{Bmatrix}, \tag{4.42a}$$

$$\boldsymbol{\vartheta_i}^* = \boldsymbol{\vartheta_i}. \tag{4.42b}$$

Taking into account all the floors, Eqs. (4.42) can be rewritten in the following form by means of the compact $3N \times 3N$ matrix $\boldsymbol{B_i}$:

$$\boldsymbol{\delta_i}^* = \boldsymbol{B_i}\boldsymbol{\delta_i}, \tag{4.43}$$

where the matrix $\boldsymbol{B_i}$ is similar to $\boldsymbol{A_i}$, the term $\boldsymbol{C_i}^{\boldsymbol{T}}$ being reduced to a null matrix:

$$\boldsymbol{B_i} = \begin{bmatrix} \boldsymbol{N_i} & \boldsymbol{0} \\ \boldsymbol{0} & \boldsymbol{I} \end{bmatrix}. \tag{4.44}$$

A relation between $\boldsymbol{F_i}^*$ and $\boldsymbol{\delta_i}^*$ is considered known through the condensed stiffness matrix $\boldsymbol{K_i}^*$, referred to the local reference system of the i^{th} resisting element:

$$\boldsymbol{F_i}^* = \boldsymbol{K_i}^* \boldsymbol{\delta_i}^*. \tag{4.45}$$

Substituting Eqs. (4.38) and (4.43) into Eq. (4.45), the load vector $\boldsymbol{F_i}$ turns out to be connected to the displacement vector $\boldsymbol{\delta_i}$ through a product of matrices, which identifies the stiffness matrix $\boldsymbol{K_i}$ of the i^{th} bracing in the global reference system XY:

$$\boldsymbol{F_i} = \left(\boldsymbol{A_i}^{-1} \boldsymbol{K_i}^* \boldsymbol{B_i}\right) \boldsymbol{\delta_i} = \boldsymbol{K_i} \boldsymbol{\delta_i}. \tag{4.46}$$

Due to the presence of in-plane rigid slabs connecting the vertical resisting elements, the transverse displacements of each element can be computed considering only three generalized displacements, ξ, η and ϑ, per floor. This step, extended to consider all the floors, is performed through the matrix $\boldsymbol{T_i}$ that takes into account the location of each bracing in the plan by means of the coordinates (x_i, y_i) and therefore the matrix $\boldsymbol{C_i}$:

$$\boldsymbol{\delta_i} = \begin{bmatrix} \boldsymbol{I} & \boldsymbol{C_i} \\ \boldsymbol{0} & \boldsymbol{I} \end{bmatrix} \boldsymbol{\delta} = \boldsymbol{T_i} \boldsymbol{\delta}, \tag{4.47}$$

where $\boldsymbol{\delta}$ is the floor displacement vector, that is, the displacement vector associated with the origin of the global reference system. The substitution of Eq. (4.47) into Eq. (4.46) allows the identification of the stiffness matrix of the i^{th} bracing, in reference to the global reference system XYZ and to the generalized floor displacements, ξ, η and ϑ:

$$\boldsymbol{F_i} = (\boldsymbol{K_i} \boldsymbol{T_i}) \boldsymbol{\delta} = \overline{\boldsymbol{K_i}} \boldsymbol{\delta}. \tag{4.48}$$

For the global equilibrium, the external load $\boldsymbol{F}$ applied to the structure is equal to the sum of the M vectors $\boldsymbol{F_i}$. In this way, a relationship between the external load and the floor displacements is obtained and the global stiffness matrix of the structure is computed. By means of this matrix, once the external load is defined, the displacements of the structure are acquired, from which the information regarding each single bracing can be deduced:

$$\boldsymbol{F} = \sum_{i=1}^{M} \boldsymbol{F_i} = \left(\sum_{i=1}^{M} \overline{\boldsymbol{K_i}} \right) \boldsymbol{\delta} = \overline{\boldsymbol{K}} \boldsymbol{\delta}, \tag{4.49}$$

and therefore:

$$\boldsymbol{\delta} = \overline{\boldsymbol{K}}^{-1} \boldsymbol{F}. \tag{4.50}$$

Recalling Eq. (4.48) and comparing it with Eq. (4.50), an equation connecting the vectors $\boldsymbol{F}$ and $\boldsymbol{F_i}$ allows the definition of the amount of the external load carried by the i^{th} vertical stiffening element:

$$\boldsymbol{\delta} = \overline{\boldsymbol{K}}^{-1}\boldsymbol{F} = \overline{\boldsymbol{K}_i}^{-1}\boldsymbol{F}_i, \tag{4.51}$$

from which we obtain:

$$\boldsymbol{F}_i = \overline{\boldsymbol{K}_i}\overline{\boldsymbol{K}}^{-1}\boldsymbol{F} = \boldsymbol{R}_i\boldsymbol{F}. \tag{4.52}$$

The load distribution matrix $\boldsymbol{R}_i$, shown in Eq. (4.52), demonstrates that each bracing is subjecting to a load $\boldsymbol{F}_i$ that is given by the external load $\boldsymbol{F}$ pre-multiplied by the own stiffness matrix and the inverse of the global stiffness matrix. Once the generalized displacement vector $\boldsymbol{\delta}$ is known, recalling Eqs. (4.43), (4.45) and (4.47), the displacements and the forces related to the i^{th} bracing in its local coordinate system can be ultimately computed. Consequently, since the loads applied to each element are clearly identified, a preliminary assessment can easily be performed [6].

The GA shown above allows to quickly evaluate the distribution of lateral forces among the resisting elements as well as to analyze the lateral deflections and torsional rotations of a three-dimensional building made up of several bracing systems, such as frames and shear walls. Based on the formulation initially proposed by Carpinteri and Carpinteri [118], the GA was further enriched by inserting open-section shear walls [119], whose behavior obeys the Vlasov's theory [120], the warping deformation being important for the torsional flexibility of these sections [121]. The GA was also used to analyze the structural behavior of shear walls of different heights [122], as well as unconventionally shaped structures, such as twisted and tapered towers [123]. It led to the comprehension of secondary effects in tall buildings under lateral loads [124] and was also used to extract the dynamical features of tall buildings [125]. Ultimately, the GA was also employed to investigate real case studies, such as the Intesa Sanpaolo Tower and the Piedmont Region Headquarters Tower, both in Turin [126–128].

4.2.2.2 Insertion of the MBM into the GA

Although the MBM has been initially developed to perform the structural analysis of diagrid systems considered as the only resisting element of the tall building, it can be also been used within the GA environment to study the distribution of forces between the diagrid and other resisting elements as well as to calculate the transverse displacements of the building. However, in order for the MBM to be suitable for insertion into the GA, some additional considerations need to be applied.

As shown above, the MBM allows to compute the $6N \times 6N$ stiffness matrix of the diagrid structure, as reported in Eqs. (4.8) and (4.9), since it considers six DOFs per floor. Therefore, in order to make the model compatible with the GA framework, it is sufficient to neglect the presence of vertical forces and to condense the contribution given by the out-of-plane rotations [117]. As shown above, Eq. (4.9) can be rewritten by separating the contributions of the horizontal displacements and torsional rotations $\boldsymbol{\delta}_H$ from those referring to the out-of-plane rotations and vertical displacements $\boldsymbol{\delta}_V$, as reported in Eq. (4.10). This equation can be expanded into two matrix equations as:

$$\boldsymbol{F}_H = \boldsymbol{K}_{HH}\boldsymbol{\delta}_H + \boldsymbol{K}_{HV}\boldsymbol{\delta}_V, \tag{4.53a}$$

$$\boldsymbol{F_V = K_{VH}\delta_H + K_{VV}\delta_V}. \quad (4.53b)$$

In agreement with the GA framework, the building is only subjected to horizontal forces and torque moments, i.e. $\boldsymbol{F_H \neq 0}$ and $\boldsymbol{F_V = 0}$. Therefore, due to the fact the vector of vertical forces and out-of-plane moments is identically null, from Eq. (4.53b) it follows that the vector of vertical displacements and out-of-plane rotations can be obtained as:

$$\boldsymbol{\delta_V = -K_{VV}^{-1} K_{VH}\delta_H}. \quad (4.54)$$

Inserting Eq. (4.54) into Eq. (4.53a), we finally obtain the direct relationship between the vector of horizontal forces and torque moments $\boldsymbol{F_H}$ and the corresponding lateral displacements and torsional rotations $\boldsymbol{\delta_H}$ as follows:

$$\boldsymbol{F_H = \left(K_{HH} - K_{HV}K_{VV}^{-1}K_{VH}\right)\delta_H = \widetilde{K}_{HH}\delta_H}. \quad (4.55)$$

The matrix $\boldsymbol{\widetilde{K}_{HH}}$ has dimensions $3N \times 3N$ and it is calculated based on all the stiffness contributions of the diagrid structure, from the partitioning reported in Eq. (4.10). Note that Eq. (4.55) is equivalent to Eq. (4.45), as the matrix $\boldsymbol{\widetilde{K}_{HH}}$ represents the diagrid stiffness matrix in its local reference system referred to lateral loads. Therefore, this matrix can be directly inserted into the GA environment to evaluate the stiffness interaction between the external diagrid and other resisting elements, such as frames, shear walls, etc.

As an example, an external steel diagrid tube is considered for a 63-meter tall building, coupled with an internal concrete core, as shown in Figure 4.9 [117].

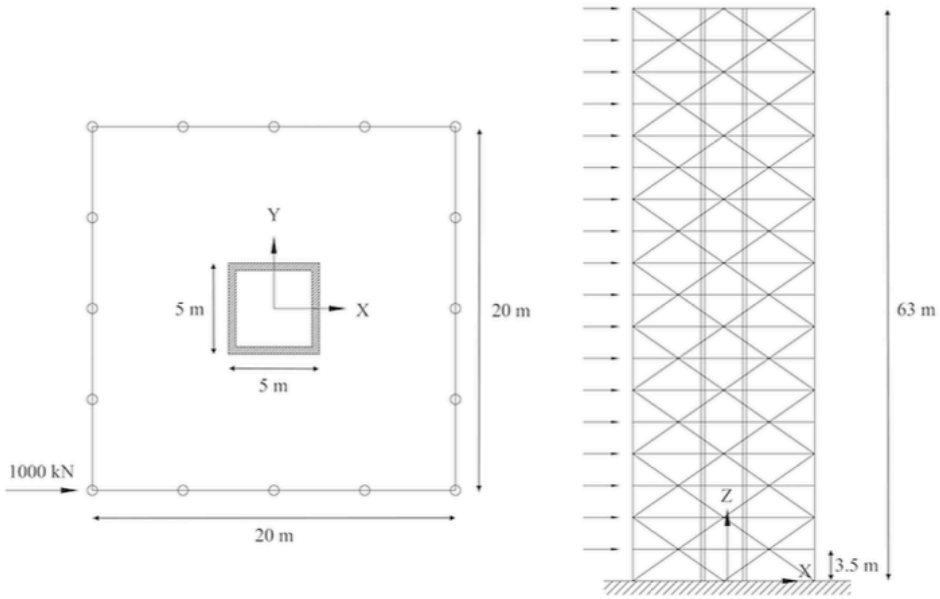

Figure 4.9. Diagrid system coupled with central core: (a) top view; (b) side view. Used with permission from Lacidogna et al. [117].

The plan of the building is shown in Figure 4.9a: it is made up of a 20 m × 20 m square diagrid system and a 5 m × 5 m central concrete core. The diagrid is composed by 18 modules and 18 floors with an inter-story height equal to 3.5 m

(Figure 4.9b). The concrete core is 40 cm thick and is characterized by a Young's Modulus of 30 GPa. Whereas, all the diagrid diagonals are made of steel (E = 210 GPa) and 508 × 25.0 mm CHS sections are assigned (A = 380 cm^2). According to the described geometry, the diagonal inclination is equal to 35°. The structure is subjected to horizontal floor forces which are constant along the elevation and equal to 1000 kN. These are applied with an eccentricity of 10 m with respect to the centroid of the building, in order to consider torque moments as well [117].

In Figure 4.10 the horizontal displacements and torque rotations of the buildings are shown, according to the GA theory as well as to FEM results. The maximum relative difference among the results are 3.0% and 0.9% for the top horizontal displacement and the top torque rotation respectively, thus confirming the validity of the MBM associated to the GA. Moreover, shear values as well as bending and torque moments acting on the structure floors are shown in Figure 4.11 [117].

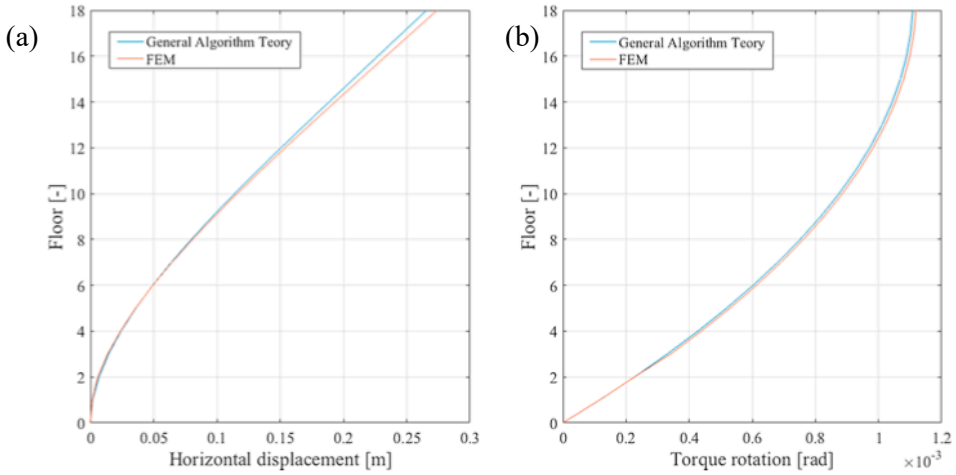

Figure 4.10. Diagrid system coupled with central core: (a) horizontal displacements; (b) torque rotations. Used with permission from Lacidogna et al. [117].

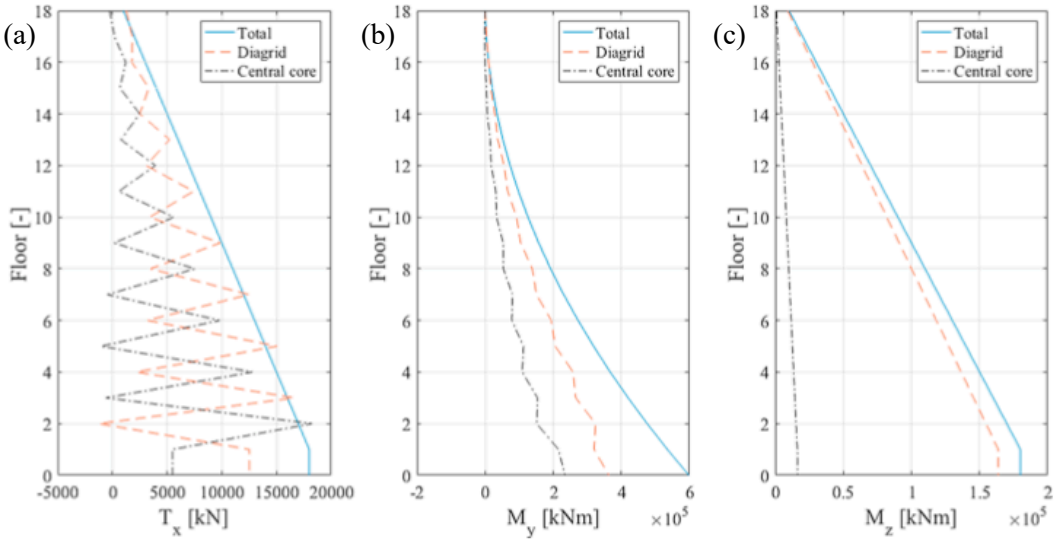

Figure 4.11. Diagrid system coupled with central core: (a) shear; (b) bending moment; (c) torque moment. Used with permission from Lacidogna et al. [117].

It is interesting to observe how these static features distribute between the two resistant elements. About the 70% of the base shear is absorbed by the diagrid, whereas about the 30% is withstood by the concrete core, although a remarkable

oscillating trend is noticeable along the elevation of the building. In the same way, about the 60% of the base bending moment is absorbed by the diagrid and the 40% by the central core. The oscillation is mainly due to the fact that the diagrid exhibits a significant variation of its flexural stiffness along the height of the building. Indeed, the resistance to the out-of-plane rotations of the diagrid is not uniform since, as can be noticed from Figure 19b referring to the vertical façades, the lever arm of the most external diagonals changes for different floors. This strongly affects the variation of the diagrid lateral stiffness. In turn, such oscillation has an impact on the distribution of the lateral actions, especially when the diagrid is coupled to the central concrete core, which conversely exhibits a uniform lateral stiffness. Regarding the torque moments produced by the eccentricity of the horizontal forces, they are withstood by the diagrid for the 91%, whereas the concrete core absorbs only the 9%. From the reported example, it is clear that the MBM, as far as subject to some restrictive hypotheses, may become a powerful tool to analyze complex spatial structures [117].

Note that, in the previous analysis, the diagonals of the external diagrid tube spanned over one single story. Therefore, the total number of building floors N corresponds to the number of floors considered for the diagrid. Otherwise, in the common cases where the diagrid diagonals span over multiple floors, the total number of building floors is usually greater than the number of floors at the end of the pinned diagonals, which are the only one used to compute the diagrid stiffness matrix. However, within the GA framework, all the building floors are always taken into account. This issue can be simply tackled by expanding the diagrid stiffness matrix $\widetilde{\boldsymbol{K}}_{\boldsymbol{HH}}$, before the insertion into the GA, and by filling all the rows and columns that are associated with the intra-module floors with zeros. In this way, the expanded matrix $\widetilde{\boldsymbol{K}}_{\boldsymbol{HH}}$ can be finally inserted into the GA to study the interaction between the diagrid and other elements, also in the cases where the diagonals span over multiple floors.

By following this approach, the MBM was recently used within the GA to study the behavior of a 40-story tall building made up of an external diagrid tube, with different diagonal inclinations, and an internal (closed- or open-section) shear wall [129]. The building's geometry is shown in Figure 4.12. The typical floor is a 25 m × 25 m square plan and the inter-story height is equal to 4 m, leading to a total building height of 160 m and an aspect ratio equal to 6.4. The diagrid tube is present on the exterior of the structure, made up of steel diagonals, having the same inclination and cross-sectional area (0.1 m^2) along the height of the structure. A 9 m × 9 m square shear wall, made up of concrete and 0.80 m thick, is placed at the center of the floor. In order to study the influence of the shear wall type on the structural response, both closed- and open-section shear walls are considered (Figure 4.12a). Moreover, six different diagrid geometries are studied, considering six different diagonal inclinations (Figure 4.12b). In conclusion, given the overall geometry of the building, twelve structures are analyzed by means of the GA, changing the shear wall type and inclination of the diagonals. As for the loading conditions, the structure is subjected to 100 kN horizontal forces along the X direction and 1000 kNm torque moments, distributed along the height of building [129].

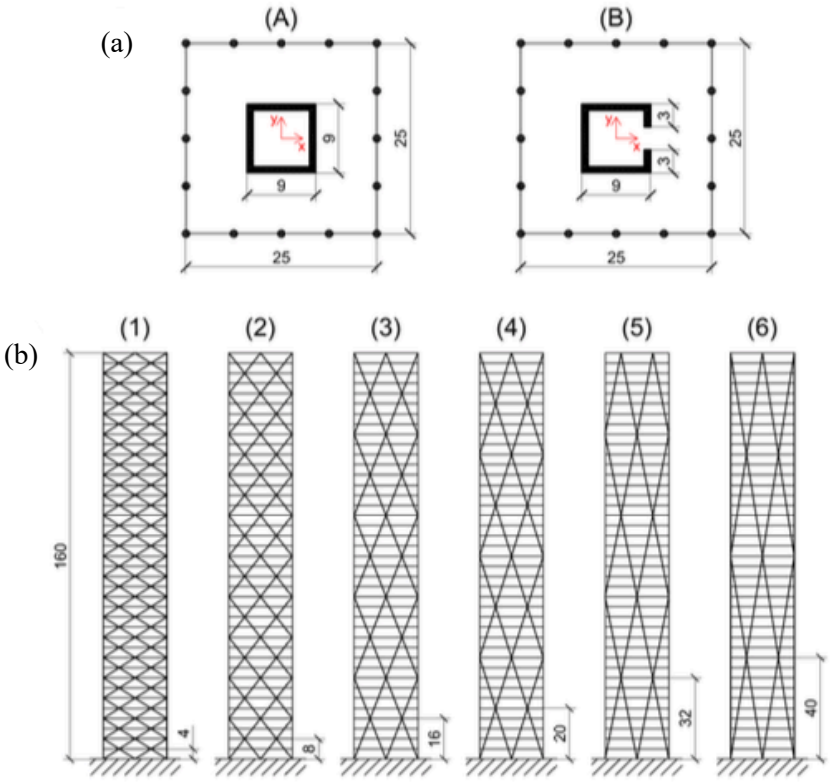

Figure 4.12. Building geometry: (a) floor plans, (b) lateral views. Used with permission from Lacidogna et al. [129].

In Figures 4.13 and 4.14, the lateral displacements and torsional rotations obtained by the GA are shown, for the case of diagrids coupled with closed- and open-section shear wall, respectively. As can be clearly seen in the figures, both the lateral displacements and torsional rotations are affected by the inclination of the external diagonals. This aspect will be deeply addressed in the following Chapter.

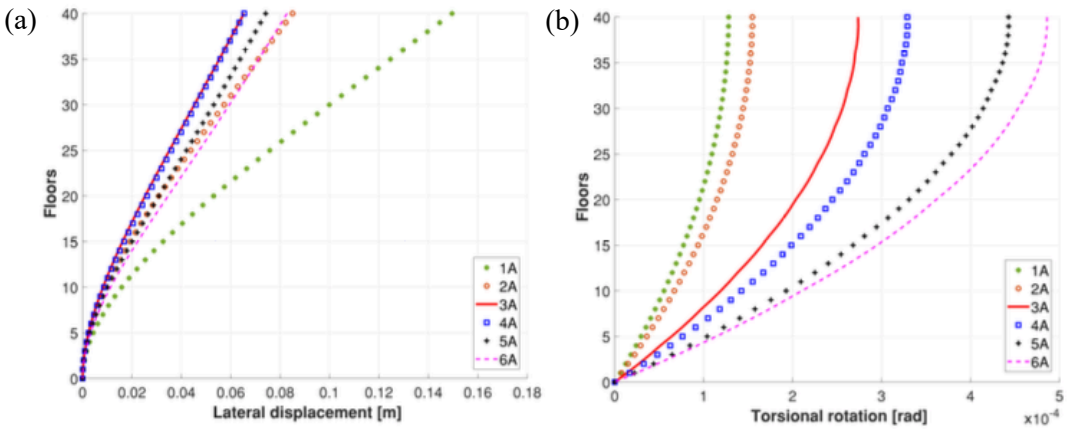

Figure 4.13. Diagrid tube coupled with closed-section shear wall: (a) lateral displacements, (b) torsional rotations. Used with permission from Lacidogna et al. [129].

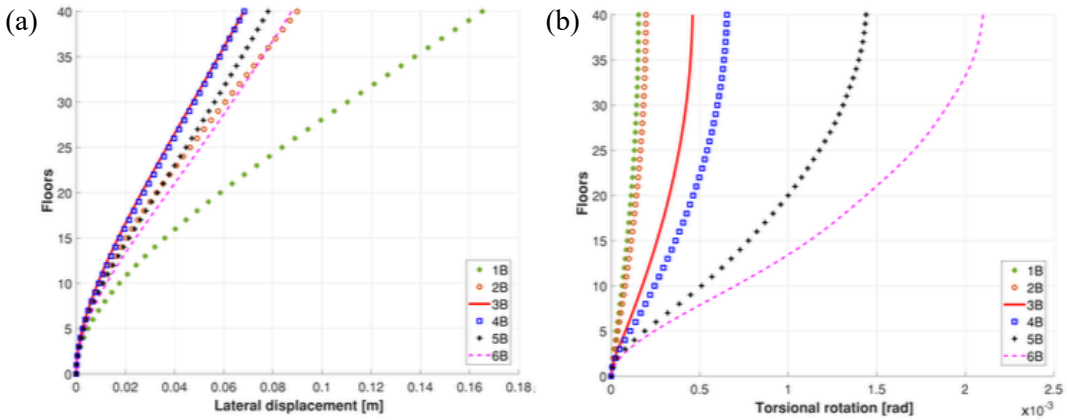

Figure 4.14. Diagrid tube coupled with open-section shear wall: (a) lateral displacements, (b) torsional rotations. Used with permission from Lacidogna et al. [129].

In Figure 4.15, the stiffness contribution of the diagrid system and the central shear wall is shown, both regarding the lateral (Figure 4.15a) and torsional (Figure 4.15b) stiffness. In order to obtain such values, the horizontal and torque actions have been applied to the separate models, i.e. the diagrid, the closed- and open-section shear walls, and the displacements at the top of each structure have been measured. Defining the global lateral (torsional) stiffness as the ratio between the total horizontal force (torque moment) at the base and the displacement (rotation) at the top of the structure, the relative stiffness between the diagrids and the shear walls could be simply evaluated as the ratio between the calculated stiffness values [129].

As shown in Figure 4.15a, the lateral stiffness of the diagrid is always higher than the shear walls' ones with the exception of scheme (1) from Figure 4.12, where the diagrid is found to be more flexible. The difference between the two shear walls (red and blue curve) is just due to the reduction of the moment of inertia due to the opening in the open-section shear wall [129].

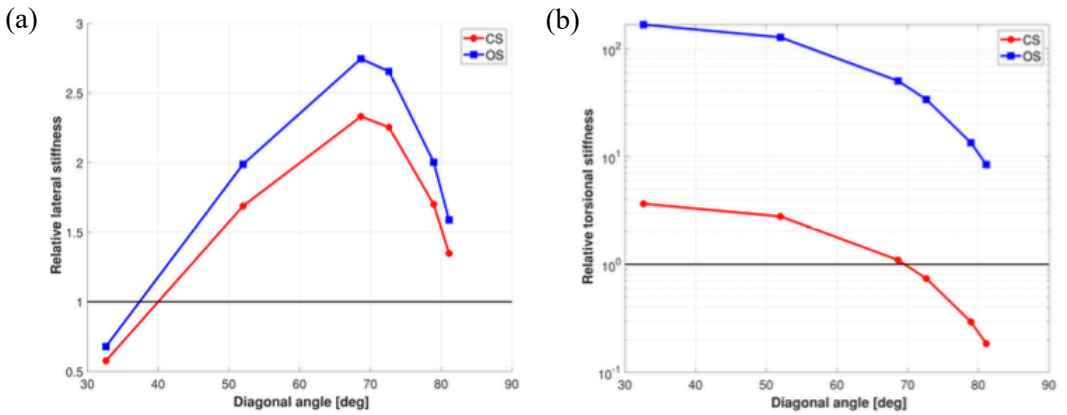

Figure 4.15. Relative stiffness of diagrid and shear wall: (a) lateral stiffness, (b) torsional stiffness. Used with permission from Lacidogna et al. [129].

As regards the relative torsional stiffness, it can be observed from Figure 4.15b (red curve) that the diagrid schemes (1) and (2) are more rigid than the closed-section shear wall, schemes (3) and (4) exhibit basically the same stiffness, whereas schemes (5) and (6) are much more flexible. Contrariwise, as far as the stiffness comparison with the open-section shear wall is concerned (blue curve), each diagrid scheme is much more rigid than the shear wall, and this is due to the

significant reduction of torsional rigidity of the open-section shear wall because of the opening. It is worth noting that, even if the diagrid schemes (5) and (6) are found to be approximately 10 times more rigid than the open-section shear wall, the torsional deformations (Fig. 4.14b) are significantly affected by the shear wall, since they show the inflection point due to the warping effect [129]. The influence of the diagonal inclination on both lateral and torsional flexibility of the diagrid tube will be thoroughly discussed in the following Chapter.

4.3 Conclusions

In this Chapter, the diagrid system, which is emerging in recent decades as an innovative solution for the design and construction of tall buildings, has been presented and analyzed by means of the Elastic Lattice modeling. In particular, after a brief overview about the main diagrid features and the most recent approaches suggested in the literature for the preliminary design and structural analysis, a matrix-based method (MBM) has been proposed for a quick analysis of the diagrid behavior. Based on the six DOFs of the rigid floors and consequent calculation of the diagrid stiffness matrix by means of the displacements method, the MBM has been shown to be effective in performing the structural analysis of generic diagrid tubes and allowing the evaluation of both the lateral and torsional flexibility of the diagrid structure.

Moreover, the MBM has been shown to be suitable for insertion into the General Algorithm (GA), which represents a semi-analytical methodology, based on matrix calculus, for the structural analysis of tall buildings made up of various resisting elements. In particular, based on the condensation of the diagrid stiffness matrix, this has been inserted into the GA environment in order to investigate the interaction between the diagrid and central cores.

The calculations shown in this Chapter refer to the linear structural analysis of the tall building, where floor forces and moments are applied to the system and the corresponding floor displacements and rotations are computed through the generalized Hooke's law. However, the MBM might be suitable for further developments, such as dynamic and non-linear structural analyses. The former needs the definition of the mass matrix $\boldsymbol{M}$ of the building, which involves the knowledge of the mass and inertia characteristics of the floors. The latter involves writing the equilibrium equations in the deformed configuration, which can be implemented in two ways. Either by re-writing the linear system reported in Eq. (4.8), that relates the floor forces and moments to the corresponding displacements and rotations, via non-linear equations thus following the same approach presented in the previous Chapter regarding the non-linear analysis of protein conformational changes (see Eqs. (3.10) and (3.11)), or by computing the geometrical stiffness matrix $\boldsymbol{K_g}$ of the diagrid system, that takes into account the influence of large displacements [6]. These extensions of the MBM will be addressed in future research efforts.

Despite the use of simplified models within the framework of linear structural analysis, these can still allow the designer to obtain pivotal information regarding the diagrid behavior, which can be crucial for preliminary design stages and optimization purposes. As a matter of fact, in this Chapter we have briefly mentioned that the geometrical features of the diagrid, especially the diagonal inclination, might play an important role in defining its structural behavior, and finally its structural efficiency. This subject will be the major focus of the following Chapter, where the MBM will be deeply exploited, due to its capability

to provide a fast yet valuable description of the diagrid structural response, to investigate the influence of the diagrid geometry on its behavior and obtain the optimal diagrid solutions.

Chapter 5

ELMs and Diagrid Tall Buildings: Influence of the Diagrid Geometry on the Structural Behavior and Multi-Response Optimization

In the previous Chapter, we have described the diagrid systems, that are recently finding broad use worldwide for the design and construction of tall buildings due to their inherent structural efficiency and aesthetic potential. It has also been shown that the structural analysis of these tubular structures can be carried out by means of simplified methodologies, such as the matrix-based method (MBM) presented above, which rely on the Elastic Lattice modeling.

As already mentioned in the previous Chapter, the great structural efficiency of the diagrid is due to the fact that it combines together the advantages of the tubular structure with the basic triangular element. The former allows to reach high stiffness performances of the tall building, while the latter exploits the structural mechanism mostly prevailed by axial stresses. Moreover, the diagrid being composed by an assembly of triangular elements placed all over the exterior of the building, their arrangement can be properly changed in order to enhance the structural response. In this way, the diagrid performance can be further increased by means of optimization procedures.

This will be the focus of the present Chapter, which aims at describing the influence of the diagrid geometry on the structural performance and proposes a new methodology for the diagrid optimization. Specifically, in the first part of the Chapter, a brief literature overview of the research works about diagrid optimization is carried out. This is mostly taken by the recent review paper by Scaramozzino et al. [100]. Then, the influence of the diagrid geometrical characteristics on the structural response of the building is investigated. The analysis is carried out by means of the MBM, investigating both the lateral and torsional flexibility of the structure. Finally, a multi-response optimization will be

presented by making use, for the first time in this field, of the desirability function approach.

5.1 Literature Overview on Diagrid Optimization

Besides the great stiffness of the diagonalized façades and their capacity to realize complex-shaped systems, one of the main successful aspects of diagrids is the possibility they offer of reaching high structural performance standards, thanks to the optimization of the geometrical features. In the last decade, various researchers have thoroughly investigated the structural behavior of diagrids upon changing the external diagonal pattern in order to reach the optimal solutions.

Moon et al. [109] showed for the first time that there exists a diagonal angle capable of satisfying the stiffness requirements with the minimum amount of employed material. The optimal angle results from the need to limit both shear and bending deformation, and it is found to increase as the aspect ratio of the building increases. As already mentioned in the previous Chapter, for 60-story tall diagrids with an aspect ratio of about 7, the optimal angle is in the range 65°–75°, while it decreases of about 10° for aspect ratios close to 5 [109]. Approximately the same results were found in [110] for a set of 40- to 100-story tall diagrids.

Under lateral actions, shear forces and bending moments have different trends along the building's elevation. For example, if we consider a uniform horizontal load, the shear force is zero at the top of the building and increases linearly towards the base, while the bending moment increases quadratically. This means that the need to resist shear and bending actions is different in different parts of the structure. Shear force prevails in the upper portion, while bending moment drives the design of the lower part.

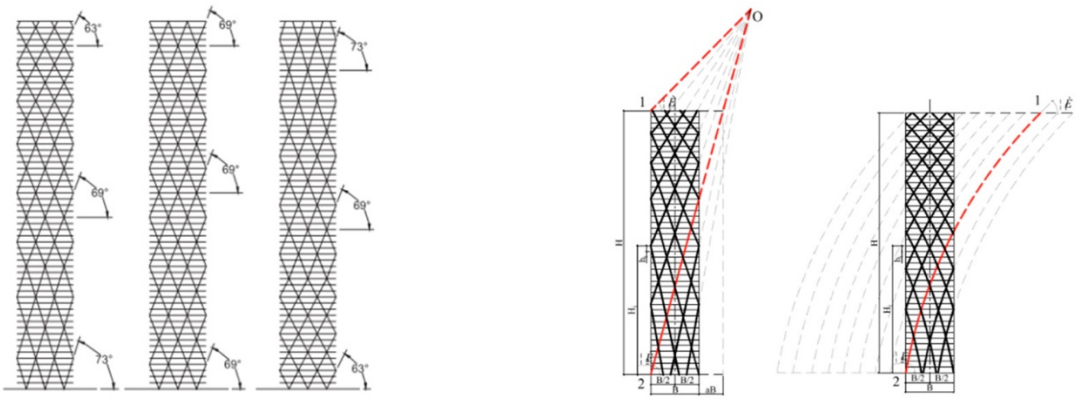

Figure 5.1. Different diagonal angle patterns: (a) varying-angle with steeper diagonals at the base; (b) uniform-angle; (c) varying-angle with steeper angle at the top, used with permission from Moon [110]; (d) varying-angle with straight diagonals; (e) varying-angle with curved diagonals, used with permission from Zhao and Zhang [130].

Based on this consideration, Moon investigated diagrid buildings with different patterns of diagonal angles [110]. Figure 5.1a shows a varying-angle diagrid with steeper angles at the base, Figure 5.1b a uniform-angle diagrid, and Figure 5.1c a varying-angle diagrid with steeper angles at the top. Steeper diagonals are more suitable for carrying bending moment, while shallower diagonals are more appropriate for carrying shear force. Therefore, the solution in Figure 5.1a should enhance the structural performance of the diagrid. Conversely,

the solution with steeper diagonals at the top behaves against structural logic, and is only considered for the sake of completeness, as it is not supposed to provide any beneficial effect.

Based on the results, it was found that, for shorter buildings with aspect ratios lower than 7, the uniform-angle configuration provides the most efficient design in terms of material consumption. Shorter buildings behave like shear beams, and while the steeper diagonals at the base enhance the bending stiffness, the negative effect of the reduced shear rigidity causes the varying-angle diagrids to lose efficiency. Contrariwise, for taller buildings with aspect ratios greater than 7, the bending behavior prevails. The reduced shear rigidity at the base due to the steeper diagonals is balanced by the significant increase in bending stiffness. Therefore, in this case, the varying-angle configuration was found to provide the most efficient solution [110]. The same results were found in another paper by Moon [131], where the author also took into account the "speed" of variation of the diagonal angles along the height of the building, with smooth or more radical changes.

In the solutions provided by Moon with variable angles, the diagonals do not remain straight across their length over the full height of the building, because of their changing direction at the interface of two diagrid modules with different angles. To overcome this, Zhang et al. [132] proposed a different strategy for the generation of varying-angle diagrid tubes. As shown in Figure 5.1d, a graphic approach was suggested to generate a varying-angle pattern with straight diagonals that extend over the full height of the building. This pattern is governed by two fundamental parameters, the top angle θ_1 and the bottom angle θ_2. The stiffness- and strength-based design criteria were applied to a set of 30- to 75-story tall, varying-angle diagrids with straight diagonals, with aspect ratios ranging from 3.6 to 9. Several θ_1–θ_2 combinations were considered to investigate the optimal solutions under gravity and wind loads. Based on the results, the following empirical formulas were suggested for the optimal values of θ_1 and θ_2, depending on the building's aspect ratio H/B:

$$\theta_{1,opt} = \begin{cases} \theta_{2,opt} & \frac{H}{B} \le 3.5 \\ \dfrac{1}{\left(1+\ln\frac{H/B}{3.5}\right)^{\frac{H}{2B}}}\left(\theta_{2,opt} - \arcsin\frac{1}{\sqrt{3}}\right) + \arcsin\frac{1}{\sqrt{3}} & \frac{H}{B} > 3.5, \end{cases} \quad (5.1a)$$

$$\theta_{2,opt} = \arctan\frac{H/B}{1+0.475\sqrt{\frac{H/B}{4.75}}}. \quad (5.1b)$$

As H/B increases, the optimal bottom angle $\theta_{2,\mathrm{opt}}$ increases, while the optimal top angle $\theta_{1,\mathrm{opt}}$ decreases. A critical value of the aspect ratio, $(H/B)_{\mathrm{crit}}$, was found, which defines the interface between the efficiency of uniform- versus varying-angle diagrids, meaning that below $(H/B)_{\mathrm{crit}}$, uniform-angle diagrids are more efficient, while above this value varying-angle structures provide the most economical solutions. In this paper, $(H/B)_{\mathrm{crit}}$ was found to be 4.5–5, smaller than the value of 7 previously suggested by Moon [110,131]. This is mainly due to the different definition of the diagonal pattern. For aspect ratios less than $(H/B)_{\mathrm{crit}}$, the bottom angle rather than the top angle drives the design. Conversely, for greater aspect ratios, the top angle becomes one of the determining factors [132].

In a following paper, Zhao and Zhang [130] proposed an additional diagrid configuration, where the varying-angle solution is obtained with curved diagonals

(Figure 5.1e). In the same paper, they also considered seismic loads in the evaluation of the optimal diagrid pattern. It was found that, for varying-angle straight diagonals, the optimal bottom angle $\theta_{2,opt}$ is not affected by the load type, thus Eq. (5.1b) holds true also for seismic loads. However, the optimal top angle $\theta_{1,opt}$ is always close to the lower limit for seismic loads, i.e. $\theta_{1,opt} = \arcsin(1/\sqrt{3})$, thus correcting Eq. (5.1a). In the case of diagrids with curved diagonals, the authors proposed the following equations for the optimal angles, which are valid for both wind and seismic loads:

$$\theta_{1,opt} = 0.8\left(\frac{H/B}{8}\right)^{\frac{1}{8}}\theta_{2,opt}, \tag{5.2a}$$

$$\theta_{2,opt} = \arctan(H/B), \tag{5.2b}$$

H/B being in the range 3.6–9. With these values, the optimal top angle $\theta_{1,opt}$ lies in the range 50°–70°, greater than the top angles in diagrids with straight diagonals (35°–45°). Thus, the lesser difference between $\theta_{1,opt}$ and $\theta_{2,opt}$ in this case results in a small curvature of the diagonals [130].

Further developments in the external diagrid patterns were carried out by Montuori et al. [133]. In addition to the consideration of uniform- and varying-angle (VA) solutions, the authors also proposed diagrid patterns with variable-density (VD) in the diagonal layout (Figure 5.2a). FE calculations were performed on a 90-story tall building with an aspect ratio of 6.62, under gravity and wind loads, and the structural responses were analyzed in terms of top lateral deflection, inter-story drifts and diagonal DCR. For each solution, an efficiency parameter was proposed as $1/D_{top}w$, D_{top} and w being the lateral displacement and the employed steel weight per total floor area, respectively. The lower the lateral displacement and the amount of steel, the greater the efficiency of the investigated solution. The obtained efficiency parameters are shown in Figure 5.2b for all the considered solutions. From the results, it was found that the 80° and VA3 solutions result in lower efficiency in the investigated case, whereas VA1 is the most efficient one. Uniform-angle solutions with 60° and 70°, as well as the variable patterns VA2, VD1 and VD2, show similar efficiency values [133].

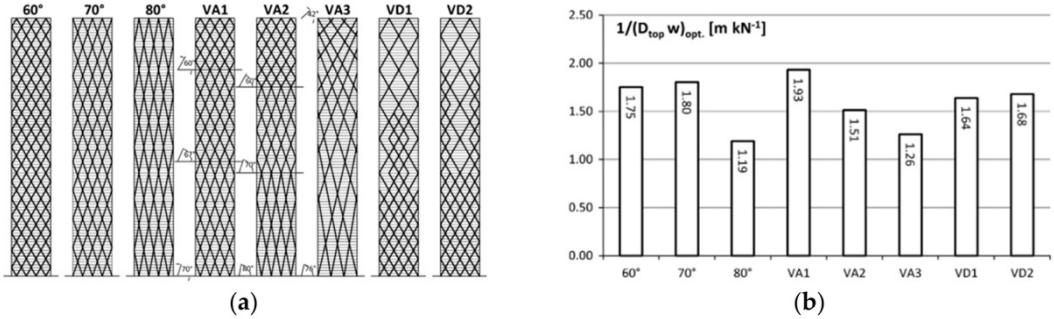

Figure 5.2. (a) Different geometrical patterns from Montuori et al. [133]: uniform-angle patterns (60°, 70°, 80°), varying-angle patterns according to Moon approach (VA1, VA2) [110,131], varying-angle pattern according to Zhang approach (VA3) [132], variable-density patterns (VD1, VD2). (b) Efficiency parameters for the investigated solutions. Used with permission from Montuori et al. [133].

Additional analyses regarding different pattern configurations can be also found in the work of Angelucci and Mollaioli [108]. After exploring the effectiveness of stiffness-based approaches for a 351-m tall diagrid with optimal

(69°) and non-optimal (82°) diagonal angles, in order to evaluate whether common approaches lead to optimized member sizes, the authors proposed additional variable-density (VD) patterns for the diagonal arrangement (Figure 5.3). Two VD strategies were suggested for the non-optimal (82°) diagrid tube in order to meet the stiffness requirements: a localized pattern, resembling one-outrigger-like (Figure 5.3a) or two-outrigger-like (Figure 5.3b) schemes; and a more uniform VD pattern, which provides additional distributed stiffness over the building elevation (Figure 5.3c,d). The outcomes from FE calculations showed that the local density increments (Figure 5.3a,b) are not efficient strategies for meeting the stiffness and strength requirements. Conversely, the solutions involving a more uniform VD pattern (Figure 5.3c,d), where the diagonal concentration rarefies towards the top of the building, turn out to be appropriate solutions for limiting the lateral displacements, while obtaining notable material savings [108].

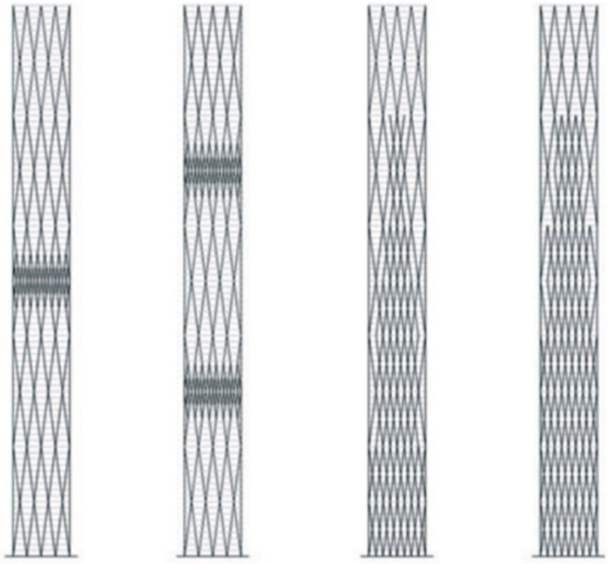

(**a**) (**b**) (**c**) (**d**)

Figure 5.3. Variable-density (VD) patterns proposed by Angelucci and Mollaioli [108]: (a-b) concentrated outrigger-like VD pattern; (c-d) distributed VD pattern. Used with permission from Angelucci and Mollaioli [108].

The previous work of Montuori et al. [133] was subsequently developed by Tomei et al. [134], who proposed additional diagonal patterns for the 90-story tall diagrid building (Figure 5.4a). Besides considering the usual uniform- and varying-angle patterns, the authors also suggested a double-density pattern (DD) (where the diagonal layout is doubled and mirrored over the diagrid façade), a variable-density pattern (VD) (generated by starting from the DD pattern with further topology optimization), and a diagrid-like pattern (ISO) (where the diagonals follow the principal stress lines obtained from the equivalent building cantilever). Stiffness- and strength-based preliminary designs were carried out, together with optimization procedures based on Genetic Algorithms through the use of commercial software. The optimization procedure aimed at minimizing the unit structural weight of the building, while complying with the stiffness and strength requirements. This was achieved by formulating an objective function (OF) to be minimized, and specifying the constraints of the optimization problem, as thoroughly described in [113,134].

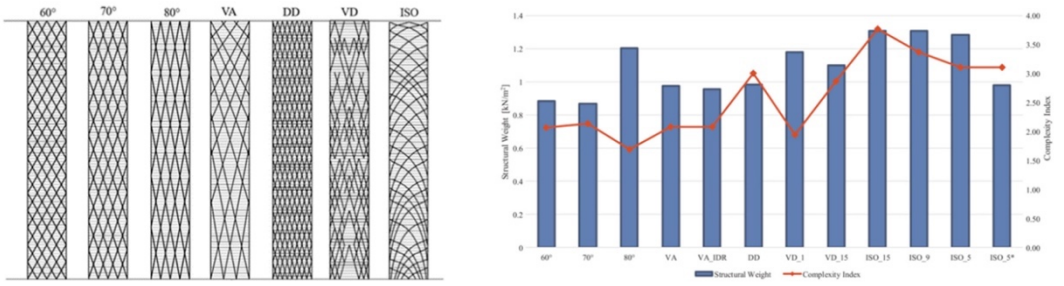

(**a**) (**b**)

Figure 5.4. (a) Geometrical patterns for the 90-story tall diagrid building considered by Tomei et al. [134]: uniform-angle patterns (60°, 70°, 80°), varying-angle pattern according to Zhang approach (VA) [132], double-density pattern (DD), variable-density pattern (VD), stress lines pattern (ISO). (b) Unit structural weight (blue bars) and complexity index (red curve) for the investigated diagrid patterns. VA_IDR, VD_1, VD_15, ISO_15, ISO_9, ISO_5, ISO_5* refer to additional subsets of the corresponding patterns, as reported in [134]. Used with permission from Tomei et al. [134].

The results were analyzed in terms of unit structural weight, diagonal cross-section distribution along the elevation, deformed configuration, lateral displacements, inter-story drifts and diagonal DCR, highlighting the most efficient solutions from the structural viewpoint. The authors also proposed a complexity index, which accounts for the "constructability" of the diagrid structure. This was defined by taking into account five main metrics, i.e., the total number of nodes, the number of different cross-sections, the number of diagonal splices necessary for transportation purposes, the total number of diagonals and the number of different diagonal lengths. The results of the complexity index, together with the obtained structural weight, are shown in Figure 5.4b for each geometrical pattern. Graphs like the one reported in Figure 5.4b can be extremely useful for evaluating both the structural efficiency and constructability of the investigated diagrid solutions [134].

The analyses above, for the assessment of diagrid performance, have taken into account only square and rectangular buildings. To consider also different plan shapes, Mirniazmandan et al. [135] recently investigated the simultaneous effect of diagonal inclination and planar shape on the top lateral displacement and diagrid weight. A total of 64 parametric models of a 180-m tall building, with various cross-sectional shapes, were generated by randomly increasing the number of sides of both the base and top plans. Five diagonal angles were also considered, in the 33°–81° range. By means of Genetic Algorithms coupled with FE structural analyses, the authors found out that the diagonal angle of 63° provides the least amount of top lateral deflection, while reducing the required structural material. Furthermore, it was found that increasing the sides of the base and top plans leads to the most efficient solutions in terms of lateral displacement, although the increase of structural performance is not as evident as when changing the diagonal inclination.

Finally, all the analyses presented so far have mainly dealt with tubular structures with vertical façades. In a very recent paper, Ardekani et al. [136] investigated the influence of the plan shape, together with the convexity and concavity of the diagrid surface. Based on FE calculations for a set of 40-story tall buildings, the outcomes showed that, compared to rectangular diagrids, other polygonal forms might lead to beneficial material savings while meeting the stiffness requirements. Furthermore, with respect to the normal models, the

buildings with convex and concave façades achieve better results in terms of structural performance.

As can be easily recognized from the studies reported in this Section, one of the main aspects that has caused the notable proliferation of the diagrid in recent years is related to the versatility of its external diagonal layout. A rational and optimized diagonal pattern allows to achieve remarkable structural performance, together with beneficial material savings. The application of expeditious FE calculations, as well as simplified methodologies such as the ones reported in the previous Chapter, together with optimization techniques, can help engineers and designers to achieve high-performance structures in the preliminary stages of tall building design.

The main approach from the optimization studies reported above has relied on the definition of the optimal diagrid geometry based on the lateral deflection and amount of employed material. In particular, the building is usually constrained to reach the target lateral deflection (typically, $H/500$), and the optimal solution is chosen as the one that minimizes the use of structural material. This is an example of two-response optimization procedure, where one response (lateral deflection) is used as a constraint and the other (structural mass) is employed as the objective function to be minimized. The best solution is the one that allows to achieve the target lateral displacement, while minimizing the amount of material.

However, besides the lateral flexibility and amount of employed material, other response variables might be equally important for the definition of the optimal solution. One has already been suggested by Tomei et al. [134], who have taken into account the construction complexity of the structure by means of the complexity index (*CI*). This is informative of the actual capability to realize the structure without too much effort, i.e. low number of nodes, diagonals with the same length and cross-section, etc. Another response variable that might be important is related to the torsional behavior of the structure. As a matter of fact, the diagrid tube is rather rigid under torque actions, as it is placed on the exterior of the building. However, the torsional flexibility depends on the shear rigidity of the diagrid modules, which in turn is strongly dependent on the diagonal inclination [109]. Therefore, in the optimization process of the diagrid building, multiple response variables should be taken into account simultaneously: a diagonal pattern that is optimal for the minimization of the material consumption and lateral deformability might be too complex from a construction perspective and lead to high torsional rotations. For this reason, a multi-response optimization procedure should be carried out, in order to find the diagrid solution that offers the best compromise to minimize both the response variables.

This aspect will be addressed in the following Sections of this Chapter. In Section 5.2 the influence of the diagrid geometry will be investigated on the structural behavior. In particular, both the lateral and torsional flexibility will be analyzed for variable diagonal inclinations and floor plane shapes. Then, in Section 5.3, the multi-response optimization will be carried out, in order to find the optimal diagrid geometry that minimizes both the lateral and torsional flexibility, the use of structural material and the construction complexity. This will be performed by making use, for the first time in this field, of the desirability function approach, initially developed for the quality assessment of industrial processes and products.

5.2 Influence of the Diagrid Geometry on the Structural Behavior

In the previous Chapter, when studying the interaction between an external diagrid tube and an internal open- or closed-section shear wall, we have already appreciated that the diagonal inclination affects both the lateral flexibility and the torsional deformation of the structure [129]. In this Section, the influence of diagrid geometry on both the lateral and torsional flexibility will be thoroughly addressed. For this purpose, various diagrid buildings, having different aspect ratios, diagonal inclinations and floor plan shapes, have been analyzed, as recently reported by Lacidogna et al. in [137].

5.2.1 Influence of the diagonal inclination and floor plan shape on the lateral and torsional flexibility

Specifically, 126-, 168-, 210- and 252-meter tall buildings have been considered with four different floor shapes and six diagonal inclinations, as reported in Figure 5.5. Figure 5.5a shows the four different building heights, that correspond to 36, 48, 60 and 72 stories, respectively, given an inter-story height of 3.5 m. Figure 5.5b reports the four investigated floor plan shapes, namely square, hexagon, octagon and circle, generated by keeping a constant floor area of 900 m^2. Finally, Figure 5.5c highlights the six uniform-angle patterns, by changing the number of intra-module floors, which in turn modifies the diagonal inclination. The number of intra-module floors vary from 1 to 12, so that the diagonal inclination varies between 35° and 84°, with slight changes among the floor shapes [137].

The external diagrid tubes are composed of twenty-four steel diagonals per module. In order not to consider the influence of the variable diagonal arrangement as well as their varying cross-sectional areas at this stage, a uniform-angle pattern has been considered with the diagonals having the same dimension along the height of the building. The case of varying diagonal dimensions has been investigated in [137] and found not to affect the main conclusions of the analysis.

The buildings have been considered to be subjected to horizontal and torque loading conditions. Initially, the loads have been kept constant along the height of the building. However, the case of linearly variable loads has also been considered and has been found not to affect the main outcomes. The top lateral displacements and torsional rotations have been evaluated by means of the MBM for each diagrid geometry, and analyzed to investigate the influence on the global structural response. The reader can refer to [137] for more details.

Figures 5.6–5.9 report the results for the 36-, 48-, 60- and 72-story building, respectively. In particular, Figures 5.6a–5.9a and 5.6b–5.9b show the computed top lateral deflection with respect to the number of intra-module floors and diagonal angle, respectively. Similarly, Figures 5.6c–5.9c and 5.6d–5.9d show the variation of the top torsional rotation with respect to the number of intra-module floors and diagonal angle.

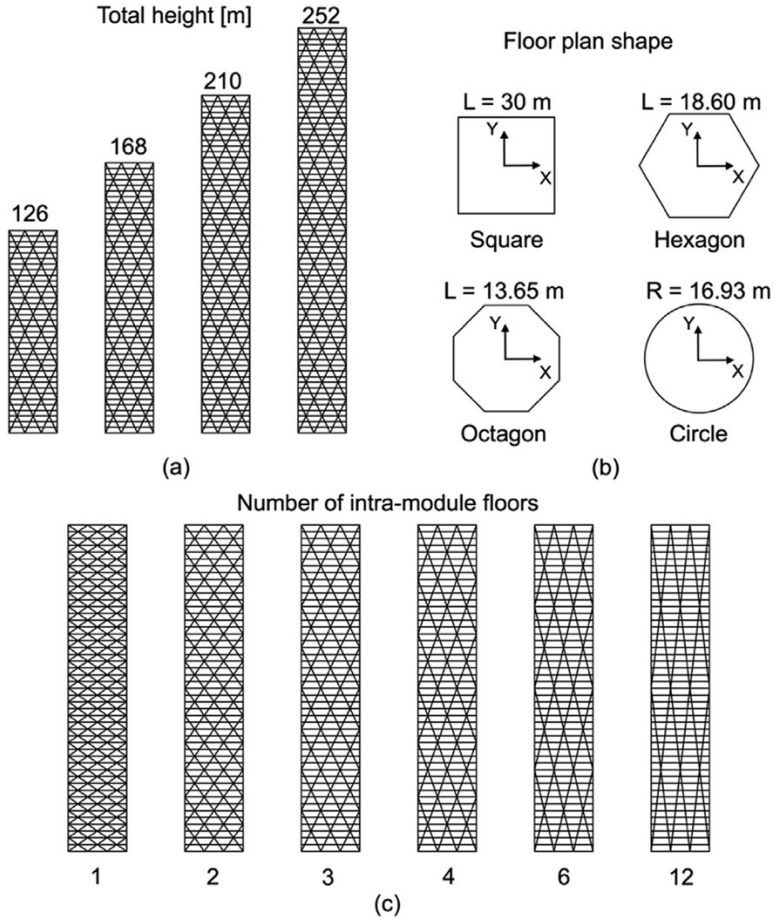

Figure 5.5. Geometry of the generated diagrid buildings: (a) four different total heights; (b) four different floor plan shapes; (c) six different diagonal inclinations. Used with permission from Lacidogna et al. [137].

As can be observed from Figure 5.6, the optimal solution to minimize the lateral displacements of the 36-story building corresponds to the configuration with three intra-module floors for each floor plan shape (Figure 5.6a). Correspondingly, the optimal diagonal inclination to minimize the lateral deflection stands in the range 64°–67° (Figure 5.6b). By examining Figure 5.6a, it is evident how the solutions related to two and four intra-module floors are not far from the optimal condition, leading to lateral displacements just 10% higher than the minimum ones. However, increasing the diagonal inclination, the total amount of employed material decreases. A balance between the need to limit the lateral displacement and reduce the amount of employed material is then needed, when selecting the optimal structural solution in the preliminary design stages.

In the optimal diagonal configuration (three intra-module floors), no significant differences can be observed when changing the plan shape. The absolute minimum displacement corresponds to the square shape (60 mm) while the highest arises from the circular one (63 mm), which is just 5% higher. The influence of the specific plan shape is otherwise important far from the optimal diagonal configuration, e.g. when considering one intra-module floor or more than six floors included within the diagonal module. In this case, as shown in Figures 5.6a and 5.6b, changing the floor plan geometry can lead to not negligible differences in terms of lateral flexibility (up to 30% difference) [137].

Different conclusions can be drawn when looking at the torsional flexibility of the building. In fact, the optimal solution to minimize torsional rotations corresponds to one intra-module floor, which is related to the shallowest diagonal

inclination (Figures 5.6c and 5.6d). This is due to the fact that torsional rigidity is related to the shear rigidity of the diagonal modules, and the latter has already been shown to achieve the highest value for low diagonal inclinations, close to 35° [109]. Note that, although the configuration associated with one intra-module floor is optimal to reduce torsional rotations, it exhibits lateral displacements much higher than the optimal ones. The results of the calculations also show that the optimal floor plan geometry to withstand torque actions corresponds to the circular shape. In fact, among the structures with the optimal diagonal inclination (one intra-module floor), the circular building exhibits the lowest torsional rotations (2.7×10^{-5} rad), the other ones providing higher values (up to 26% higher for the square building) [137].

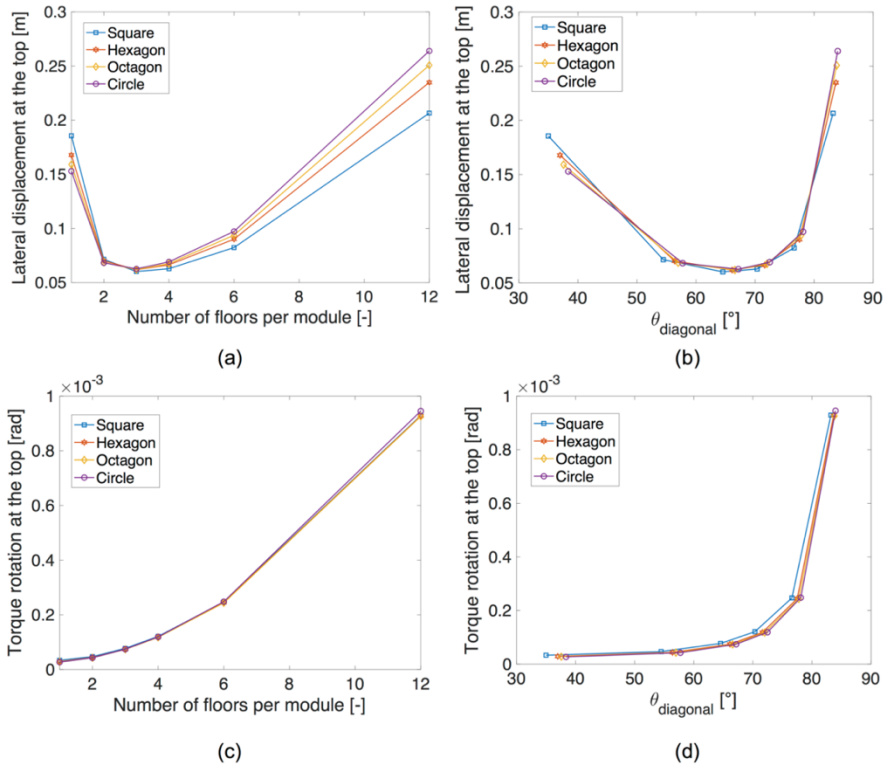

Figure 5.6. Displacements and rotations for the 36-story building: (a–b) lateral displacements; (c–d) torsional rotations. Used with permission from Lacidogna et al. [137].

The results obtained for the 48-story tall diagrid buildings are shown in Figure 5.7. In this case, the optimal solution to minimize lateral displacements is found to be associated to four intra-module floors for the square floor plan geometry and three intra-module floors for the other plan shapes (hexagonal, octagonal and circular). Accordingly, the optimal diagonal inclination is found to lie in the range 64°–70° (Figure 5.7b). The case of the square building demonstrates that, by increasing the aspect ratio of the building, higher diagonal inclinations are expected in order to minimize the lateral displacement. Again, as in the case of the 36-story building, the influence of the specific plan geometry is significant only in the region which is far from the optimal solution, e.g. for one, six or twelve intra-module floors (Figure 5.7a), and it leads to negligible differences in the region of the optimal diagonal inclination (3.5% difference). As far as the torsional behavior is concerned, in line with the outcomes of the 36-story building, the optimal solution to reduce torsional rotations corresponds to

the configuration with one intra-module floor and the circular plan shape (Figures 5.7c and 5.7d) [137].

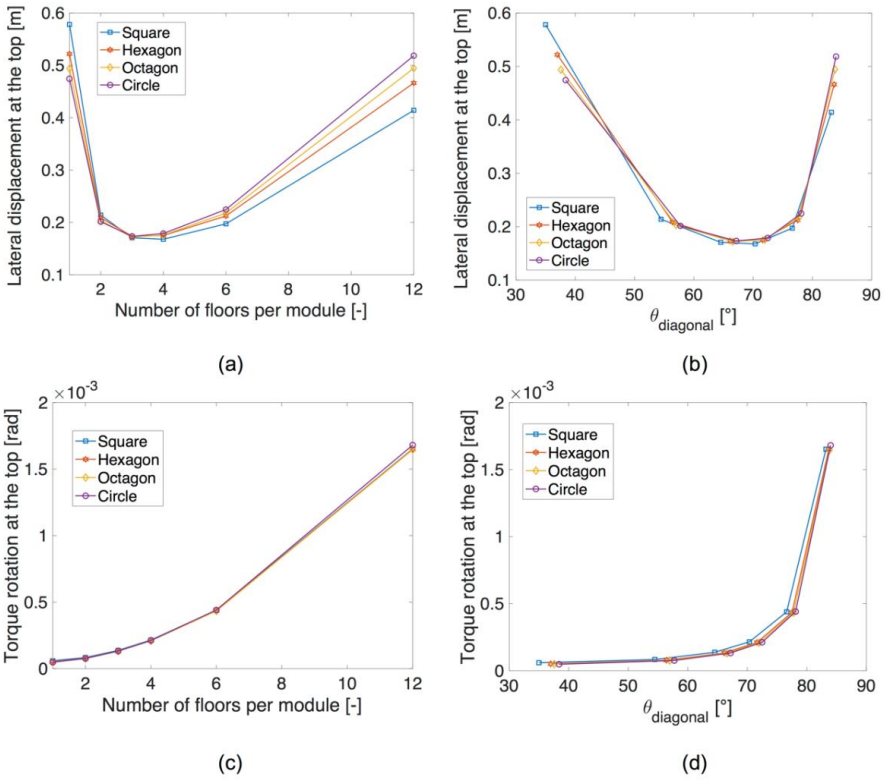

Figure 5.7. Displacements and rotations for the 48-story building: (a–b) lateral displacements; (c–d) torsional rotations. Used with permission from Lacidogna et al. [137].

In Figure 5.8, the results are displayed which are related to the 60-story tall diagrid buildings. In this case, the configurations associated to four intra-module floors are found to be the optimal ones in order to minimize lateral displacements for all the floor plan geometries. Again, the influence of the specific plan shape is not negligible only when considering one or more than six intra-module floors (Figure 5.8a). In this case, the diagonal inclination associated to the minimum lateral displacements is found to lay in the range 70°–72° (Figure 5.8b). As can be seen, increasing the aspect ratio of the building leads to higher values of the optimal diagonal angle. Analyzing the results related to the torsional flexibility, the optimal solution to minimize the torsional rotations involves again only one intra-module floor and the circular floor geometry (Figure 5.8c and 5.8d) [137].

Finally, the results arising from the analysis of the 72-story tall buildings are shown in Figure 5.9. In this case, the same outcomes observed for the 60-story structures are found: the best configurations which minimize the lateral displacements imply four intra-module floors for all the plan geometries (Figure 5.9a), the optimal diagonal angle lies in the range 70°–72° (Figure 5.9b) and the differences among the different floor plan shapes are not negligible just for one, six or twelve intra-module floors (Figure 5.9a). Again, as far as the torsional behavior is concerned, the one intra-module floor circular building is the most capable one to withstand torque actions, since it provides the lowest torsional deformability (Figure 5.9c and 5.9d) [137].

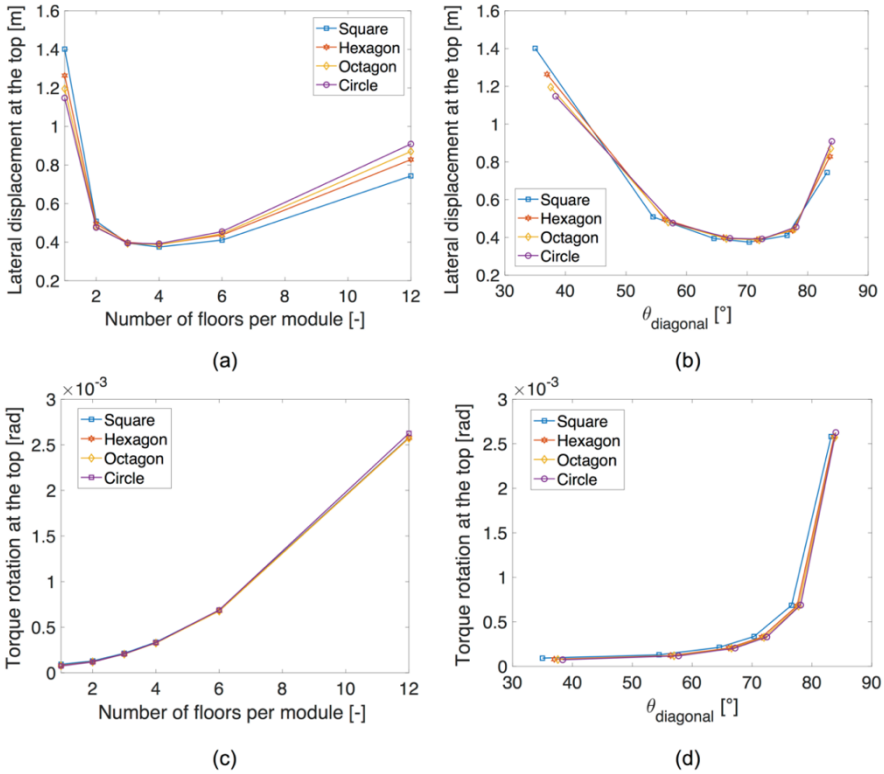

Figure 5.8. Displacements and rotations for the 60-story building: (a–b) lateral displacements; (c–d) torsional rotations. Used with permission from Lacidogna et al. [137].

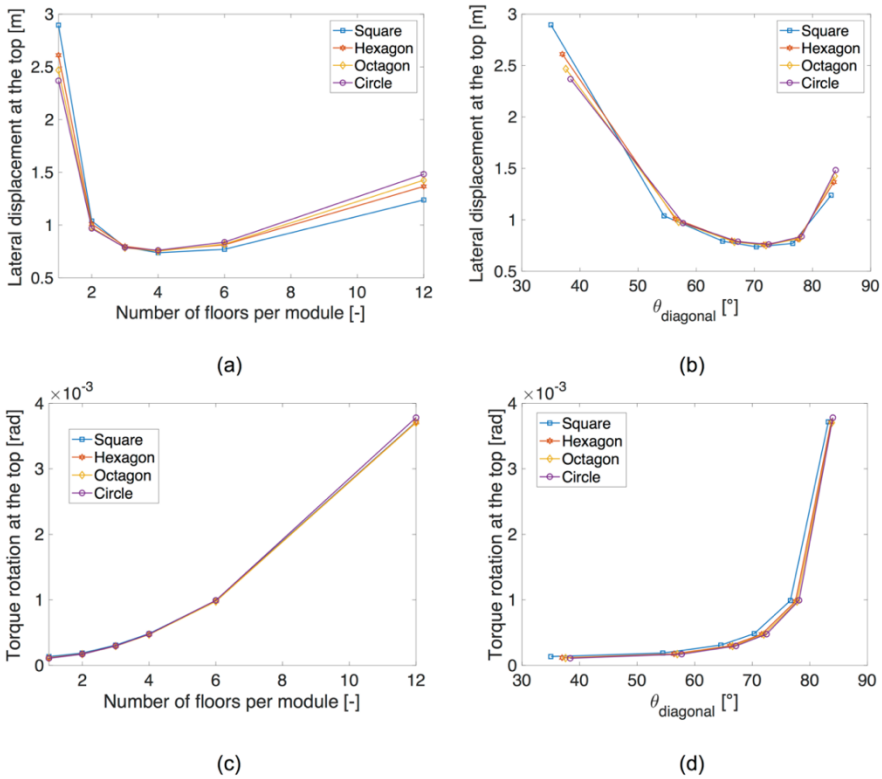

Figure 5.9. Displacements and rotations for the 72-story building: (a–b) lateral displacements; (c–d) torsional rotations. Used with permission from Lacidogna et al. [137].

5.2.2 Influence of the building aspect ratio on the optimal diagonal inclination and floor plan shape

As described above, the total height of the building has an influence mostly on defining the optimal structural configurations to minimize lateral displacements. In fact, by increasing the total height of the building, the number of intra-module floors which leads to the minimum lateral displacements increases from three to four, for each plan shape. As a consequence, the optimal range for the diagonal inclination increases from 64°–67° to 70°–72°. This is due to the fact that both shear and bending rigidity compete to define the lateral stiffness of the building. As shown by Moon et al. [109], the shear rigidity of the diagrid modules reaches the highest value for a diagonal inclination of about 35° and it decreases significantly for higher diagonal angles; contrariwise, bending rigidity is maximum if the diagonal angle is 90° and decreases for lower inclinations. By the competition of shear and bending rigidity, the optimal solution is usually found between these two values, depending on the building aspect ratio. Since shear behavior prevails for lower buildings and bending behavior for taller buildings, increasing the total high of the building leads to an increasing predominance of bending over shear deformation mode. Therefore, by increasing the height of the building, the diagonal inclination which provides the lowest lateral displacement exhibits higher values (Figures 5.6b–5.9b). Contrariwise, no competition between shear and bending rigidity occurs when dealing with the torsional behavior because, as mentioned above, this is governed only by the shear rigidity of the diagrid modules. For this reason, the diagonal inclination which leads to the lowest torsional rotations is always found to be the shallowest one, in the range 35°–38° [137].

With regards to the influence of the floor plan geometry on the structural response, this is usually found to be very small when the diagonal inclination lies in the optimal range. Although the differences are usually lower than 5%, it is interesting to note that the configurations which lead to the minimum lateral displacements are always associated to the square buildings. At first sight, this result seems in contrast with the findings of Mirniazmandan et al. [135], where the buildings with square geometry were not included in the list of the most performant solutions for the limitation of the lateral displacements. However, this difference mainly arises from the different choice of keeping distinct geometrical parameters constant when changing the floor plan shapes. As a matter of fact, in the present work, we choose to keep the total floor area constant (this being one fundamental parameter for architectural purposes), whereas Mirniazmandan et al. [135] decided to keep the total external perimeter constant in their calculations. Choosing different geometrical parameters to be constant leads to different results in terms of floor dimensions. For example, by taking the circle geometry as the reference, considering the external perimeter constant leads to obtain a square geometry which is 12% smaller than it would be in the case of considering the total floor area constant. Since the base dimensions play a key role in governing the stiffness of the building, as they strongly affect the bending rigidity, this difference is the one which makes our results deviate from the ones of Mirniazmandan et al. [135]. Anyway, from both this analysis and the one of Mirniazmandan et al. [135], it is evident how the geometrical characteristic which mainly affects the lateral flexibility of the diagrid is the diagonal inclination, whereas the influence of the plan shape geometry is less evident.

Conversely, far from the optimal number of intra-module floors, the differences between the different floor plan shapes is found to be significant; for a number of intra-module floors lower than the optimum ones the optimal geometry is usually associated to the circular plan shape, whereas for higher numbers of intra-module floors the square plan geometry is the one providing the highest stiffness of the building (Figures 5.6a-5.9a). The hexagonal and octagonal plan geometries always exhibit structural responses in between [137].

Regardless the total height of the building, the optimal configuration which leads to the highest torsional stiffness is always associated to the circular plan geometry with the lowest inclination of the diagonals (one intra-module floor). As already remarked above, this is due to the torsional mechanism of the diagrid structure, which only involves the shear rigidity of the diagonal modules, and not their bending rigidity as in the case of lateral deformability. So far, all the researchers have focused their attention only on the limitation of the lateral displacements, not considering the torsional rotations [108,109,111,113,114,132–135,138]. Sometimes, torque actions can be particularly severe, e.g. in the case of a strong asymmetry in the resisting elements placed in the interior of the building which leads to a not negligible eccentricity between the mass and stiffness centroids of the floors. In these cases, the torsional rotations induced by these actions should be properly taken into account.

5.2.3 The need for a multi-response optimization technique

Unfortunately, in the analysis reported above, it has been shown that a unique diagonal inclination which minimizes the lateral displacement and the torsional rotation simultaneously does not exist. Therefore, when adopting the diagonal inclination that minimizes the lateral displacements, attention should be paid to the corresponding torsional rotations, as they might create problems to the façade elements as well [137]. Moreover, by changing the diagonal inclination, the total amount of structural weight obviously varies, and this is another object to be minimized in order to limit the material consumption. Furthermore, Tomei et al. [134] have recently shown that different diagrid patterns are associated with different levels of construction complexity. Based on the chosen diagonal arrangement, one can evaluate the total number of nodes, number of different diagonal cross-sections, etc. In order for the structure to be easily and quickly realized, the construction complexity of the diagrid should be minimized as well.

Summarizing, we are dealing with a problem where multiple responses need to be simultaneously minimized, namely the lateral deflection, torsional rotation, structural mass and construction complexity. The optimal structure should be stiff (both under lateral and torque actions in order to comply with safety and serviceability requirements), light (to limit the amount of employed material as well as to reduce the seismic loads), and easily constructible (to speed up the construction process). Therefore, a multi-response optimization technique is needed to solve this problem.

In the next Section of this Chapter, the application of the desirability function approach will be presented for this purpose. It is a widely used approach for the quality assessment of industrial products and processes, and it is applied here for the first time to the case of tall building structural optimization. The desirability function approach will be applied to find the optimal diagrid solution that allows to obtain the most desirable values of the different response variables. Here, the lateral deflection, torsional rotation, structural mass and construction complexity

are considered as the four response variables. Obviously, this is not a unique choice, since other responses can be considered as well, such as the maximum inter-story drift, the maximum acceleration under seismic loading conditions, the fundamental frequency of vibration, etc. However, these four selected responses are believed to represent fairly complete information about the structural solution under investigation, as they are informative both of the structural behavior (lateral deflection and torsional rotation), material consumption (structural mass) and easiness of the construction process (construction complexity).

5.3 Multi-Response Diagrid Optimization based on the Desirability Function Approach

In this Section, the multi-response optimization of the diagrid structure will be carried out by means of the desirability function approach. Firstly proposed by Harrington in 1965 [139] and further developed by Derringer and Suich in 1980 [140], the desirability function is nowadays a widely used methodology for the assessment of the optimal solutions in several fields, ranging from industrial engineering to biology. This function is based on the idea that the quality of a product or process that has many features is completely unacceptable if one of them is outside of a "desirable" limit [141]. The goal of the desirability function is to associate the highest desirability value to the product or process that exhibits the response variables that simultaneously have the best fitness with the target value or the target interval. This is achieved by converting the multiple responses into a single one, combining the individual responses into a composite function, which immediately leads to the identification of the optimal solution [141].

In the most general case, the Derringer's approach leads to the evaluation of an individual desirability function $d_i(y_i)$ for each response variable $y_i(x)$, being x the set of parameters that characterizes the response variable y_i. The individual desirability always takes values between 0 and 1, where 0 corresponds to a completely undesirable response and 1 stands for the most desirable response. The other solutions exhibit individual desirability values that lie in between these two, indicating more or less desirable responses.

The shape of the individual desirability function $d_i(y_i)$ can take various forms and depends on whether the goal is to maximize or minimize the response in a certain interval, or whether the response should reach a target value within the interval. The desirable interval is usually indicated as $(L_i - U_i)$, where L_i is the lower acceptable limit and U_i is the upper acceptable limit. Note that, in certain cases, L_i, U_i or both can be equal to infinity, representing a not finite interval. Finally, the target value within the interval $(L_i - U_i)$ is usually indicated as T_i.

If the response variable has to be maximized within the interval $(L_i - U_i)$, the individual desirability function $d_i(y_i)$ usually takes the following form:

$$d_i(y_i(x)) = \begin{cases} 0 & y_i(x) < L_i \\ \left(\dfrac{y_i(x) - L_i}{U_i - L_i}\right)^{r_i} & L_i \le y_i \le U_i, \\ 1 & y_i(x) > U_i \end{cases} \tag{5.3}$$

where the exponent r_i represents the weight that is associated to the importance of the response variable $y_i(x)$ to reach the maximum value. From Eq. (5.3), it follows that when the response $y_i(x)$ exhibits values higher than the upper limit U_i its

desirability is equal to 1, when it exhibits values less than the lower limit L_i its desirability is equal to 0. In between, the desirability function is an increasing function, whose trend depends on the value of r_i. If r_i is equal to 1, the trend is linear, whereas the trend is non-linear for r_i values different from 1. Figure 5.10a shows the trend of $d_i(y_i)$ when Eq. (5.3) is applied.

Conversely, when the response variable $y_i(x)$ needs to be minimized, the individual desirability function can take the following form:

$$d_i(y_i(x)) = \begin{cases} 1 & y_i(x) < L_i \\ \left(\dfrac{U_i - y_i(x)}{U_i - L_i}\right)^{r_i} & L_i \le y_i \le U_i, \\ 0 & y_i(x) > U_i \end{cases} \tag{5.4}$$

and its trend is reported in Figure 5.10b.

Finally, when a target value T_i is the most desirable response for $y_i(x)$, $d_i(y_i)$ is usually given by:

$$d_i(y_i(x)) = \begin{cases} 0 & y_i(x) < L_i \\ \left(\dfrac{y_i(x) - L_i}{T_i - L_i}\right)^{r_{i,1}} & L_i \le y_i < T_i \\ 1 & y_i(x) = T_i \quad , \\ \left(\dfrac{U_i - y_i(x)}{U_i - T_i}\right)^{r_{i,2}} & T_i < y_i \le U_i \\ 0 & y_i(x) > U_i \end{cases} \tag{5.5}$$

being $r_{i,1}$ and $r_{i,2}$ the two exponent weights for the two sub-intervals (L_i – T_i) and (T_i – U_i). Equation (5.5) is graphically reported in Figure 5.10c.

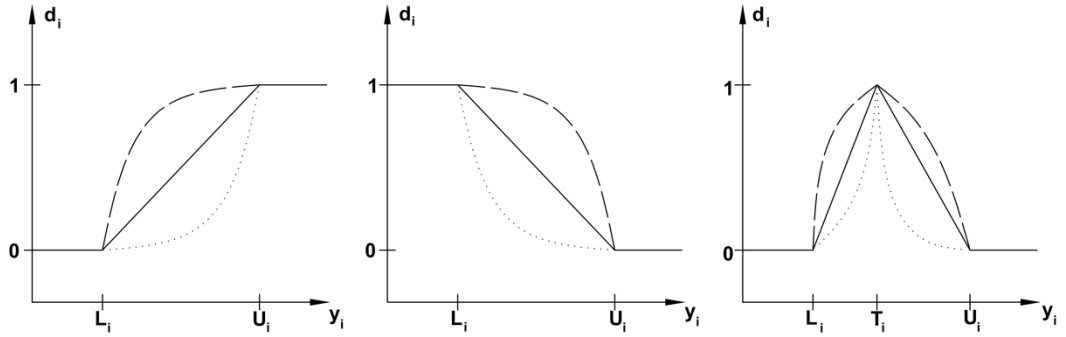

Figure 5.10. Graphical representation of the individual desirability functions $d_i(y_i)$ for different optimization criteria. The response y_i is most desirable if it reaches (a) the upper value U_i, (b) the lower value L_i, (c) a specified target value T_i. Continuous lines are obtained with r_i equal to 1, dashed lines with r_i less than 1 and dotted lines with r_i higher than 1.

By observing the individual desirability functions shown in Figure 5.10, it can be noted that low values of the weight parameters indicate that the response does not require to be strictly near the target value, reaching satisfactory desirability levels for a wide range of responses. In contrast, a choice of larger

weight exponents implies that the desirability is very low unless the response gets very close to the target [141].

Once all the n individual desirability functions $d_i(y_i)$ are evaluated for all the n response variables y_i, the methodology yields the definition of the overall desirability (OD) to find out the best joint responses, by using the following equation:

$$OD(x) = [d_1(y_1) \cdot d_2(y_2) \cdot \ldots \cdot d_n(y_n)]^{\frac{1}{n}} = \left[\prod_{i=1}^{n} d_i(y_i)\right]^{\frac{1}{n}}. \tag{5.6}$$

When OD reaches a value different from zero, all the variables which are being simultaneously optimized can be considered to have a desirable value. On the other hand, if one of the responses is completely undesirable, i.e. $d_i(y_i) = 0$, OD will be zero. The optimization procedure implies to maximize OD in order to obtain the optimal solution [141].

In the next sub-sections, the desirability function approach will be applied to the case of uniform-angle (Section 5.3.1) and varying-angle (Section 5.3.2) diagrid buildings. In both cases, as mentioned above, the response variables are the top lateral deflection under uniform lateral loads, the top torsional rotation under uniform torque moments, the structural mass of the external diagrid and the construction complexity, measured by the complexity index (CI) as suggested by Tomei et al. [134]. Therefore, referring to Eq. (5.6), in our problem n is equal to 4. Moreover, since all the responses need to be minimized to reach the optimal diagrid solution, Eq. (5.4) is used for the calculation of the individual desirability functions. Since the aim here is just to pick up the optimal solution out of a range of considered structures, the upper and lower limits of the intervals, i.e. U_i and L_i, are simply the maximum and minimum values of the responses obtained among the various solutions. Therefore, with these additional considerations, the desirability approach for the diagrid optimization yields the following equations for the individual desirability functions:

$$d_i(y_i(x)) = \left(\frac{\max\limits_x y_i(x) - y_i(x)}{\max\limits_x y_i(x) - \min\limits_x y_i(x)}\right)^{r_i}, \tag{5.7}$$

being x the set of input parameters affecting the solution (diagonal inclination, floor shape, etc.), $y_i(x)$ the response variable (top lateral deflection $\delta(x)$, top torsional rotation $\varphi(x)$, structural mass $M(x)$ and construction complexity $CI(x)$), $d_i(y_i)$ the resulting individual desirability value of the i^{th} response variable, r_i the weight parameter for the i^{th} response variable, whereas $\max\limits_x y_i(x)$ and $\min\limits_x y_i(x)$ represent the maximum and minimum values of the i^{th} response variable among all the considered solutions.

Based on Eq. (5.7), it is clear that the solutions that exhibit the maximum values of the responses have an individual desirability of 0, while those that exhibit the minimum values lead to individual desirability of 1. The individual desirability functions are finally combined together into the overall desirability (OD), via the following equation:

$$OD(x) = \left[\prod_{i=1}^{4} d_i(y_i)\right]^{\frac{1}{4}} = [d(\delta(x)) \cdot d(\varphi(x)) \cdot d(M(x)) \cdot d(CI(x))]^{\frac{1}{4}}. \quad (5.8)$$

Eventually, the analysis of the *OD* with respect to the input parameters x allows to evaluate the optimal diagrid solution that minimizes simultaneously the four response variables.

5.3.1 Multi-response optimization of uniform-angle diagrids

The desirability function approach is applied here to find the optimal geometry among the uniform-angle diagrids considered in Section 5.2. This Section mostly derives from the work recently reported by Lacidogna et al. in [142]. In particular, 126-, 168-, 210- and 252-meter tall buildings are investigated, with four different floor shapes and six different diagonal inclinations (Figure 5.5). For each building height, twenty-four different geometries are then generated by changing the diagonal angle and floor plan shape, as reported in Table 5.1.

Table 5.1. Twenty-four diagrid structures with different diagonal inclination and floor plan shape. Used with permission from [142].

Number of intra-module floors / Floor shape	1	2	3	4	6	12
Square	S1	S2	S3	S4	S6	S12
Hexagon	H1	H2	H3	H4	H6	H12
Octagon	O1	O2	O3	O4	O6	O12
Circle	C1	C2	C3	C4	C6	C12

The geometrical features of the diagrid buildings are the same considered above [137], with the only difference that here a tapered distribution of the diagonal cross-sections is considered: the steel diagonals at the ground module have a cross-section of 1000 cm^2, the ones at the upper module a cross-section of 100 cm^2, and the cross-sections of those in the intermediate modules follow a linear interpolation between the two. As reported above, the buildings are subjected to uniform lateral loads and torque moments, and the MBM is used to compute the top lateral deflection δ and torsional rotation φ for each geometry x. The diagrid mass *M* is evaluated for each geometrical pattern based on the specific arrangement and unit density of the steel diagonals. The construction complexity is assessed via the complexity index *CI* defined by Tomei et al. [134].

The *CI* is computed based on five metrics, i.e. N_1, N_2, N_3, N_4 and N_5. These are related to the construction complexity of the structure and are defined in [134] as follows: N_1 is the weighted number of nodes, i.e. the number of joints of the pattern multiplied by a numerical coefficient, differently attributed on the basis of the joint connectivity (number of connecting members); N_2 is the number of different cross-sections utilized for the diagonals in the pattern; N_3 represents the number of splices required for the diagonals in the pattern, calculated assuming a maximum member length of 12 m; N_4 is the number of diagonals of the pattern; N_5 is the number of different lengths of diagonal members in the pattern.

In this work, the same definition of the five metrics above is applied, with one minor difference regarding N_1. Instead of considering the weighted number of nodes based on the joint connectivity, due to the fact that we do not necessarily

know the connectivity degree of the nodes that connect the diagonals to the beams of the intra-module floors, the total number of diagrid panel nodes has been considered, i.e. only the nodes connecting the external diagonals [142]. After the five metrics N_j have been computed for the diagrid geometries, each metric is normalized to the maximum value among all the different geometries. Finally, the sum of the normalized parameters gives the *CI* of each geometry [134], i.e.:

$$CI = \sum_{j=1}^{5} \frac{N_j}{\max_x N_j}. \tag{5.9}$$

It is clear that high values of the five metrics involve greater values of the *CI*, meaning higher construction complexity.

Based on the presented methodology, Table 5.2 reports the results obtained for the twenty-four geometries of the 168-meter tall building (Figure 5.5), in terms of computed lateral displacement δ, torsional rotation φ, structural mass *M* and construction complexity index *CI*.

Table 5.2. Response variables (δ, φ, M, CI) for the twenty-four diagrid geometries of the 168-meter tall building (minimum values are in **bold**). Adapted from [142].

Diagrid geometry	$\boldsymbol{\delta}$ **(cm)**	$\boldsymbol{\varphi}$ **(10^{-5} rad)**	***M*** **(ton)**	$\boldsymbol{N_1}$ **(-)**	$\boldsymbol{N_2}$ **(-)**	$\boldsymbol{N_3}$ **(-)**	$\boldsymbol{N_4}$ **(-)**	$\boldsymbol{N_5}$ **(-)**	***CI*** **(-)**
S1	28.1	3.8	3016	576	48	**0**	1152	**1**	4.00
S2	10.5	5.3	2126	288	24	**0**	576	**1**	2.50
S3	**8.6**	8.8	1916	192	16	**0**	384	**1**	**2.00**
S4	8.7	13.8	1837	144	12	288	288	**1**	2.75
S6	11.0	28.9	1778	96	8	192	192	**1**	2.17
S12	29.0	124.2	1742	**48**	**4**	288	**96**	**1**	2.25
H1	25.3	3.3	2876	576	48	**0**	1152	**1**	4.00
H2	10.3	4.9	2077	288	24	**0**	576	**1**	2.50
H3	8.8	8.5	1892	192	16	**0**	384	**1**	**2.00**
H4	9.2	13.5	1823	144	12	288	288	**1**	2.75
H6	11.9	28.6	1772	96	8	192	192	**1**	2.17
H12	32.8	123.9	1740	**48**	**4**	288	**96**	**1**	2.25
O1	24.0	3.1	2837	576	48	**0**	1152	**1**	4.00
O2	10.0	4.8	2063	288	24	**0**	576	**1**	2.50
O3	8.7	8.4	1885	192	16	**0**	384	**1**	**2.00**
O4	9.2	13.4	1819	144	12	288	288	**1**	2.75
O6	12.2	28.5	1770	96	8	192	192	**1**	2.17
O12	34.0	123.7	1740	**48**	**4**	288	**96**	**1**	2.25
C1	23.0	**3.0**	2790	576	48	**0**	1152	**1**	4.00
C2	10.0	4.8	2047	288	24	**0**	576	**1**	2.50
C3	8.8	8.4	1877	192	16	**0**	384	**1**	**2.00**
C4	9.4	13.6	1814	144	12	288	288	**1**	2.75
C6	12.6	29.0	1768	96	8	192	192	**1**	2.17
C12	35.8	126.3	**1739**	**48**	**4**	288	**96**	**1**	2.25

The second column of Table 5.2 shows the obtained lateral deflection at the top of the building due to the lateral load. As can be seen, the top lateral deflection is strongly dependent on the number of intra-module floors, i.e. on the diagonal inclination. The influence of the floor shape is less important, as already reported in Section 5.2. Based on the obtained results, it is found that the geometrical solutions that minimize the lateral displacements are always the ones with three intra-module floors (S3, H3, O3, C3), that correspond to a diagonal inclination of 64°–67°. Among these, the stiffest solution that minimizes the lateral deflection corresponds to the S3. Conversely, the solutions with twelve intra-modules floors (S12, H12, O12, C12), i.e. diagonal angles of 83°–84°, are the ones providing the highest lateral deflection. Among these, the most flexible one is C12. For this reason, as will be seen below, the geometrical solution S3 will have the highest individual desirability value with respect to the lateral displacement ($d(\delta(S3)) = 1$), whereas the solution C12 will exhibit a null individual desirability value ($d(\delta(C12)) = 0$). The other solutions will be assigned an individual desirability lying between these values according to Eq. (5.7).

Similarly, the third column of Table 5.2 reports the computed torsional rotation at the top of the building due to the external torque moments, as obtained from the MBM. From the results, it can be inferred that the lowest torsional rotation is always provided by the geometrical solutions with the lowest number of intra-module floors (S1, H1, O1, C1), thus corresponding to the shallowest diagonal inclination (35°–38°). Among these, the stiffest solution is the circular diagrid tube C1, which provides the highest torsional rigidity. Conversely, the highest torsional rotations are obtained for the diagrid structures with the highest number of intra-module floors (S12, H12, O12, C12), the maximum one obtained with the solution C12. Accordingly, we will obtain the highest individual desirability value for the solution C1 ($d(\varphi(C1)) = 1$) and the lowest value for the geometry C12 ($d(\varphi(C12)) = 0$). Again, the other solutions will exhibit desirability values in between, according to Eq. (5.7).

From the results obtained in these first two columns, it can be inferred that the different flexibilities (lateral and torsional) are minimized by different geometrical solutions. As already discussed in Section 5.2, the lateral deflection is usually minimized by intermediate values of the diagonal angle, due to the competition between shear and bending rigidity. Conversely, the torsional rigidity of the building only depends on the shear rigidity of the diagrid module, therefore it is maximum for very shallow diagonals. These considerations make the choice of the optimal geometry difficult, as one should limit both the lateral and torsional flexibility of the structure. To this purpose, the desirability function approach seems an effective yet simple way to tackle this problem.

The fourth column of Table 5.2 reports the total steel mass of the external diagrid tube, which is directly calculated based on the steel density and the actual diagrid geometry. The solutions with higher numbers of intra-module floors (S12, H12, O12, C12) involve the lowest amount of employed material. This is simply due to the fact that, when the diagonal inclination is very steep, the density of the diagonals in the pattern gets remarkably lower (Figure 5.5c). Based on the mass response, the highest individual desirability score is assigned to the solution C12 ($d(M(C12)) = 1$), whereas the lowest one to the solution S1 ($d(M(S1)) = 0$).

Finally, the last columns of Table 5.2 report the five metrics N_1, N_2, N_3, N_4 and N_5 that are used to calculate the complexity index. Note that, although in the previous cases the variation of the first three responses (δ, φ, M) among the

different floor shapes was not so evident, in this case, the five metrics N_1, N_2, N_3, N_4 and N_5 do not vary at all with respect to the floor shape, being only dependent on the diagonal inclination. N_1 represents the total number of diagrid nodes, therefore it is minimum for the solutions S12, H12, O12 and C12, while it is maximum for S1, H1, O1 and C1. Similarly, N_2 is the number of different diagonal cross-sections used in the pattern, thus in this case it corresponds to the number of diagrid modules, as each module has its own cross-sectional area. Therefore, it is minimum for S12, H12, O12 and C12, while it is maximum for S1, H1, O1 and C1. N_3 takes into account the maximum diagonal length of 12 meters for transportability issues, and it is found to be minimum for all the solutions with one, two and three intra-module floors, while it is higher for steeper diagonals. N_4 is the total number of diagonals in the pattern, thus it is minimum for S12, H12, O12 and C12, while it is maximum for S1, H1, O1 and C1. Finally, N_5 takes into account the different lengths of the diagonals in the pattern. In this case, it is equal to one for each solution, as each pattern has all the diagonals with the same length, being uniform-angle solutions.

Based on the evaluation of N_1, N_2, N_3, N_4 and N_5, Eq. (5.9) is applied to compute the *CI* of each geometrical solution, obtaining the results reported in the last column of Table 5.2. According to what already reported above, no variation is found for this response variable across the different floor shapes. Conversely, it can be seen that the diagrid solutions that minimize the *CI* are the ones with three intra-module floors ($d(CI(S3)) = d(CI(H3)) = d(CI(O3)) = d(CI(C3)) = 1$), whereas the ones that maximize the construction complexity are the ones with one intra-module floor ($d(CI(S1)) = d(CI(H1)) = d(CI(O1)) = d(CI(C1)) = 0$). The other geometrical solutions exhibit *CI*s that lie in between these values.

Based on the response variables reported in Table 5.2, Eq. (5.7) has been applied to calculate the individual desirability value for each geometrical solution referred to each response variable. The results are shown in Table 5.3, calculated by adopting a unit value of the exponent r_i for all the responses, i.e. $r_\delta = r_\varphi = r_M = r_{CI} = 1$. The obtained individual desirability values are also represented in graphical form in Figure 5.11a. As can be seen, the influence of the floor shape is negligible, whereas the diagonal inclination has a strong influence on the individual desirability values for each given floor shape.

Finally, the individual desirability values are combined together to obtain the *OD* according to Eq. (5.8). The results are reported in the last column of Table 5.3 and are represented graphically in Figure 5.11b. As can be seen from the obtained *OD* values, the most desirable solution ($OD_{\max} = 95.94\%$) is C3, thus the circular diagrid building with three intra-module floors, corresponding to a diagonal inclination of 67°. This result arises from the fact that the solution C3 is indeed one of the best performing with respect to all the four response variables. As a matter of fact, this geometrical solution allows to reach very low lateral deflections ($d(\delta(C3)) = 99.32\%$) and torsional rotations ($d(\varphi(C3)) = 95.62\%$), it is also highly desirable with respect to the minimization of the structural weight ($d(M(C3)) = 89.19\%$) and it is one of the best structures from a construction complexity perspective ($d(CI(C3)) = 100.00\%$).

Note that the other solutions with three intra-module floors and different floor shapes, i.e. S3, H3 and O3, provide similar values of *OD*: *OD*(S3) = 95.21%, *OD*(H3) = 95.62% and *OD*(O3) = 95.86%. This confirms what already reported above, i.e. the influence of the floor shape on the optimal diagrid geometry is less important. This can also be seen from Figure 5.11b, where the *OD* graph shows a similar trend for the different floor shapes. Moreover, Figure 5.12 reports a

surface representation of the *OD* values with respect to the diagonal inclinations and floor shapes. From the figure, it is evident that most of the *OD* variation occurs with respect to the diagonal inclination, whereas the surface is almost cylindrical in the direction of the floor shape axis.

Table 5.3. Individual and overall desirability values for the four response variables (r_i = 1). Adapted from [142].

Diagrid geometry	$\boldsymbol{d(\delta)}$ **(-)**	$\boldsymbol{d(\varphi)}$ **(-)**	$\boldsymbol{d(M)}$ **(-)**	$\boldsymbol{d(CI)}$ **(-)**	$\boldsymbol{OD}$ **(-)**
S1	0.2840	0.9941	0.0000	0.0000	0.0000
S2	0.9292	0.9817	0.6975	0.7500	0.8311
S3	**1.0000**	0.9535	0.8618	**1.0000**	0.9521
S4	0.9958	0.9123	0.9237	0.6250	0.8510
S6	0.9124	0.7899	0.9696	0.9167	0.8946
S12	0.2490	0.0176	0.9979	0.8750	0.2486
H1	0.3839	0.9981	0.1096	0.0000	0.0000
H2	0.9375	0.9845	0.7359	0.7500	0.8448
H3	0.9931	0.9560	0.8806	**1.0000**	0.9562
H4	0.9799	0.9147	0.9348	0.6250	0.8507
H6	0.8776	0.7922	0.9747	0.9167	0.8878
H12	0.1078	0.0193	0.9992	0.8750	0.2065
O1	0.4338	0.9992	0.1404	0.0000	0.0000
O2	0.9477	0.9853	0.7465	0.7500	0.8503
O3	0.9964	0.9568	0.8858	**1.0000**	0.9586
O4	0.9791	0.9155	0.9378	0.6250	0.8514
O6	0.8689	0.7931	0.9761	0.9167	0.8861
O12	0.0650	0.0210	0.9996	0.8750	0.1859
C1	0.4686	**1.0000**	0.1771	0.0000	0.0000
C2	0.9504	0.9855	0.7590	0.7500	0.8545
C3	0.9932	0.9562	0.8919	**1.0000**	**0.9594**
C4	0.9721	0.9140	0.9413	0.6250	0.8503
C6	0.8533	0.7889	0.9777	0.9167	0.8813
C12	0.0000	0.0000	**1.0000**	0.8750	0.0000

The *OD* drops to lower values for different numbers of intra-module floors. The solutions with one intra-module floor (S1, H1, O1, C1) have always an *OD* equal to 0, due to the fact that, despite their high torsional rigidity ($d(\varphi)$ ~ 99–100%), they are quite flexible under lateral loads ($d(\delta)$ ~ 28–47%), quite heavy ($d(M)$ ~ 0–18%) and very complex ($d(CI)$ = 0%). The solutions with two intra-module floors (S2, H2, O2, C2) show *OD*s in the range 83–85%: their lateral and torsional rigidity is quite high ($d(\delta)$ ~ 92–95%, $d(\varphi)$ ~ 98–99%), but they are still not so light ($d(M)$ ~ 70–76%) and easily constructible ($d(CI)$ = 75%). The solutions with four intra-module floors (S4, H4, O4, C4) provide *OD*s around 85%: they exhibit a great lateral rigidity ($d(\delta)$ ~ 97–99%), a good torsional behavior ($d(\varphi)$ ~ 91%), quite low values of structural weight ($d(M)$ ~ 92–94%), but they are still quite complex ($d(CI)$ = 62%). The solutions with six floors per module (S6, H6, O6, C6) show *OD*s in the range 88–89%: they show a lower lateral and torsional rigidity ($d(\delta)$ ~ 85–91%, $d(\varphi)$ ~ 79%), although their mass and complexity responses show satisfactory desirability values ($d(M)$ ~ 97–98%, $d(CI)$ = 92%). Finally, the solutions with twelve intra-module floors lead to low

*OD*s in the range 0–24%: despite their low structural weight and satisfactory complexity ($d(M)$ ~ 100%, $d(CI)$ = 87%), they are extremely flexible under lateral and torque actions ($d(\delta)$ ~ 0–25%, $d(\varphi)$ ~ 0–2%).

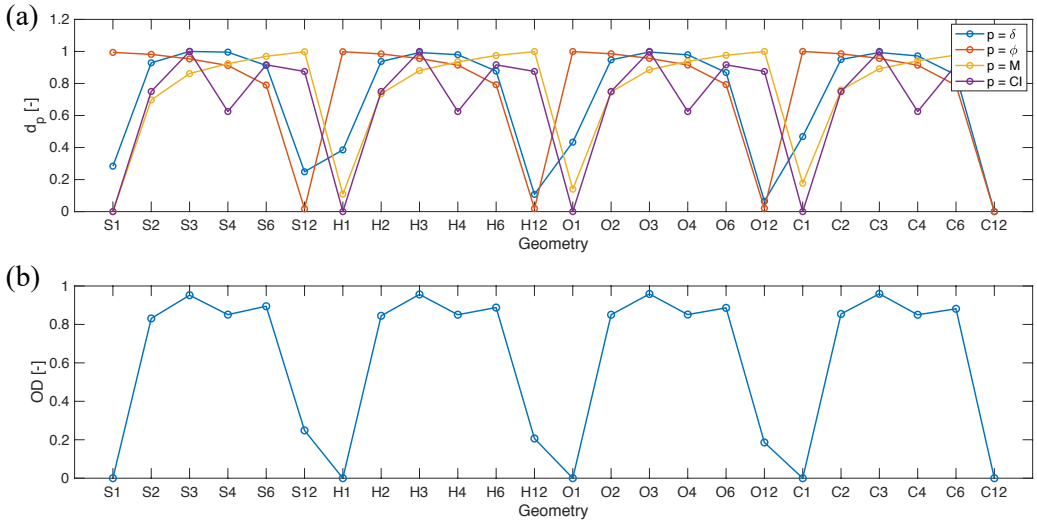

Figure 5.11. (a) Individual desirability values for the four response variables (r_i = 1) and (b) *OD* values. Used with permission from [142].

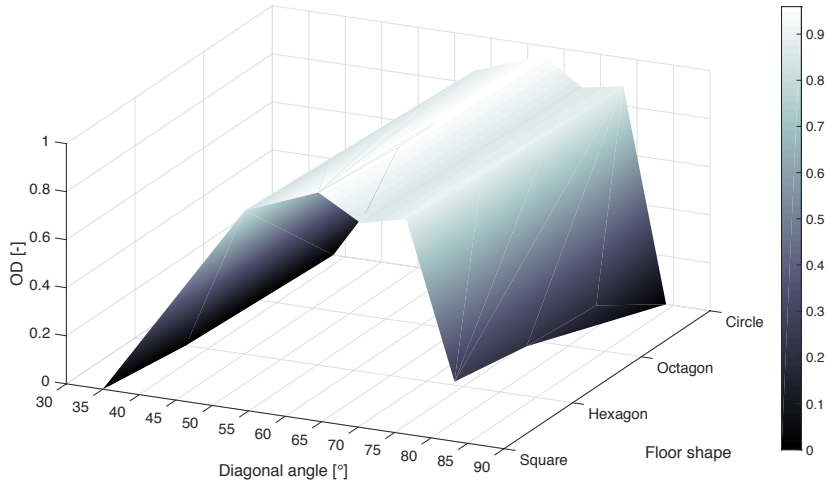

Figure 5.12. Surface representation of the *OD* with respect to the diagrid geometrical parameters (diagonal angle and floor shape). *OD* values are reported in the vertical axis and represented by means of color shades. Used with permission from [142].

Therefore, based on the results reported in Table 5.3 and Figures 5.11 and 5.12, the optimal diagrid solutions that simultaneously minimize the lateral and torsional flexibility, as well as the diagrid structural weight and the construction complexity can be selected. This approach, based on the desirability function, seems to be a powerful yet simple tool to select the optimal geometry of the diagrid among a set of geometrical solutions and based on different responses.

The previous analysis is quite arbitrary as the condition $r_\delta = r_\varphi = r_M = r_{CI} = 1$ was chosen. This implicitly means assigning the four response variables the same importance in the definition of the optimal diagrid geometry. For this reason, a parametric analysis has also been carried out by considering $r_\delta \neq r_\varphi \neq r_M \neq r_{CI} \neq$

1, in order to investigate how the optimal diagrid geometry is influenced by the different weights assigned to the different response variables (δ, φ, M, CI).

In order to carry out the sensitivity analysis based on the weights r_i, eight values of r_i have been considered for each variable, namely 0.25, 0.50, 0.75, 1.00, 1.25, 1.50, 1.75, 2.00. Then, we obtain $8^4 = 4096$ combinations of exponents, as synthetically shown in Table 5.4. Based on the response variables obtained in Table 5.2, for each combination of exponents r_δ, r_φ, r_M and r_{CI}, the same analysis presented above can be carried out by applying Eqs. (5.7) and (5.8). Eventually, the optimal geometry can be found out, based on the maximum value of the obtained *OD* values.

Table 5.4. The possible combinations by considering eight different exponents r_i for each response variable. Used with permission from [142].

Combination	r_δ [-]	r_φ [-]	r_M [-]	r_{CI} [-]
1	0.25	0.25	0.25	0.25
2	0.25	0.25	0.25	0.50
3	0.25	0.25	0.25	0.75
…	…	…	…	…
1755	1.00	1.00	1.00	0.75
1756	1.00	1.00	1.00	1.00
1757	1.00	1.00	1.00	1.25
…	…	…	…	…
4094	2.00	2.00	2.00	1.50
4095	2.00	2.00	2.00	1.75
4096	2.00	2.00	2.00	2.00

Figure 5.13 reports the obtained optimal geometry, expressed as relative frequency of occurrence out of the 4096 simulations. From the outcomes, it was obtained that the solution C3, which was assessed as the optimal geometry in the previous analysis (with $r_\delta = r_\varphi = r_M = r_{CI} = 1$), is found as the optimal one for 3072 exponent combinations (75.00% of the total cases). It was also found that, in 1000 simulations (24.41% of the total), the optimal geometry is the solution O3, which is the octagonal diagrid with three intra-module floors. This should not surprise as we have already seen in the previous analysis (with $r_\delta = r_\varphi = r_M = r_{CI} = 1$) that the solution O3 ($OD$(O3) = 95.86%) was not so different from the C3 (OD(C3) = 95.94%). Therefore, out of 4096 combinations of exponents, 4072 cases (99.41% of the total) provided O3 or C3 as the optimal diagrid geometry, based on their lateral and torsional flexibility, structural mass and construction complexity. The remaining 24 combinations (0.59% of the total) assigned the optimal geometry to the solution S6 (14 cases – 0.34%) and O6 (10 cases – 0.25%), which correspond to the square and octagonal geometry with six intra-module floors, respectively. However, these rare cases were found to correspond to highly unbalanced exponents, where the top lateral deflection and torsional rotation, i.e. the structural responses, were much underweighted with respect to the diagrid mass and construction complexity, i.e. the geometrical responses.

In conclusion, the sensitivity analysis carried out here demonstrates that, for the investigated 168-meter tall diagrid building, the optimal diagonal inclination should always correspond to three intra-module floors in order to minimize both the lateral deflection, torsional rotation, structural weight and construction complexity. The floor shape seems to be less important, as already shown in

Section 5.2, although a slight bias towards curved floor shapes, i.e. circular and octagonal, has been obtained.

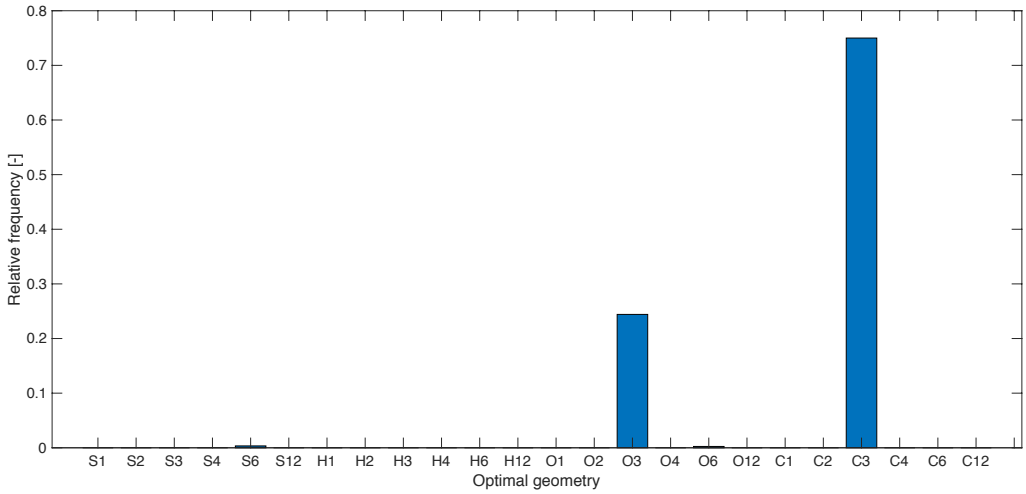

Figure 5.13. Optimal diagrid geometry based on 4096 simulations with different exponents of the individual desirability values. Used with permission from [142].

Based on the analysis carried out for the 168-meter tall building, the optimal diagrid geometry has also been investigated for the other buildings with different heights considered in Section 5.2, i.e. 126-, 210- and 252-meter tall structures. Figures 5.14a, 5.15a and 5.16a show the *OD* surface for the three buildings, obtained by applying Eqs. (5.7) and (5.8) and by considering $r_\delta = r_\varphi = r_M = r_{CI} = 1$. In both cases, the optimal diagrid geometry is found to be associated with the solution C3, with *OD*(C3) values of 96.04% for the 126-, 95.68% for the 210- and 95.52% for the 252-meter building. Also in these cases, the influence of the specific floor shape is found to be almost negligible, the diagonal inclination being the main parameter affecting the variation of the individual and overall desirability values.

The sensitivity analysis by varying the exponents r_i has been carried out as well, and the results are shown in Figures 5.14b, 5.15b and 5.16b for the three building heights. Similarly to Figure 5.13, these graphs report the obtained optimal diagrid geometry expressed as relative frequency of occurrence out of the 4096 combinations from Table 5.4. The results are similar to what already found for the 168-meter building investigated above.

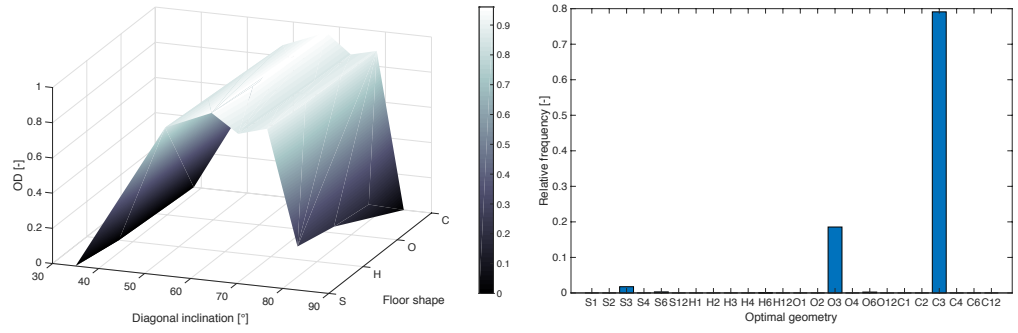

(a) (b)

Figure 5.14. Results for the 126-meter tall building: (a) surface representation of the *OD* obtained with $r_\delta = r_\varphi = r_M = r_{CI} = 1$; (b) optimal diagrid geometry based on 4096 simulations with different exponents r_i. Used with permission from [142].

Specifically, for the 126-meter tall building (Figure 5.14b), the C3 solution is found to be the optimal one for 3240 combinations of the exponents r_i (79.10% of the total), the O3 solution is the optimal one for 760 cases (18.55% of the total), whereas the S3, S6, O6 and H6 geometries are assigned the highest overall desirability in 72 (1.76%), 12 (0.29%), 10 (0.25%) and 2 cases (0.05%), respectively. As can be seen, in 99.41% of the combinations the optimal solutions still refer to three intra-module floors, with a preference towards more curved floor shapes, whereas the solutions with six intra-module floors are to be preferred only in 0.59% of the cases. Similarly to what already reported above, these few cases usually refer to very unbalanced combinations of the weight exponents, where the importance of the construction complexity and diagrid mass largely prevails over the minimization of the lateral and torsional deformability.

As for the 210-meter tall building, the results are shown in Figure 5.15b. Again, the C3 solution is found to be the most desirable one for 3209 combinations (78.34% of the total), the O3 solution is the optimal one for 840 cases (20.51% of the total), whereas the S6 and O6 geometries are assigned the highest overall desirability in 34 (0.83%) and 13 combinations (0.32%), respectively. In this case, 98.85% of the combinations lead to the optimal solutions with three intra-module floors, again with a preference towards more curved floor shapes, whereas the solutions with six intra-module floors are to be preferred only in 1.15% of the cases.

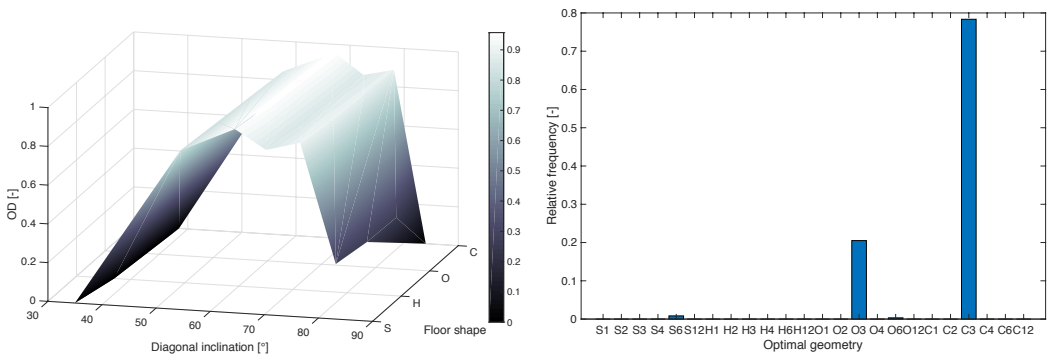

(a) (b)

Figure 5.15. Results for the 210-meter tall building: (a) surface representation of the *OD* obtained with $r_\delta = r_\varphi = r_M = r_{CI} = 1$; (b) optimal diagrid geometry based on 4096 simulations with different exponents r_i. Used with permission from [142].

Finally, Figure 5.16b shows the outcomes related to the 252-meter tall building. Once again, the C3 solution is found to be the most desirable one for 3436 combinations (83.89% of the total), the O3 solution is the optimal one for 544 cases (13.28% of the total), whereas the S6 and O6 geometries are assigned the highest overall desirability in 88 (2.15%) and 28 combinations (0.68%), respectively. In this case, 97.17% of the combinations lead to the optimal solutions with three intra-module floors, whereas the solutions with six intra-module floors are to be preferred only in 2.83% of the cases.

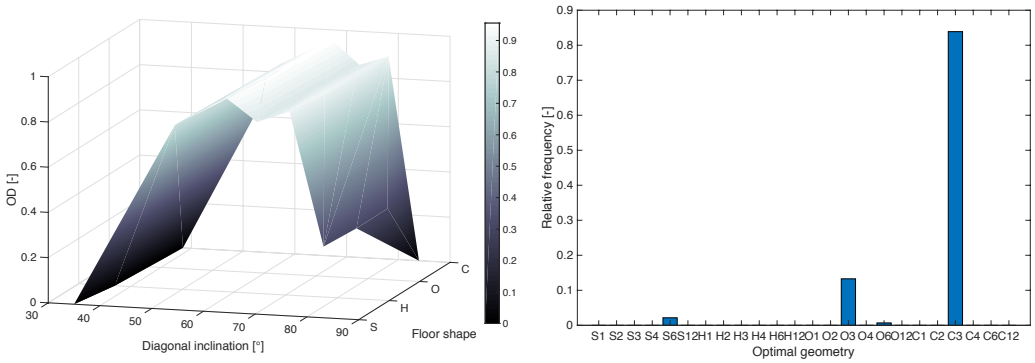

(a) (b)

Figure 5.16. Results for the 252-meter tall building: (a) surface representation of the *OD* obtained with $r_\delta = r_\varphi = r_M = r_{CI} = 1$; (b) optimal diagrid geometry based on 4096 simulations with different exponents r_i. Used with permission from [142].

From the results shown above, it is evident how the optimal geometry is only slightly affected by the specific set of weight exponent for the different response variables. Moreover, for the investigated buildings, having aspect ratios in the range 4.1–8.4, the optimal geometry is also found to be slightly affected by the building height, being the solution C3 always the prevailing one. From previous studies [110,131], we know that for higher aspect ratios the bending behavior prevails over the shear deformation mode, thus the diagonal angle that minimizes the lateral diagrid deflection increases with the building height. In this case the optimal diagonal inclination does not increase as we need to minimize multiple responses simultaneously, not only the lateral deflection.

As already shown by Lacidogna et al. in [137], increasing the building height leads to greater diagonal inclinations needed to minimize the lateral displacement. However, higher diagonal inclinations also lead to higher torsional rotations, thus worsening the torsional behavior. The *CI* also varies when modifying the diagonal inclination: specifically, it is found to increase when moving from the solution with three intra-module floors to the one with four intra-module floors. Therefore, although the solutions with four intra-module floors might be better candidates to minimize the lateral deflections and the structural mass for higher buildings [137], their higher torsional flexibility and construction complexity prevent their suitability as optimal geometries.

In conclusion, due to its inherent simplicity and its ability to consider the simultaneous optimization of several responses, the desirability function approach is a good candidate to assist the designer through the preliminary design stages in assessing the optimal diagrid geometries. In the next Section, the methodology will be further exploited to find the optimal diagrid geometry when varying-angle diagonal patterns are considered.

5.3.2 Multi-response optimization of varying-angle diagrids

In this Section, the multi-response optimization based on the desirability function approach will be carried out on the same 168-meter tall building considered above, by generating a wider population of varying-angle diagrids. Specifically, the same four floor plan shapes have been considered, namely the square, hexagonal, octagonal and circular floor shape. For each of these, several varying-angle diagonal patterns have been generated for the external diagrid system.

To do so, the 48 stories of the building have been subdivided into different combinations of diagrid modules. In this analysis, the basic triangular module can span over from one to six floors, i.e. 1, 2, 3, 4, 5 and 6. Therefore, several combinations of diagonal arrangements are possible to cover the total 48 stories, e.g. 48 modules made up of only one intra-module floor, 8 modules made up of six intra-module floors, 4 modules made up of five intra-module floors plus 7 modules made up of four intra-module floors, etc.

It is obvious that, in order to cover the total 48 stories of the building, the total number of modules for each basic triangular element cannot be greater than the total number of the building stories divided by the number of floors contained within the triangular unit. For example, for the one intra-module triangular unit, no more than 48/1 = 48 modules can be present in order to cover the entire building façade. Therefore, the one intra-module unit can occur in the varying-angle diagonal pattern 0, 1, 2, …, 48 times, but not more. Therefore, the one intra-module floors unit has 49 possibilities of occurrence within each varying-angle diagrid patterns. For the two intra-module triangular unit, the total number of allowable modules is 48/2 = 24, then it can occur for a total of 25 times within each diagrid pattern. Applying the same procedure to all the triangular units, i.e. 1, 2, 3, 4, 5 and 6 intra-module floors, it is found out that they have 49, 25, 17, 13, 10 and 9 possibilities of occurrence, respectively. This leads us to a total number of combinations which is equal to the product of these numbers, namely 49 × 25 × 17 × 13 × 10 × 9 = 24365250 possible combinations. These are in turn 24365250 potential varying-angle diagrid patterns that can be generated for the 168-meter 48-story diagrid building.

However, not all of these combinations are feasible, as they should obey the following constraint equation:

$$N = \sum_{j=1}^{6} M_j \, j. \tag{5.10}$$

being N the total number of the building floors (N = 48), j the number of intra-module floors for the considered triangular unit (j = 1, 2, …, 6), and M_j the number of modules for the triangular units with j intra-module floors. Moreover, based on the considerations reported in Section 5.1, the case where steeper diagonals are placed within the base of the building and shallower diagonals are towards the top (Figure 5.1a) has only been considered here, as the opposite situation (Figure 5.1c) is not supposed to provide any beneficial effect to the building performance. Based on these considerations and Eq. (5.10), the 24365250 potential combinations are reduced to 7760, which is still a high number of geometrical solutions.

Therefore, for each floor plan shape, 7760 varying-angle diagrid patterns have been generated based on the combinations of the different triangular units as reported above. Three examples of these varying-angle combinations are shown in Figure 5.17 for the square floor shape. Finally, considering the four different floor shapes, this leads us to a total of 7760 × 4 = 31040 structures, with different floor shape and diagonal inclination, among which we need to select the optimal geometry based on the desirability function approach.

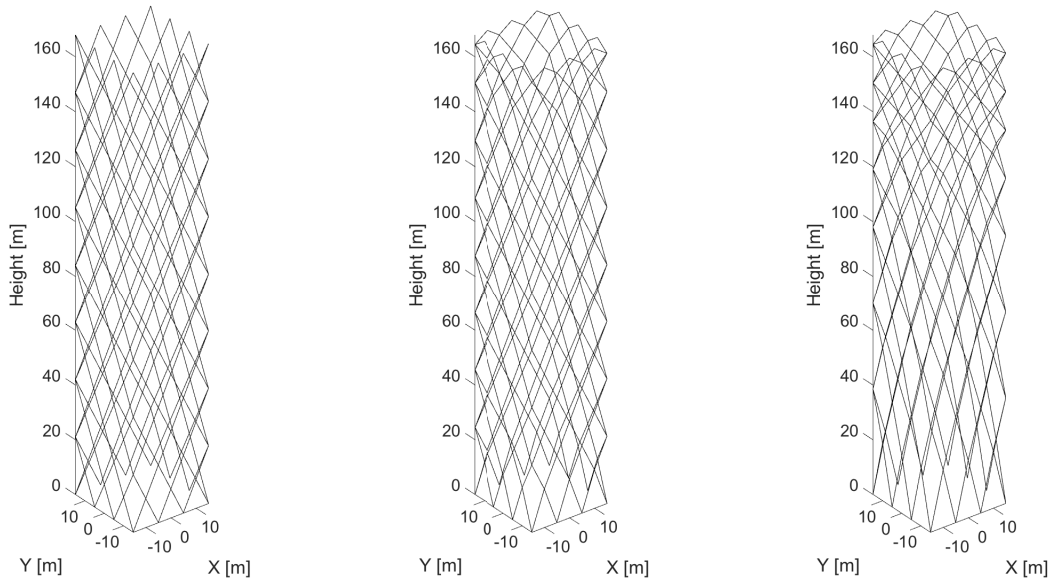

Figure 5.17. Three different varying-angle diagrid generated from the combination of the basic triangular units for the square plan shape: (a) combination #88: $M_1 = M_2 = M_4 = M_5 = M_6 = 0$, $M_3 = 16$; (b) combination #872: $M_1 = 1$, $M_2 = 2$, $M_3 = 13$, $M_4 = 1$, $M_5 = M_6 = 0$; (b) combination #1004: $M_1 = 1$, $M_2 = 5$, $M_3 = 3$, $M_4 = 3$, $M_5 = 2$, $M_6 = 1$.

Once all the 31040 structures have been generated as reported above, the four response variables, i.e. top lateral deflection, top torsional rotation, diagrid mass and complexity index, have been obtained as explained in the previous Section. The results are shown in Figure 5.18. Figure 5.18a reports the trends of the values obtained for each diagrid geometry, while Figure 5.18b shows the distributions of the four responses across the generated diagrid structures.

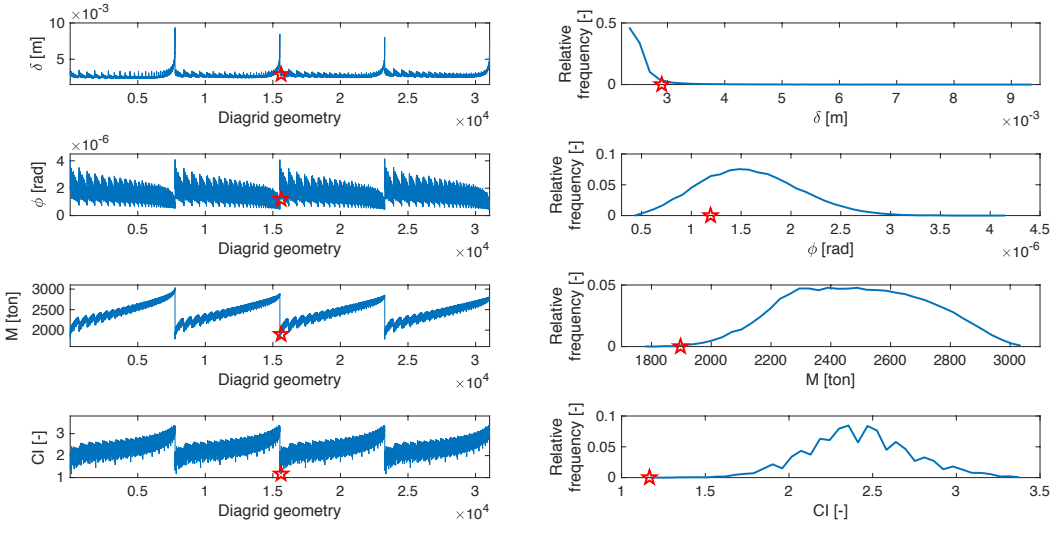

Figure 5.18. Results for the 168-meter tall building with 31040 varying-angle geometries: (a) top lateral displacement, top torsional rotation, steel mass and complexity index obtained for each of the 31040 diagrid geometries; (b) distribution of the four response variables across the population of diagrid geometries. The red star refers to the optimal geometry (#15608), which has been obtained from the desirability approach with $r_\delta = r_\varphi = r_M = r_{CI} = 1$.

The first observation that can be made by scrutinizing Figure 5.18a is that the floor plan shape plays a minor role on the results. The 31040 diagrid structures are listed consequently according to the square, hexagonal, octagonal and circular shape, meaning that diagrid structures from 1 to 7760 refer to the square shape, from 7761 to 15520 to the hexagon, from 15521 to 23280 to the octagon, while from 23281 to 31040 to the circle. From Figure 5.18a, it is evident that all the four response variables exhibit a repetitive pattern according to the floor shapes, with just minor differences among them. Conversely, the results are quite diverse by changing the diagonal pattern within the same floor shape group.

As for the top lateral deflection, it can be observed that the statistical distribution resembles an exponential distribution, with many structures leading to similar small displacements and few solutions leading to very high displacements. Notably, the solutions that generate very high lateral displacements (about four times the minimum ones) are the ones with the shallowest diagonal inclinations, e.g. $M_1 = 48$ and $M_j = 0$ for $j = 2, 3, 4, 5, 6$. As we already observed in Section 5.1, these geometries are usually found to exhibit unsatisfactory results in terms of lateral deflections.

Conversely, the other three response variables, namely the torsional rotation, the diagrid mass and complexity index, show more uniform distributions, which actually resemble Gaussian-like distributions (Figure 5.18b). This means that for these response variables we usually find few geometrical solutions that lead to the minimum (most desirable) responses, few geometries that lead to the highest (least desirable) values, whereas most of the diagrid structures collocate themselves in between the extreme values.

If these three response variables are individually observed and by considering that increasing the number of the diagrid geometry combination there is a bias towards shallower diagonals (higher M_1 and M_2) in the diagrid pattern, we can infer that the torsional rotation decreases, while the diagrid mass and the complexity index increase. This is reasonable, since in the previous Sections it has already been shown that the torsional rotations are minimized for shallower diagonal inclinations, whereas the diagrid mass and construction complexity usually are lower for the geometrical solutions with steeper diagonals.

Once the results for the four response variables are obtained for each diagrid geometry, the desirability analysis can be carried out, in the same way as reported in the previous Section. As already done above, initially the four exponent weights r_δ, r_φ, r_M and r_{CI} have been set to 1, whereas a sensitivity analysis has been carried out subsequently in order to investigate their influence on the obtained optimal geometry.

The results of the desirability analysis, obtained with $r_\delta = r_\varphi = r_M = r_{CI} = 1$, are shown in Figure 5.19. Specifically, Figure 5.19a reports the trend of the *OD* values with the diagrid geometry, Figure 5.19b shows the statistical distribution of the *OD* values across the population of the geometries and Figure 5.19c reports the optimal structure, i.e. the one with the highest *OD*. This is found to correspond to the combination #15608, that is the octagonal diagrid with uniform angle and three intra-module floors, i.e. $M_3 = 16$ and $M_j = 0$ for $j \neq 3$.

From the analysis, it is found that the highest *OD* is equal to 90.2%. Un both Figures 5.18 and 5.19, the optimal solution (#15608) is marked with a red star, in order to show its position within the four response variables distribution. The *OD* value of the optimal geometrical solution (#15608) arises from quite high individual desirability values for the four individual responses. As a matter of fact,

the individual desirability values for structure #15608 are as follows: $d(\delta)$ = 91.9%, $d(\varphi)$ = 79.5%, $d(M)$ = 90.6% and $d(CI)$= 100%. These results suggest that this structure is fairly rigid under both lateral and torque actions, it is among the lightest ones and it is the least complex from a construction perspective. By combining these individual desirability values together by means of Eq. (5.8), this structure is then found to be the optimal one.

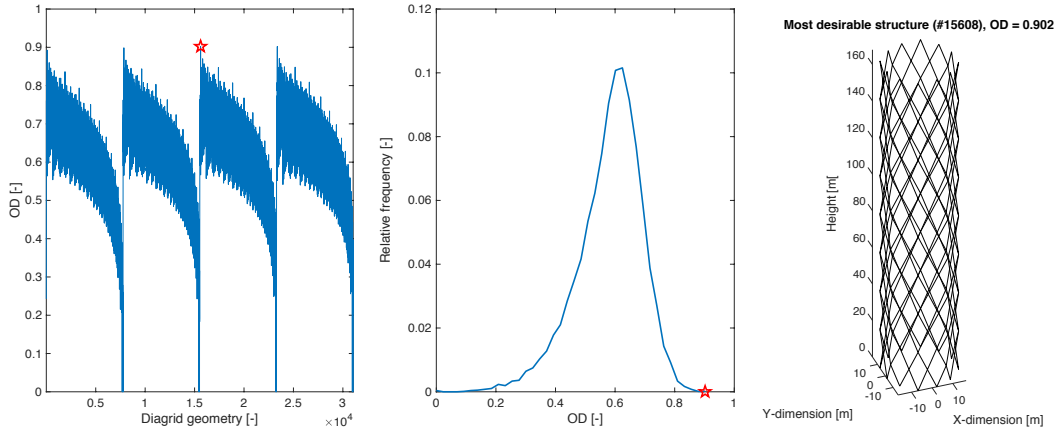

(a) (b) (c)

Figure 5.19. Optimal geometry for the 168-meter varying-angle diagrids based on the desirability function, obtained with $r_\delta = r_\varphi = r_M = r_{CI} = 1$: (a) *OD* values obtained for each geometry; (b) distribution of the *OD* across the population of diagrid geometries. The red star refers to the optimal geometry (#15608), which is shown in panel (c).

Few considerations need to be made at this point. First, it should be noted that, although this is obtained as the optimal structure based on the desirability function, the solution #15608 is not the one that minimizes the top lateral deflection, the top torsional rotation and the structural mass individually.

In fact, the structure that leads to the minimum lateral displacement, i.e. $d(\delta)$ = 100%, is found to be #5164, which corresponds to the square diagrid with M_1 = 11, M_2 = 2, M_3 = 4, M_4 = 4, M_5 = 1, M_6 = 0. However, this solution is unsatisfactory for the other response variables, as it leads to $d(\varphi)$ = 77.2%, $d(M)$ = 37.4% and $d(CI)$ = 34.0%, finally leading to *OD* = 56.0%. Conversely, the structure that minimizes the torsional flexibility, i.e. $d(\varphi)$ = 100%, is found to be #31040, which corresponds to the circular diagrid with M_1 = 48, $M_2 = M_3 = M_4 = M_5 = M_6$ = 0. However, this solution is unsatisfactory for the other response variables, as it leads to $d(\delta)$ = 23.8%, $d(M)$ = 18.4% and $d(CI)$ = 9.4%, finally leading to *OD* = 25.4%. Eventually, the structure that leads to the minimum diagrid mass, i.e. $d(M)$ = 100%, is found to be #23281, which corresponds to the circular diagrid with $M_1 = M_2 = M_3 = M_4 = M_5$ = 0, M_6 = 8. However, this solution is unsatisfactory for the other response variables, as it leads to $d(\delta\varphi)$ = 73.5%, $d(\varphi)$ = 0% and $d(CI)$ = 92.4%, finally leading to *OD* = 0%, since it is the worst one from a torsional flexibility perspective.

Secondly, it can be noted from Figure 5.19a that the influence of the floor plan shape plays a minor role, as the *OD* values show the same repetitive trend already observed in Figure 5.18a. This leads us to observe that structures #88, #7848 and #23368 are also very good candidates for the optimal diagrid geometry. As a matter of fact, these structures correspond to the same diagonal pattern of the optimal geometry #15608 (Figure 5.19c), but they are associated with the square, hexagonal and circular plan shape. From the desirability analyses,

for these structures an *OD* of 89.3%, 89.9% and 90.2% has been obtained, respectively. These values are very close to the maximum *OD*, which has been found for #15608 (*OD* = 90.21%). In particular, the *OD* associated to structure #23368 (circular shape) is basically coincident with the maximum *OD*, with a minor different only at the second digit (*OD* = 90.20%). This consideration suggests us that, if we only rely on the maximum value of *OD*, the optimal shape is the octagon with uniform-angle pattern composed of triangular units made up of three intra-module floors. However, the other plan shapes with the same diagonal pattern, i.e. structures #88, #7848 and #23368, can still be very good candidate for the optimal geometry (especially structure #23368). As reported in Table 5.5, the similarity among the solutions is reflected in the similar individual desirability values and, in turn, in the final *OD*.

Table 5.5. Individual and overall desirability values for structures with uniform-angle patterns composed of three intra-module floor triangular units (r_i = 1).

Structure	Shape	$d(\delta)$ [-]	$d(\varphi)$[-]	$d(M)$ [-]	$d(CI)$ [-]	OD [-]
#88	Square	0.9239	0.7795	0.8813	1.000	0.8926
#7848	Hexagon	0.9150	0.7916	0.9005	1.000	0.8987
#15608	Octagon	0.9192	0.7953	0.9058	1.000	0.9021
#23368	Circle	0.9152	0.7927	0.9126	1.000	0.9020

Third, a consideration also needs to be done on the shape of the *OD* distribution shown in Figure 5.19b. This can be derived as the product of the partial distributions shown in Figure 5.18b, and eventually it resembles a skewed Gaussian-like or log-normal distribution. It is worth observing that the highest *OD* values (right tail of the distribution) are reached only by a small fraction of the considered structures. Similarly, a very low number of geometries leads to completely unsatisfactory solutions, i.e. with very low *OD* values (left tail of the distribution). Finally, most of the geometrical solutions collocate themselves in the middle of the distribution, whose mean and median values are 58.87% and 59.84%, respectively. This means that, although few structures allow to reach the highest desirability values, plenty of geometrical solutions lie within an average range, where the *OD* lies around its mean value.

Finally, it has to be noted that all the four top optimal solutions, which are reported in Table 5.5, refer to the uniform-angle diagonal pattern, with elementary triangular units having three intra-module floors, i.e. M_3 = 16 and M_j = 0 for $j \neq 3$. Therefore, out of the 31040 geometrical solutions that have been considered here (most of which are actual varying-angle diagrids), it is found out that the optimal geometry still is biased towards the uniform-angle pattern. Obviously, this outcome arises from the specific 168-meter building, which has an aspect ratio of about 5.5, and depends on the selected four response variables. It is quite clear that, if the same methodology were to be applied to a different building and if different response variables were to be considered, the uniform-angle solution could also be outperformed by certain varying-angle ones.

As reminded above, the analysis shown so far in this Section has been carried out by assuming the same importance for the four response variables, namely r_δ = r_φ = r_M = r_{CI} = 1. A sensitivity analysis has then been carried out to investigate the influence of such parameters on the obtained optimal geometry, as already reported in the previous Section. Based on the set of weight exponents shown in Table 5.4, 4096 simulations have been performed by varying each r_i in the range 0.25 – 2.00. For each of the 4096 simulations, the optimal geometry has been

selected as the one exhibiting the highest value of the *OD*. The results are shown in Figure 5.20, which reports the relative frequency of occurrence of the obtained optimal geometry, out of the 4096 different set of exponent combinations.

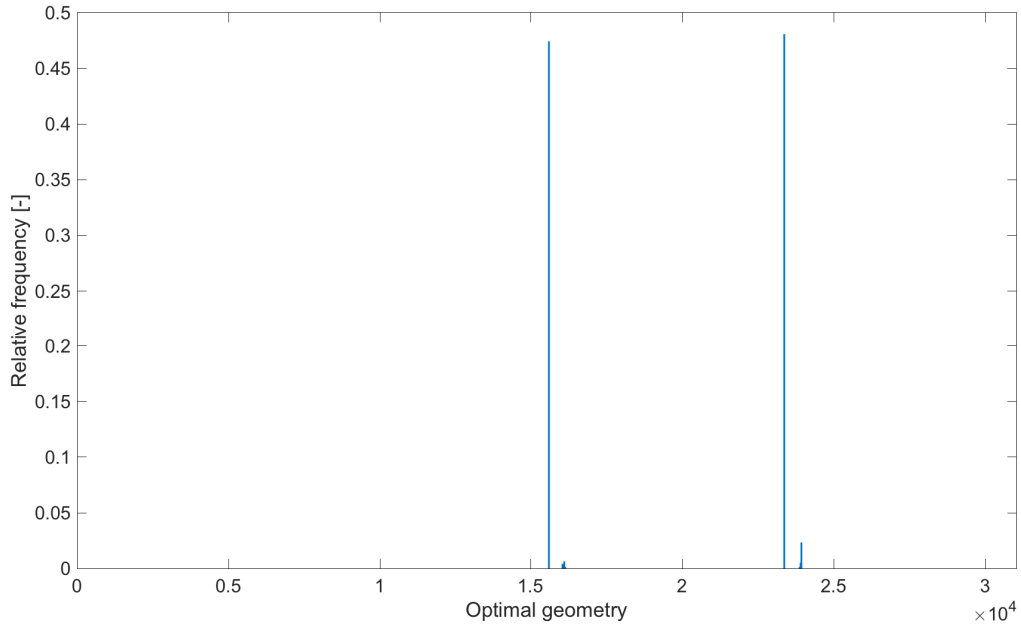

Figure 5.20. Optimal diagrid geometry based on 4096 simulations with different exponents r_i.

The outcomes reveal that in 1969 (48.07% of the total) and 1943 (47.44%) cases, the optimal geometries are the structures #23368 and #15608, respectively. These correspond to the circular and octagonal uniform-angle diagrid pattern (M_3 = 16) already discussed above. Therefore, out of the 4096 simulations, these diagrid patterns are found to be optimal ones for 3912 cases (95.51% of the total).

In the remaining 184 simulations (4.49% of the total), the optimal structures are found to be (in decreasing order of occurrence): #23936 in 96 cases (2.33% of the total), which corresponds to the uniform-angle circular diagrid with M_2 = 24 and M_j = 0 for $j \neq 2$); #16116 in 26 cases (0.63%), which corresponds to the varying-angle octagonal diagrid with M_2 = 12, M_3 = 8 and M_j = 0 for $j \neq 2$, 3; #23910 in 22 cases (0.54%), which corresponds to the varying-angle circular diagrid with M_2 = 15, M_3 = 6 and M_j = 0 for $j \neq 2$, 3; #16056 in 17 cases (0.42%), which corresponds to the varying-angle octagonal diagrid with M_2 = 9, M_3 = 10 and M_j = 0 for $j \neq 2$, 3; #23927 in 11 cases (0.27%), which corresponds to the varying-angle circular diagrid with M_2 = 18, M_3 = 4 and M_j = 0 for $j \neq 2$, 3; #23876 in 6 cases (0.15%), which corresponds to the varying-angle circular diagrid with M_2 = 12, M_3 = 8 and M_j = 0 for $j \neq 2$, 3; and finally, #16056 in 6 cases (0.15%), which corresponds to the varying-angle octagonal diagrid with M_2 = 15, M_3 = 6 and M_j = 0 for $j \neq 2$, 3.

As can be seen, in 4008 cases (97.85% of the total), the desirability function approach leads to uniform-angle diagrid patterns as the optimal geometries (#15608, #23368 and #23936), with a strong preference towards three intra-module floors (corresponding to diagonal inclinations of about 67°). In the remaining 88 cases (2.15%), the optimal pattern corresponds to actual varying-angle diagrid patterns, that use a mixture of different triangular units having two and three intra-module floors. Note that, despite we have seen that the influence of the floor plan shapes is minor, all the optimal structures involve octagonal and

circular diagrids. This has already been shown in Table 5.5 where, although the numerical difference between the *OD* values is almost negligible, it is clear that there is a slight preference towards floor shapes having higher curvatures.

5.4 Conclusions

In this Chapter, the optimization of the diagrid geometry has been addressed. After a brief overview of the research works that have been published in the last decades about this intriguing subject, the Chapter has presented the analyses aimed at investigating the influence of the diagrid geometry on the structural performance and at suggesting a novel methodology to carry out the multi-response optimization.

In the existing literature, the optimization procedures were usually carried out by assessing the lateral deformability of the building, which is generally required to meet the maximum displacement of *H*/500, and finding the diagrid geometry that leads to the lowest amount of structural material. No research work focused on the influence of diagrid geometry on the torsional response. Moreover, most of the studies focused on square diagrid buildings. To fill this research gap, the analyses reported in Section 5.2 had the primary objective of studying the influence of both diagonal inclination and floor plan shape on both the lateral and torsional deformability of the diagrid. From the outcomes, it became clear that the geometrical solutions that minimize the lateral deflection of the building are not the most desirable ones for the limitation of torsional rotations, and vice versa.

Hence, needing a methodology that allows to minimize at the same time multiple response variables, such as the lateral and torsional flexibility, the material usage, the construction complexity of the building, etc., the industrial engineering-based desirability function approach has been introduced in Section 5.3. This method is widely used worldwide for the quality assessment of various products and processes in several fields. It seems to be a simple yet proper choice for the subject of diagrid optimization. The desirability function approach has then been applied for the optimization of uniform- and varying-angle diagrid geometries, showing interesting outcomes and a certain numerical robustness.

The analyses carried out in the Chapter have made use of the desirability approach to find the optimal diagrid solution that simultaneously minimizes the lateral displacements under horizontal loads, the torsional rotation under torque actions, the steel diagrid mass and the constructional complexity, evaluated through a complexity index (*CI*). It is clear that neither the selected variable geometrical characteristics nor the selected set of response variables are unique. The methodology presented above can in fact involve not only the variation of the diagonal inclination and floor shape, but also the total floor area, the twisting and titling angle of the building, etc. Moreover, it can be applied to consider other (and more numerous) response variables that involve aspects related to other fields, such as architecture, economics, sustainability, energy, in-door environment, aesthetic, etc. This will surely be beneficial for designers and researchers across various disciplines interested in finding the optimal diagrid shape in the preliminary design stages. The method might also be coupled with conventional optimization processes used in the structural engineering field, such as Genetic Algorithm, Particle Swarm Optimization, etc. Finally, the integration of the proposed method to topology optimization approaches might provide excellent outcomes in terms of enhancement of the structural response and material savings.

Chapter 6

Conclusions

In this Thesis, the Elastic Lattice Models (ELMs) were deeply exploited in two different fields of application, namely proteins and diagrid tall buildings. Proteins are nanoscopic biological systems whose activity is pivotal for a variety of physiological processes. Conversely, diagrids are macroscopic structural systems used in recent years worldwide for the realization of tall buildings. Proteins and diagrids have nothing in common, except one thing that is highlighted in this Thesis: the behavior of both can be efficiently investigated through the ELMs. As a matter of fact, it has been shown that the application of ELMs to the field of proteins allows to obtain extremely useful information regarding their flexibility, dynamics as well as their biological mechanisms. Similarly, the application of the ELMs to the field of diagrid systems allows to perform the structural analysis, investigate their behavior within complex tall buildings as well as to carry out optimization processes in a computationally efficient way.

The goal of this Thesis has therefore been to exploit a somewhat simple structural system, such as the ELM, to investigate a variety of complex behaviors from a purely Structural Mechanics perspective. After a short Introduction about the general features and structural analyses about the ELMs, this Thesis dedicates two Chapters to the application of the ELMs to the field of proteins (Chapters 2 and 3) and two Chapters to the application of the ELMs to the field of diagrid tall buildings (Chapters 4 and 5).

Specifically, in Chapter 2, the ELMs were deeply exploited to analyze the protein dynamics and biological mechanisms. A recently developed finite-element-based ELM was presented for the purpose of investigating the low-frequency protein vibrations. These vibrations were found to occur in the THz frequency range and involve large portions of the macromolecule. Moreover, these were found to correlate fairly accurately with the biological mechanism. The FE-based ELM was also shown to provide a good accordance with the experimental protein flexibility, as measured from the crystallographic B-factors, as well as to be theoretically consistent with the famous Anisotropic Network Model (ANM). The proposed FE-based ELM is believed to represent a simple yet powerful tool for the investigation of the protein global vibrations and biological

mechanisms, easily accessible to the engineering community, as it was developed by following a pure Structural Mechanics approach.

In the same Chapter, space was also given to discuss the astonishing correlation that was observed between the low-frequency protein vibrations, evaluated by simplified ELMs, and the protein conformational changes, which are the fingerprints of the biological mechanism. Moreover, the low-frequency modes were also found to correlate accurately with the Principal Components (PCs) extracted from the sets of experimental crystal structures, meaning that these vibrations are able to represent the dynamic ensemble of the protein. Based on the observations that the protein low-frequency modes extracted from coarse-grained ELMs correctly describe the protein biological mechanism, a further coarse-grained ELM was developed for the prediction of the large-scale global motions. This novel method was still grounded on the Elastic Lattice Modeling, but it reduced the protein motion to a sum of translations and rotations of rigid blocks (the domains), accommodated by the deformation of flexible parts (the hinges). For this reason, the method has been called the hinge-domain Anisotropic Network Model (hdANM). Besides the fact that the hdANM allows to increase the computational efficiency with respect to other approaches such as the ANM, RTB, FE-based ELM, etc., it was shown to capture the fundamental conformational changes of the protein as well as the PCs extracted from the experimental crystal structure ensemble. Hence, the hdANM was shown to correctly describe the biological mechanisms as well as the global protein flexibility. The method is currently being improved by generating an extrapolation of the linear modes in order to follow the large-scale curvilinear pathways. The preliminary results (not shown in this Thesis) suggest that the hdANM is indeed able to provide more realistic motions for the protein biological mechanism.

The results presented in this Chapter are believed to be very interesting as they imply that very complex entities, such as proteins, can be successfully modeled and their behavior can be accurately analyzed by means of simplified structural models, such as the ELMs. Despite being extremely complicated, protein dynamics and biological behavior can thus be analyzed via models that exploit pure Structural Mechanics concepts, without tackling the problem by using complicated formulations that include complex chemo-physical features. Therefore, simplified models such as the ELMs can shed an important light on the overall behavior of the protein system and make the analysis and results interpretation much easier and accessible to the scientific community.

In Chapter 3, we still discussed the use of the ELMs to the field of proteins, but from a force application perspective. In particular, two novel force application patterns were presented in the first part of the Chapter, where external forces were applied to the protein ELM, either via couplets of opposite forces or via random force perturbations. From the results of linear static analysis calculations, it was shown that the small-scale displacements resulting from the external force perturbations exhibit a good correlation with the experimental B-factors, which are the fingerprints of the protein internal flexibility. These outcomes suggested that the protein flexibility does not only arise from the intrinsic protein vibrations, as shown in Chapter 2, but also from the residue-residue mechanical interactions (pairwise force application pattern) and from the external random collisions due to the external environment (random force application pattern). The results of these analyses are very encouraging, as they indicate that simply applying point forces on the protein ELM can provide good estimates of the protein flexibility and, in turn, of the protein behavior.

In the second part of this Chapter, attention was paid to the possible role of geometrical non-linearities of the ELM within the protein conformational changes. As a matter of fact, it is well-known from Structural Mechanics that spatial truss systems such as the ELMs are usually sensible to geometrical non-linearities when they exhibit fairly large displacements. Conformational changes in proteins usually show large deformations, therefore the application of linear static analysis might not be enough, as the influence of geometrical non-linearities might play an important role on the equilibrating forces. In the first place, given the two known end conformations of the protein conformational change, such role was investigated by comparing the force fields obtained from the equilibrium equations on the undeformed (initial) and deformed (final) conformations. From the comparison, as expected, it was found that the force fields only match if the involved displacements were very small. Conversely, when the displacements were rather great, the forces that equilibrate the structures often differed both in magnitude and directionality. This suggested that non-linearities can indeed be significant within the protein conformational change. Secondly, to understand whether these non-linearities were only the result of the curvilinear transition pathways (non-linearity of the displacement field) or also the result of a non-linear structural response (non-linearity of the force-displacement curve), the geometrical non-linear analysis was applied in a step-by-step fashion to the whole transition pathway. The previous equilibrium equations were applied to all the intermediate configurations and the evolution of the force field was analyzed with respect to the increasing displacements. From the outcomes, it was found that non-linearities could definitely occur both in the displacement field (curvilinear pathways) and structural response (non-linear force-displacement curves for various residues). These analyses ultimately tell us that, in order to fully comprehend and describe protein transitions throughout their entire pathway, geometrical non-linearities should also be taken into account when making use of the ELMs. Further developments of this work are left for future research efforts.

In Chapter 4 we switched the focus of this research, as the ELMs were used for the analysis of the diagrid structural system for tall buildings. In particular, a matrix-based method (MBM) was proposed for the structural analysis of generic three-dimensional diagrid systems. The MBM was developed based on the Elastic Lattice Modeling of the diagrid structural system and grounded on matrix calculus. The MBM was proven to be effective to carry out the structural analysis as it reduced the degrees of freedom (DOFs) of the structure compared to detailed FE calculations. As a matter of fact, within the MBM framework, only six DOFs were considered for each floor. The outcomes of the MBM allowed to obtain quick yet complete information on the overall flexibility of the diagrid structure, both under lateral, vertical and torsional actions. Furthermore, the MBM was developed in such a way that it could be inserted within the General Algorithm (GA), a semi-analytical formulation developed to investigate the force distribution among several resisting elements in tall buildings. The MBM, coupled with the GA, allowed to study the interaction between an external diagrid tube and internal concrete cores, under both lateral and torque actions.

The analyses shown in this Chapter are believed to be very useful to obtain a quick estimate of the diagrid overall structural response, which is particularly useful in the preliminary design stages. Moreover, the MBM could be further developed in order to investigate the dynamic and the non-linear behavior of the diagrid tubes. The former could be implemented by taking also into account the mass characteristics of the building. The latter by considering the contribution of

the geometric non-linearities to the deformation process, i.e. by means of the geometrical stiffness matrix. This will be the subject of further research studies in the future.

In Chapter 5, the outcomes of the ELM-based structural analysis of the diagrid systems were used to carry out a novel optimization procedure to select the optimal diagrid geometry. In particular, in the first part of the Chapter, the MBM was used to investigate the influence of the diagrid geometry (diagonal inclination, floor plan shape, building aspect ratio) on both the lateral and torsional flexibility. From the results, it became pretty clear that the geometries that minimize the lateral displacements did not lead to minimum torsional rotations, and vice versa. Moreover, other than the lateral and torsional flexibility of the building, other responses should be minimized as well. Examples are the total mass of the diagrid structure as well as its construction. Therefore, there came the need to exploit a multi-response optimization procedure, where several responses were simultaneously minimized in order to find the most desirable structure. This was addressed by making use, for the first time in this research field, of the desirability function approach.

Firstly developed for the optimization of products and processes in industrial engineering, the desirability function approach was thoroughly exploited in the second part of this Chapter to select the optimal diagrid geometry. In particular, for a set of uniform- and varying-angle diagrid structures, the desirability function approach yielded the individuation of the most desirable structure in order to minimize both the lateral and torsional flexibility (for safety and serviceability purposes), the amount of structural mass (for sustainability and economic issues), and the complexity of the diagrid structure (for the purpose of construction easiness). Based on the results of the desirability calculations, which arose from the outcomes of the MBM-based structural analyses, the optimal diagrid structures were selected among a large set of solutions. The approach described in this Chapter will surely be beneficial for designers and researchers across various disciplines interested in finding the optimal diagrid shape in the preliminary design stages. Further research studies are also planned, in order to couple the desirability function approach with conventional optimization processes used in the structural engineering field, such as Genetic Algorithms, Particle Swarm Optimizations, etc.

In conclusion, as might have been appreciated throughout the reading of the previous Chapters, the focus of this Thesis has been directed onto the application of the same methodological framework, i.e. the ELM, to address different problems rather than addressing a very specific issue alone. To do so, the ELMs have shown their great versatility, as they allowed to tackle a variety of topics and explain a wide range of behaviors. It is also worthy of note that, as mentioned at the beginning of the Introduction, the ELMs can be seen as the structural systems that most simply exploit the generalized Hooke's law. This law is maybe one of the simplest yet most used concepts in Structural Mechanics, and this Thesis has exploited it to the greatest extend. Ultimately, in this Thesis, we have shown that the complexity of various systems can be tackled by cleverly using the right structural approaches, though simplified.

References

1. Hooke, R. *Lectiones Cutlerianae or a Collection of Lectures*; John Martyn Printer: London, 1679;
2. Kosteski, L.; Iturrioz, I.; Batista, R.G.; Cisilino, A.P. The truss-like discrete element method in fracture and damage mechanics. *Eng. Comput.* **2011**, *28*, 765–787.
3. Verdier, C. Rheological Properties of Living Materials. From Cells to Tissues. *J. Theor. Med.* **2003**, *5*, 67–91.
4. Nayfeh, A.H.; Hefzy, M.S. Continuum modeling of three-dimensional truss-like space structures. *AIAA J.* **1978**, *16*, 779–787.
5. Ingber, D. Tensegrity I. Cell structure and hierarchical systems biology. *J. Cell Sci.* **2003**, *116*, 1157–1173.
6. Carpinteri, A. *Advanced Structural Mechanics*; CRC Press, Taylor & Francis Group: Boca Raton, 2017;
7. Bazant, Z.P.; Cedolin, L. *Stability of Structures*; Oxford University Press, 1991;
8. Alberts, B.; Johnson, A.; Lewis, J.; Morgan, D.; Raff, M.; Roberts, K.; Walter, P. *Molecular Biology of the Cell, 6th Edition*; Garland Science: New York, 2002;
9. Bahar, I.; Jernigan, R.L.; Dill, K.A. *Protein Actions: Principles & Modeling*; Garland Science: New York, 2017;
10. Steward, K. Amino Acids – the Building Blocks of Proteins 2019.
11. Jana, N.D.; Das, S.; Sil, J. Backgournds on Protein Structure Prediction and Metaheuristics. In *A Metaheuristic Approach to Protein Structure Prediction. Emergence, Complexity and Computation, vol. 31*; Springer, Cham, 2018.
12. Pauling, L.; Corey, R.B.; Branson, H.R. The structure of proteins: Two hydrogen-bonded helical configurations of the polypeptide chain. *Proc. Natl. Acad. Sci. U. S. A.* **1951**, *37*, 205–211.
13. Pauling, L.; Corey, R.B. The pleated sheet, a new layer configuration of polypeptide chains. *Proc. Natl. Acad. Sci. U. S. A.* **1951**, *37*, 251–256.
14. Berman, H.M.; Westbrook, J.; Feng, Z.; Gilliland, G.; Bhat, T.N.; Weissig, H.; Shindyalov, I.N. The Protein Data Bank. *Nucleic Acids Res.* **2000**, *28*, 235–242.
15. Huang, D.M.; Chandler, D. Temperature and length scale dependence of hydrophobic effects and their possible implications for protein folding. *Proc. Natl. Acad. Sci. U. S. A.* **2000**, *97*, 8324–8327.
16. Anfinsen, C.B. The formation and stabilization of protein structure. *Biochem. J.* **1972**, *128*, 737–749.
17. Anfinsen, C.B. Principles that govern the folding of protein chains. *Science (80-.).* 1973.
18. Levinthal, C. Are there pathways for protein folding? *J. Chim. Phys.* **1968**.
19. Levinthal, C. How to Fold Graciously. In Mossbauer Spectroscopy in Biological Systems. *Univ. Illinois Press* **1969**.
20. Onuchic, J.N.; Luthey-Schulten, Z.; Wolynes, P.G. Theory of Protein Folding: The Energy Landscape Perspective. *Annu. Rev. Phys. Chem.* **1997**, *48*, 545–600.

21. Nunes, J.M. Tracking chaperone-mediated folding using force spectroscopy, 2012.
22. Go, N. Theoretical studies of protein folding. *Annu. Rev. Biophys. Bioeng.* **1983**, *12*, 183–210.
23. Dill, K.A.; Bromberg, S.; Yue, K.; Chan, H.S.; Ftebig, K.M.; Yee, D.P.; Thomas, P.D. Principles of protein folding — A perspective from simple exact models. *Protein Sci.* **1995**, *4*, 561–602.
24. Shirts, M.; Pande, V.S. Screen Savers of the World Unite! *Science (80-.).* **2000**, *290*, 1903–1904.
25. Karplus, M.; Kuriyan, J. Molecular dynamics and protein function. *Proc. Natl. Acad. Sci. U. S. A.* **2005**, *102*, 6679–6685.
26. Brooks, B.; Karplus, M. Harmonic dynamics of proteins: Normal modes and fluctuations in bovine pancreatic trypsin inhibitor. *Proc. Natl. Acad. Sci. U. S. A.* **1983**, *80*, 6571–6575.
27. Go, N.; Noguti, T.; Nishikawa, T. Dynamics of a small globular protein in terms of low-frequency vibrational modes. *Proc. Natl. Acad. Sci. U. S. A.* **1983**, *80*, 3696–3700.
28. Levitt, M.; Sander, C.; Stern, P.S. Protein normal-mode dynamics: Trypsin inhibitor, crambin, ribonuclease and lysozyme. *J. Mol. Biol.* **1985**, *181*, 423–447.
29. Tirion, M.M. Large amplitude elastic motions in proteins from a single-parameter, atomic analysis. *Phys. Rev. Lett.* **1996**, *77*, 1905–1908.
30. Bahar, I.; Atilgan, A.R.; Erman, B. Direct evaluation of thermal fluctuations in proteins using a single-parameter harmonic potential. *Fold. Des.* **1997**, *2*, 173–181.
31. Atilgan, A.R.; Durell, S.R.; Jernigan, R.L.; Demirel, M.C.; Keskin, O.; Bahar, I. Anisotropy of fluctuation dynamics of proteins with an elastic network model. *Biophys. J.* **2001**, *80*, 505–515.
32. Yang, L.; Song, G.; Jernigan, R.L. Protein elastic network models and the ranges of cooperativity. *Proc. Natl. Acad. Sci. U. S. A.* **2009**, *106*, 12347–12352.
33. Zimmermann, M.T.; Kloczkowski, A.; Jernigan, R.L. MAVENs: Motion analysis and visualization of elastic networks and structural ensembles. *BMC Bioinformatics* **2011**, *12*.
34. Eyal, E.; Yang, L.W.; Bahar, I. Anisotropic network model: Systematic evaluation and a new web interface. *Bioinformatics* **2006**, *22*, 2619–2627.
35. Hinsen, K. Analysis of Domain Motions by Approximate Normal Mode Calculations. *Proteins Struct. Funct. Genet.* **1998**, *429*, 417–429.
36. Durand, P.; Trinquier, G.; Sanejouand, Y. -H A new approach for determining low-frequency normal modes in macromolecules. *Biopolymers* **1994**, *34*, 759–771.
37. Tama, F.; Gadea, F.X.; Marques, O.; Sanejouand, Y.H. Building-block approach for determining low-frequency normal modes of macromolecules. *Proteins Struct. Funct. Genet.* **2000**, *41*, 1–7.
38. Hoffmann, A.; Grudinin, S. NOLB: Nonlinear Rigid Block Normal-Mode Analysis Method. *J. Chem. Theory Comput.* **2017**, *13*, 2123–2134.
39. Kurkcuoglu, O.; Jernigan, R.L.; Doruker, P. Mixed levels of coarse-graining of large proteins using elastic network model succeeds in extracting the slowest motions. *Polymer (Guildf).* **2004**.
40. Kurkcuoglu, O.; Jernigan, R.L.; Doruker, P. Collective dynamics of large proteins from mixed coarse-grained elastic network model. In Proceedings

of the QSAR and Combinatorial Science; 2005.
41. Song, G.; Jernigan, R.L. An enhanced elastic network model to represent the motions of domain-swapped proteins. *Proteins Struct. Funct. Genet.* **2006**.
42. Bahar, I.; Cui, Q. *Normal Mode Analysis: Theory and Applications to Biological and Chemical Systems*; Chapman & Hall: London, 2006;
43. Dykeman, E.C.; Sankey, O.F. Normal mode analysis and applications in biological physics. *J. Phys. Condens. Matter* **2010**, *22*, 423202.
44. Bahar, I.; Rader, A.J. Coarse-grained normal mode analysis in structural biology. *Curr. Opin. Struct. Biol.* **2005**, *15*, 586–592.
45. Rader, A.J. Coarse-grained models: Getting more with less. *Curr. Opin. Pharmacol.* **2010**, *10*, 753–759.
46. Keskin, O.; Jernigan, R.L.; Bahar, I. Proteins with similar architecture exhibit similar large-scale dynamic behavior. *Biophys. J.* **2000**, *78*, 2093–2106.
47. Mishra, S.K.; Jernigan, R.L. Protein dynamic communities from elastic network models align closely to the communities defined by molecular dynamics. *PLoS One* **2018**, *13*, 1–21.
48. Yang, L.; Song, G.; Carriquiry, A.; Jernigan, R.L. Close Correspondence between the Essential Protein Motions from Principal Component Analysis of Multiple HIV-1 Protease Structures and Elastic Network Modes. *Structure* **2008**, *16*, 321–330.
49. Sankar, K.; Mishra, S.K.; Jernigan, R.L. Comparisons of Protein Dynamics from Experimental Structure Ensembles, Molecular Dynamics Ensembles, and Coarse-Grained Elastic Network Models. *J. Phys. Chem. B* **2018**.
50. Yang, L.; Song, G.; Jernigan, R.L. Comparisons of Experimental and Computed Protein Anisotropic Temperature Factors. *Proteins* **2008**, *76*, 164–175.
51. Bathe, M. A finite element framework for computation of protein normal modes and mechanical response. *Proteins Struct. Funct. Bioinforma.* **2007**, *70*, 1595–1609.
52. Sedeh, R.S.; Yun, G.; Lee, J.Y.; Bathe, K.J.; Kim, D.N. A framework of finite element procedures for the analysis of proteins. *Comput. Struct.* **2018**, *196*, 24–35.
53. Rygula, A.; Majzner, K.; Marzec, K.M.; Kaczor, A.; Pilarczyk, M.; Baranska, M. Raman spectroscopy of proteins: A review. *J. Raman Spectrosc.* **2013**, *44*, 1061–1076.
54. Bunaciu, A.A.; Aboul-Enein, H.Y.; Hoang, V.D. Raman spectroscopy for protein analysis. *Appl. Spectrosc. Rev.* **2015**, *50*, 377–386.
55. Kuhar, N.; Sil, S.; Verma, T.; Umapathy, S. Challenges in application of Raman spectroscopy to biology and materials. *RSC Adv.* **2018**, *8*, 25888–25908.
56. Brown, K.G.; Erfurth, S.C.; Small, E.W.; Peticolas, W.L. Conformationally dependent low-frequency motions of proteins by laser Raman spectroscopy. *Proc. Natl. Acad. Sci. U. S. A.* **1972**, *69*, 1467–1469.
57. Chou, K.C. Identification of low-frequency modes in protein molecules. *Biochem. J.* **1983**, *215*, 465–469.
58. Chou, K.; Chen, N. The biological functions of low-frequency phonons. *Sci. Sin.* **1977**, *20*, 447–457.
59. Painter, P.C.; Mosher, L.; Rhoads, C. Low-frequency modes in the raman spectra of proteins. *Biopolymers* **1982**, *21*, 1469–1472.

60. Carpinteri, A.; Lacidogna, G.; Piana, G.; Bassani, A. Terahertz mechanical vibrations in lysozyme: Raman spectroscopy vs modal analysis. *J. Mol. Struct.* **2017**, *1139*, 222–230.
61. Lacidogna, G.; Piana, G.; Bassani, A.; Carpinteri, A. Raman spectroscopy of Na/K-ATPase with special focus on low-frequency vibrations. *Vib. Spectrosc.* **2017**, *92*, 298–301.
62. Falconer, R.J.; Markelz, A.G. Terahertz spectroscopic analysis of peptides and proteins. *J. Infrared, Millimeter, Terahertz Waves* **2012**, *33*, 973–988.
63. Markelz, A.G.; Roitberg, A.; Heilweil, E.J. Pulsed terahertz spectroscopy of DNA, bovine serum albumin and collagen between 0.1 and 2.0 THz. *Chem. Phys. Lett.* **2000**, *320*, 42–48.
64. Markelz, A.; Whitmire, S.; Hillebrecht, J.; Birge, R. THz time domain spectroscopy of biomolecular conformational modes. *Phys. Med. Biol.* **2002**, *47*, 3797–3805.
65. Acbas, G.; Niessen, K.A.; Snell, E.H.; Markelz, A.G. Optical measurements of long-range protein vibrations. *Nat. Commun.* **2014**, *5*, 1–7.
66. Niessen, K.A.; Xu, M.; Paciaroni, A.; Orecchini, A.; Snell, E.H.; Markelz, A.G. Moving in the Right Direction: Protein Vibrational Steering Function. *Biophys. J.* **2017**, *112*, 933–942.
67. Niessen, K.A.; Xu, M.; Markelz, A.G. Terahertz optical measurements of correlated motions with possible allosteric function. *Biophys. Rev.* **2015**, *7*, 201–216.
68. Carpinteri, A.; Piana, G.; Bassani, A.; Lacidogna, G. Terahertz vibration modes in Na/K-ATPase. *J. Biomol. Struct. Dyn.* **2019**, *37*, 256–264.
69. Lacidogna, G.; Scaramozzino, D.; Piana, G.; Carpinteri, A. Terahertz Protein Vibrations: The Usefulness of Coarse-Grained Numerical Models. In *Mechanics of Biological Systems and Materials & Micro-and Nanomechanics*; 2020; pp. 1–6.
70. Lacidogna, G.; Scaramozzino, D.; Piana, G.; Carpinteri, A. Exploring THz Protein Vibrations by Means of Modal Analysis: All-Atom vs Coarse-Grained Model. In *Proceedings of XXIV AIMETA Conference 2019. AIMETA 2019. Lecture Notes in Mechanical Engineering*; Carcaterra A., Paolone A., G.G., Ed.; Springer, Cham, 2020; pp. 881–888.
71. Scaramozzino, D.; Lacidogna, G.; Piana, G.; Carpinteri, A. A finite-element-based coarse-grained model for global protein vibration. *Meccanica* **2019**, *54*, 1927–1940.
72. https://www.lusas.cm.
73. Eyal, E.; Lum, G.; Bahar, I. The anisotropic network model web server at 2015 (ANM 2.0). *Bioinformatics* **2015**.
74. Allemang, R.J.; Brown, D.L. Correlation Coefficient for Modal Vector Analysis. *Proc. Int. Modal Anal. Conf. Exhib.* **1982**, 110–116.
75. Pastor, M.; Binda, M.; Harčarik, T. Modal assurance criterion. *Procedia Eng.* **2012**, *48*, 543–548.
76. Tama, F.; Sanejouand, Y.H. Conformational change of proteins arising from normal mode calculations. *Protein Eng.* **2001**, *14*, 1–6.
77. Mahajan, S.; Sanejouand, Y.H. On the relationship between low-frequency normal modes and the large-scale conformational changes of proteins. *Arch. Biochem. Biophys.* **2015**, *567*, 59–65.
78. Tobi, D.; Bahar, I. Structural changes involved in protein binding correlate with intrinsic motions of proteins in the unbound state. *Proc. Natl. Acad.*

Sci. U. S. A. **2005**, *102*, 18908–18913.
79. Zheng, W.; Brooks, B.R. Normal-modes-based prediction of protein conformational changes guided by distance constraints. *Biophys. J.* **2005**, *88*, 3109–3117.
80. Petrone, P.; Pande, V.S. Can conformational change be described by only a few normal modes? *Biophys. J.* **2006**, *90*, 1583–1593.
81. Yang, L.; Song, G.; Jernigan, R.L. How well can we understand large-scale protein motions using normal modes of elastic network models? *Biophys. J.* **2007**.
82. Scaramozzino, D.; Lacidogna, G.; Carpinteri, A. Protein Conformational Changes and Low-Frequency Vibrational Modes: A Similarity Analysis. *Mech. Biol. Syst. Mater. Micro-and Nanomechanics* **2020**, *4*, 7–10.
83. Khade, P.M.; Scaramozzino, D.; Kumar, A.; Jernigan, R.L.; Lacidogna, G.; Carpinteri, A. hdANM: elastic network model to study domain-hinge motion in protein. *Unpubl. Mater.* 2020.
84. Teodoro, M.L.; J, G.N.P.; Kavraki, L.E. A Dimensionality Reduction Approach to Modeling Protein Flexibility. In Proceedings of the Int. Conf. Comput. Mole. Biol; 2002; pp. 299–308.
85. Khade, P.M.; Kumar, A.; Jernigan, R.L. Characterizing and Predicting Protein Hinges for Mechanistic Insight. *J. Mol. Biol.* **2020**, *432*, 508–522.
86. Liu, J.; Sankar, K.; Wang, Y.; Jia, K.; Jernigan, R.L. Directional Force Originating from ATP Hydrolysis Drives the GroEL Conformational Change. *Biophys. J.* **2017**, *112*, 1561–1570.
87. Ikeguchi, M.; Ueno, J.; Sato, M.; Kidera, A. Protein structural change upon ligand binding: Linear response theory. *Phys. Rev. Lett.* **2005**, *94*, 1–4.
88. Atilgan, C.; Atilgan, A.R. Perturbation-response scanning reveals ligand entry-exit mechanisms of ferric binding protein. *PLoS Comput. Biol.* **2009**, *5*.
89. Atilgan, C.; Gerek, Z.N.; Ozkan, S.B.; Atilgan, A.R. Manipulation of conformational change in proteins by single-residue perturbations. *Biophys. J.* **2010**, *99*, 933–943.
90. Gerek, Z.N.; Ozkan, S.B. Change in allosteric network affects binding affinities of PDZ domains: Analysis through perturbation response scanning. *PLoS Comput. Biol.* **2011**, *7*, 18–25.
91. Eyal, E.; Bahar, I. Toward a molecular understanding of the anisotropic response of proteins to external forces: Insights from elastic network models. *Biophys. J.* **2008**, *94*, 3424–3435.
92. Scaramozzino, D.; Khade, P.M.; Jernigan, R.L.; Lacidogna, G.; Carpinteri, A. Structural Compliance: A New Metric for Protein Flexibility. *Proteins Struct. Funct. Bioinforma.* **2020**.
93. Scaramozzino, D.; Khade, P.M.; Jernigan, R.L.; Lacidogna, G.; Carpinteri, A. External random force bombardment on Elastic Network Models to measure protein flexibility. *Unpubl. Mater.* **2020**.
94. Kim, M.K.; Jernigan, R.L.; Chirikjian, G.S. Efficient generation of feasible pathways for protein conformational transitions. *Biophys. J.* **2002**, *83*, 1620–1630.
95. Kim, M.K.; Chirikjian, G.S.; Jernigan, R.L. Elastic models of conformational transitions in macromolecules. *J. Mol. Graph. Model.* **2002**, *21*, 151–160.
96. Maragakis, P.; Karplus, M. Large amplitude conformational change in proteins explored with a plastic network model: Adenylate kinase. *J. Mol.*

Biol. **2005**, *352*, 807–822.
97. Togashi, Y.; Mikhailov, A.S. Nonlinear relaxation dynamics in elastic networks and design principles of molecular machines. *Proc. Natl. Acad. Sci. U. S. A.* **2007**, *104*, 8697–8702.
98. Togashi, Y.; Yanagida, T.; Mikhailov, A.S. Nonlinearity of mechanochemical motions in motor proteins. *PLoS Comput. Biol.* **2010**, *6*, 1–9.
99. Scaramozzino, D.; Lacidogna, G.; Carpinteri, A. Protein Conformational Changes: What Can Geometric Nonlinear Analysis Tell Us? In *Proceedings of XXIV AIMETA Conference 2019. AIMETA 2019. Lecture Notes in Mechanical Engineering*; Carcaterra A., Paolone A., G.G., Ed.; Springer, Cham, 2020; pp. 889–897.
100. Scaramozzino, D.; Lacidogna, G.; Carpinteri, A. New Trends Towards Enhanced Structural Efficiency and Aesthetic Potential in Tall Buildings: The Case of Diagrids. *Appl. Sci.* **2020**, *10*, 3917.
101. Ali, M.M.; Moon, K.S. Structural Developments in Tall Buildings: Current Trends and Future Prospects. *Archit. Sci. Rev.* **2007**, *50*, 205–223.
102. Ali, M.M.; Moon, K.S. Advances in structural systems for tall buildings: Emerging developments for contemporary urban giants. *Buildings* **2018**, *8*, 104.
103. Maqhareh, M.R. The Evolutionary Process of Diagrid Structure Towards Architectural, Structural and Sustainability Concepts: Reviewing Case Studies. *J. Archit. Eng. Technol.* **2014**, *3*, 121.
104. Rahimian, A.; Eilon, Y. Hearst headquarters: Innovation and heritage in harmony. *CTBUH 2008, 8th World Congr. - Tall Green Typology a Sustain. Urban Futur. Congr. Proc.* **2008**, 648–653.
105. Munro, D. Swiss Res Building, London. *Nyheter Stålbyggnad* **2004**, 36–43.
106. Boake, T.M. *Diagrid Structures: Systems, Connections, Details*; De Gruyter, Ed.; De Gruyter: Basel, Switzerland, 2014; ISBN 9783038215646.
107. Asadi, E.; Adeli, H. Diagrid: An innovative, sustainable, and efficient structural system. *Struct. Des. Tall Spec. Build.* **2017**, *26*, e1358.
108. Angelucci, G.; Mollaioli, F. Diagrid structural systems for tall buildings: Changing pattern configuration through topological assessments. *Struct. Des. Tall Spec. Build.* **2017**, e1396.
109. Moon, K.S.; Connor, J.J.; Fernandez, J.E. Diagrid structural systems for tall buildings: Characteristics and methodology for preliminary design. *Struct. Des. Tall Spec. Build.* **2007**, *16*, 205–230.
110. Moon, K.S. Sustainable structural engineering strategies for tall buildings. *Struct. Des. Tall Spec. Build.* **2008**, *17*, 895–914.
111. Montuori, G.M.; Mele, E.; Brandonisio, G.; De Luca, A. Design criteria for diagrid tall buildings: Stiffness versus strength. *Struct. Des. Tall Spec. Build.* **2014**, *23*, 1294–1314.
112. Mele, E. 19.04: Diagrid: the renaissance of steel structures for tall buildings geometry, design, behavior. *Ce/Papers* **2017**, *1*, 4437–4446.
113. Mele, E.; Imbimbo, M.; Tomei, V. The effect of slenderness on the design of diagrid structures. *Int. J. High-Rise Build.* **2019**, *8*, 83–94.
114. Mele, E.; Toreno, M.; Brandonisio, G.; De Luca, A. Diagrid structures for tall buildings: Case studies and design considerations. *Struct. Des. Tall Spec. Build.* **2014**, *23*, 124–145.
115. Liu, C.; Ma, K. Calculation model of the lateral stiffness of high-rise diagrid tube structures based on the modular method. *Struct. Des. Tall*

Spec. Build. **2017**, *26*, e1333.
116. Scaramozzino, D. Diagrid structural systems for high-rise buildings: An analytical approach, Politecnico di Torino, Torino, Italy, 2017.
117. Lacidogna, G.; Scaramozzino, D.; Carpinteri, A. A matrix-based method for the structural analysis of diagrid systems. *Eng. Struct.* **2019**, *193*, 340–352.
118. Carpinteri, A.; Carpinteri, A. Lateral loading distribution between the elements of a three-dimensional civil structure. *Comput. Struct.* **1985**, *21*, 563–580.
119. Carpinteri, A.; Lacidogna, G.; Puzzi, S. A global approach for three-dimensional analysis of tall buildings. *Struct. Des. Tall Spec. Build.* **2010**, *19*, 518–536.
120. Vlasov, V.Z. *Thin-Walled Elastic Beams*; Israel program for scientific translation, 1961;
121. Carpinteri, A.; Lacidogna, G.; Montrucchio, B.; Cammarano, S. The effect of the warping deformation on the structural behaviour of thin-walled open section shear walls. *Thin-Walled Struct.* **2014**, *84*, 335–343.
122. Carpinteri, A.; Corrado, M.; Lacidogna, G.; Cammarano, S. Lateral load effects on tall shear wall structures of different height. *Struct. Eng. Mech.* **2012**, *41*, 313–337.
123. Carpinteri, A.; Lacidogna, G.; Cammarano, S. Conceptual design of tall and unconventionally shaped structures: A handy analytical method. *Adv. Struct. Eng.* **2014**, *17*, 767–783.
124. Lacidogna, G. Tall buildings: Secondary effects on the structural behaviour. *Proc. Inst. Civ. Eng. Struct. Build.* **2017**, *170*, 391–405.
125. Carpinteri, A.; Lacidogna, G.; Nitti, G. Open and closed shear-walls in high-rise structural systems: Static and dynamic analysis. *Curved Layer. Struct.* **2016**, *3*, 154–171.
126. Carpinteri, A.; Lacidogna, G.; Cammarano, S. Structural analysis of high-rise buildings under horizontal loads: A study on the Intesa Sanpaolo Tower in Turin. *Eng. Struct.* **2013**, *56*, 1362–1371.
127. Nitti, G.; Lacidogna, G.; Carpinteri, A. Structural Analysis of High-rise Buildings under Horizontal Loads: A Study on the Piedmont Region Headquarters Tower in Turin. *Open Constr. Build. Technol. J.* **2019**, *13*, 81–96.
128. Nitti, G.; Lacidogna, G.; Carpinteri, A. Tall buildings subjected to horizontal loading: Analysis of two case studies by an in-house numerical code. In Proceedings of the AIMETA 2017 - Proceedings of the 23rd Conference of the Italian Association of Theoretical and Applied Mechanics; 2017.
129. Lacidogna, G.; Nitti, G.; Scaramozzino, D.; Carpinteri, A. Diagrid systems coupled with closed- and open-section shear walls : Optimization of geometrical characteristics in tall buildings. *Procedia Manuf.* **2020**, *00*.
130. Zhao, F.; Zhang, C. Diagonal arrangements of diagrid tube structures for preliminary design. *Struct. Des. Tall Spec. Build.* **2015**, *24*, 157–175.
131. Moon, K.S. Optimal grid geometry of diagrid structures for tall buildings. *Archit. Sci. Rev.* **2008**, *51*, 239–251.
132. Zhang, C.; Zhao, F.; Liu, Y. Diagrid tube structures composed of straight diagonals with gradually varying angles. *Struct. Des. Tall Spec. Build.* **2012**, *21*, 283–295.
133. Montuori, G.M.; Mele, E.; Brandonisio, G.; De Luca, A. Geometrical

patterns for diagrid buildings: Exploring alternative design strategies from the structural point of view. *Eng. Struct.* **2014**, *71*, 112–127.
134. Tomei, V.; Imbimbo, M.; Mele, E. Optimization of structural patterns for tall buildings: The case of diagrid. *Eng. Struct.* **2018**, *171*, 280–297.
135. Mirniazmandan, S.; Alaghmandan, M.; Barazande, F.; Rahimianzarif, E. Mutual effect of geometric modifications and diagrid structure on structural optimization of tall buildings. *Archit. Sci. Rev.* **2018**, *61*, 371–383.
136. Ardekani, A.; Dabbaghchian, I.; Alaghmandan, M.; Golabchi, M.; Hosseini, S.M.; Mirghaderi, S.R. Parametric design of diagrid tall buildings regarding structural efficiency. *Archit. Sci. Rev.* **2020**, *63*, 87–102.
137. Lacidogna, G.; Scaramozzino, D.; Carpinteri, A. Influence of the geometrical shape on the structural behavior of diagrid tall buildings under lateral and torque actions. *Dev. Built Environ.* **2020**, *2*, 100009.
138. Moon, K.S. Diagrid structures for complex-shaped tall buildings. *Procedia Eng.* **2011**, *14*, 1343–1350.
139. Harrington, E.C. The desirability function. *Ind. Qual. Control* **1965**, *4*, 494–498.
140. Derringer, G.C.; Suich, R. Simultaneous optimization of several response variables. *J. Qual. Technol.* **1980**, *12*, 214–219.
141. Vera Candioti, L.; De Zan, M.M.; Camara, M.S.; Goicoechea, H.C. Experimental design and multiple response optimization. Using the desirability function in analytical methods development. *Talanta* **2014**, *124*, 123–138.
142. Lacidogna, G.; Scaramozzino, D.; Carpinteri, A. Optimization of diagrid geometry based on the desirability function approach. *Curved Layer. Struct.* **2020**, *7*, 139–152.

List of Publications

Publications in International Peer-Reviewed Journals

1. Lacidogna, G.; Scaramozzino, D.; Carpinteri, A. A matrix-based method for the structural analysis of diagrid systems. *Eng. Struct.* 2019, *193*, 340–352.
2. Scaramozzino, D.; Lacidogna, G.; Piana, G.; Carpinteri, A. A finite-element-based coarse-grained model for global protein vibration. *Meccanica* 2019, *54*, 1927–1940.
3. Lacidogna, G.; Scaramozzino, D.; Carpinteri, A. Influence of the geometrical shape on the structural behavior of diagrid tall buildings under lateral and torque actions. *Dev. Built Environ.* 2020, *2*, 100009.
4. Scaramozzino, D.; Lacidogna, G.; Carpinteri, A. New trends towards enhanced structural efficiency and aesthetic potential in tall buildings: The case of diagrids. *Appl. Sci*. 2020, *10*, 3917.
5. Scaramozzino, D.; Khade, P. M.; Jernigan, R. L.; Lacidogna, G.; Carpinteri, A. Structural compliance: A new metric for protein flexibility. *Proteins Struct. Funct. Bioinforma.* 2020, *88*, 1482-1492.
6. Lacidogna, G.; Scaramozzino, D.; Carpinteri, A. Optimization of diagrid geometry based on the desirability function approach. *Curved Layer. Struct.* 2020, *7*, 139-152.
7. Carpinteri, A.; Lacidogna, G.; Scaramozzino, D. Geometrically nonlinear behavior of lattice domes coupled with local Eulerian instability. *Curved Layer. Struct.* 2020, accepted.

Publications in Conference Proceedings

1. Lacidogna, G.; Scaramozzino, D.; Piana, G.; Carpinteri, A. Terahertz protein vibrations: The usefulness of coarse-grained numerical models. In *Mechanics of Biological Systems and Materials & Micro- and Nanomechanics.* 2020, *4*, 1–6.
2. Scaramozzino, D.; Lacidogna, G.; Carpinteri, A. Protein conformational changes and low-frequency vibrational modes: A similarity analysis. In *Mechanics of Biological Systems and Materials & Micro- and Nanomechanics.* 2020, *4*, 7–10.
3. Lacidogna, G.; Scaramozzino, D.; Piana, G.; Carpinteri, A. Exploring THz protein vibrations by means of modal analysis: All-atom vs coarse-grained model. In *Proceedings of XXIV AIMETA Conference 2019. AIMETA 2019. Lecture Notes in Mechanical Engineering.* Carcaterrra, A.; Paolone, A.; Graziani, G. 2020, 881–888.

4. Scaramozzino, D.; Lacidogna, G.; Carpinteri, A. Protein conformational changes: What can geometric nonlinear analysis tell us? In *Proceedings of XXIV AIMETA Conference 2019. AIMETA 2019. Lecture Notes in Mechanical Engineering.* Carcaterrra, A.; Paolone, A.; Graziani, G. 2020, 889–897.
5. Lacidogna, G.; Nitti, G.; Scaramozzino, D.; Carpinteri, A. Diagrid systems coupled with closed- and open-section shear walls: Optimization of geometrical characteristics in tall buildings. *Procedia Manuf.* 2020, *44*, 402–409.